TUM School of Natural Sciences

New Analysis Methods for Enhanced Sensitivity to Light Dark Matter at CRESST-III and Studies of Discovery Potential for Next Generation Cryogenic Experiments

Dominik Raphael Fuchs

Vollständiger Abdruck der von der TUM School of Natural Sciences der Technischen Universität München zur Erlangung des akademischen Grades eines Doktors der Naturwissenschaften (Dr. rer. nat.) genehmigten Dissertation.

Vorsitz: Prof. Dr. Alejandro Ibarra

Prüfer*innen der Dissertation:
1. Prof. Dr. Susanne Mertens
2. Prof. Dr. Lothar Oberauer

Die Dissertation wurde am 23.05.2023 bei der Technischen Universität München eingereicht und durch die TUM School of Natural Sciences am 21.09.2023 angenommen.

Contents

Abstract

The search for dark matter is one of the biggest challenges of modern-day physics. Convincing evidence for the existence of this non-luminescent matter has been found on various scales of the Universe over the course of the last century. However, despite many experimental efforts, the nature of dark matter has still to be unveiled.

The CRESST-III (Cryogenic Rare Event Search with Superconducting Thermometers) experiments main goal is the direct detection of dark matter particles via their scattering off target nuclei in cryogenic detectors. The detectors are equipped with transition edge sensors (TES), operated at around 15 mK. These sensors reach sensitivities down to very low energy depositions ($\leq$ 100 eV), allowing for the search of dark matter particles with sub-GeV masses. This makes CRESST one of the world-leading experiments in low-mass dark matter search. Since the expected rate of a dark matter signal is extremely low, a low-background environment is necessary. The CRESST experiment is therefore located in an underground facility and is protected against environmental radioactivity by several shielding layers. The background is further reduced by using particle discrimination on an event-by-event basis, which is possible by simultaneously measuring every event's heat and light signal.

As CRESST started to explore the energy regions below a few hundred eV, an unexpected rise in the number of events was observed. The origin of this Low Energy Excess (LEE) is not yet understood. A dark matter explanation of these events is disfavoured, making this excess the main limitation for further improving the sensitivity of CRESST. It is therefore a crucial factor for the experiment to understand the origin of the LEE.

This thesis consists of two main parts: The first part will focus on the analysis of two sapphire (Al_2O_3) modules. This analysis includes two novel ways for energy calibration. Furthermore, the LEE is investigated, focusing on the rate and spectral shape's time, energy and temperature dependencies, in order to narrow down the list of possible origins of the LEE. The dark matter analysis of the data of one of the detectors allows a new leading exclusion limit for spin-independent dark matter interactions.

The second part will focus on sensitivity studies for future experiments using cryogenic detectors for direct detection. Once these experiments reach the necessary exposures to become sensitive to coherent elastic neutrino-nucleus scattering (CEνNS) with solar neutrinos, it will become crucial to have a good description of the corresponding expected backgrounds. Understanding the solar neutrino signal allows for having sensitivity to a potential dark matter signal even below the neutrino floor. Furthermore,

being sensitive to solar neutrinos is an opportunity to study the solar model and some aspects of neutrino physics. This thesis gives an overview of the exposures, thresholds and background levels necessary to measure the coherent scattering of solar neutrinos with nuclei in cryogenic detectors.

Zusammenfassung

Die Suche nach Dunkler Materie ist eine der größten Herausforderungen der modernen Physik. Im Laufe des letzten Jahrhunderts wurden überzeugende Hinweise auf die Existenz dieser nicht leuchtenden Materie auf verschiedenen Größenskalen des Universums gefunden. Dennoch konnte trotz der vielen experimentellen Bemühungen die tatsächliche Natur der Dunklen Materie noch nicht enthüllt werden.

Das Hauptziel des CRESST-III Experiments ist der direkte Nachweis Dunkler Materie-Teilchen über deren Streuung an Atomkernen in kryogenen Detektoren. Die Detektoren sind mit einem Übergangskantensensor (TES) ausgestattet, welcher bei einer Temperatur von ungefähr 15 mK betrieben wird. Diese Sensoren erreichen Sensitivitäten zu sehr niedrigen Energiedepositionen ($\leq$ 100 eV), was die Suche nach Dunklen Materie Teilchen mit Massen von weniger als einem GeV ermöglicht. Dies macht CRESST zu einem der weltweit führenden Experimente in der Suche nach leichter Dunkler Materie. Da die erwartete Rate eines Dunkle Materie Signals extrem niedrig ist, ist eine Umgebung mit niedrigem Untergrund notwendig. Deshalb befindet sich das CRESST Experiment in einem Untergrundlabor und ist durch mehrere Schichten Abschirmung vor Radioaktivität aus der Umgebung geschützt. Durch die gleichzeitige Messung des Wärme- und Licht-Signals eines jeden Ereignisses ist eine Unterscheidung verschiedener Teilchenarten und dadurch eine weitere Untergrundunterdrückung möglich.

Als CRESST begann die Energiebereiche unterhalb einiger hundert eV zu erforschen, wurde ein unerwarteter Anstieg in der Anzahl an gemessenen Ereignissen beobachtet (LEE). Der Ursprung des LEE bei niedrigen Energien ist noch nicht verstanden. Eine Dunkle Materie Erklärung dieser Ereignisse ist jedoch unwahrscheinlich, wodurch der LEE zum hauptsächlich limitierenden Faktor für die Sensitivität von CRESST wird. Es ist daher von großer Wichtigkeit für das Experiment, den Ursprung des LEE bei niedrigen Energien zu verstehen.

Diese Arbeit besteht aus zwei Teilen: Der erste Teil beschäftigt sich mit der Analyse von zwei Saphir (Al_2O_3) Modulen. Diese Analyse umfasst unter anderem zwei neue Methoden der Energiekalibration. Darüber hinaus wird der LEE bei niedrigen Energien untersucht. Der Fokus liegt dabei auf den Abängigkeiten der Rate und der spektralen Form von Zeit, Energie und Temperatur, um die Liste an möglichen Ursprüngen des LEEs einzuschränken. Die Analyse der Daten von einem der Detektoren führt zu einer neuen führenden Ausschlussgrenze für spin-unabhängige Wechselwirkungen zwischen Dunkler Materie und Atomkernen.

Der zweite Teil beschäftigt sich mit Sensitivitätsstudien für zukünftige Experimente, welche kryogene Detektoren für einen direkten Nachweis von Dunkler Materie verwenden. Mit einer ausreichend großen Kombination aus Detektormasse und Messzeit werden diese empfindlich für kohärente elastische Streuung zwischen solaren Neutrinos und Atomkernen. Sobald diese Sensitivitäten erreicht werden, ist es unumgänglich eine gute Beschreibung des damit verbundenen erwarteten Untergrunds zu haben. Ein Verständnis des Signals das von solaren Neutrinos erzeugt wird ermöglicht es auch in Präsenz dieses Neutrino Untergrunds sensitiv auf potentielle Dunkle Materie Signale zu sein. Des Weiteren bietet sich dadurch die Möglichkeit sowohl das Modell unserer Sonne als auch einige Aspekte der Neutrino Physik zu untersuchen. In dieser Arbeit wird ein Überblick über die Bedingungen gegeben, die ein Experiment erfüllen muss, um kohärente Streuung von solaren Neutrinos an den Atomkernen in kryogenen Detektoren messen zu können. Diese umfassen eine Kombination aus benötigter Detektormasse und Messzeit, den notwendigen Energieschwellen und den maximal erlaubten Untergrundraten.

Chapter 1

Introduction

The idea of the existence of some non-luminous matter started to come up already at the beginning of the 20th century when physicists and astronomers studied stellar velocities. In 1922, in an attempt to provide a theory that could explain the observed motions of stars, J.C. Kapteyn used the term *dark matter* to describe an invisible matter whose effect could only be seen gravitationally [1]. More attempts to estimate the amount of dark matter by studying stellar motions in our galaxy were done by J.H. Jeans in 1922 [2] and J.H. Oort in 1927 [3] and 1932 [4]. In 1933, F. Zwicky was the first to find evidence for the existence of dark matter on larger scales by looking at the velocities of galaxies inside the COMA cluster [5]. The individual galaxies were moving too fast to be gravitationally bound to the cluster, at least unless the total mass of the cluster would be much higher than the mass that could be attributed to the observable luminous matter. Decades later, further strong evidence came from measurements of the rotation curves of stars in galaxies. The work of V. Rubin, W. K. Ford and N. Thonnard in the 1960s and 70s showed that dark matter is needed to explain the velocity curve of spiral galaxies [6, 7].

At present, the need to include dark matter in our description of the universe is widely accepted. The ΛCDM (Lambda Cold Dark Matter) model is currently used as the standard model of Big Bang cosmology. It parameterizes the contribution of single components to the total energy density of our universe. Based on the results of the Planck collaboration and using this model, about 68.9% of the universes content consists of so-called dark energy while the contribution of matter is about 31.1%, which can be divided into the contribution of baryonic matter (4.9%) and dark matter (26%) [8]. This shows that dark matter is a major building block of our universe, which naturally raises the question about its nature.

In the last decades the field of dark matter physics kept growing as an increasing number of observations pointed towards its existence. At the same time, theorists came up with a large variety of possible dark matter candidates. Many, but not all of them, suggest that dark matter consists of at least one new particle not included in the standard model of particle physics. Today, despite the immense efforts from both, experiments and theory, the mystery about the origin of dark matter could still not be solved.

In Chapter 2 the dark matter problem will be described in more detail. Starting with

the cosmological framework, followed by the evidences we have for the existence of dark matter and a list of the most important particle candidates, as well as some alternative ideas.

Chapter 3 will give an overview of the different experimental techniques in the search for dark matter. The focus here will be on direct detection experiments. After an introduction to the general theoretical foundations, the different approaches that are commonly used will be covered. This chapter will also give an introduction on coherent elastic neutrino-nucleus scattering (CEνNS), which poses a major challenge for the future of direct detection experiments.

One of the still unknown properties of dark matter include its mass. With direct detection experiments it is possible to cover a wide range of dark matter particle masses ($\mathcal{O}$(keV) - $\mathcal{O}$(TeV)). Here one has to distinguish between experiments looking for a signature of dark matter scattering on electrons ($\mathcal{O}$(keV) - $\mathcal{O}$(MeV)) and experiments looking for a scattering on nuclei ($\mathcal{O}$(MeV) - $\mathcal{O}$(TeV)). The CRESST (Cryogenic Rare Event Search with Superconducting Thermometers) experiment belongs to the second type. Over the years the experiment has been optimized to become especially sensitive to very small energy depositions, which helped to establish its position as one of the world leading experiments in the sub-GeV dark matter mass regime. The CRESST detector modules consist of single crystals used as cryogenic calorimeters. These are equipped with a Tungsten Transition Edge Sensor (W-TES) that is operated at temperatures of $\mathcal{O}$(15 mK). These sensors are sensitive to $\mathcal{O}$(µK) changes of temperature, induced by the scattering of an incoming particle on a single nucleus. For simple kinematic reasons, given a fixed target mass, the lighter the mass of an incoming dark matter particle is, the smaller the energy will be. Herein lies one of the big challenges for the experiments. The dark matter mass range CRESST has specialized on ($\mathcal{O}$(MeV) - $\mathcal{O}$(GeV)) typically leads to recoil energies of only $\mathcal{O}$(eV) - $\mathcal{O}$(keV). Sensitivity to these low energies is achieved by continuous improvement and optimization of the sensor and detector designs, read-out methods and analysis tools. Another big challenge are the very low expected signal rates. This is a common problem for all rare event searches and, like most other experiments of this kind, in order to reduce the backgrounds as much as possible, CRESST is located in an underground laboratory, where the flux of cosmic radiation, muons in particular, are reduced by several orders of magnitude. Additionally, CRESST is surrounded by several layers of shielding and an active muon veto system.

A more detailed introduction to the CRESST-III experiment is given in chapter 4. After a short illustration of the experimental setup, an in-depth description of the working principle of the detectors as well as the data acquisition systems will be presented.

The following chapter will cover the basics of data analysis in CRESST. Going from the raw data processing to the creation of the final energy spectra and eventually the calculation of either dark matter exclusion limits or, in case of a signal, a fit of the dark matter parameters. During the first step most of the relevant parameters of single events

are calculated. Based on these parameters the selection criteria are defined and applied to the data. The data set is then calibrated using a combination of a radioactive source and artificially injected events of known energy. Finally the energy dependent survival probability of the events is determined, which is needed for the comparison of spectra between different detectors and for the computation of exclusion limits or of a possible dark matter signal fit.

With the detector module design of the third phase of CRESST (CRESST-III) it became possible to probe the energy regions below a few hundred eV nuclear recoil energies, which allowed CRESST to become sensitive to sub-GeV dark matter masses and set the aforementioned world leading exclusion limits. At the same time a sharp rise of the event rate at low energies that exceeded the expections of the known backgrounds was observed. This excess of events turned out to be present in all detectors that had sufficiently low thresholds in the same measurement phase, as well as the following measurement campaigns of CRESST-III. Since the presence of these events severly affects the further improvement of the CRESST sensitivity, it became the top priority to study the origin of this Low Energy Excess (LEE). The ultimate goal is to either be able to remove the excess events completely or to understand their underlying nature well enough to include them in an accurate description of the background. For this reason a number of modifications has been applied to the standard detector module design in the recent measurements. Each of these modifications was done to test a specific hypothesis about the origin of the LEE. Chapter 6 will be fully dedicated to the LEE in the CRESST-III measurements. First, all the modifications that were applied to the modules are listed, then the observations are presented. One important characteristic of the LEE that was observed is the exponential decrease of the rate over time. Another interesting obervation is an increased rate after a warm-up of the cryostat to certain temperatures, which is followed by a relatively fast exponential decrease of the rate. Finally the conclusions that can be drawn from the current data are given.

Chapter 7 will focus on the analysis of two sapphire detector modules. In the beginning some studies of the noise distribution of these modules is presented. Afterwards the data obtained during a neutron calibration is studied. The energy spectrum of the neutron calibration contains a small peak at 1.1 keV, which might originate from nuclear recoils that occur due to the emission of single gammas after a preceding capture of a thermal neutron in ^{27}Al. This peak could be used for low energy calibration, which would remove the need to put other radioactive sources in the vicinity of the detectors. Before moving to the final energy spectra, a special focus is made on the light detector of one of the sapphire modules. This detector could be calibrated via the detection of single luminescence photons, which were observed in CRESST for the first time. Afterwards, the final energy spectra are shown and compared with each other. In one of the modules an unexpected peak-like feature in the energy spectrum was observed at about 190 eV. Despite thorough investigations, the origin of this peak could not be determined

with certainty. Furthermore some detailed studies of the LEE in the sapphire detectors were done. Especially the time dependence of the rate and the parameters empirically describing the excess is investigated. At last, the dark matter results obtained from the sapphire modules are shown, including a new, world-leading limit at low dark matter masses.

The last part of this thesis concentrates on sensitivity studies regarding the influence of CEνNS on future direct detection experiments. CRESST is currently planning and preparing for a major upgrade of the experimental setup, which will increase the exposures significantly. Once the excess is understood and the exposures are increased, CRESST will eventually start to approach the neutrino floor. This makes it important to study the expected signals and the influence they have on the search for dark matter. In the energy range that is most interesting for CRESST, solar neutrinos are by far the most dominant component of neutrino backgrounds. In the beginning of chapter 8 the solar neutrino model is introduced. In the first part of this chapter neutrinos are treated as a background for dark matter searches. After the definition and calculation of the solar neutrino floor, the sensitivities to dark matter signals in presence of this neutrino background are calculated. The second part of chapter 8 treats solar neutrinos as the main signal. CEνNS from the Sun hold a lot of potential for interesting research in non dark matter related fields of physics. Therefore the experimental conditions needed to have sensitivity to solar neutrinos are explored for two different experimental settings.

Finally the last chapter will give a summary of the results of this thesis and an outlook.

Chapter 2

Dark Matter

This chapter is giving a brief overview of *dark matter*. The cosmological framework is presented in sec. 2.1, followed by a list of important observations that are interpreted as evidences for the existence of dark matter in sec. 2.2. A short introduction to some important dark matter particle candidates is given in sec. 2.3. At last, sec. 2.4 shows some alternative, 'non-particle'-solutions to the dark matter problem.

2.1 Cosmological Framework

In the framework of general relativity, the universe is described by **Einstein's field equation**:

$$G_{\mu\nu} + \Lambda g_{\mu\nu} = \frac{8\pi G}{c^4} T_{\mu\nu} \tag{2.1}$$

which relates the geometry of space-time, described by the Einstein tensor $G_{\mu\nu}$, with the flux and density of energy in space and time, described by the stress-energy tensor $T_{\mu\nu}$. G is the Newton gravitational constant, $g_{\mu\nu}$ is the metric tensor and Λ is the cosmological constant.

Expansion of the Universe: In 1929, E. Hubble published his observations on the measurements of the redshift of spectral lines of galaxies at various distances [9]. Induced by the Doppler effect, the measured wavelength of the emitted light is shifted to shorter (longer) wavelenghts, if the observed galaxy is approaching (moving away) from us. Hubble found, that (with the exception of a few very close ones) all galaxies are moving away from our Milky Way. Moreover, he found that the redshift depends on the relative distance of the observed galaxy. The relation between this distance, d, and the galaxies velocity[1], v, is described by the **Hubble's law**:

$$v = H_0 d \tag{2.2}$$

[1]The velocity of a galaxy can be inferred from its redshift.

with H_0 being the Hubble constant at present time. Knowing about the observations of an expanding Universe, in 1927[2], G. Lemaître provided a theoretical explanation by introducing a time-dependent scale factor $a(t)$ to describe the expansion of the Universe [10]:

$$v = \frac{\dot{a}(t)}{a(t)} d \tag{2.3}$$

which is equal to the Hubble's law, if the expansion rate of the Universe is defined as: $H(t) = \frac{\dot{a}(t)}{a(t)}$.

Solution to Einstein's field equation: Using the **cosmological principle**, which states that the Universe is isotropic and homogeneous on very large scales, the distance between two points can be described by the **Friedmann-Lemaître-Robertson-Walker** (FLRW) metric:

$$ds^2 = c^2 dt^2 - a^2(t) \left[\frac{dr^2}{1 - kr^2} + r^2 \left(d\theta^2 + sin^2 \theta d\phi^2 \right) \right] \tag{2.4}$$

in the comoving coordinates (r, θ, ϕ), with $a(t)$ being the scale factor, introduced in eq. 2.3, and $k\,(k = 0, \pm 1)$ describing the curvature of the Universe. Inserting this into Einstein's field equation leads to the **Friedmann equation**:

$$H^2(t) = \left(\frac{\dot{a}(t)}{a(t)} \right)^2 = \frac{8\pi G\rho}{3} - \frac{kc^2}{a^2(t)} + \frac{c^2 \Lambda}{3} \tag{2.5}$$

With the definition of the **critical density**, ρ_c, as:

$$\rho_c = \frac{3H_0^2}{8\pi G} \tag{2.6}$$

the present day densities can be expressed as the fraction of the critical density, called the density parameter:

$$\Omega_i = \frac{\rho_i}{\rho_c} \tag{2.7}$$

The Friedmann equation (eq. 2.5) can be written in terms of the density parameters as:

$$\Omega = \Omega_R + \Omega_M + \Omega_\Lambda - \Omega_k = 1 \tag{2.8}$$

with the total density Ω being a sum of the individual contributions from radiation, Ω_R, matter, Ω_M and the cosmological constant, Ω_Λ[3]. The term Ω_k corresponds to the curvature, k, of space-time. The case $k = -1$ corresponds to a hyperbolic (or open) Universe, while a $k = +1$ corresponds to a spherical (or closed) Universe.

[2]The observations of the expansion were already available at this time.
[3]This contribution is typically assigned to the so-called *dark energy*.

Measurements of the Planck collaboration [8] and the WMAP collaboration [11] show that the curvature of the Universe is nearly flat ($k = 0$) and thus, the term Ω_k vanishes. In the ΛCDM model, the largest contributions to the total energy density of the universe are Ω_Λ and Ω_M, with the latter being further subdivided into the contribution of baryonic matter, Ω_B, neutrinos, Ω_ν and dark matter, Ω_χ, etc.:

$$\Omega_M = \Omega_B + \Omega_\nu + \Omega_\chi + ... \tag{2.9}$$

The largest contribution to Ω_M comes from dark matter, which is roughly five times larger than the contribution of baryonic matter.

2.2 Evidence for Dark Matter

In this section, some of the main observations indicating the existence of dark matter are discussed. Interestingly, evidence for the existance of dark matter is found on all different astronomical scales.

2.2.1 Cosmic Microwave Background (CMB)

In the early Universe, electrically charged matter was strongly coupled with electromagnetic radiation, so the production and disintegration of hydrogen were in equilibrium:

$$p + e^- \leftrightarrow H + \gamma \tag{2.10}$$

With the expansion of the Universe also its temperature decreased until eventually, 380.000 years after the Big Bang, the mean energy of photons became too low[4] to break up the neutral hydrogen atoms into protons and electrons. Since then, photons can travel freely through matter and thus, the Universe is said to have become *transparent*.

The **Cosmic Microwave Background** (CMB) that we observe today consists of these photons (produced during the last recombinations). After the discovery of the CMB in 1964 by A. Penzias and R. Wilson [12], this was immediately interpreted as an echo of the Big Bang by R. H. Dicke [13]. Measurements of the CMB reveal an almost perfect black body spectrum with a temperature of T = (2.7260 $\pm$ 0.0013) K [14]. With increasing precision measurements of the CMB, small anisotropies of $\mathcal{O}(10^{-5}\text{K})$ became apparent. A temperature map of the CMB, measured by the Planck collaboration, is shown in fig. 2.1 [15].

These anisotropies in the temperature of the CMB are a reflection of the distribution of the baryonic matter at the time of the decoupling of the CMB photons. A photon produced in a dense region of the Universe looses energy while escaping the gravitational potential, which leads to a stronger redshift compared to an average CMB photon. Vice

[4] At this time, the temperature of the Universe was roughly $0.3\text{eV}/k_B$.

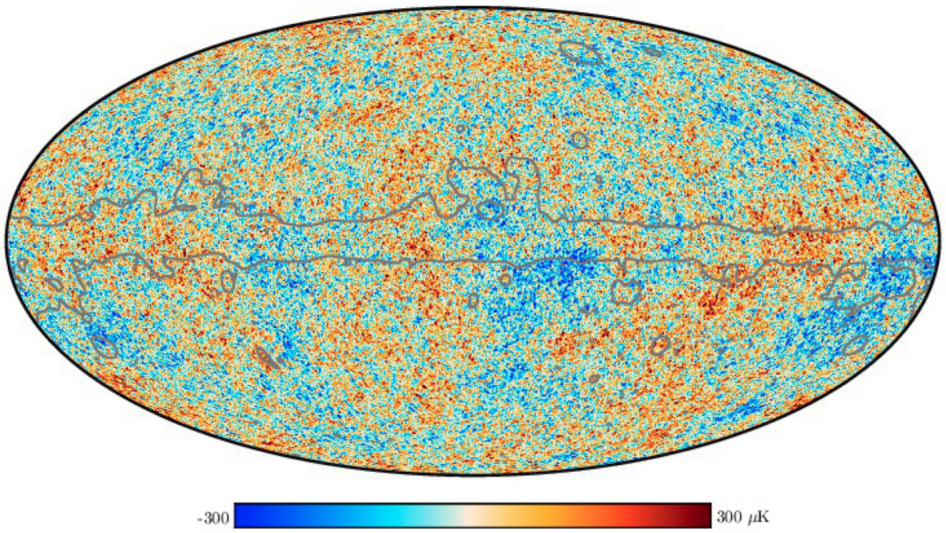

Figure 2.1: Temperature map of the CMB. The colors refer to the deviation from the mean temperature. The grey contour marks the region of the galactic foreground substraction. Image taken from [15].

versa, photons emitted in a low-density area of the Universe appear blueshifted. This effect is known as the Sachs-Wolfe-Effect [16].

The fact that the baryonic matter was not perfectly homogeneous at the time of the decoupling is already a strong hint for the existence of dark matter. The dominant electromagnetic radiation would have immediately washed out any random fluctuations, leading to a perfect black body spectrum. The appearance of anisotropies can be explained, if an additional massive component, which is not or at least not significantly affected by the radiation, is added to the picture. The gravitational potential of this dark matter affects the baryonic matter distribution, forming the structures we see today.

The spherical distribution of the CMB can be expressed in terms of spherical harmonics, with the angular parameter l (index of the multipole expansion), shown in fig. 2.2 [8].

The intensity of the three prominent peaks in fig. 2.2 are connected to the **Baryonic Acoustic Oscillations** (BAOs) and are particularly sensitive to the dark matter content of the Universe. As already mentioned in the introduction, a fit of the ΛCDM model to the latest Planck data leads to a contribution of only 4.9% of the baryonic matter to the total energy density of the Universe, while the dark matter contribution is about 5 times larger (26%) [8].

2.2.2 Big Bang Nucleosynthesis (BBN)

Minutes after the Big Bang, the production of light elements started, beginning with the production of deuterium:

$$p + n \rightarrow d + \gamma \tag{2.11}$$

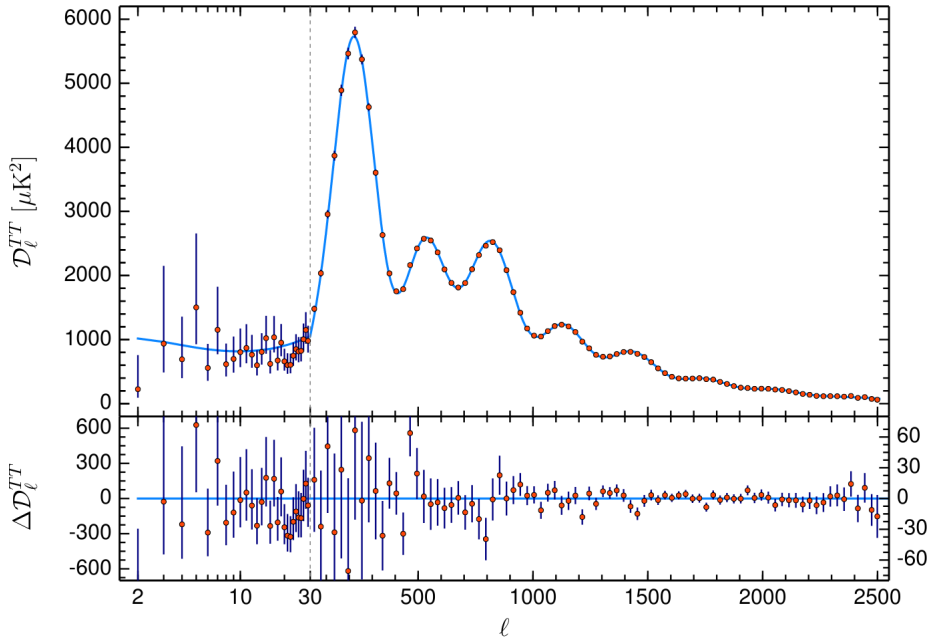

Figure 2.2: Temperature power spectrum of the CMB as a function of the angular parameter l. Smaller values of l correspond to larger angular scales, larger values of l correspond to smaller anglular scales in the CMB. Image taken from [8].

Additional reactions formed elements up to ^{7}Li. This is known as **Big Bang Nucleosynthesis** (BBN). As the Universe was cooling down, the amount of deuterium (and heavier elements) was increasing as their disintegration became inefficient, since the photons did not have enough energy to overcome the binding energy of the nuclei anymore. The formation of light elements stopped when the Universe cooled down to a temperature at which the Coulomb barrier could no longer be overcome.

The rates of the formation reactions, and with that also the primordial abundances of light elements, depends on the density of the baryons, which is typically expressed in terms of the baryon-to-photon density ratio:

$$\eta_{10} = 10^{10} \cdot \frac{n_b}{n_\gamma} \tag{2.12}$$

which is related to the baryonic density parameter, Ω_B, by [17]:

$$\eta_{10} = 10^{10} \cdot \frac{\rho_c}{\langle m \rangle n_\gamma^0} \Omega_B \tag{2.13}$$

with $\langle m \rangle$ being the mean mass per baryon (roughly the proton mass), ρ_c the critical density from eq. 2.6 and n_γ^0 the present day photon number density [17].

The light-element abundances can be explained with $\eta_{10} = 6.143 \pm 0.190$ [18]. Together with n_γ (given by the CMB temperature), this leads to $\Omega_B \simeq (0.02244 \pm 0.00069) \cdot (H_0/100\,km\,s^{-1}Mpc^{-1})^{-2}$ [18], which is roughly equal to a value of $\Omega_B \simeq 4.13$ %. The

important point is that the baryon density, inferred from BBN, can only explain less than 5% of the total energy density of the universe. Combined with the value of Ω_M, this is leaving the need to include an additional component, such as dark matter.

2.2.3 Bullet Cluster

As already mentioned in the introduction, the first evidence for the existence of dark matter came from observations of the velocities of galaxies in the COMA cluster in 1933 [5]. Since this time, the observation of many different galaxy clusters supports the hypothesis of dark matter. One of the most known evidences comes from the galaxy cluster 1E 0657-56, also known as the **bullet cluster**. The bullet cluster actually shows the collision of two galaxy clusters [19]. Figure 2.3 shows an overlayed image of the bullet cluster. Shown in white and yellow are the galaxies within the clusters (optical image of the visible spectrum). The intergalactic gas is shown in magenta (X-ray image) and the mass distribution in blue (as measured via gravitational lensing).

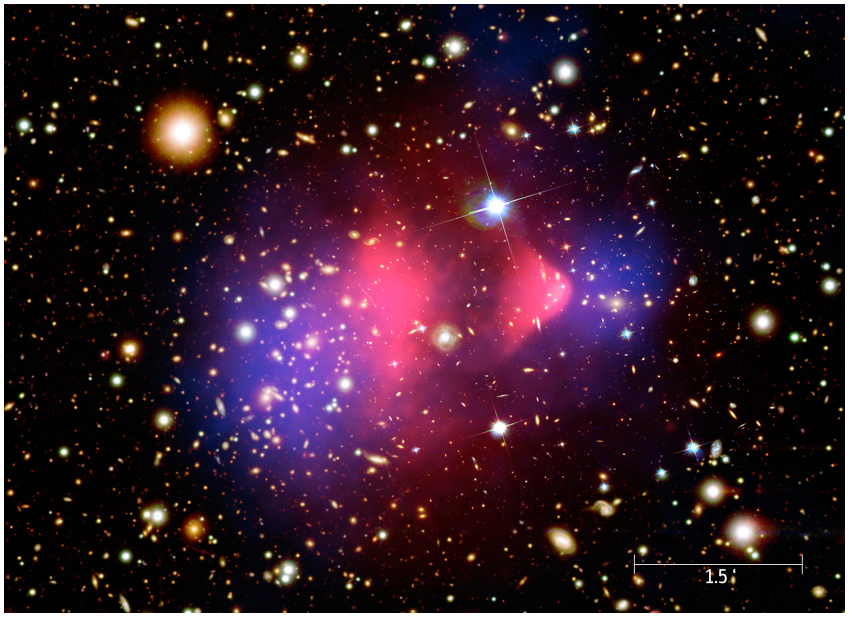

Figure 2.3: Image of the bullet cluster. The optical image shows galaxies in yellow and white. The hot interstellar gas is shown in magenta. Indicated in blue are the regions containing the majority of the mass of the cluster, as measured by gravitational lensing. Image taken from [20]. Credit: X-ray: NASA/CXC/CfA/M.Markevitch et al.; Optical: NASA/STScI; Magellan/U.Arizona/D.Clowe et al.; Lensing Map: NASA/STScI; ESO WFI; Magellan/U.Arizona/D.Clowe et al.

The density of galaxies within the cluster is too low to create a significant number of collisions between them. The majority of the visible mass of galaxy clusters is in the form of intergalactic gas. The particular shape of the gas in fig. 2.3 is caused by the electromagnetic interaction, causing a 'friction' between the gas of the two colliding galaxies. As can be seen, the centers of the gas distribution do not match with the centers

of the mass distribution of the galaxy clusters. This can be explained if the galaxies contain a large amount of dark matter. While the gas is slowed down due to the friction, dark matter passed through each other with very little to no interaction.

2.2.4 Galactic Rotation Curves

Another type of evidence for dark matter on a smaller scale, as was already mentioned in the introduction, comes from the rotation curves of individual galaxies. A rotation curve describes the velocity of stars in a galaxy as a function of their distance to the galactic center. Classically, the velocity v of a star with mass m on a stable circular orbit of radius r around the galactic center should be described by:

$$v = \sqrt{G\frac{M(r)}{r}} \tag{2.14}$$

with:

$$M(r) = 4\pi \int_0^r \rho(r')r'^2 dr' \tag{2.15}$$

For galaxies with a bulge in the center[5], containing the majority of the mass, the velocity should decrease with $v \propto 1/\sqrt{r}$ for radii far outside of the bulge, $r \gg r_{bulge}$, where the mass of the galaxy in eq. 2.15 can be approximated as $M_{bulge} = M_{total}$. Figure 2.4 shows the measured rotation curve of the galaxy M33 [21]. The dashed line depicts the expected rotation curve following the classic approach shown above, only including the visible matter. There is a strong discrepancy of this dashed line to the data. The addition of a spherical dark matter halo to the calculation leads to the solid line, which perfectly matches the measured data.

A large number of galactic rotation curves has been measured, which are consistent with a dark matter halo hypothesis, more details can be found for example in [23].

2.3 Dark Matter Particle Candidates

As was shown in the previous section, there are various different observations providing convincing evidence for the existence of non-baryonic matter, which makes up most of the matter content in our Universe. To this day, the nature of this dark matter is still an open question. In the last decades, a large number of possible dark matter candidates has been proposed. This section focuses on some of the most important *particle* candidates.

[5] Like for example our Milky Way

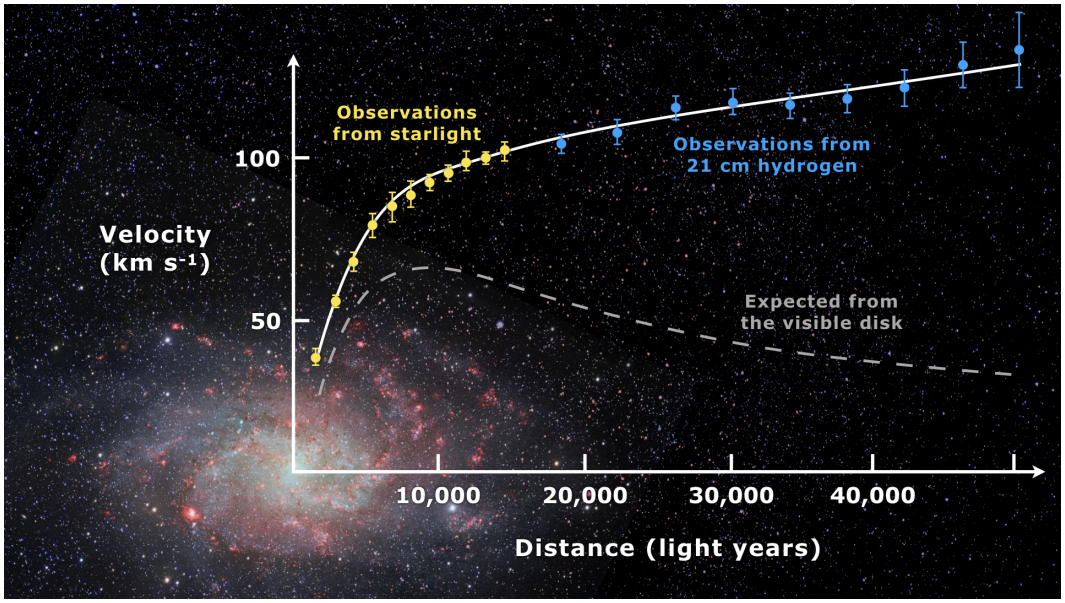

Figure 2.4: Rotation curve of the galaxy M33. The dashed line shows the prediction of the velocity of starts as a function of distance to the galactic center, if only the visible mass is included. The yellow and blue points show the measured data and the solid line shows the model predictions including a dark matter halo. Image taken from [22], data and model taken from [21]. Credit: Mario De Leo.

2.3.1 Requirements

Assuming that dark matter consists of at least one new particle, there is a list of requirements these particles have to fulfill to be considered a dark matter candidate:

Lifetime: From BBN and the CMB we know that dark matter already existed in the early Universe. Furthermore dark matter plays an essential role in the formation of structures in the late Universe, and we also know that it is still present today. Therefore, dark matter particles are generally considered to be either stable or have a lifetime in the order of the age of the Universe[6].

Content in our Universe: The contribution of dark matter to the total energy density of the Universe is given by the ΛCDM model. Thus, any particle candidate must be present in the correct abundance, which can be used to rule out several candidates as an explanation for 100% of dark matter[7].

Cold (non-relativistic): The structures we observe today in the Universe cannot be explained by relativistic (hot) dark matter particles, as they would effectively wash

[6] This requirement is relaxed in models including an efficient production mechanism for dark matter, allowing for decaying dark matter.

[7] There is still the possibility that dark matter consists of different types of particles, with each type only contributing a fraction to the total content of dark matter in our Universe

out small scale structures. Simulations of structure formation of both, hot dark matter models and cold dark matter models confirm that the structures we observe today can only be formed in the case of cold (non-relativistic) dark matter.

Interactions: Dark matter interacts gravitationally, as most of the evidence for the existence of dark matter we have today comes from gravitational observations. Various observations, like the bullet cluster or searches for dark matter annihilation signals from regions of high dark matter densities set strong limits on the self-interactions or interactions with baryonic matter. From all available observations it can be concluded that the coupling of dark matter to the strong or weak nuclear force, as well as to the electromagnetic force must be very weak or zero. Any possible new interaction should be on some sub-weak scale.

2.3.2 Axions and ALPs

Axions are particles that were originally introduced by R.D. Peccei and H.R. Quinn [24] to solve the **strong CP-problem**: In contrast to the weak interaction, CP symmetry is not violated in QCD, even though this violation is explicitly allowed. The strongest experimental bounds come from measurements of the electric dipole moment of the neutron, which point towards a vanishing CP violating term in the QCD lagrangian [25]. This causes tensions regarding the *naturalness* of QCD, which states that the parameters of a fundamental physical theory should not have to be *fine-tuned*[8]. The **Peccei-Quinn mechanism** introduces a new global symmetry, which is spontaneously broken. As independently shown by F. Wilczek [26] and S. Weinberg [27], this leads to a new particle: the axion, which provided a solution that avoided any fine-tuning of the theory.

This idea was generalized beyond the QCD-axion[9] to include so-called **Axion-Like-Particles** (ALPs)[10] [28].

Axions or ALPs fulfill the necessary requirements to explain a large fraction of dark matter content in our Universe [29], which makes them very interesting particle candidates. Experimentally, the searches for axions and ALPs can be divided into two main categories: helioscopes and haloscopes. While helioscopes are searching for axions emitted by the Sun, haloscopes are searching for relic axions of the galactic halo. Despite huge experimental efforts, no observation of axions could be achieved so far.

2.3.3 Sterile neutrinos

Neutrinos are the only standard model particles that fulfill most of the requirements listed in sec. 2.3.1, as they don't couple to the strong nuclear force and are electrically

[8] Parameters of a fundamental physical theory should be of $\mathcal{O}(1)$.
[9] The QCD-axion is the axion that arises from the Peccei-Quinn mechanism.
[10] ALPs are generally very light, very weakly interacting pseudo-scalar particles.

neutral. However, due to their light mass, neutrinos would be considered hot dark matter and therefore cannot constitude all the dark matter. Moreover, their energy density is constrained to $\Omega_\nu = \frac{\rho_\nu^0}{\rho_c^0} = \frac{\sum m_\nu}{93.14eV} \cdot (H_0/100\,km\,s^{-1}Mpc^{-1})^{-2}$ [18]. Considering the light masses of neutrinos, this leads to a too small energy density to explain all dark matter.

Sterile neutrinos on the other hand are a natural extension of the standard model. Analogous to the right-handed charged leptons, sterile neutrinos would be the right-handed versions of the three known neutrinos. The weak interaction does not couple to right-handed fermions. Other than the charged leptons, neutrinos do not interact via electromagnetic or strong interactions and thus, right-handed neutrinos do not couple to any of the known standard model interactions other than gravity.

Depending on the particular model, sterile neutrinos in the mass range of $\mathcal{O}$(keV) pose a viable dark matter candidate. Such models typically assume a mixing with the three active neutrinos as otherwise their detection would be impossible. The parameter space for sterile neutrino dark matter in the keV mass range is already very constrained, for more details see [30].

2.3.4 WIMPs

WIMPs (**W**eakly **I**nteracting **M**assive **P**articles) are a general class of new particles without any strict definition, other than that they have to be *massive*, *stable* (on cosmological timescales) and are *interacting on the weak scale or below*. Generally, WIMPs are assumed to have been created in the early Universe, in which they were in thermal equilibrium with other particles:

$$\chi\bar{\chi} \leftrightarrow f\bar{f} \tag{2.16}$$

As the Universe cooled down, the production ('$\leftarrow$') was no longer possible and the number of WIMPs decreased due to annihilation ('$\rightarrow$'). At some point, caused by the expansion of the Universe, the number density of WIMPs becomes so diluted that the annihilation processes stop at the abundance of WIMPs we see today. This is generally known as *freeze-out* mechanism and is depicted in fig. 2.5 [31].

The expected annihilation cross section $\langle\sigma_A v\rangle$ can be calculated from the abundance we observe today. If a dark matter particle mass that is typical for the weak scale is assumed ($\mathcal{O}(10\,\mathrm{GeV/c^2})$), this results in a typical weak scale cross section. This apparent coincidence is commonly known as the **WIMP miracle**. In the case of thermal WIMPs, the electroweak mass scale can be seen as being the most natural, and was therefore mostly studied in the last decades. Though in general no strict lower limit on the thermal WIMP mass exists, other than from the requirement of being CDM.

Currently, much of the parameter space of the "classical" WIMP[11] has already been

[11] Referring to the WIMP miracle, covering a mass range from a few GeV/c^2 up to the TeV/c^2 scale.

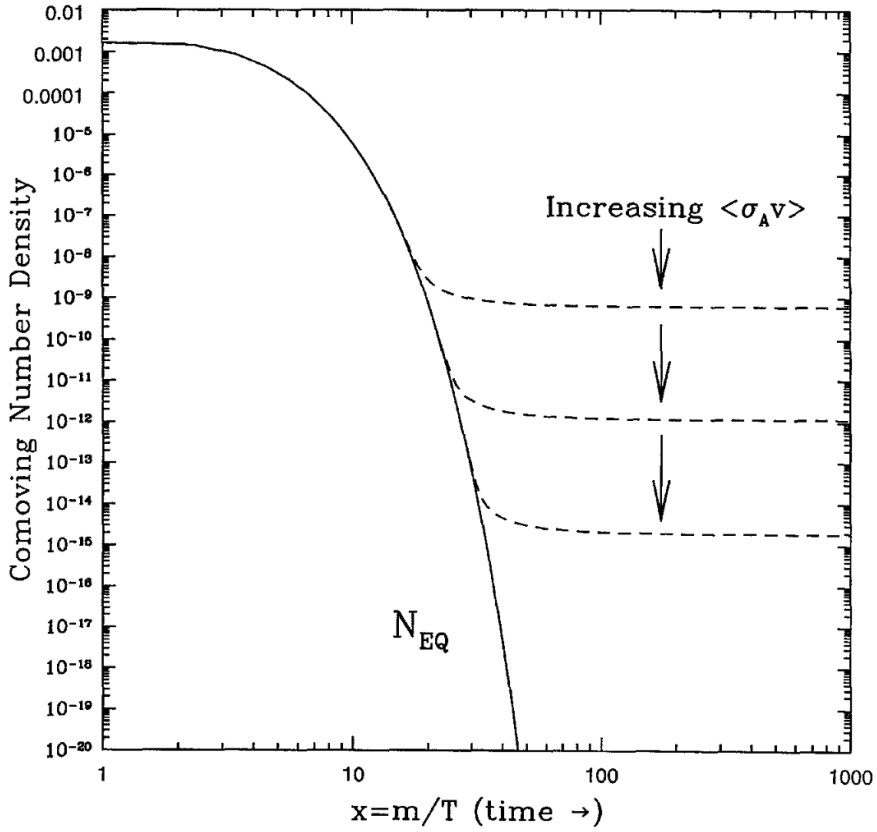

Figure 2.5: Comoving number density of the WIMP as a function of the mass over temperature, depicting the thermal freeze-out of the WIMP. Figure taken from [31].

experimentally excluded. Nevertheless, there is still large unexplored regions of the parameter space that are theoretically motivated.

2.3.5 Asymmetric Dark Matter Models and the Dark Sector

A well-motivated alternative to WIMPs are models of **Asymmetric Dark Matter** (ADM). The main motivation for these models comes from the observation that the energy densities of dark matter and baryons just differ by a small factor of about 5: $\Omega_\chi \simeq 5 \cdot \Omega_B$. While this similarity is neglected in most standard WIMP scenarios[12], ADM models take this into account by assuming a common origin in the evolution of baryonic and dark matter. The asymmetry between matter and anti-matter in the present Universe is parametrized as [32]:

$$\eta_B = \frac{n_B - n_{\bar{B}}}{s} \simeq 10^{-10} \tag{2.17}$$

with n being the number densities of baryons (B) and anti-baryons ($\bar{B}$) and s being the entropy density. After all baryons annihilated with anti-baryons, this tiny excess

[12]The similarity is just accepted as a coincidence.

of baryons over anti-baryons leads to the abundance of baryons in the Universe today. ADM models assume that a similar asymmetry exists between dark matter and anti dark matter and that this asymmetry is connected to the one we observe in the baryonic sector. This often involves more than just a single particle, but instead a multitude of particles following physical laws similar to the one of the baryonic sector[13]. For a more detailed review see e.g. [32] or [33].

While most ADM models predict dark matter masses in the few GeV regime, they are not explicitly limited by any boundary and also allow for sub-GeV masses [33].

2.4 Alternative theories

For this thesis, only particle solutions to the dark matter problem are relevant. Nevertheless, for the sake of completeness, a few alternative theories are listed in this section.

One of the earliest suggested ideas was the existence of so-called MACHOs (**M**assive **A**strophysical **C**ompact **H**alo **O**bjects) consisting of e.g. neutron stars, black holes or brown dwarfs. One particularly interesting solution that is still relevant today are the existence of **P**rimordeal **B**lack **H**oles (PBHs). Current results[14] point out that PBHs and other MACHOs of planetary to multi-Solar masses cannot be the dominant form of dark matter [34, 35]. The asteroid mass region (10^{17}g $- 10^{22}$g) is not constrained and PBHs of this mass could make up 100% of dark matter [35]. The existence of MACHOs and particle candidates are not mutually exclusive and it is possible that the dark matter content of the Universe consists of both types.

An alternative approach attempts to modify our theory of gravity in order to explain the observed phenomena without the necessity to add any type of new particle (or MACHOs). One of the most known theories of this kind is **MO**dified-**N**ewtonian-**D**ynamics (MOND) [36]. A general problem of these types of theories is that they often only succeed in the explanation of some observations, but cannot be applied to, or fail to explain, other observations on different scales. In the case of MOND for example, the theory offers an alternative explanation for the observed galactic rotation curves, but not for the dark matter signatures seen in e.g. the CMB power spectrum.

[13] These types of models (containing multiple particles) are generally called the **dark sector** or **hidden sector**.

[14] Mostly obtained via gravitational lensing and gravitational wave measurements.

Chapter 3

The Search for Dark Matter

The experimental search for dark matter can be divided into three categories, namely **collider searches**, **indirect searches** and **direct searches**. A common assumption in all of them is that dark matter particles couple to standard model particles via some interaction other than gravity. Without specifying the type of interaction, the search for dark matter can then be approached from three different angles, represented by the schematic diagram in fig. 3.1.

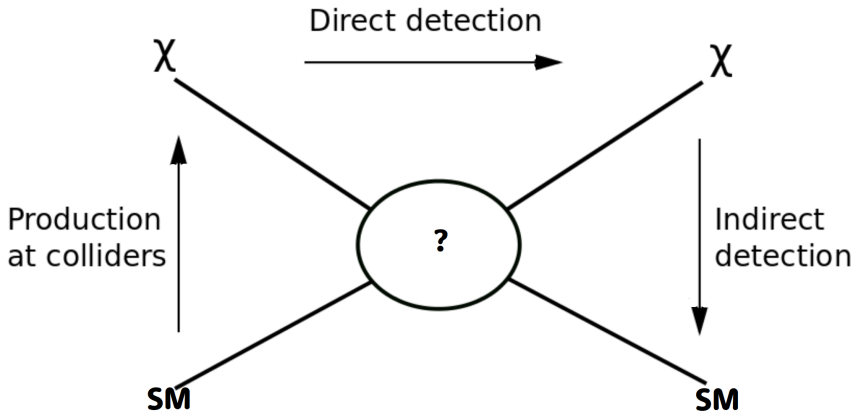

Figure 3.1: Schematic representation of the different dark matter detection channels.

This thesis will focus on direct detection techniques. Therefore the production at colliders and indirect detection will only be introduced very briefly.

Production at colliders: Collider experiments aim to produce dark matter via the collision of standard model particles. The extremely high energies that can be reached in colliders (up to $\mathcal{O}$(TeV)) create an environment similar to the early, hot Universe and thus allow for the creation of particles that otherwise could not be created under the conditions of the present Universe. Since any possible dark matter candidate has to fulfill the requirements mentioned in sec. 2.3.1, the created dark matter particle would not interact with the surrounding detectors and therefore escape detection. Its presence could be only inferred by its missing energy in the products of the collision. Since these

particles are produced by the collisions of particles in an accelerator, no statement can be made if such particles are indeed the same particles making up the dark matter content of our Universe. Nevertheless, a dark matter signature in a collider experiment would be a striking complementary result to other types of dark matter searches. A review of dark matter searches at colliders can be found in [37].

Indirect detection: Indirect detection experiments aim to detect signals from the annihilation or decay of dark matter particles into standard model particles in cosmic rays. Such signals would be expected from regions with a high gravitational potential and thus, a high density of dark matter particles. Depending on the type of cosmic ray, different signatures are expected. Generally the main signatures that are expected are γ's, charged particles/antiparticles or neutrinos. A review on indirect searches for dark matter can be found in [38].

The focus in this chapter will be on direct detection techniques. The theoretically expected signature of dark matter in a detector is discussed in sec. 3.1, followed by an overview of the important backgrounds in direct detection in sec. 3.2. A short list of experimental approaches is given in sec. 3.3. Lastly, sec. 3.4 introduces Coherent Elastic Neutrino-Nucleus Scattering (CEνNS), which is an irreducible background for direct detection experiments.

3.1 Direct Detection

The goal of direct detection experiments is to measure the interaction of a dark matter particle with an Earth-bound detector. In general, direct detection experiments are looking for both, interactions with electrons as well as with nuclei. In this work, only the interaction on nuclei is discussed. This interaction is typically thought of as a dark matter particle scattering on a nucleus (fig. 3.2), leading to a recoil of the nucleus that can be measured.

This section presents the expected recoil spectrum (sec. 3.1.5) in a detector for the basic scenario of an elastic, coherent and spin independent scattering process. This also involves some assumptions on astrophysical quantities (sec. 3.1.4) and nuclear physics (sec. 3.1.3).

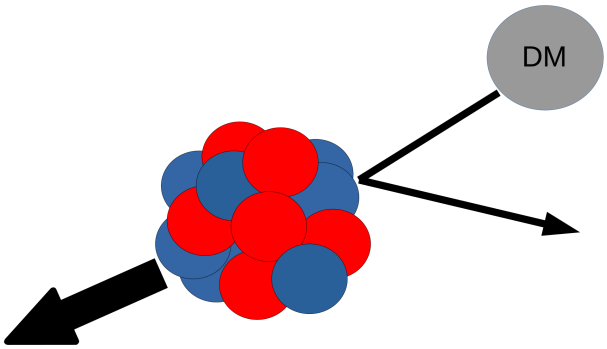

Figure 3.2: Schematic drawing of an elastic, coherent scattering of a dark matter (DM) particle on a nucleus.

3.1.1 Elastic Scattering

The coherent scattering of a dark matter particle, in the following denoted with χ, and a target nucleus, N, is a two body problem. The energy of the recoiling nucleus, E_R, can be written as (see app. A.1):

$$E_R = \frac{q^2}{2m_N} = \frac{\mu_N^2 v^2}{m_N} \cdot (1 - cos\theta) \tag{3.1}$$

with q being the momentum transferred to the nucleus, m_N the mass of the nucleus, v the relative velocity of the incident particle, θ the scattering angle in the center-of-mass frame and μ_N the reduced mass of the system of the nucleus and the dark matter particle with mass m_χ:

$$\mu_N = \frac{m_N \cdot m_\chi}{m_N + m_\chi} \tag{3.2}$$

It can be seen that, depending on the scattering angle $\theta \in [0, \pi]$, the energy of the recoiling nucleus is between zero and $E_{R,max}$:

$$0 \leq E_R \leq E_{R,max} = \frac{2\mu_N^2 v^2}{m_N} \tag{3.3}$$

3.1.2 Interaction Cross Section

The spin-independent differential cross section of dark matter interacting with the nucleus is given by [39]:

$$\frac{d\sigma}{dE_R} = \frac{m_N \cdot \sigma_0}{2\mu_N^2 v^2} \cdot F^2(E_R) = \frac{\sigma_0}{E_{R,max}} \cdot F^2(E_R) \tag{3.4}$$

The first term ($\frac{\sigma_0}{E_{R,max}}$) is the differential cross section of dark matter scattering on a nucleus in the approximation of a *point-like nucleus*, with σ_0 being the cross section at

zero-momentum transfer. To take the structure of the nucleus into account, this point-like cross section is multiplied with the *nuclear form factor* $F^2(E_R)$ (see sec. 3.1.3).

The zero-momentum transfer cross section on a point-like nucleus has the form [39]:

$$\sigma_0 = \frac{\mu_N^2}{\pi} A^2 f_n^2 \tag{3.5}$$

with f_n being the coupling strength of the dark matter particle to single nucleons (protons and neutrons). These couplings are usually considered to fulfill the isosinglet condition ($f_p = f_n$), which leads to the above equation, showing the A^2 dependence of the cross section. Since the cross section increases quadratically with the mass number of the target material, heavier elements are generally preferred as a detector material. On the other hand, for very light dark matter ($m_\chi \ll m_N$), the recoil energy in eq. 3.1 scales as $1/m_N$ and thus, lighter elements have a higher chance of reaching recoil energies above the energy threshold of a real detector.

Conventionally, the cross section is transformed into the material independent cross section with a single nucleon, σ_n [39]:

$$\sigma_0 = \sigma_n \cdot A^2 \cdot \frac{\mu_N^2}{\mu_n^2} \tag{3.6}$$

This allows for a comparison between different target materials used by different experiments. The differential cross section of dark matter with the nucleus can now be written as:

$$\frac{d\sigma}{dE_R} = \frac{m_N}{2\mu_n^2 v^2} \cdot A^2 \cdot \sigma_n \cdot F^2(E_R) \tag{3.7}$$

For more details, see app. A.2.

3.1.3 Nuclear Form Factor

At low momentum transfers, $q = \sqrt{2 m_N E_R}$, the nucleus can be approximated as being point-like. For higher q's, the wavelength ($\propto 1/q$) becomes smaller than the size of the nucleus and the nuclear structure has to be taken into account. This is typically done via the so-called form factor, which depends on the momentum transfer $F(E_R) \rightarrow F(q)$. In the Born approximation, the form factor is given as the Fourier transform of the density distribution of 'scattering centers' of the nucleons, $\rho(r)$ [40]:

$$F(q) = \int \rho(r) e^{iqr} d^3 r \tag{3.8}$$

In the context of dark matter scattering on the nucleus, the assumption is made that the dark matter 'scattering centers' follow the same distribution as the one of the charge distribution [41].

The charge density parameterization proposed by Helm considers the nucleus as a solid sphere with constant density and a nuclear radius of R_0 and a smoothly decreasing density over the 'thickness' of the nuclear surface of width s. This has the advantage of leading to an analytic expression of the form factor [40]:

$$\begin{aligned} F(q) &= 3\frac{j_1(qR_0)}{qR_0} \cdot e^{-\frac{1}{2}(qs)^2} \\ &= 3\frac{sin(qR_0) - qR_0 \cdot cos(qR_0)}{(qR_0)^3} \cdot e^{-\frac{1}{2}(qs)^2} \end{aligned} \tag{3.9}$$

with $j_1(qR_0)$ being the first spherical Bessel function. A useful approximation for both of the parameters (R_0 and s) is given in [41]:

$$R_0 = \sqrt{c^2 + \frac{7}{3}\pi^2 a^2 - 5s^2} \tag{3.10}$$

with:

$$\begin{aligned} c &= (1.23 \cdot A^{1/3} - 0.6)fm \\ a &= 0.52fm \\ s &= 0.9fm \end{aligned} \tag{3.11}$$

with A being the mass number of the target nucleus. In the context of this thesis, the approximation $R_0 \simeq (1.14 \cdot A^{1/3})fm$ [41] is sufficient. The squared form factor $F^2(q)$ in eq. 3.9 as a function of the recoil energy is shown for different target materials in fig. 3.3.

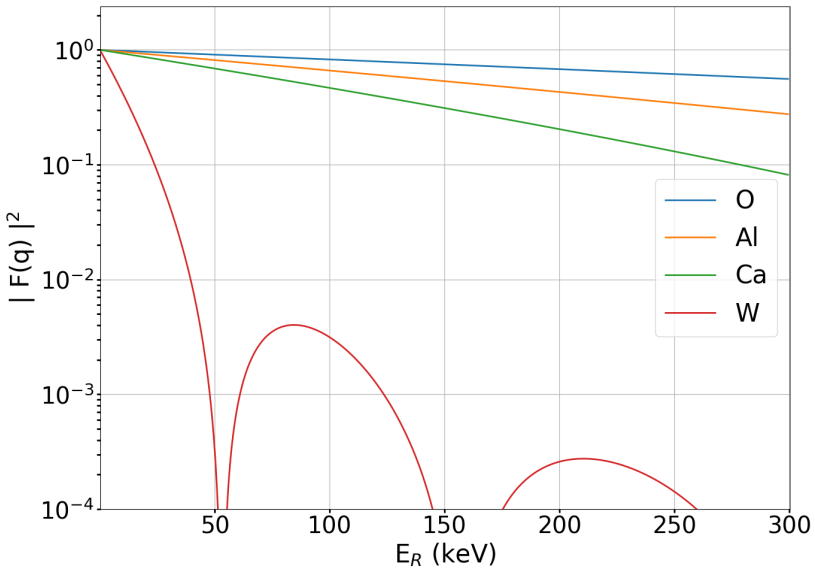

Figure 3.3: The squared nuclear form factor as a function of the recoil energy for different target materials.

While the form factor is mostly negligible for light elements and at low recoil energies, it has a considerable impact on heavy elements, such as tungsten (W) and therefore needs to be included in the calculation of the expected dark matter interaction rate in materials like $CaWO_4$.

3.1.4 Dark Matter Halo Model

Before moving to the expected dark matter interaction rate in an Earth-bound detector, some assumptions on astrophysical parameters have to be made. This includes the local density of dark matter and the velocity distribution of dark matter particles at the local position in the Milky Way. Dark matter is considered as a spherical halo around the center of our galaxy. The local dark matter density, ρ_χ, is typically set to 0.3 GeV/cm^3 [41]. Since dark matter particles are assumed to be thermalized, their velocity is expected to follow a Maxwell-Boltzmann distribution. Considering a cut-off at an escape velocity[1] v_{esc}, the velocity distribution in the galactic restframe (isothermal sphere) is described by [42]:

$$f(v) = \mathcal{N}\left(\frac{3}{2\pi w^2}\right)^{3/2} exp\left(-\frac{3v^2}{2w^2}\right) \tag{3.12}$$

with the normalization factor:

$$\mathcal{N} = \left[erf(z) - \frac{2}{\sqrt{\pi}} \cdot z \cdot exp(-z^2)\right]^{-1} \tag{3.13}$$

with $z = \sqrt{\frac{3}{2}}\frac{v_{esc}}{w}$ and w being the root mean square velocity, which is given by: $w = \sqrt{\frac{3}{2}}v_s$, where v_s is the rotational velocity of the local system (our solar system). Finally this is transformed into the rest frame of the Earth moving through the galaxy with v_o. The values used in this thesis are: $v_{esc} = 544\,km/s$ [43], $v_s = 220\,km/s$ and $v_o = 232\,km/s$ [42].

3.1.5 Recoil Spectrum

The previous sections present all the necessary elements to construct the expected rate of dark matter interactions:

$$R = N_T \cdot \frac{\rho_\chi}{m_\chi} \cdot \langle v \rangle \cdot \sigma(v) \tag{3.14}$$

with N_T being the number of target nuclei per target mass and $\langle v \rangle$ being the average

[1] At higher velocities, objects are not gravitationally bound to the galaxy anymore.

indident velocity of dark matter particles. This is obtained by an integral over the velocity distribution given in eq. 3.12:

$$\langle v \rangle = \int_{v_{min}(E_R)}^{v_{esc}} v \cdot f(v) d^3v \tag{3.15}$$

where $v_{min}(E_R) = \sqrt{\frac{m_N E_R}{2\mu_N^2}}$ corresponds to the minimal velocity a dark matter particle needs to create a recoil of energy E_R in the target.

Accordingly, the differential recoil rate is expressed as:

$$\frac{dR}{dE_R} = N_T \cdot \frac{\rho_\chi}{m_\chi} \cdot \int_{v_{min}(E_R)}^{v_{esc}} v \cdot f(v) \cdot \frac{d\sigma(v)}{dE_R} \, d^3v \tag{3.16}$$

Inserting eq. 3.7 for the differential cross section leads to:

$$\begin{aligned} \frac{dR}{dE_R} &= N_T \cdot \frac{\rho_\chi}{m_\chi} \cdot \frac{m_N}{2\mu_n^2} \cdot A^2 \cdot \sigma_n \cdot F^2(q) \cdot \int_{v_{min}(E_R)}^{v_{esc}} \frac{f(v)}{v} \, d^3v \\ &= N_T \cdot \frac{\rho_\chi}{m_\chi} \cdot \frac{m_N}{2\mu_n^2} \cdot A^2 \cdot \sigma_n \cdot F^2(q) \cdot \mathcal{I}(v_{min}) \end{aligned} \tag{3.17}$$

The integral over the velocity distribution is defined as $\mathcal{I}(v_{min})$. An analytic expression for $\mathcal{I}(v_{min})$ for a non-rotating maxwellian model is given in [42] and in app. A.3.

Figure 3.4 shows the expected differential recoil spectrum in a $CaWO_4$ detector. In fig. 3.4a, the contribution of the individual target nuclei to a spectrum of a 1 GeV/c^2 dark matter particle is highlighted. It can be seen how the heavy element W reaches much higher count rates than the lighter elements, due to the A^2 dependence of the cross section. At the same time, the end point of the W spectrum is at much lower energies compared to the lighter elements, due to the $\sim 1/m_N$ dependence of the recoil energy for light dark matter ($m_\chi \ll m_N$). In fig. 3.4b, the recoil spectra in a $CaWO_4$ detector are shown for different dark matter particle masses. While the interaction cross section, σ_n, is just a linear scaling parameter in eq. 3.17, the dark matter particle mass parameter, m_χ, heavily influences the endpoint and shape of the spectrum.

In a real experiment, these spectra cannot be measured down to arbitrarily low energies. The lower boundary is given by the energy threshold of the detector, E_{thr}. The expected total count rate of dark matter events is then given by an integral of the recoil rate over the energy range above the threshold:

$$R(E_{thr}) = \int_{E_{thr}}^{\infty} \frac{dR}{dE_R} \, dE_R \tag{3.18}$$

The expected total rate of events above the threshold as a function of the threshold is

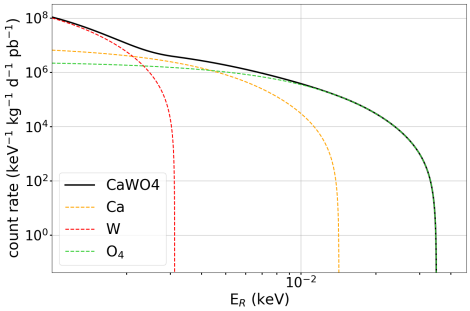

(a) Contribution of the individual target nuclei to the recoil spectrum of a 1 GeV/c^2 dark matter particle in a $CaWO_4$ detector.

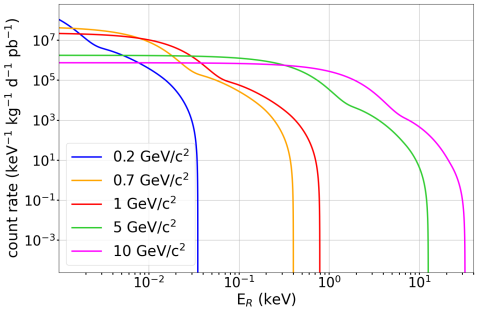

(b) Expected recoil spectra in $CaWO_4$ for different dark matter particle masses.

Figure 3.4: Expected differential recoil spectrum in a $CaWO_4$ detector a) for a 1 GeV/c^2 dark matter particle and b) for different dark matter particle masses.

shown in fig. 3.5a for a fixed dark matter particle mass of $m_\chi = 1$ GeV/c^2 in a $CaWO_4$ detector. In fig. 3.5b, the total number of events is instead given as a function of the dark matter particle mass for a fixed threshold of 10 eV.

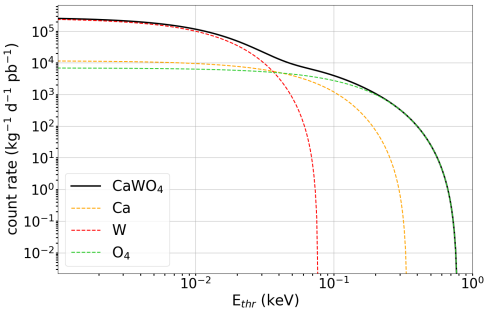

(a) Expected total number of events as a function of the energy threshold for a 1 GeV/c^2 dark matter particle.

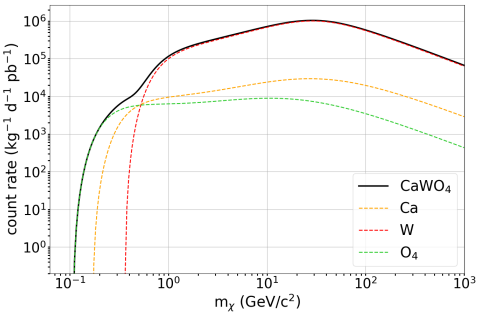

(b) Expected total number of events as a function of the dark matter particle mass for a 10 eV energy threshold.

Figure 3.5: Expected total number of events in a $CaWO_4$ detector a) as a function of the threshold for a fixed dark matter particle mass and b) as a function of the dark matter particle mass for a fixed energy threshold. Both plots show the contribution of the individual target nuclei to the total rate.

In fig. 3.5a it can be seen that, for low thresholds, the total count rate is dominated by recoils on W. With an energy threshold above about 40 eV, dark matter ($m_\chi = 1$ GeV/c^2) scatterings on W do not transfer enough energy anymore to the recoiling nuclei to be seen and the rate is dominated by scatterings on the lighter elements (Ca and O). This is also reflected in fig. 3.5b: Below a dark matter mass of about 0.4 GeV/c^2, recoils of W do not have energies above the energy threshold of 10 eV anymore. Recoils of the lighter elements (Ca and O) still lead to events above the energy threshold. Generally, a detector

material with a mixture of heavy and light elements, like it is used in CRESST, is very advantageous. The A^2 dependence of the cross section leads to a high interaction rate on the heavy elements. In the low mass regime, in which recoils of the heavy element are no longer energetic enough to be measured, the recoils of lighter elements extend the sensitivity of the experiment towards smaller dark matter masses.

Lastly, fig. 3.6 shows the total number of expected events in a $CaWO_4$ detector as a function of the dark matter particle mass for several fixed energy thresholds. At dark matter particle masses above $\mathcal{O}(10\,\mathrm{GeV/c^2})$, the total number of events starts to decrease. This can be explained by the fixed value of the dark matter density ($\rho_\chi = 0.3\,\mathrm{GeV/cm^3}$). With an increasing mass of the dark matter particles, the number density of dark matter particles, and thus also the number of interactions in the detector, has to decrease.

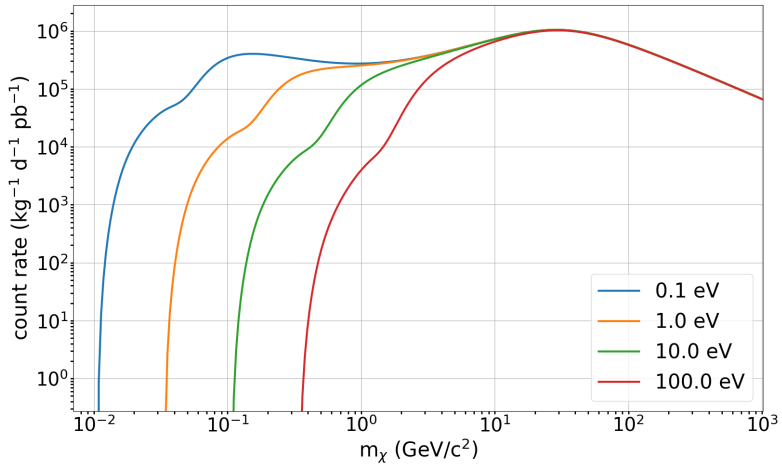

Figure 3.6: Expected total number of events in a $CaWO_4$ detector as a function of the dark matter mass for different energy thresholds, indicated in the legend.

Figure 3.6 also shows the crucial role of the threshold in the low dark matter mass regime. As an example, for a dark matter particle with a mass of $m_\chi = 100\ \mathrm{MeV/c^2}$, the expected total number of events is more than an order of magnitude higher with a threshold of 0.1 eV, compared to a threshold of 1 eV. For thresholds above 10 eV, no more events are expected for dark matter particles lighter than about $100\ \mathrm{MeV/c^2}$ (this consideration does not include the effect of a finite energy resolution of the detectors).

3.2 Backgrounds in direct detection

Since the expected rate of dark matter interactions is extremely low, it is of great importance to operate direct detection experiments in a low background environment. This section is giving a general overview over the backgrounds that are of relevance for direct detection experiments.

Cosmic radiation: When cosmic rays hit the Earth's atmosphere, they produce showers of secondary particles. The most dangerous component of these showers are muons, which are able to reach the Earth's surface with a high flux. In order to reduce this type of background, most direct detection experiments choose deep underground facilities as their experimental site, where the muon flux is highly suppressed. Figure 3.7 shows the muon flux for different underground laboratories around the world [44].

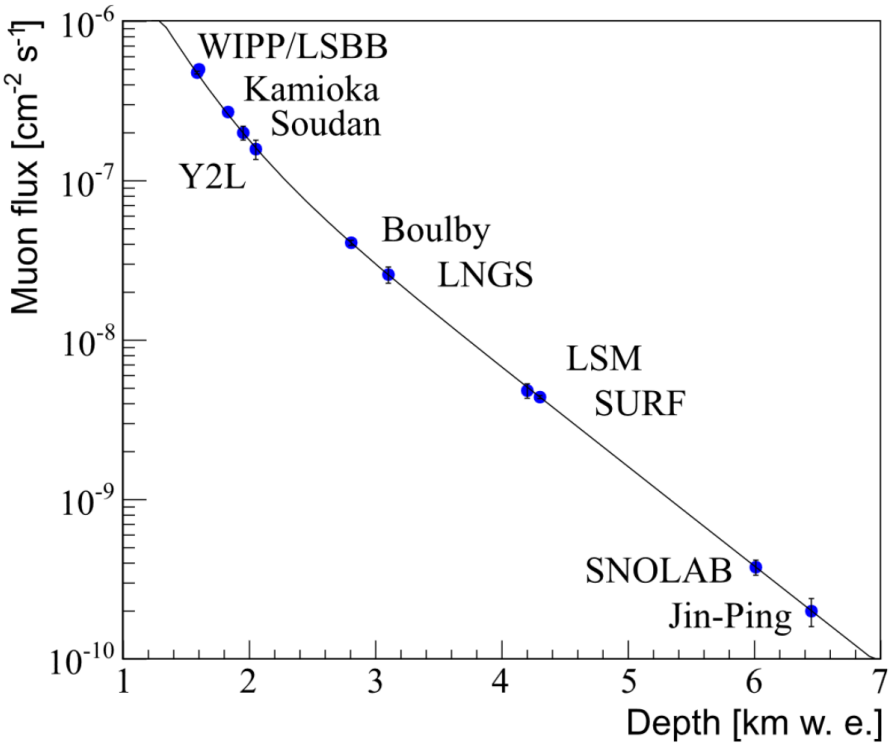

Figure 3.7: Muon flux as a function of depth in kilometers water equivalent for different underground laboratories. Figure taken from [44].

Many experiments additionally make use of veto systems to identify events induced by remaining muons in the experimental setup.

Environmental radioactivity: While the rock overburden effectively reduces the background signals originating from cosmic radiation, it is also a source of environmental radioactivity. Radioactive isotopes are naturally present in the rock surrounding the underground laboratory and in the materials used for constructing the experiment. The latter is usually kept under control by purification processes of the materials. The experiments can be protected against natural radioactivity (typically isotopes belonging to the decay chains of ^{238}U, ^{232}Th or ^{40}K) by additional layers of shielding. Typical choices are Pb and Cu. Due to its high atomic number and density, Pb has a high stopping power for γ radiation. A disadvantage of Pb is the existence of the radioactive isotope ^{210}Pb.

Copper, which is available with high radiopurity, is therefore often used as an additional inner shielding.

Neutrons and neutrinos: Neutrons and neutrinos are an especially dangerous background for direct detection experiments. Elastic scattering on a nucleus of these electrically neutral particles can easily mimick a dark matter interaction. **Neutrinos** cannot be shielded at all and therefore form an irreducible background. This background is one of the main subjects of the studies in this thesis and is therefore covered in more detail in sec. 3.4 and in chapter 8. **Neutrons** cannot be shielded in the same way as β and γ radiation. Instead, the neutrons are moderated to lower energies, at which they can no longer be detected. Hydrogen rich materials (or generally light elements) are very effective in moderating neutrons. Therefore, most experiments choose water or polyethylene as a shielding material against neutrons.

Active background rejection: Most experiments have developed additional strategies of background rejection that are typically very specific for each experiment. Generally this involves fiducialization of the active detector volume and/or active rejection of signals in the analysis, mostly based on the expected signal shape or the tagging of secondary, coincident signals in the detector.

3.3 Experimental approaches

Since the first proposal by M. W. Goodman and E. Witten for a direct detection experiment in 1985 [45], the field of direct detection has grown strongly. In this section, a very short summary of some commonly used techniques is given.

Most of the recoil energy in a direct scattering of dark matter in the target material is transferred into atomic motion (heat). In a solid material, this leads to phonons. Only a small fraction of the energy deposited in a scattering process can be transferred into electronic excitations (charge) or scintillation signals, which is known as *quenching*. Due to the different mechanism for energy loss in nuclear vs. electron recoils, the charge or scintillation signals of nuclear recoils are quenched more strongly compared to the same energy deposition in an electron scattering. Many experiments make use of this by exploiting a combination of two detection channels in order to discriminate against background signals, which are dominantly interacting with the electrons of the detector material.

3.3.1 Sodium iodide (NaI) scintillating detectors

Sodium iodide (NaI) is a scintillating material that can be operated at room temperature. The scintillation light produced by the particle interactions is measured with

photomultiplier tubes (PMTs). Experiments using NaI crystals are looking for an annual modulation signal: Due to Earth's annual rotation around the Sun, the relative velocity of the Earth with respect to the galactic halo varies periodically over time, which leads to a modulating rate of dark matter interactions (in a time range of a year). Experiments that fall into this category are e.g. DAMA [46], ANAIS [47], COSINE [48] and SABRE [49].

3.3.2 Single-phase liquid noble gas detectors

These detectors are spherical or cylindrical vessels filled with a liquid noble gas. The particle interactions inside the detector cause the production of scintillation light inside the target material, which is measured with surrounding PMTs. The DEAP-3600 experiment uses liquid Ar detectors [50]. Different incident particles create different signatures in Ar, which can be distinguished by the arrival time distribution of the measured scintillation light of an event. Therefore background events can be identified via a pulse shape discrimination. Another example is the XMASS experiment, using liquid Xe [51]. Background rejection via pulse shape discrimination is not possible in liquid Xe, therefore XMASS is looking for an annual modulation signal.

3.3.3 Dual-phase Time Projection Chambers (TPCs)

Experiments using dual-phase TPCs are mostly using liquid noble gases (typically Xe or Ar) as a target material. Particle interactions in the liquid produce scintillation light, which is measured with PMTs on the top and bottom of the cylindrical TPC, allowing for a reconstruction of the radial position of the interaction inside the detector. Dual-phase TPCs have an additional layer of gas at the top of the TPC. Electrons created by the interaction are drifted along the z-axis of the TPC by an electric field. Once they reache the interface between the two phases, a strong electric field accelerates them in the gas, leading to another scintillation signal. The time difference between these two scintillation signals can be used to extract the z-coordinate of the interaction. Therefore a full 3D reconstruction of the position of the interaction inside the detector is possible. This allows the experiments to *fiducialize* their detector, which means that events close to the surface of the TPC are rejected, and only events originating from an 'inner' (fiducial) volume of the detector are used in the analysis. The advantage of this experimental approach comes from the fact that the majority of background events are close to the surface of these chambers, which can then be discarded. Lastly, as mentioned before, the ratio between the two scintillation signals allows for a discrimination between electron recoils (causing a higher charge production and thus, a higher second scintillation signal) and nuclear recoils.

These types of experiments have the largest exposures and are therefore leading to strong exclusion limits in the classical WIMP mass range. Examples for experiments

using **dual phase TPCs** to read out ionization and scintillation are XENON1T [52], LUX [53], PandaX [54], LZ [55] and DarkSide [56].

3.3.4 Spherical proportional counters (SPCs)

These detectors are spherical vessels, filled with a gas. Ionizations, created by dark matter interactions in the gas, are drifted along the radial electrical field, created by a high voltage at the vessels center. Electrons are accelerated towards the center. With increasing energy they can create secondary electron-ion pairs. The ions are collected in the grounded outer vessel. The current that is generated by the collection of the ions is then integrated and converted into a voltage. A big advantage of these detectors is the versatility of the gas mixtures they can use. By using light elements like H, He and Ne very low energy thresholds for nuclear recoils can be achieved $\mathcal{O}(100\text{ eV})$, which makes them excellent for light dark matter searches. Surface related backgrounds can be discriminated via their pulse shape. Since most backgrounds are related to the surface, SPC experiments typically also use a fiducialization of their detectors. For a more in-depth review see [57]. An example of an experiment using SPCs is NEWS-G [58].

3.3.5 Bubble chambers

Bubble chambers fall under the category of so-called *superheated detectors*. The experimental chamber is filled with a liquid (CF_3I or C_3F_8 in PICO [59]) that is heated to a temperature above its boiling point, bringing it into a superheated, metastable phase. Particle interactions that release energy above a certain threshold within a given radius can nucleate macroscopic bubbles that are recorded with cameras. Electron and gamma events have a too low differential energy loss in the liquid ($\frac{dE}{dx}$) to create bubbles, which already largely reduces the backgrounds. The recording of the bubbles with cameras allows for a fiducialization of the detector volume, leading to an additional degree of background rejection. Dangerous backgrounds from α-particles can be discriminated via their acoustic signal [60]. Lastly, a big advantage of using e.g. CF_3I or C_3F_8 is the nuclear spin of ^{19}F of $1/2$, which allows the experiments to be also sensitive to spin-dependent dark matter interactions. Examples for such experiments are PICO-60 and PICO-40L [59].

3.3.6 Cryogenic experiments

As already mentioned before, the majority of the transferred energy of a dark matter interaction is converted into heat in the target material. While in the detectors listed above this information is lost, the big advantage of cryogenic solid state detectors is that the energy released by the dark matter interaction is measured in an unquenched channel (phonons). The basic idea is that an interaction in the target leads to a small

temperature rise $\mathcal{O}(\mu\text{K})$. Due to a coupling to a thermal bath, the detector is cooled back to its original temperature after the interaction. These thermal pulses are then read out by ultra sensitive thermometers.

Semiconductors: Cryogenic experiments using semiconductors as targets are additionally reading out a charge signal by applying an electric field to the detector. The electron-hole pairs formed in the particle interaction are then drifted towards electrodes, in which they are collected (ionization signal). Experiments reading out charge and heat are e.g. EDELWEISS [61] and SuperCDMS [62].

Scintillating materials: Cryogenic experiments using scintillating materials as targets are additionally measuring the light signal produced by particle interactions. Experiments belonging to this category are e.g. CRESST [63], which will be discussed in more detail in chapter 4, and COSINUS [64].

As in the other experimental techniques, the dominant backgrounds are β and γ particles, which interact with the electrons of the target material. Since the charge/scintillation signal is different for electron interactions and nuclear recoils, the ratio between the measured heat signal and the measured charge/scintillation signal is used to discriminate against this background.

3.3.7 Charge-coupled devices (CCDs)

Charge-coupled devices contain an array of capacitors (pixels), that are electrically coupled to each other. Similar to the semiconductor detectors, particle interactions inside the CCD generate charge carriers proportional to the energy deposition. These are drifted in an electric field and read out by electrodes at the edges of the CCD array, allowing for spatial reconstruction of an event inside the detector. Different types of events lead to different patterns of charge-clusters in the pixels, high-energetic charged particles like e.g. muons or electrons lead to tracks in the detector, while nuclear recoils have a point-like signature. Thus, CCDs allow for a good background discrimination.

The energy needed to create charge-carriers in the CCD is of the order of the bandgap of the used material (usually Si). This, together with the low level of electronic noise[2], allows CCDs to achieve very low energy thresholds for electron recoils. Therefore, experiments using CCDs are looking for **dark matter particles interacting with electrons** (instead of nuclear recoils), making them excellent detectors for a low-mass dark matter search. Modern experiments are using so-called *skipper CCDs*, which can make multiple non-destructive charge measurements. This allows for the reach of single-charge resolutions and sub-electron noise thresholds [65].

[2]The noise in CCDs is mostly dominated by the read-out.

Examples for experiments using CCDs are DAMIC [65] and SENSEI [66]. Even though this section is focusing on experiments looking for **nuclear recoils**, these two experiments are mentioned here as they currently experience the same challenge as many other low-threshold solid state detector experiments: An unexplained background at the lowest energies, which will be covered in chapter 6 and sec. 7.5.2.

3.3.8 Current landscape of direct detection experiments

In absence of a statistically significant dark matter signal, experiments typically calculate dark matter exclusion limits on the material independent dark matter interaction cross section per nucleon (see sec. 3.1.2) as a function of the dark matter particle mass. Figure 3.8 shows the current[3] status of direct detection experiments searching for spin-independent elastic dark matter nucleus scatterings [67]. The green shaded area is the excluded parameter space under standard assumptions.

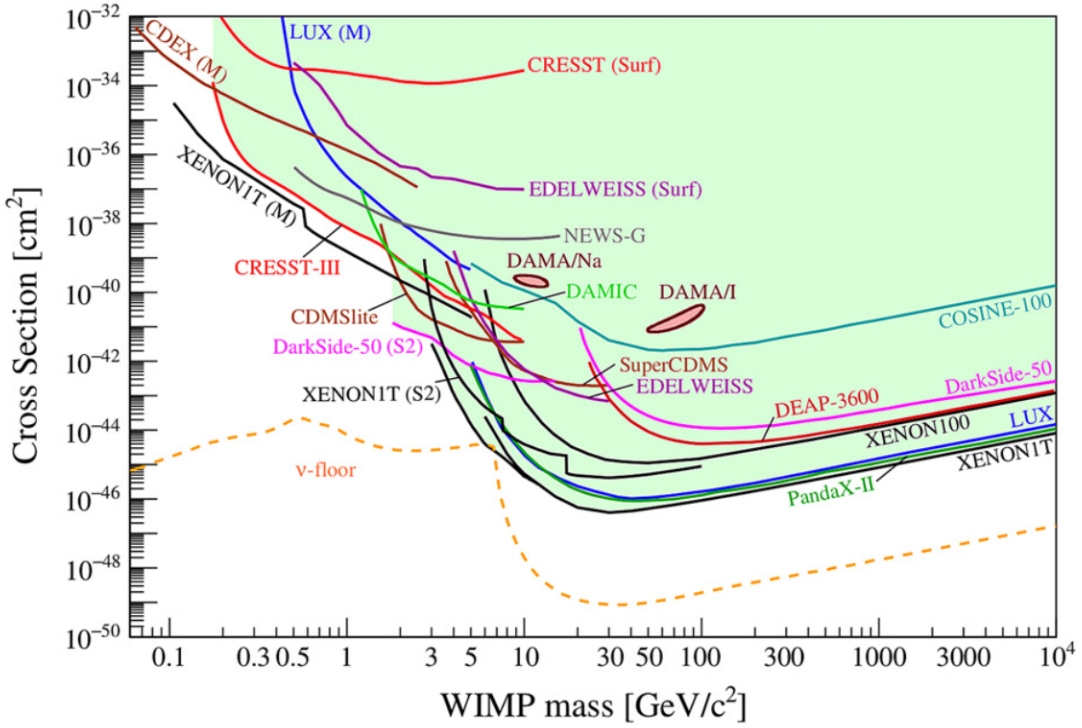

Figure 3.8: Current status of direct detection experiments. The neutrino floor is calculated for a Ge target (for details see sec. 8.2). The results shown are from CDEX [68], CDMSlite [69], COSINE-100 [70], CRESST [63, 71], DAMA/LIBRA [72] (contours from [73]), DAMIC [74], DarkSide-50 [75, 76], DEAP-3600 [77], EDELWEISS [78, 79], LUX [53, 80], NEWS-G [58], PandaX-II [81], SuperCDMS [82], XENON100 [83] and XENON1T [52, 84, 85, 86]. Figure taken from [67].

[3]Current at the time of the publication of the "Direct detection of dark matter APPEC committee report 2022".

3.4 Coherent elastic neutrino-nucleus scattering (CEνNS)

The coherent elastic neutrino-nucleus scattering (CEνNS) is a neutral current process, predicted by D. Freedmann in 1974 [87], in which a neutrino ν_α of any flavor ($\nu_\alpha \in \{\nu_e, \nu_\mu, \nu_\tau, \overline{\nu_e}, \overline{\nu_\mu}, \overline{\nu_\tau}\}$) scatters off a nucleus via the exchange of a virtual Z^0 boson. Analogous to the dark matter discussion above, at low momentum transfers $q = \sqrt{2m_N E_R}$, the wavelength of the Z^0 boson is larger (or in the order of) the size of the nucleus and the scattering is a coherent process. This is depicted in the Feynmann diagram in fig. 3.9.

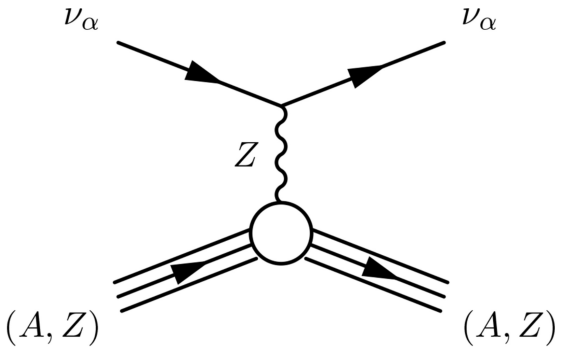

Figure 3.9: Tree-level Feynman diagram of a CEνNS process. Figure taken from [88].

The first observation of this process was only as recent as in 2017 by the COHERENT collaboration [89]. Since nuclear recoil signals induced by CEνNS cannot be distinguished from a dark matter recoil signal, there is a high interest of the direct detection community in understanding this process.

3.4.1 Cross section

The elastic scattering process of a neutrino with energy E_ν off a nucleus with mass m_N is (analogous to the dark matter scattering) a two body problem. The recoil energy of the nucleus, E_R, is described by:

$$E_R = \frac{q^2}{2m_N} = \frac{E_\nu^2}{m_N}(1 - \cos\theta) \tag{3.19}$$

with θ being the scattering angle in the center-of-mass frame. Considering that $m_N \simeq \mathcal{O}(\mathrm{GeV/c^2})$, neutrinos with energies $E_\nu \simeq \mathcal{O}(\mathrm{MeV})$ lead to recoil energies of $E_R \simeq \mathcal{O}(\mathrm{keV})$. Thus, the momentum transfer $q \simeq \mathcal{O}(\mathrm{MeV/c})$ is small compared to the size of the nucleus ($E_R \ll q \ll m_N$), i.e. neutrinos of $\mathcal{O}(\mathrm{MeV})$ energies dominantly scatter coherently.

The (simplified) differential CEνNS cross section is given by [88]:

$$\frac{d\sigma}{dcos\theta} = \frac{G_F^2}{2\pi} \cdot E_\nu^2(1 + cos\theta) \cdot |\langle g.s.|\,|\hat{\mathcal{M}}|\,|g.s.\rangle|^2 \tag{3.20}$$

with G_F being the Fermi constant and $\langle g.s.|\,|\hat{\mathcal{M}}|\,|g.s.\rangle$ being the matrix element for ground state to ground state transitions (valid for small momentum transfers). Using eq. 3.19, this expression can be transformed into:

$$\frac{d\sigma}{dE_R} = \frac{G_F^2}{\pi} \cdot m_N \left(1 - \frac{E_R}{E_{R,max}}\right) \cdot |\langle g.s.|\,|\hat{\mathcal{M}}|\,|g.s.\rangle|^2 \tag{3.21}$$

with $E_{R,max} = \frac{2E_\nu}{m_N}$. Using the definition of the weak nuclear charge in [88] (see app. A.4):

$$Q_W \simeq \frac{1}{2}\left[(4sin^2\theta_W - 1)Z + N\right] \tag{3.22}$$

with θ_W being the Weinberg angle and Z and N being the number of protons and neutrons, respectively, this can be written as:

$$\frac{d\sigma}{dE_R} = \frac{G_F^2}{2\pi} \cdot Q_W^2 \cdot m_N \cdot \left(2 - \frac{E_R m_N}{E_\nu^2}\right) |F(q)|^2 \tag{3.23}$$

Under the assumption that the weak charge distribution of the nucleus follows the same distribution of the charge density, the form factor $F(q)$ can be described with the parameterization presented in 3.1.3. Since $sin^2\theta_W \simeq 0.23142$ [90], it can be seen that $Q_W^2 \simeq N^2$ and thus, the CEνNS cross section scales roughly with the number of neutrons squared.

3.4.2 Possible sources

There are several possible sources of neutrinos:

- Atmospheric neutrinos
- Solar neutrinos
- Diffuse supernova neutrinos
- Terrestrial (geo) neutrinos and anthropogenic radioactivity (reactor neutrinos)

Reactor neutrinos are not of concern for dark matter direct detection, since the experimental sites are chosen to be in a low-radioactivity environment. Experiments actively looking for CEνNS on the other hand often choose nuclear reactors as a neutrino source. Figure 3.10 shows the fluxes on Earth of several natural neutrino sources [91].

The cosmic neutrino background (CνB) is too low energetic to be measured with todays technologies. Neutrinos from active galactic nuclei (AGN), gamma ray bursts (GRB) and cosmogenic neutrinos (GZK) have extremely low fluxes and are therefore also not considered a serious background for direct detection experiments. The remaining neutrino sources (atmospheric, solar, (diffuse) supernova and terrestrial) are typically

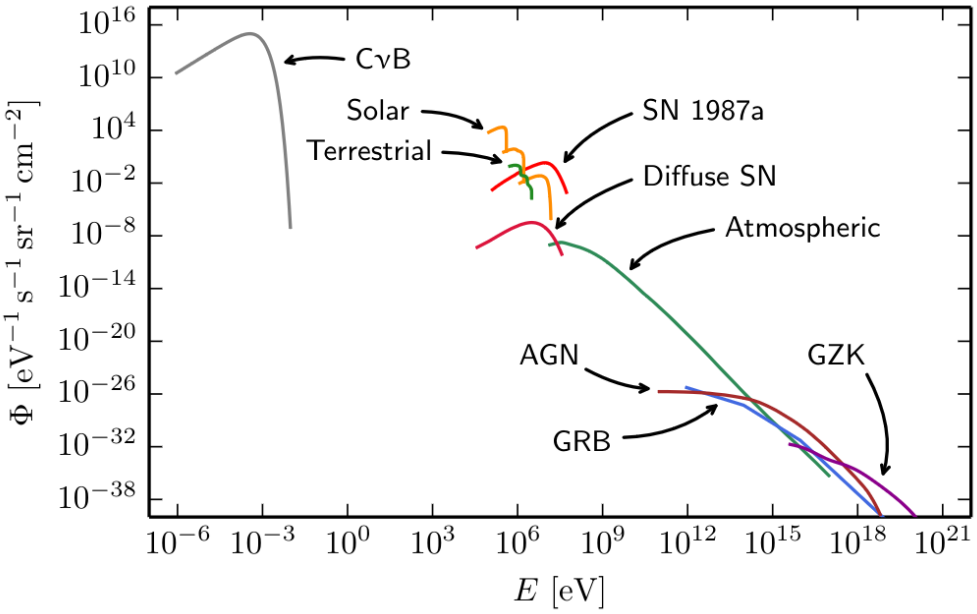

Figure 3.10: Fluxes of natural neutrino sources. Figure taken from [91].

considered as potential backgrounds in direct detection. Chapter 8 contains a detailed investigation of the expected signals of **solar neutrinos**, which is the most intense source, in direct detection experiments.

Chapter 4

The CRESST-III experiment

The CRESST (**C**ryogenic **R**are **E**vent **S**earch with **S**uperconducting **T**hermometers) experiment is a long established and well known dark matter direct detection experiment, located in the **L**aboratori **N**azionali del **G**ran **S**asso (LNGS) underground laboratory in Italy. First measurements started shortly after its construction in the 1990's. Since the last 10 years it has been one of the world leading experiments in the field of dark matter direct detection. This chapter is giving an overview of the experimental setup (sec. 4.1), the working principle (sec. 4.2) and the data aquisition (sec. 4.3).

4.1 Experimental Setup

A schematic drawing of the cross section of the experimental setup of CRESST is shown in fig. 4.1, illustrating the various layers of shielding and the veto systems as well as the structure of the cryostat and the centrally located carousel, holding the detector modules.

4.1.1 Minimizing Backgrounds

The relevant backgrounds for direct detection experiments have already been discussed in sec. 3.2. This section gives a brief overview of the methods of background reduction specific to the CRESST experiment.

Muons: The LNGS laboratory has a rock overburden of 1400 m (corresponding to 3800 m.w.e.), reducing the flux of cosmic muons to $(3.41 \pm 0.01) \cdot 10^{-4}$ $\mathrm{m}^{-2}\mathrm{s}^{-1}$ [93]. While the remaining muons are not directly a background for CRESST, they can interact with the surrounding materials of the detectors, causing the creation of secondary particles. Therefore the setup is surrounded by a muon veto system, consisting of 20 plastic scintillator panels equipped with photomultipliers. Particle events in the detectors that are in coincidence with an event in the muon veto panels can be rejected in the analysis. The overall geometrical coverage of the muon veto panels is 98.7 % [94].

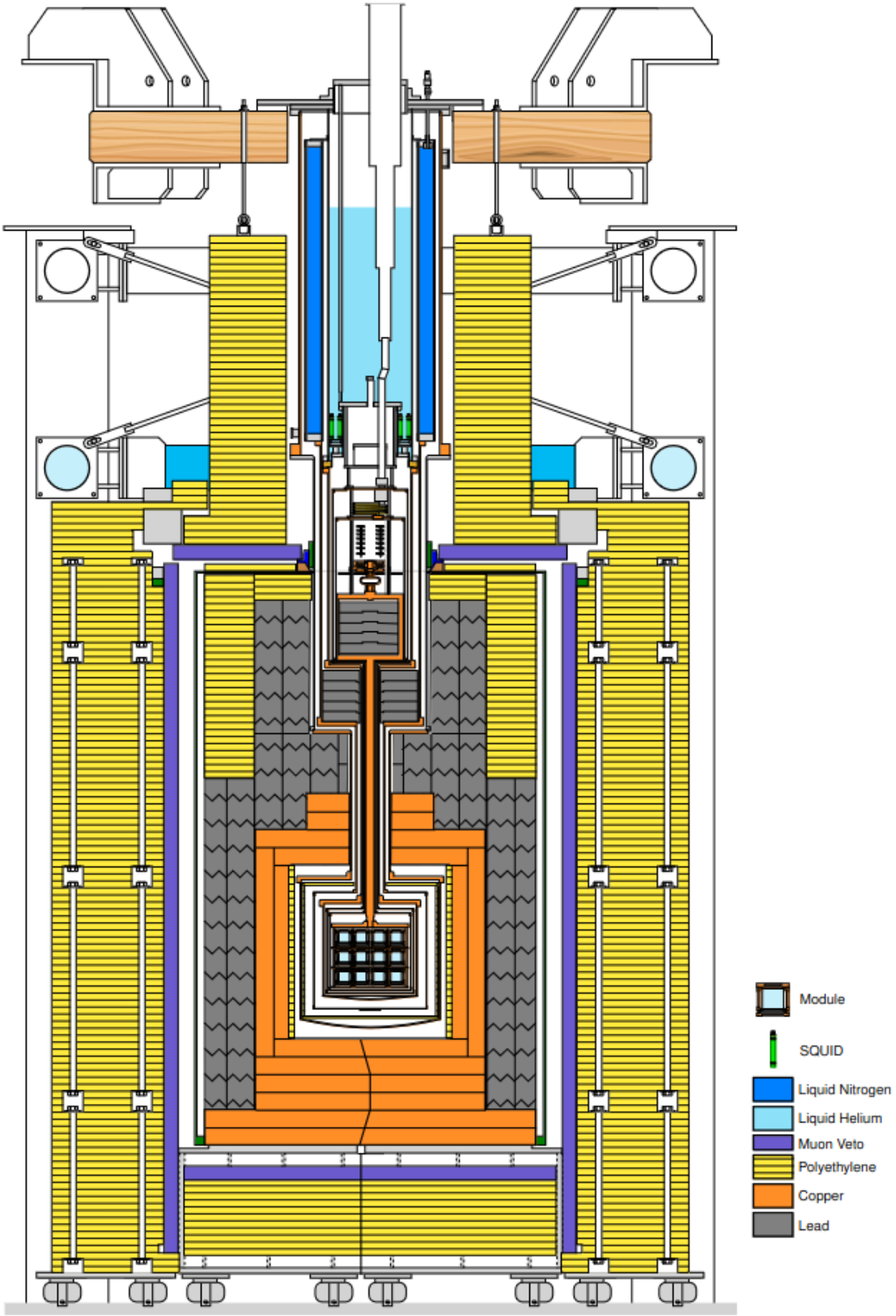

Figure 4.1: Schematic drawing of the cross section of the CRESST setup, showing the structure of the cryostat and the various layers of shielding. The detector modules are located in the center, held by the so-called *carousel*. Figure taken from [92].

Radon-222: A specific background not mentioned in sec. 3.2 is coming from ^{222}Rn, a gaseous radioactive isotope that belongs to the ^{238}U decay chain. It has a half-life of 3.82 days, which is long enough to escape from the surrounding rocks into the experimental halls, where it can bypass the shieldings by diffusion and contaminate exposed surfaces. The subsequent decays in the ^{222}Rn chain occur relatively fast, until the long-lived isotope ^{210}Pb (22 years) is reached. The ^{210}Pb decays via β-decay to ^{210}Bi, which subsequently β-decays to ^{210}Po with a half-life of 5 days, before reaching the stable isotope ^{206}Pb via an α-decay (138 days). This makes ^{222}Rn a dangerous background. The level of ^{222}Rn in the air of the experimental halls at LNGS is measured to be about 20 Bq m^{-3} [95]. To prevent the contamination with ^{222}Rn, the experimental setup inside the muon veto system is enclosed in the so-called *radon box*, which is an air-tight box, continuosly flushed with nitrogen and kept in overpressure. To additionally prevent any radon contamination of materials facing the detectors, all detector parts are etched and stored under a nitrogen atmosphere before being installed in the experimental setup.

Gammas and electrons: To shield the experimental volume against radioactive backgrounds, CRESST is using 20 cm of radiopure[1] lead with a total of 24 t of weight. Just below the mixing chamber (central part in fig. 4.1), there is a layer of very low background lead in order to protect the detectors from the radioactivity of the commercial cryostat. To shield against remaining intrinsic radioactivity of the lead, an additional layer of 14 cm of copper is used inside of the lead shield (with a total weight of 10 t). A big advantage of copper is the high level of radiopurity that can be achieved. Therefore it is also used for all support structures in the direct vicinity of the detectors.

Neutrons: To moderate neutrons, the outermost layer of the CRESST setup is made of Polyethylene with a thickness of 40 cm and a total weight of 10 t. Neutrons might also be produced inside the lead and copper shieldings, e.g. by muons. If the muon is missed by the veto, these neutron events are not tagged as muon induced events. Therefore an additional layer of 3.5 cm of Polyethylene is installed close to the detectors (see fig. 4.1)

Particle discrimination: The CRESST detector module design allows for an additional active background discrimination in the analysis: The production of scintillation light in the detectors is a keypoint in distinguishing potential signal events from background. Details about the detector design are given in sec. 4.2.

4.1.2 Cryostat

The extremely low temperatures that are required to operate the CRESST detectors ($\mathcal{O}$(mK)) are achieved by the use of a commercial dilution refrigerator. The thermal

[1] Even in the low-background lead used for the shielding, there is always some residual radioactivity present.

coupling between the cryostat and the carousel, holding the detectors, is provided by the so-called *cold finger*. For the operation of the wet cryostat it is necessary to regularly refill cryogenic liquids[2]. During these refills the operating conditions of the detectors are not stable and thus data taking has to be interrupted for a few hours (usually about 3 hours per refill).

4.2 Detector Modules

This section focuses on the working principle and the standard detector design of the CRESST-III experiment. The goal is to directly measure dark matter particle interactions via elastic scattering in a scintillating crystal (which in the standard design is made of $CaWO_4$), operated as a cryogenic calorimeter. The energy deposition is precisely measured as a temperature rise (phonon signal) with a transition edge sensor (TES), which is an ultra sensitive thermometer. The scintillation light produced in the crystals is measured with a second detector. This second detector is also a phonon detector, the energy depositions of the scintillation light are detected following the exact same working principle as the main absorber. The amount of scintillation light is indicative for the type of interaction and is therefore used for an active discrimination of background events.

4.2.1 Cryogenic Calorimeter

In the most basic picture, a cryogenic calorimeter consists of an absorber that is equipped with a thermometer and is linked to a heat bath. An energy deposition of ΔE leads to a temperature rise ΔT of the absorber according to:

$$\Delta T \propto \frac{\Delta E}{C} \tag{4.1}$$

where C is the heat capacity of the absorber material. The deposited energy is fully transferred into the temperature change, hence the name *cryogenic calorimeter*. To maximize the temperature change ΔT for a fixed energy deposition ΔE, the heat capacity C has to be as small as possible.

Heat capacities of different parts of detectors play a fundamental role because they define the achievable temperature rise for a defined energy deposition. In general, the heat capacity decreases with decreasing temperature. Therefore, the operating temperature should be very low ($\mathcal{O}$(mK)).

[2] In the current data taking campaign, the refills are done three times per week.

4.2.2 Transition Edge Sensors (TES)

In order to measure the energy deposition ΔE, the absorber is equipped with a TES, which acts as an ultra sensitive thermometer. The TES main component is a thin W film, deposited on the crystal surface. It is operated in the transition between the superconducting and normal conducting state, which is at a temperature of about ∼ 15 mK. Small temperature changes of ΔT = $\mathcal{O}(\mu K)$ lead to a measurable change of resistance in the TES of $\mathcal{O}(m\Omega)$. Figure 4.2 shows an example of two transition curves at temperatures of about 22 mK and 24 mK.

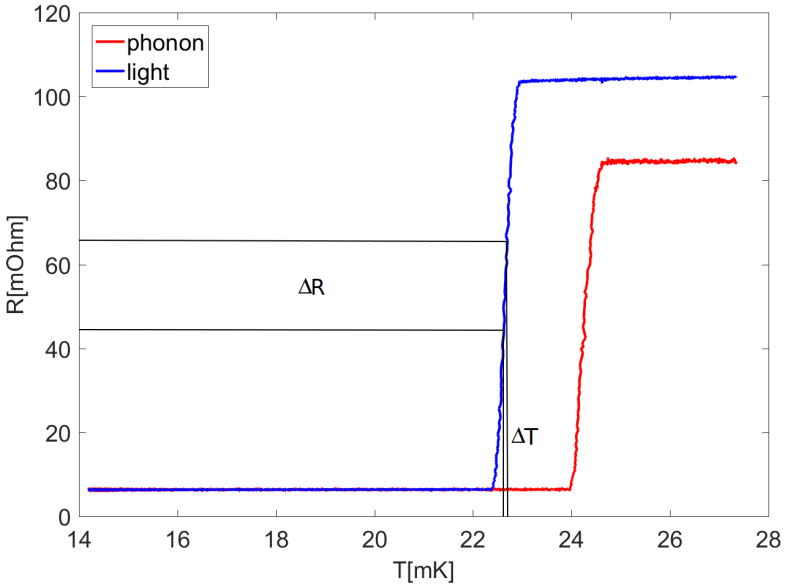

Figure 4.2: Example of TES transition curves of a CRESST detector module. The TES is operated in between the superconducting and the normal conducting state. Due to the steep rise of the transition curve, small temperature changes lead to a measurable change in the resistance of the sensor.

4.2.3 Pulse formation in the target

The theoretical description of the temperature rise as a function of the deposited energy in eq. 4.1 is a simplification. In 1995, F. Pröbst et al. worked out a theoretical model for the expected signal shape, involving thermal couplings and the heat capacity of the thermometer [96]. This section gives a short summary, for more details see [96]. Figure 4.3 shows a schematic drawing of the thermal system of the absorber, thermometer and the heat bath.

The initial particle interaction in the absorber leads to the creation of high-frequency optical phonons. These phonons decay rapidly ($\mathcal{O}$(ns)) into acoustical phonons with a frequency of about half of the Debye frequency ($\sim \frac{\nu_D}{2}$). The Debye frequency is related to the Debye temperature by: $\nu_D = \frac{k_B \Theta_D}{\hbar}$, with k_B being the Boltzmann constant and $\hbar$

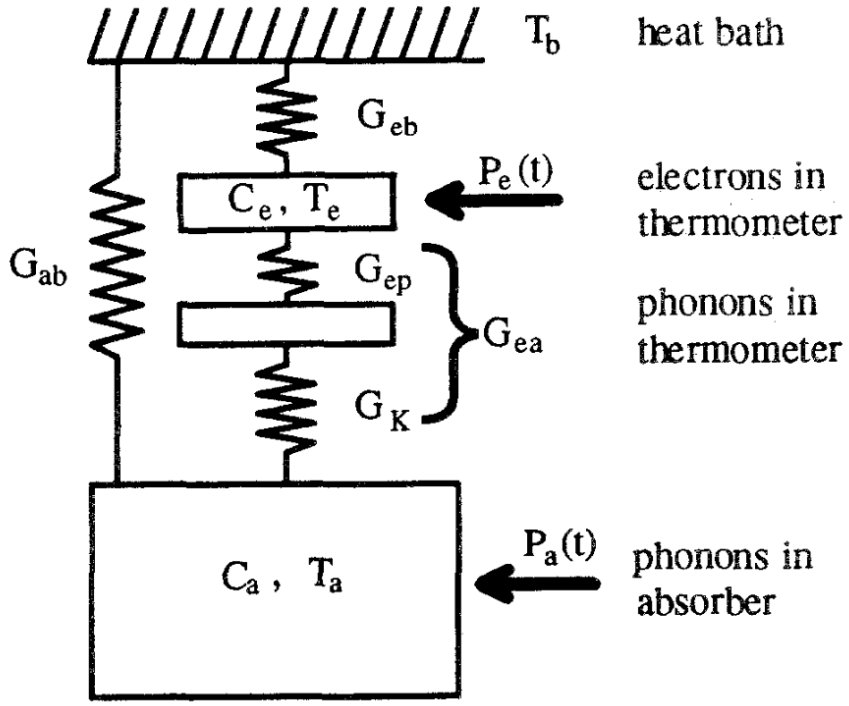

Figure 4.3: Thermal model of the detector. T_b is the temperature of the heat bath, T_e and T_a are the temperatures of the electron system in the thermometer and of the phonon system in the absorber, respectively, C_e and C_a are their heat capacities and P_e and P_a are the energy flows from non-thermal phonons into them. G_{ab}, G_{eb} and G_{ea} are the thermal conductances. Figure and caption taken from [96].

the Planck constant. The acoustic phonons are down converted into phonons of $\mathcal{O}$(100 GHz) via the decay into two phonons with a decay rate strongly proportional to the frequency: $\Gamma_d \propto \nu^5$. After a few surface reflections, a crystal with dimensions of $\mathcal{O}$(cm) (with a typical sound velocity of $\sim 10^3 \frac{m}{s}$) is uniformly filled with non-thermal phonons. This happens on time scales too short for the phonons to thermalize in the absorber. The high-frequency phonons that enter the thermometer are efficiently absorbed by the free electrons of the metal film. They are quickly thermalized, leading to a heating of the electron-system in the thermometer, which determines the time dependent power input $P_e(t)$ (see fig. 4.3). The temperature rise in the absorber (T_a) is mainly given by the initial phonons that did not enter the thermometer, but instead thermalize in the crystal.

The final signal is the temperature T_e of the electrons in the thermometer. The signal component induced by the thermalization in the TES is indicated as fast component of the signal, while the component due to the absorber temperature rise is indicated as the slow signal component. For thermal phonons at low temperatures the coupling of the absorber to the electron system of the thermometer is weak: $G_{ep} \propto T^5$. The transmission of thermal phonons between the interface of the thermometer and the absorber is

defined by the Kapitza thermal conductance: $G_K \propto T^3$. The effective coupling G_{ea} between absorber and TES is given by:

$$G_{ea} = \left(\frac{1}{G_{ep}} + \frac{1}{G_K} \right)^{-1} \tag{4.2}$$

The thermal coupling of the thermometer to the heat bath, G_{eb}, is given by the heat conductance along the film and an Au structure (and wire) with $G_{Au} \propto T$ (thermal link to the bath). The coupling G_{eb} defines the time constant of the detector, τ_{in} (see eq. 4.3 and explanations below).

While $P_e(t)$ describes the power input in the thermometer, $P_a(t)$ describes the power input into the absorber, given by the thermalization of high-frequency phonons. The calculation of the thermometer response $\Delta T_e(t) = T_e(t) - T_b$ is based on the solution of the differential equations for the power inputs $P_e(t)$ and $P_a(t)$ (see [96]):

$$\Delta T_e(t) = \Theta(t - t_0) \left[A_n \left(e^{-\frac{t-t_0}{\tau_n}} - e^{-\frac{t-t_0}{\tau_{in}}} \right) + A_t \left(e^{-\frac{t-t_0}{\tau_t}} - e^{-\frac{t-t_0}{\tau_n}} \right) \right] \tag{4.3}$$

The physical interpretation of the parameters is given in the following:

- A_n**:** Amplitude of the non-thermal (fast) component
- A_t**:** Amplitude of the thermal (slow) component
- τ_n**:** Time constant for the thermalization of non-thermal phonons in the film and the crystal
- τ_{in}**:** Intrinsic time constant of the thermometer (thermal relaxation time of the film).
- τ_t**:** Thermal relaxation time of the absorber

The amplitude of the non-thermal component, A_n, is especially interesting as it holds most of the information of the initial energy deposition. Depending on the exact values of the time constants, CRESST can be operated in two different modes:

Bolometric mode: If $\tau_{in} \ll \tau_n$, the intrinsic thermal relaxation time in the film is much faster than the time constant for the thermalization of the non-thermal phonons. Therefore the flux of the non-thermal component is measured and the amplitude is given by:

$$A_n \simeq \frac{P_0}{G_{ea} + G_{eb}} \tag{4.4}$$

with P_0 being the initial power input into the thermometer, given by:

$$P_0 = \frac{\epsilon \Delta E}{\tau_n} \tag{4.5}$$

with ϵ being the fraction of phonons thermalized in the thermometer[3].

Calorimetric mode: If instead $\tau_{in} \gg \tau_n$, the intrinsic thermal relaxation time of the thermometer film is much slower than the time constant for the thermalization of the non-thermal phonons and the thermometer basically integrates $P_e(t)$, leading to the amplitude:

$$A_n \simeq -\epsilon \frac{\Delta E}{C_e} \tag{4.6}$$

The CRESST-III experiment detectors are designed to operate in the calorimetric mode.

SQUID readout and final signal: The TES is connected in a parallel circuit to a coil with two resistors, each with $\frac{1}{2}R_{shunt}$, with R_{shunt} being a reference resistance. A bias current of $\mathcal{O}(\mu A)$ is applied to the circuit. Figure 4.4 shows a drawing of this circuit.

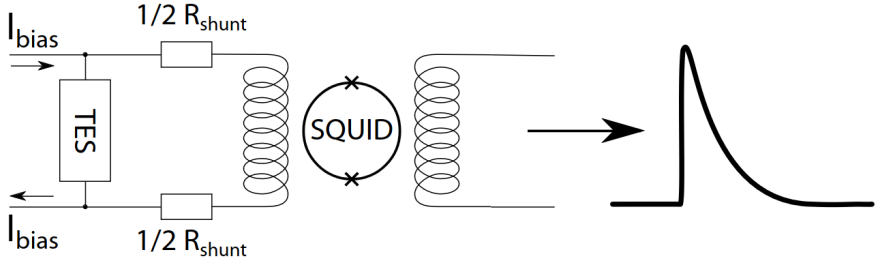

Figure 4.4: Readout of the TES signal with a SQUID. Figure taken from [97].

A small resistance change of the TES is changing the branching of I_{bias} and therefore the magnetic field of the coil. **S**uperconducting **QU**antum **I**nterference **D**evices (SQUIDs) are used to precisely convert small magnetic field changes into a voltage signal. This voltage signal is then read out and saved by the data aquisition system (see sec. 4.3). Figure 4.5 shows an example of such a pulse in units of Volt. As long as the energy deposition in the absorber leads to a temperature rise that is within the linear regime of the transition curve, the amplitude of the pulses (in V) are linearly proportional to the deposited energy in the crystal.

4.2.4 Standard design and event discrimination

The standard design of a CRESST-III detector module can be seen in fig. 4.6. The central piece is the block-shaped main absorber crystal (24 g of scintillating $CaWO_4$ crystal), equipped with a W-TES. The scintillation light produced by the particle interactions in the main absorber is detected by the light detector, which is a thin wafer made of Silicon-on-Sapphire (SOS), likewise equipped with a W-TES. The housing of the detector module

[3] Accordingly, (1-ϵ) is the fraction of phonons thermalized in the absorber

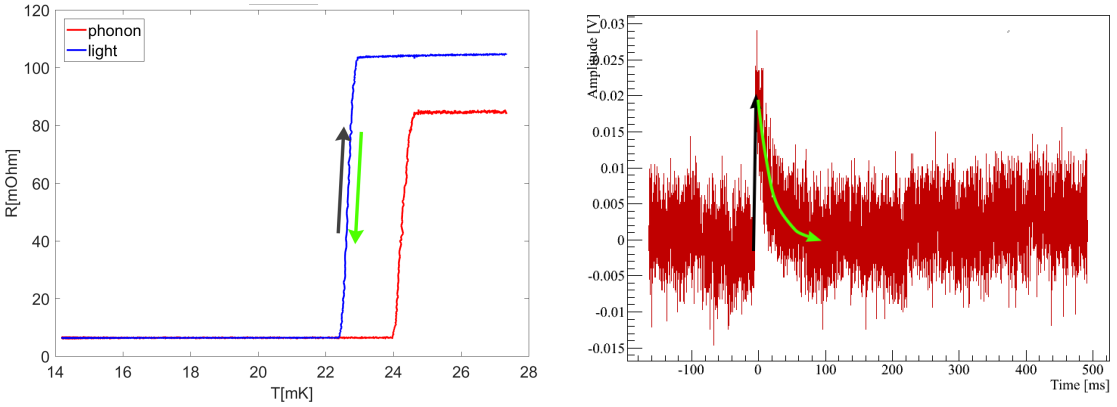

Figure 4.5: Left: A particle interaction causes the temperature in the sensor to rise (black arrow). Due to the coupling to a heat bath, the sensor is cooling down to its operating temperature after the interaction (green arrow). Right: The resistance change in the TES, caused by this temperature change, is readout with a SQUID and converted into a voltage signal (The scaling of the arrows is just for illustration and does not reflect an actual correspondance between the change in resistance and the converted voltage).

is covered with reflecting and scintillating foil. This maximizes the light collection in the light detector and helps tagging surface related backgrounds. Furthermore, the modules can contain an instrumented holding system: The main absorber can be held by $CaWO_4$ sticks, equipped with a W-TES, thus they are also called iSticks (instrumented sticks). Their purpose is to investigate/veto holder-induced backgrounds.

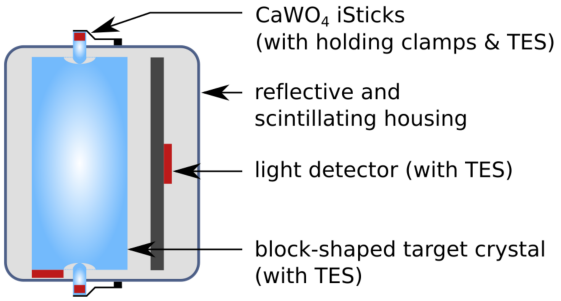

(a) Schematic drawing of a detector module.

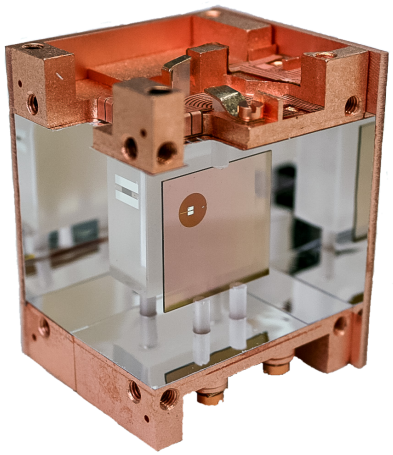

(b) Picture of an open detector module.

Figure 4.6: Standard design of a CRESST-III detector module. a) Schematic drawing and b) Picture of an open module.

The detection of the scintillation light allows for a background discrimination on an event-by-event base. β and γ radiation dominantly interact via electron scatterings, which produce more scintillation light than nuclear recoils. The light yield of an event is

defined as the ratio of the energy E_l, measured in the light channel and the energy E_p, measured in the phonon channel:

$$LY = \frac{E_l}{E_p} \tag{4.7}$$

Since only a very small fraction of the deposited energy is emitted as scintillation light, the energy measured in the phonon channel, E_p, is used as an estimator of the total deposited energy. The measured scintillation light, E_l, is calibrated to a value of one for β and γ events. The scintillation light produced by nuclear recoils is strongly quenched, compared to electron interactions, which makes a discrimination possible. A schematic depiction of the LY versus energy plot is shown in fig. 4.7.

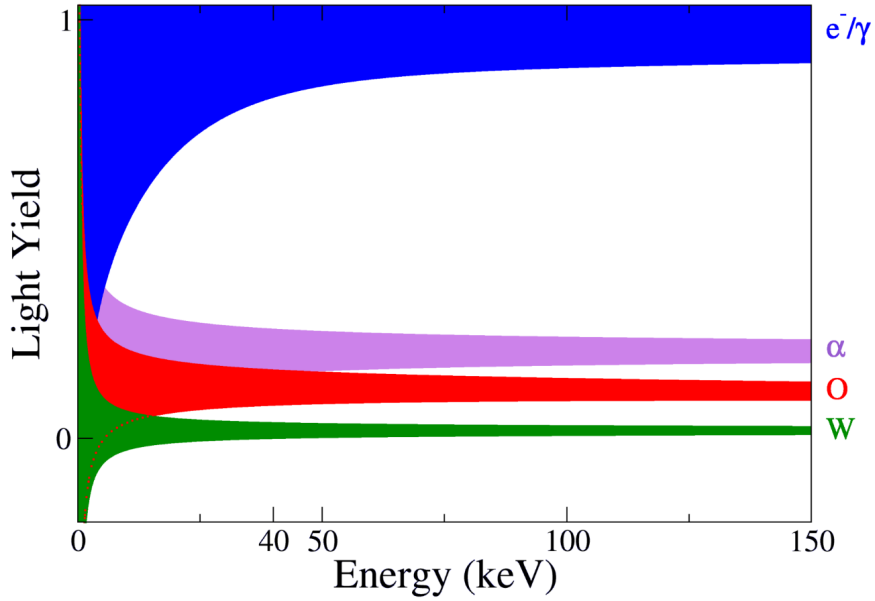

Figure 4.7: Schematic drawing of the light yield plot. Figure taken from [98].

4.3 Data Acquisition

There are two different methods of data acquisition (DAQ) in CRESST-III: The **Hardware trigger (HW)** and the **Continuous DAQ (CDAQ)**. The voltage signal output of the detector is digitized and then, depending on the method, partially or fully written to disk. The sampling rate of the digitizer for the data presented in this thesis was set to 25 kHz, which corresponds to 1 sample every 40 μs.

Hardware trigger: In the first stages of the CRESST experiment (previous to CRESST-III), the hardware trigger was the only form of data acquisition. There the SQUID output signal is split: One part is send to a transient digitizer with a ring buffer, constantly

recording the samples of the voltage output[4]. The other part is send to the trigger electronics, which include additional filters, an amplifier and a comparator unit. The comparator checks if a recorded sample exceeds the **trigger threshold**, which causes the DAQ to **trigger**. In that case the DAQ waits for the so-called **post-trigger time** to read out the transient digitizer, including a set of **pre-trigger** samples. This method has some disadvantages: The trigger is not active during the read out and is only activated after another set of samples, corresponding to the pre-trigger range, is recorded in the digitizer again, causing a certain amount of dead-time of the DAQ. The trigger threshold has to be chosen really carefully at the beginning of the data taking. Since data that has not been triggered is lost after the ring buffer is overwritten, the threshold should be set as low as possible. At the same time it is important to avoid random noise triggers, as they introduce unnecessary amounts of dead-time.

Since in CRESST-III also the CDAQ data is available, the hardware trigger threshold is not crucial anymore. The HW data is mostly used for a first iteration of the analysis, which is then refined by using the CDAQ data (see sec. 5.1).

Continuous DAQ: In the continuous acquisition the full, dead-time free output of the detector is recorded and saved to disk. This is achieved by using two digitizers running in parallel in switching mode. Details of the principles and the implementation of the CDAQ in CRESST can be found in [98]. The big advantage of this type of DAQ is that no data is lost. The triggering of the data is done offline with a software using an optimum filter (see sec. 5.1.3) and can be iteratively repeated as the analysis is getting more refined. Furthermore, the full stream of data of a detector is available and can be used to perform simulations, which are necessary in order to estimate the survival probability of events (see sec. 5.2.4).

[4]Once the buffer is full, it starts overwritting the oldest samples, thus the name *ring buffer*.

Chapter 5

Data Analysis

This chapter gives a detailed overview of all relevant steps of the standard data analysis in CRESST[1], which can be divided into three main parts. The first part is the raw data processing, in which most parameters that are used for further analysis are extracted. The second part, in the following called low level analysis, consists of several individual steps, which lead to the production of the final energy spectra. The data selection criteria are defined and applied. Then the reconstructed amplitudes of the surviving events are calibrated. In the end, the energy dependent survival probabilities of events are determined. The last part, called high level analysis, involves the physics interpretations of the final energy spectra. In general, the data can be used to search for any kind of signal, as long as it is physically motivated and has a non vanishing theoretical expectation. In the CRESST standard analysis the energy spectra are used to look for the signal of elastic coherent spin-independent scattering of dark matter off nuclei, as described in sec. 3.1.5. In the case of no statistically significant dark matter signal, mass dependent exlusion limits on the interaction cross section are calculated. In the case of a statistically significant signal, the data can be used to constrain or estimate the parameters of the dark matter model considered.

5.1 Raw data processing

As mentioned in 4.3, there are two types of data acquisition: the hardware triggered (HW) data and the continuous stream (CDAQ) data. Usually, an analysis of a CRESST detector module starts using the HW data, as these already contain triggered pulses that can be used for a first study. The HW data are used to create the first iteration of an optimum filter and to determine the trigger threshold for the CDAQ data (see secs. 5.1.3 and 5.1.4). After the CDAQ data has been filtered and triggered, the subsequent steps of the raw data processing are the same for both types of data (HW and CDAQ). These steps, which will be explained in sec. 5.1.2, include the calculation of the parameters of each event, required for the low level analysis.

[1] Unless specified otherwise, all example plots shown in this chapter contain data of the *Sapp2* detector module.

5.1.1 Terminology

Before going into the initial steps of the raw data processing, I will define some terms commonly used in the CRESST analysis.

Run: A full CRESST measurement campaign done in one cooldown is called a run. A typical run takes anything between several months up to a few years of measuring time and can be split into several **datasets**: The three important ones are the **gamma calibration**, the **neutron calibration** and the **background data taking**, the latter one is used for the dark matter analysis.

Run segment: The data taking is interrupted in regular intervals for cryogenic maintenance. This leads to the data being split into smaller segments that are saved into individual files. Each of these segments contains on average about 45 h to 55 h of measuring time.

Read-out channel: Most detector modules in CRESST have more than one channel. In the standard case these are the phonon and the light channel (see sec. 4.2). Each of these channels can be triggered individually.

Record window: The record window is defined as the interval of data samples that are considered whenever the trigger is fired[2]. The sample that caused the triggering by exceeding the threshold is always positioned at exactly one quarter of the record window and splits it into two sections: The **pre-trigger** range and the **post-trigger** range (see fig. 5.1). The default size of a record window in CRESST-III has 16384 samples, which correspond to a time of 655.36 ms. An example of a recorded pulse is shown in fig. 5.1.

Event: Whenever at least one of the read-out channels of a module triggers, the other channels are read out simultaneously. The combination of the records of all channels of a single module at the same time form an event.

Heater pulses: These artificial pulses are periodically injected into the detectors via an electric heater. They can be categorized into **Test Pulses (TP)** and **Control Pulses (CP)**, that serve different purposes. **Test pulses** are sent at different energies that should cover the whole dynamic range of the detector (see sec. 4.2.2). Their main purpose is to track the time dependent response of the detectors, which is then used for the calibration. **Control pulses** are sent at a constant high energy that should lead to pulses going into saturation. The pulse height of these pulses is sensitive to the position of the operating

[2]This is the case for both, HW and CDAQ data.

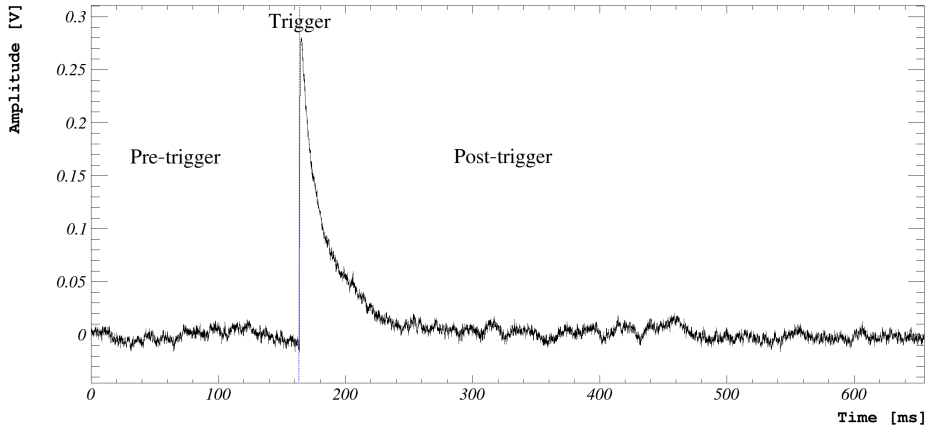

Figure 5.1: Record window of a pulse. The sample that fired the trigger is placed at one quarter of the window, splitting it into the pre-trigger and post-trigger range.

point in the transition curve (see sec. 4.2.2). Due to this, control pulses can be used to monitor the position of the operating point and to actively stabilize it during the data taking.

Particle events: These are the events of main interest. Any particle interaction in the detector falls into this category. These events are used to create the final energy spectra.

Empty baselines: Record windows that are randomly extracted from the data without any channel exceeding the threshold are called **empty baselines (EBLs)**. Given the low event rate of the experiment, they should contain only samples of noise and no pulses. EBLs are used for creating **noise power spectra (NPS)** and to determine the trigger threshold of the CDAQ data. They are also used for simulations, as explained below.

Simulated events: To create simulated events, a signal of the desired pulse shape can be superimposed onto the data stream (mostly EBLs). These simulated events are used to determine the efficiency of the analysis chain and to estimate the survival probabilites of real events.

5.1.2 Parameter calculation

This stage of the analysis requires the existence of an already triggered dataset. In the first iteration of the analysis this is only the case for the HW data. After the creation of an optimum filter and the determination of a threshold (see secs. 5.1.3 and 5.1.4), also the CDAQ data can be triggered, and then processed as explained below.

Event Building: In the very first step, called the **event building**, the trigger timestamps of single read-out channels are grouped into their respective detector modules to form the events, which are saved into data files together with some basic parameters like e.g. their timestamps, the run segment name and their read-out channel numbers for identification. In this step the events are also categorized into different event types. Every time a heater pulse is injected, its timestamp and its amplitude parameter, called the **test pulse amplitude (TPA)**, are saved by the DAQ. By comparing the trigger timestamps with the known timestamps of heater pulses, test pulses and control pulses can be identified and separated from particle events. Particle events are assigned a TPA of zero. In the case of a particle event and a test pulse being in the same record window, the test pulse is prioritized by the event builder, tagging it with its corresponding non-zero TPA value.

Differences between HW and CDAQ data: For the HW data the event building is already done by the DAQ for every run segment. For the CDAQ data this has to be done manually after creating the files containing the trigger timestamps. While doing this, the analyst has the option to decide on some parameters like the exact size of the record window, the pre-trigger range and the percentage of random triggers (EBLs) that should be extracted from the continuous stream. Another difference between the HW and the CDAQ data is the **optimum filter amplitude** parameter. Since during the filtering of the continuous stream the amplitudes of pulses are already reconstructed by the filter, this parameter is saved together with the trigger timestamps. In contrast to this, the raw HW data files do not contain any parameter estimating the amplitudes of particle pulses.

Calculation of Main Parameters: In the subsequent step all pulse shape related parameters are calculated. This is also called **Calculation of Main Parameters (CMP)**. For each pulse, first the baseline parameters are calculated by applying a linear fit to the pre-trigger range. These parameters contain:

- **Baseline offset:** Due to the SQUID electronics the voltage output of an empty baseline (before the pulse) can be shifted by a quantized value between -10 and 10 V (e.g. see fig. 5.2a with a baseline offset of -1.75V).
- **Baseline slope:** A small drift of the operating point within the time of a record-window can lead to a slight tilt of the baseline.
- **Baseline RMS:** Root Mean Square deviation of the data from the linear fit.

The first two parameters form the baseline model, which is subtracted from the pulse record window before the other parameters are calculated. Fig. 5.2 shows an example

of a raw pulse before and after the correction with the baseline model. Most other parameters are based on a moving average of the samples of the corrected pulse. The number of averaged samples can be chosen freely, a typical choice is 50 samples. In fig. 5.2 the averaged pulses are plotted on top of the original pulses.

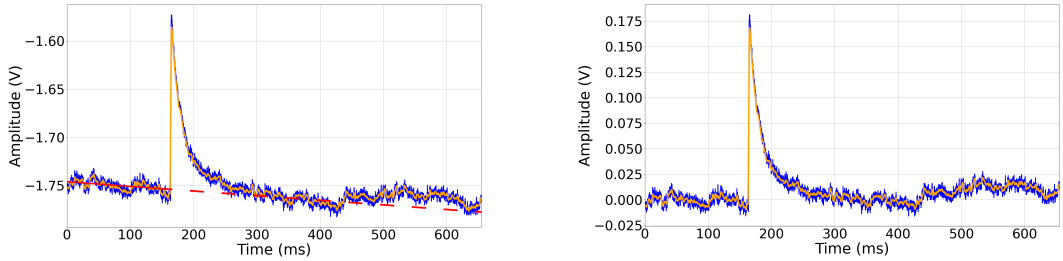

(a) Raw pulse.

(b) Corrected pulse.

Figure 5.2: Example of a pulse (blue) and the moving average (orange). a) The raw pulse and the linear fit of the baseline model (red), the solid part of the line represents the range used for the fit. b) The same pulse corrected by the baseline model.

In the following, the most important CMP parameters (in addition to the baseline parameters listed above), that are most commonly used in the low level analysis of CRESST will be briefly explained:

- **Baseline difference:** Difference between the average of the last 50 samples of the record window and the average of the first 50 samples.
- **Pulse height:** Maximum of the averaged pulse.
- **Peak position:** Position of the maximum in the record window in ms.
- **Onset:** Position of the start of the pulse in ms. Per default, this is defined as the last sample in the rising pulse at which the pulse is still below a height corresponding to three times the Baseline RMS.
- **Rise time and decay time:** The rise time is defined as the time it takes the pulse to rise from 10% to 90% of its pulse height. Respectively, the decay time is defined as the time it takes the pulse to decay from 90% to 10% of its pulse height.
- **Minimum and Maximum derivatives:** Respectively the minimum and the maximum value of the derivative of the raw pulse. These parameters give the steepest rise and decrease in between two samples within the record window. Additionally, also their positions in the record window are saved.

Calculation of coincidence and stability parameters: The last two steps of the parameter calculation are both related to the timestamps of the events. These are the calculation of the **muon coincidence** parameters and the **stability** parameter. The moun

coincidence parameters contain the time difference of each event to the closest muon event detected in the muon veto in ms, the number of muon veto panels that got triggered by the same muon event and the summed pulse height of all muon panels. The stability is defined via the control pulses. As mentioned earlier, the pulse height of control pulses can be used as a proxy for the position of the operating point of the detectors on their transition curve. The time window between two consecutive control pulses is considered unstable if at least one of the two pulses has a pulse height outside of a predefined interval. This pulse height interval is individually defined for each read-out channel. During the stability calculation, the time windows between all control pulses are labeled as either unstable or stable. Then the timestamps of all triggered pulses are compared with these time windows and each pulse is assigned a parameter, marking it as either stable or unstable. The calculation of this parameter is mentioned here for completeness and will be explained in more detail in sec. 5.2.1.3.

5.1.3 Optimum Filter

The optimum filter (OF), based on the work of E. Gatti and P.F. Manfredi [99], is a widely used technique to maximize the signal-to-noise ratio (SNR) of a data record. The two main advantages gained by applying an OF to the CRESST data are the possiblity to significantly lower the energy threshold compared to the HW triggered data and to get the best energy resolution from the reconstructed amplitude of the pulses. An additional advantage is the fact that the same amplitude estimator is used for both, the threshold evaluation and the energy reconstruction, allowing a precise estimation of the threshold in energy units.

Every recorded event is represented by a time series $s(t)$, which can be described as a superposition of the noise $n(t)$ and a signal of known pulse shape $s_0(t)$ scaled with amplitude A:

$$s(t) = A \cdot s_0(t) + n(t) \tag{5.1}$$

It can be demonstrated that there is a unique transfer function maximizing the SNR at the time τ_M (corresponding to the position of the pulse maximum) [98]. This can be written in the frequency domain as:

$$H(\omega) = K\frac{\widehat{s_0}^*(\omega)}{N(\omega)}e^{-i\omega\tau_M} \tag{5.2}$$

with $N(\omega)$ being the noise power spectrum and $\widehat{s_0}^*(\omega)$ the complex conjugate of the fourier transformed pulse template. The normalization constant K is chosen such that the amplitude of the filtered pulse is preserved. This transfer function of the optimum filter, $H(\omega)$, is built using the noise power spectrum, $N(\omega)$, and the pulse shape function, $s_0(t)$

(pulse template). In simpler terms, the role of this transfer function is to filter frequencies that are dominantly present in the noise, adapting the filter to a specific measurement.

The noise power spectrum (NPS) is created from a large set of samples of empty baselines. Empty in this context means the absence of any pulse shaped signal. To achieve this, the list of randomly triggerd EBLs has to be cleaned from any remaining pulses. Each of the empty baselines $n_i(t)$ is discretely fourier transformed into $\widehat{n}_i(\omega_k)$. The NPS $N(\omega_k)$ is the ensemble average $\langle \widehat{n}_i(\omega_k)\widehat{n}_i^*(\omega_k)\rangle_i$ of all empty baselines.

The pulse template is a template of the known pulse shape of the signal of interest, which in this case is the pulse shape of particle events, that is the same for both, nuclear recoils and e^-/γ events. The template is created by averaging a set of pulses that are in the linear regime of the transition curve of the TES. The averaging helps to surpress the noise. Choosing pulses from the linear regime ensures that only pulses with the same pulse shape are used. To completely remove any noise in the template pulse, the parametric model introduced in sec. 4.2.3 can be used to fit the averaged pulse. An example of such a pulse template can be seen in fig. 5.3a.

The measured event $s(t)$ is Fourier transformed into the frequency domain $\widehat{s}(\omega)$, where it is weighted with the transfer function. Then, after a back-transformation into time space, the filtered signal output is:

$$s_F(t) = \frac{1}{\sqrt{2\pi}} \int_{-\infty}^{\infty} H(\omega)\widehat{s}(\omega)e^{i\omega t}\,\mathrm{d}\omega \tag{5.3}$$

The filtered output of the template pulse is shown in fig. 5.3b. The noise power spectrum and the fourier transformed template that are used for the creation of the optimum filter, as well as the resulting transfer function are shown in fig. 5.4.

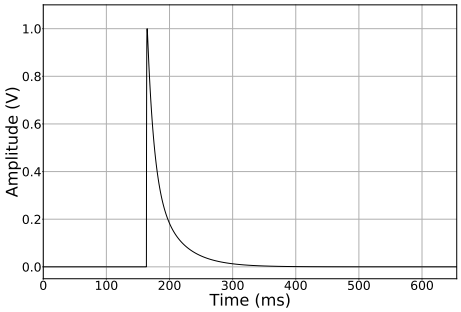

(a) Pulse template of a nuclear recoil event.

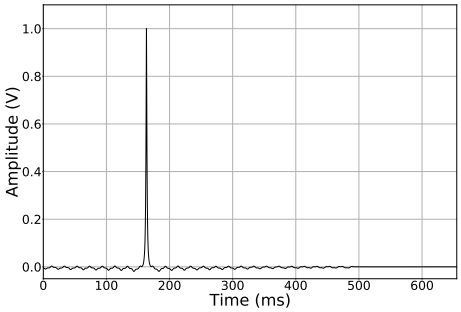

(b) Filtered template pulse.

Figure 5.3: Example of a template pulse, normalized to an amplitude of 1, before and after filtering.

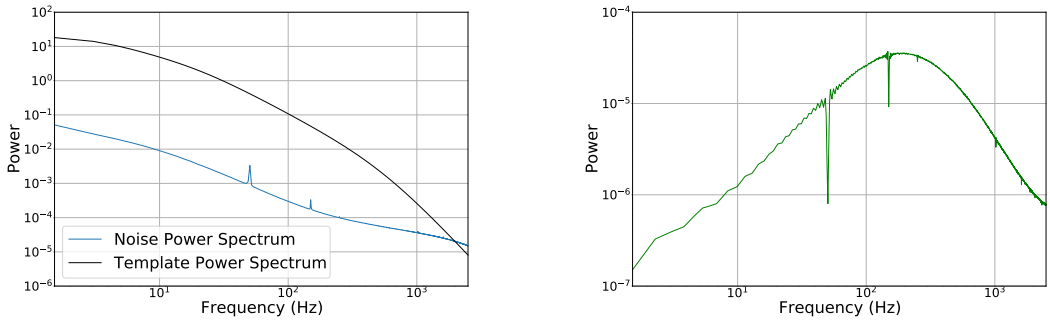

(a) NPS and template power spectrum.

(b) Transfer function of the optimum filter.

Figure 5.4: Example of a) the noise and template power spectra and b) the resulting transfer function of an optimum filter.

Figure 5.5 shows an example of a 60 eV event before and after filtering. The red line symbolizes a trigger threshold, which is set to an arbitrary low value in this example to better illustrate the point. While the threshold is well above the noise in the filtered data, setting it to the same value in the unfiltered data would lead to a high number of unwanted noise triggers.

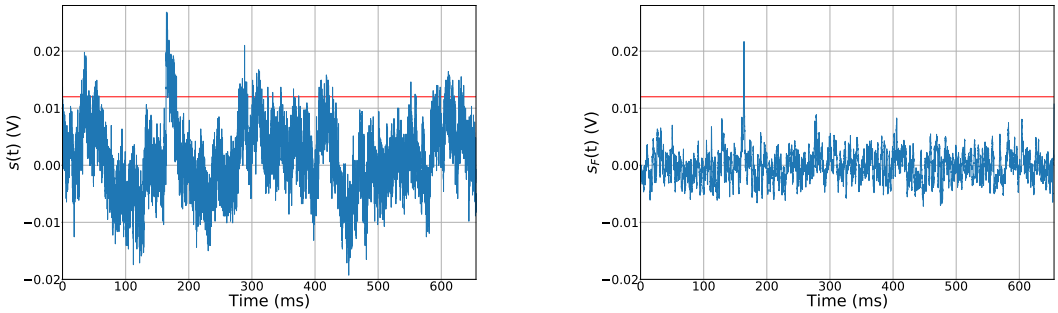

(a) Unfiltered Pulse.

(b) Filtered Pulse.

Figure 5.5: 60 eV pulse before and after filtering with an OF. The red line indicates a trigger threshold.

There is one important caveat to mention at this point. As sketched out in this section, the concept of the optimum filter is based on the assumption that the sought for signal is a superposition of a constant pulse shape and the noise (see eq. 5.1). The transfer function is created using a template pulse from the linear regime of the TES. Consequently, the optimum filter is optimized for pulses with this exact pulse shape only and cannot be used to reconstruct the amplitudes of pulses in the non-linear and saturated range of the TES.

5.1.4 Threshold determination

Once the OF for a detector has been created, the following step is to determine the threshold at which the filtered stream of data should be triggered. This follows the method presented in [100]. Ideally, the threshold should be as low as possible to increase the sensitivity to lower energies. At the same time the threshold needs to be high enough to prevent triggering in the noise. In order to have a compromise between these conflicting requirements, the threshold is defined by choosing a maximal number of noise triggers that should be accepted. In CRESST, the typical choice is to accept one noise trigger per kg day of exposure.

For the estimation of the number of noise triggers as a function of the threshold, a large set of empty baselines (EBLs) is needed. Typically, the same set that was used for creating the NPS is also used to determine the threshold. Each EBL is filtered with the OF that was created beforehand. Afterwards, a maximum search is performed on the samples of every filtered EBL. The maxima are then saved into a histogram as shown in fig. 5.6b.

Analytically, the probability of one sample being equal to x_{max} and all other samples of the same filtered EBL being smaller, can be described by a binomial distribution:

$$P_d(x_{max}) = \frac{d!}{1!(d-1)!} \cdot (P(x_{max})) \cdot \left(\int_{-\infty}^{x_{max}} P(x)dx \right)^{d-1} \tag{5.4}$$

with d being the number of statistically independent samples and $P(x)$ the distribution of all noise samples within the filtered EBL. If the samples follow a Gaussian distribution centered around zero, $P(x)$ can simply be written as:

$$P(x) = \frac{1}{\sqrt{2\pi}\sigma} \cdot e^{-\left(\frac{x}{\sqrt{2}\sigma}\right)^2} \tag{5.5}$$

Inserting this into eq. 5.4 leads to the analytical description of the distribution of maxima:

$$P_d(x_{max}) = \frac{d}{\sqrt{2\pi}\sigma} \cdot \left(e^{-\left(\frac{x_{max}}{\sqrt{2}\sigma}\right)^2} \right) \cdot \left(\frac{1}{2} + \frac{erf\left(\frac{x_{max}}{\sqrt{2}\sigma}\right)}{2} \right)^{d-1} \tag{5.6}$$

Figure 5.6a shows a histogram of all samples of a large set of filtered EBLs, demonstrating that the assumption of $P(x)$ following a Gaussian distribution is correct, so the function in eq. 5.6 can be used to fit the histogram of the maxima of the individual EBLs, as shown in fig. 5.6b.

Using the parameters obtained from the fit, the noise trigger rate as a function of the

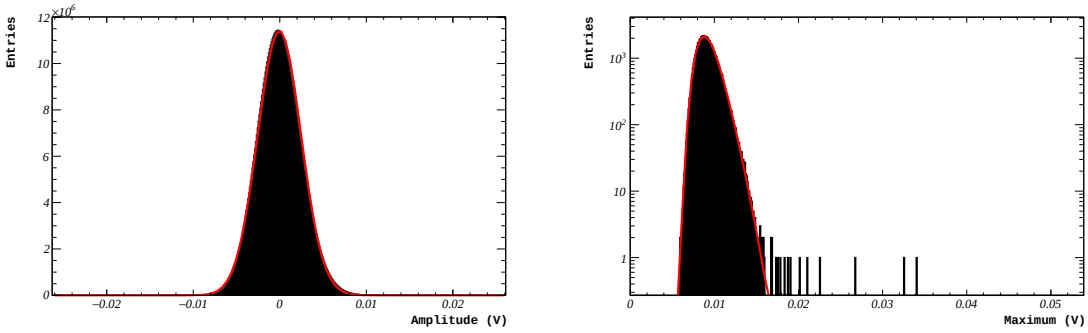

(a) Distribution of samples of filtered EBLs.

(b) Distribution of maxima of a large set of filtered EBLs. The red line shows the fit of the analytical description to the histogram.

Figure 5.6: Example for a) the Gaussian noise distribution and b) the distribution of maxima of filtered EBLs.

threshold, $NTR(x_{thr})$, can be easily calculated by integrating over the distribution of maxima:

$$NTR(x_{thr}) = \frac{1}{t_{win} \cdot m_{det}} \cdot \int_{x_{thr}}^{\infty} P_d(x_{max}) dx \tag{5.7}$$

By scaling this function with the detector mass m_{det} and the time of measurement t_{win}, the threshold for one noise trigger per kg day of exposure can then be extracted, as depicted in fig. 5.7. The measurement time t_{win} is calculated from the sum of all individual EBLs used for the threshold estimation.

5.2 Low level analysis

At the end of the raw data processing, a set of files containing all necessary information and parameters is available for further analysis. All steps from this point until the final energy spectra is called **low level analysis**. This can be separated into three main parts: The cleaning of the data (see 5.2.1), the calibration of the cleaned data (see 5.2.3) and the correction of the spectra with the detector response (see 5.2.4).

5.2.1 Data selection criteria

The data selection criteria are designed to keep only pulses whose amplitude can be properly reconstructed. While this cleaning process is done for all the different datasets, the focus in this section will be on the background dataset. Since the energy spectra created from the background data are used for the dark matter analysis, some degree of data blinding needs to be applied to avoid a biased choice of the selection criteria. For this reason the background data are divided into a training set and a blind set. The

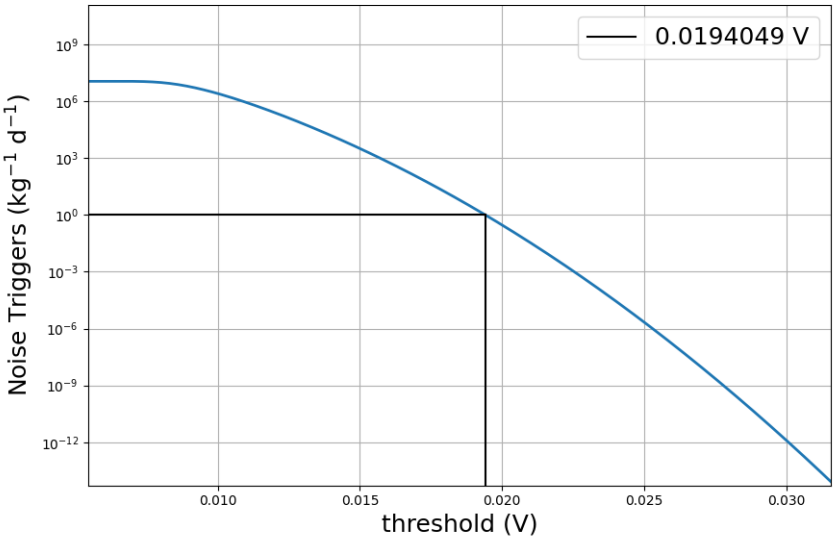

Figure 5.7: Noise trigger rate as a function of trigger threshold. The black line shows the threshold leading to one noise trigger per kg day of exposure, which in this case is 19.40 mV.

training set is created by selecting individual files, evenly distributed over the length of the background dataset until a percentage of roughly 20% of the entire dataset is reached. All data selection criteria are defined on this training set. Afterwards, these are applied to the remaining blind set without changes. Obviously, the calibration datasets (gamma and neutron calibrations) do not need such a blinding scheme. In the following some important selection criteria are discussed.

5.2.1.1 Preselection of files

Some run segments are completely removed from the analysis before the background data is divided into the training set and the blind set. Typical reasons for files being sorted out during the preselection are mostly related to severe electronic disturbances, strong disturbances in the magnetic fields or problems with the DAQ. Also information about earthquakes or nearby construction work can lead to the rejection of files. At last, also segments with a total measuring time of less than a few hours are usually rejected. During these very short files problems with the monitoring of the detector response can occur if not enough test pulses are available.

5.2.1.2 Rate cut

The rate cut is typically applied as one of the first cuts. The goal is to remove time periods with an unusually high trigger rate. The known backgrounds as well as a potential dark

matter signal are not expected to produce short 'bursts' of events, but rather a constant count rate in the detectors. The number of triggered events is binned in time. If the number of triggers in a bin is significantly higher than the average count rate, these time bins and the two adjacent ones are removed. These short bursts of increased rate are mostly due to electrical or mechanical disturbances. In the case of the data analyzed in this thesis, the stability cut (explained below) was sufficient to remove time periods with unusually high rates and therefore the rate cut was not used and is listed here solely for completeness.

5.2.1.3 Stability cut

The stability cut is performed to remove time periods in which the temperature of the detectors has moved too far away from their operating points. In sec. 5.1.2 it has already been explained how the stability parameter is calculated for each triggered event. This cut simply removes all events that have been marked as unstable[3]. In the following the definition of the pulse height interval used for the stability calculation and the effect of the cut is explained in more detail. Figure 5.8a shows the distribution of pulse heights of all control pulses, which follows a Gaussian distribution. As long as the pulse height of control pulses does not deviate too far from the center of this (a typical choice is 3σ), it is considered to be in stable operation conditions. All control pulses outside of this interval are labeled as unstable. In fig. 5.8b the pulse heights of control pulses are plotted against their timestamps. The timestamps of all other triggered events are always in a time window between two consecutive control pulses. If any of the control pulses defining this time window is labeled as unstable, all events inside this time window are marked as unstable and are removed by the stability cut.

5.2.1.4 Data quality cuts

While all previously discussed selection criteria are performed to remove entire time periods from the data, the quality cuts are designed to remove single pulses. Since the final energy spectra are based on the amplitudes of pulses, all "non-standard" pulse shapes need to be removed. All pulses whose amplitude cannot be reliably reconstructed should not survive these cuts. In the following, the most important quality cuts will be discussed.

Baseline difference cut: This is one of the most effective cuts. It removes several different types of invalid events. In some cases the feedback control of the SQUID electronics, operating in flux locked mode, cannot follow the fast rise of pulses. This

[3] A high event rate in a cryogenic detector typically causes instability of the operating point. Therefore the rate cut discussed before and the stability cut can be somewhat redundant, as in the case of the data analyzed in this thesis, where the stability cut was sufficient to remove periods with unusually high rate.

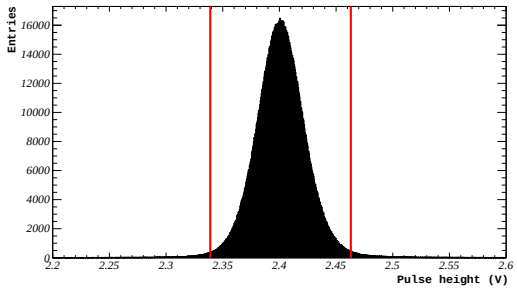

(a) Gaussian distribution of pulse heights of control pulses. The red lines are set at the 3σ levels around the center and define the interval of pulse heights that are considered to be in stable operation.

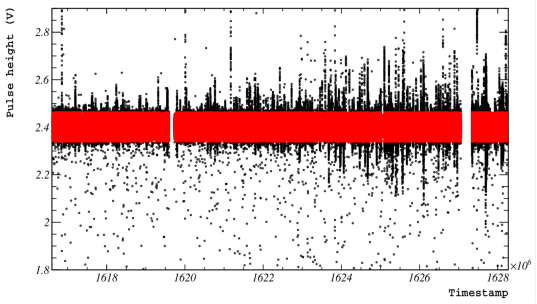

(b) Pulse heights of all control pulses over time. Any event in between 2 red points (within 3σ) is marked as stable. If at least one of the control pulses adjacent to an event is outside of the 3σ range (black points), the event is marked as unstable.

Figure 5.8: Definition and application of the stability cut. The gaps visible in b) are due to files discarded during the preselection.

can cause an offset in the readout voltage (i.e. flux quantum loss), originating from the periodicity of the flux-voltage characteristics of the SQUID, and lead to a different baseline of the SQUID after the event. In other cases, the SQUID can reset from the lowest readout voltage to a higher level (i.e. SQUID reset). Examples for these can be seen in fig. 5.9b and 5.9c. Another type of event removed by this cut are decaying baselines, shown in fig. 5.9d. These events typically occur after a large energy deposition in the detector. In these cases the initial large pulse is triggered a second time if the pulse has not fully decayed back to the baseline and the decaying samples are still above threshold after the post-trigger range of the initial pulse. A typical distribution of baseline differences and the interval outside of which pulses are removed is shown in fig. 5.9a.

Baseline RMS cut: As described in 5.1.2, the first step of the CMP involves a linear fit to the pre-trigger range. One of the parameters of this fit is the baseline RMS. Cutting on this value removes pulses with irregularities in the pre-trigger range. Often, these consist of strong deviations from the linear model or smaller pulses. If several pulses are triggered close to each other, the OF trigger algorithm places the largest pulse at the right position in the record window. This can lead to smaller pulses being pushed into the pre-trigger range when followed by a larger event. The cut value for one of the detectors analyzed in this thesis and an example of a pulse containing a pile-up with a smaller event in the pre-trigger region is shown in fig. 5.10.

Delta voltage cut: The delta voltage is defined as the ratio of the minimum derivative (see sec. 5.1.2) and the baseline RMS. With this cut, very fast changes between consecutive samples that go beyond the normal level of the noise can be identified. In principle

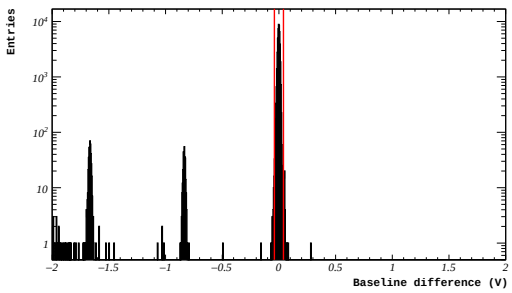

(a) Distribution of baseline differences and cut interval.

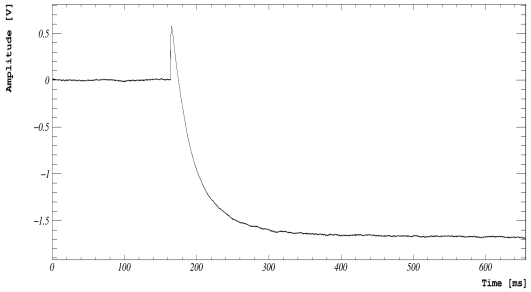

(b) Example of a flux quantum loss.

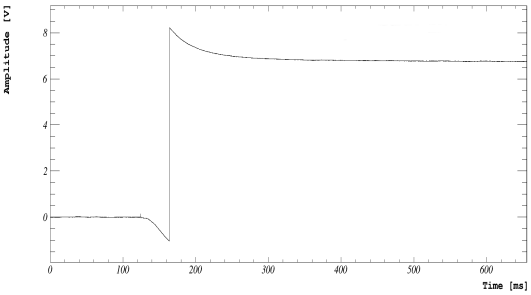

(c) Example of a SQUID reset.

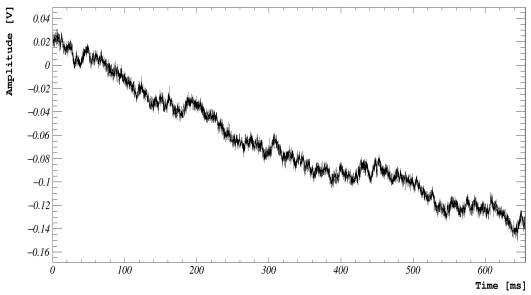

(d) Example of a decaying baseline.

Figure 5.9: Distribution of baseline differences and some examples of events getting removed by the cut. Events outside of the interval described by the red lines in a) are removed by the baseline difference cut.

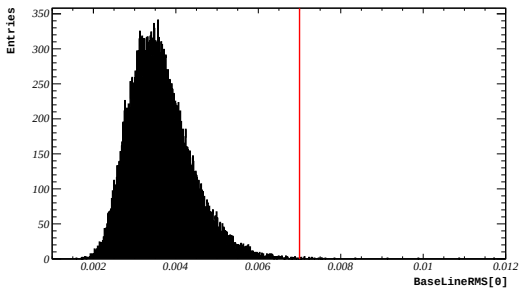

(a) Distribution of baseline RMS (black) and the cut value (red).

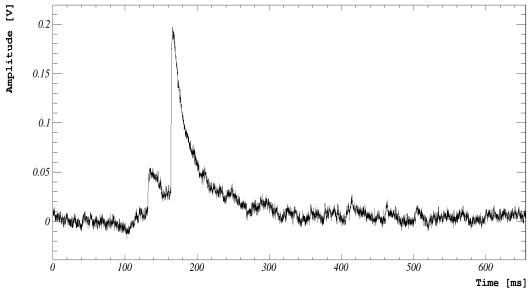

(b) Example of a pulse removed by the baseline RMS cut.

Figure 5.10: Distribution of baseline RMS and an example of a pulse above the cut value.

also the maximum derivative can be used for this parameter. By using the minimum derivative instead, the risk of accidentally discarding valid pulses with fast rise times is removed. The distribution of the delta voltage parameter and an example of such an event can be seen in fig. 5.11. These voltage spikes are presumably not related to any actual physical process in the detector, but rather connected to electronic disturbances.

All of the cuts mentioned above are typically performed on all read-out channels

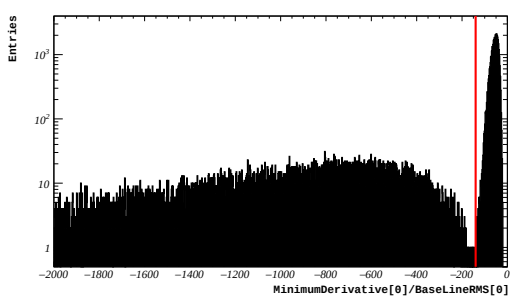

(a) Distribution of delta voltages (black) and the cut value (red). Events with a high absolute value (left of the cut line) are removed.

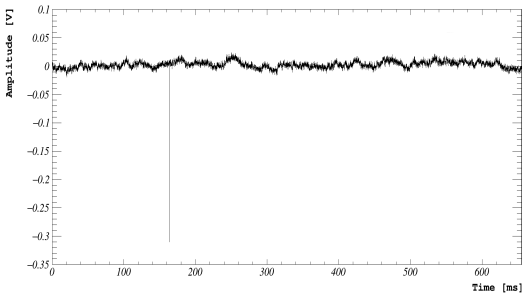

(b) Example of a delta spike.

Figure 5.11: Distribution of the delta voltage parameter and an example of a delta spike.

of a module to ensure that pulses on both, phonon and light channel, can be properly reconstructed.

Trigger cut: This cut is relevant if all read-out channels of a module are actively triggered. As described earlier in the definition of an event, whenever any of the read-out channels of a module triggers, all other channels are read out simultaneously. In the standard case of a phonon and a light detector this means that the phonon channel is also recorded and labeled as a pulse, even if only the light channel causes the trigger to be fired. Since the purpose of the light channel is mainly the discrimination of different event types and the energy reconstruction is based on the phonon channel, these so-called 'light-only' events need to be discarded. During the OF triggering of the CDAQ data, every event is assigned an OF amplitude parameter. While triggered pulses are assigned their corresponding OF amplitude, pulses in read-out channels that did not fire the trigger are assigned an OF amplitude of -10. This way, light-only events can be easily removed by cutting all events with a negative OF amplitude in the phonon channel. An example of such an event can be seen in fig. 5.12.

At this point, all events that survived the selection criteria are filtered a second time with the same OF that was used for triggering. By applying the OF to individual record windows instead of the continuous stream, several parameters are produced in addition to the **OF amplitude** parameter that was already produced during triggering. These parameters include:

- **OF RMS:** Describes the difference of the filtered pulse to the corresponding filtered template pulse (e.g. in fig. 5.3b), scaled to the same amplitude.
- **Peak RMS:** Created in the same way, but using only a region close to the maximum of the pulse.

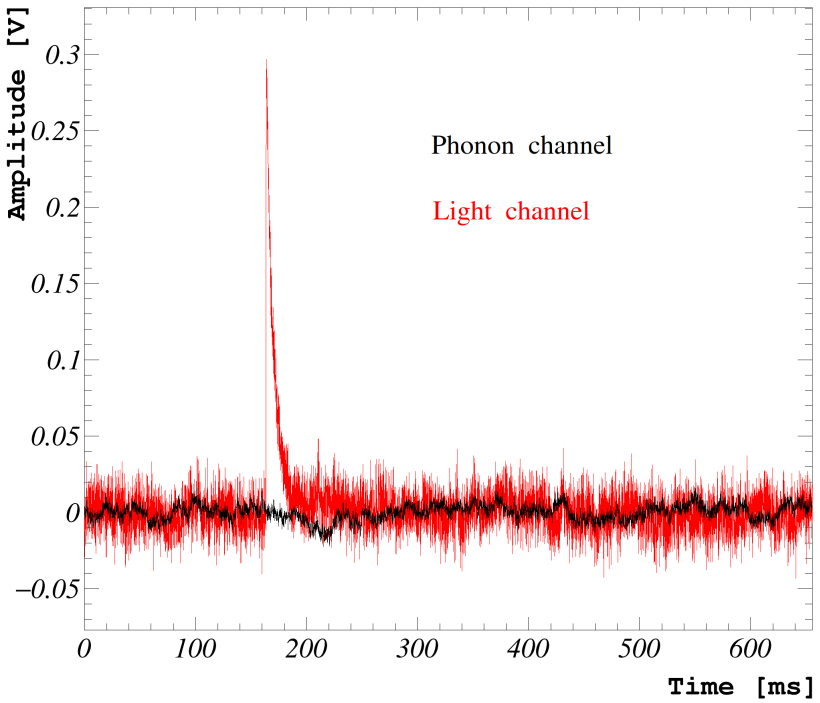

Figure 5.12: Example of an event that was triggered by a pulse in the light channel, but contains no pulse in the phonon channel.

- **OF maximum position:** Position of the maximum (OF amplitude) within the recordwindow.

The trigger algorithm places the triggered pulses at exactly one quarter of the record window. Generally, there can be a shift between different read-out channels in the trigger timestamps of an event. In these cases, the phonon channel is prioritized. This means that the pulse in the phonon channel will be placed correctly in the record window, while the pulse in the light channel can have a shift relativ to the position of the phonon channel (Negative shift: the light channel triggered earlier. Positive shift: the light channel triggered later). This shift can be caused by a difference in the pulse shape. If the pulses in one channel have a faster rise time than pulses in the other channel, they can be triggered earlier even if both pulses are in coincidence with each other. By running the filter a second time, this systematic shift between channels can be extracted with the **OF maximum position** parameter. The shift is important in order to evalute the filter amplitude of pulses that did not fire the trigger, but are in coincidence with the phonon channel of the same module, at the correct position in the record window (i.e. at the correct shift in samples with respect to the phonon channel). This is normally done by filtering a third time, but with a fixed position for the amplitude evaluation. Furthermore, the information about the shift needs to be incorporated into the simulation (see sec. 5.2.4).

Linearity cut: Before any OF related parameters can be used to define data selection criteria, the spectrum of amplitudes has to be truncated at the value at which the pulses are no longer in the linear regime. Pulses that start to go into saturation have a different pulse shape and will therefore lead to higher OF RMS values by definition.

OF RMS cut: After the linearity cut, the OF RMS should not show any dependence on the amplitudes of pulses. This is indeed the case, as can be seen in fig. 5.13. In this regime a higher RMS typically means other deviations from the standard pulse shape or pile-up of pulses. These need to be removed, as their amplitudes can not be reconstructed reliably. Examples of a record window with pile-up of several pulses and a pulse with deviations from the standard pulse shape are shown in fig. 5.14. Just as before, this cut is done for all read-out channels of a module.

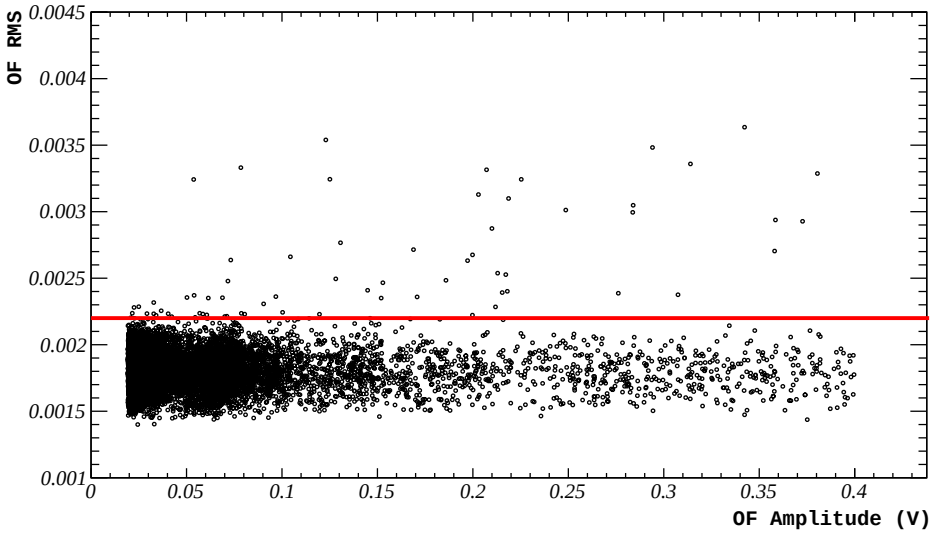

Figure 5.13: OF RMS plotted against the OF amplitude. All events above the red line are removed.

5.2.1.5 Coincidence cuts

After the quality cuts, all surviving events should contain only valid pulses. However, some of these surviving events can be excluded to originate from a dark matter interaction due to either a coincidence with one of the muon veto panels, or coincidences between different detectors. During the raw data processing, the time differences of each triggered event to the closest event that triggered in one of the muon veto panels is saved as a parameter. The **muon coincidence cut** is based on this parameter. Figure 5.15a shows the distribution of the time differences of each event to the muon events. A positive value means the muon veto triggered before the detector. As expected from random coincidences, the time differences are distributed exponentially on both sides

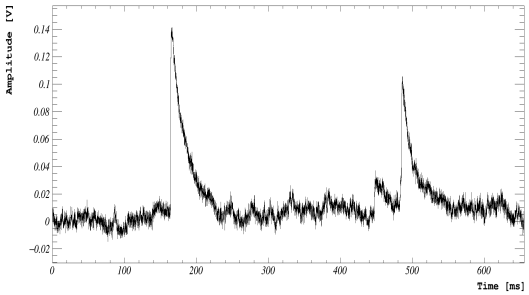

(a) A pile-up of pulses leads to an increased value of the OF RMS.

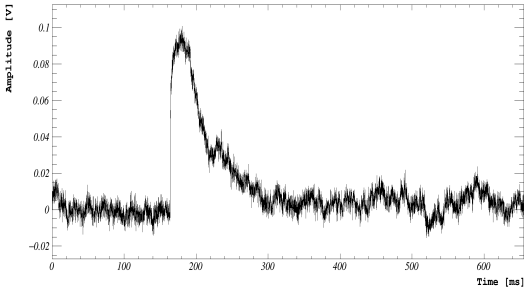

(b) Example of a pulse with a different pulse shape than the standard shape expected from nuclear recoils.

Figure 5.14: Examples of pulses that are removed by the OF RMS cut.

(positive and negative values). Since the muon flux in the underground laboratory is extremely low, most events triggering the muon veto panels are due to environmental or internal radioactivity. This means that cutting events in coincidence with an event in the muon panels also removes some events that are not actually caused by a muon. Moreover, in the case of a muon induced neutron signal, the muon trigger should always trigger before the detectors. Despite this, the cut is chosen rather conservatively, removing all events within a window of 5 ms before or after a trigger in the muon panels. This window is illustrated in fig. 5.15b.

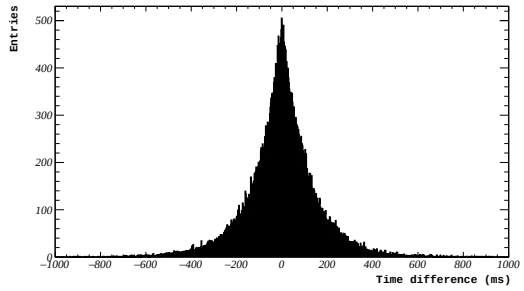

(a) Distribution of time differences of events in the detector with triggers in the muon veto panels.

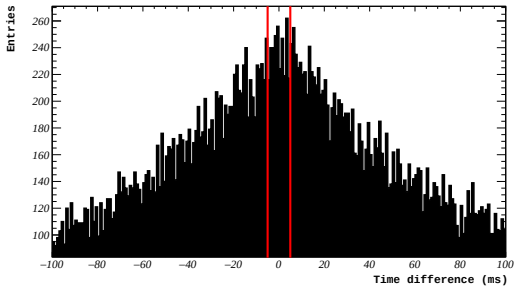

(b) Events within 5 ms before or after a muon event are removed from the data.

Figure 5.15: The muon coincidence cut is based on the time difference of a triggered event to the closest muon event.

Since the expected interaction cross section of dark matter particles with ordinary matter is extremely low, the probability of a dark matter particle scattering multiple times within the detectors is negligibly small. Therefore, events in coincidence between two or more detectors in a window of a few ms can be discarded. These coincidences are very rare. Thus, this cut removes only a tiny fraction of events and is negligible in most cases.

5.2.2 Amplitude reconstruction

The amplitude of a pulse carries the information of the deposited energy in the detector and is therefore one of the most important parameters of the pulses. For this reason it is crucial to have an accurate method of reconstructing their amplitudes. The main approaches of doing this are listed in this section. The first two options have already been explained above and are just listed here for completeness.

Pulse Height: The raw pulse height is one of the CMP parameters. The pulse height parameter is the maximum of the moving average of the pulse, after correcting the pulse for a linear baseline model (see sec. 5.1.2).

Optimum Filter Amplitude: The OF Amplitude is the main way of reconstructing the amplitude of pulses since it has the best energy resolution of all available methods. A detailed description of the OF is given in sec. 5.1.3.

Template fit: The classic way of reconstructing amplitudes in CRESST is the template fit, also called standard event (SEV) fit. The template, as already explained in sec. 5.1.3, contains the pulse shape of the signal. It is created by averaging real pulses from the linear regime of the detector to surpress noise. A parametric model can be fit to the averaged pulses to remove the noise entirely from the template. This template, together with a polynomial model to describe the baseline, can be used to fit pulses. A typical choice for the baseline model is a third degree polynomial. The parameters describing the pulse are a shift in time to match the onset of the pulse in the record window and the scaling of the template to match the amplitude of the pulse. Additionally, a fit RMS parameter holds information of the compatibility of the template with the given pulse. An example of such a fit and its residuals is shown in fig. 5.16.

Truncated template fit: All methods mentioned above are bound to the linear regime of the detector. There are cases in which it is necessary to also reconstruct the amplitudes of saturated pulses. This is especially important if the events of a calibration source fall into this regime, since otherwise an energy calibration of the spectrum would not be possible. Furthermore, being able to reconstruct saturated pulses increases the energy range of the spectrum that can be used for a dark matter analysis. A method to overcome the issue of saturated pulses is the **truncated** template fit. The truncation limit is given by the point in the transition curve of the TES at which non-linearity sets in. This is usually determined by an untruncated fit of the pulses. Within the linear regime, the RMS of the fit should stay constant independently of the amplitude of the pulses. When the pulses start to saturate, the pulse shape changes and the RMS of the template fit rises accordingly. An example of a highly saturated pulse is shown in fig. 5.17. The truncation

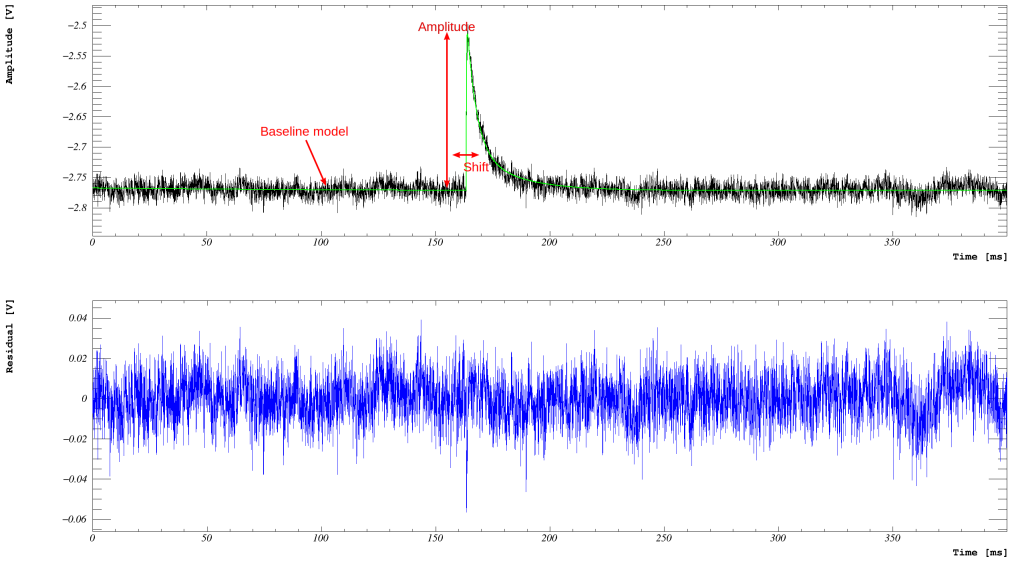

Figure 5.16: Top: The template fit. The template in green, which contains a fixed pulse shape, is shifted onto the right position in the record window and scaled to match the amplitude of the real pulse in black. The baseline is fitted with a third degree polynomial. Bottom: The residuals show a good agreement between the template and the real pulse.

limit in this example is at 1V. Below this limit the pulse behaves like it is expected from the linear regime. Using only samples of the pulse below this limit, it is possible to fit it with the template. The amplitude of the template pulse is then used as the reconstructed amplitude of the pulse.

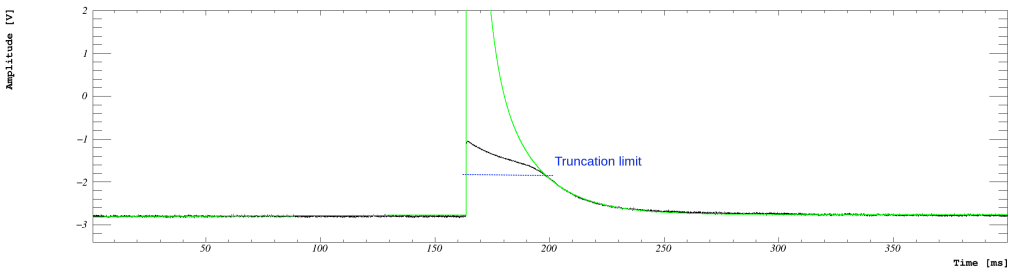

Figure 5.17: Example of a truncated template fit. The samples of the real pulse are shown in black. For the fit, only the samples below the truncation limit, shown in blue, are used. The amplitude of the scaled template pulse in green is then used as the reconstructed amplitude of the saturated pulse.

Parametric fit: The parametric model of the pulses, introduced in sec. 4.2.3, can of course also be used to directly fit pulses. Since the pulse shape of pulses of the same type is expected to be constant within the linear regime of the detector, the template fit with only two parameters for the pulse (time shift and scaling of amplitude) is the preferred option compared to the six parameters of the analytical model. In the scope

of this thesis, the parametric model is only used to fit the averaged template pulses to create completely noise free standard events. It is listed here as an option for the amplitude reconstruction for the sole purpose of completeness.

5.2.3 Calibration

After all selection criteria have been applied, the spectrum of reconstructed amplitudes needs to be calibrated. There are two types of calibrations in CRESST: The gamma calibration, translating the reconstructed amplitudes from volts into energies in electronvolts, and the neutron calibration, used to determine the light yield of different event types.

5.2.3.1 Gamma calibration

The gamma calibration is converting the reconstructed amplitudes of pulses from a voltage to energy units. This involves an intermediate step of correcting the reconstructed amplitudes for their time dependent behaviour, which is monitored with the test pulses. This corrected amplitude is then calibrated using the response to a radioactive source of known energy. Traditionally, a CRESST run contains a separate dataset for the **gamma calibration**, in which a ^{57}Co source is placed in close vicinity to the experimental setup. This source is removed after the calibration dataset. In the data analyzed in this thesis, an ^{55}Fe source was placed directly inside the detector modules in addition. This source could not be removed and remained present for the entire run. The reasons for this will be given in section 6.1.

The test pulse response: As already mentioned in 5.1.1, test pulses are heater pulses that are periodically injected into the detector with various pulse heights. To reconstruct the amplitude of test pulses in the data they are filtered with an OF created from a test pulse template and the same NPS that is used for the creation of the particle OF. The fixed values at which these pulses are injected is called **Test Pulse Amplitude (TPA)**, as already defined earlier. The initial voltage of the pulser is passed to a square-rooter, ensuring a direct proportionality of this voltage to the electric power injected into the heater. The mean value of the amplitudes at which pulses of a certain TPA are reconstructed by the OF depends on the exact settings at which the detector is operated. However, within the linear regime of the detectors the conversion factor from TPA (injected voltage) to reconstructed voltage should be a constant (due to the square-rooter of the injected voltage output). Figure 5.18 shows the spectrum of the injected amplitudes (TPA) and the spectrum of reconstructed amplitudes (TP OF amplitudes). The reconstructed amplitude of the higher test pulses are not equally spaced because these pulses are high enough to start saturating and thus have a different detector response then the one in the linear regime.

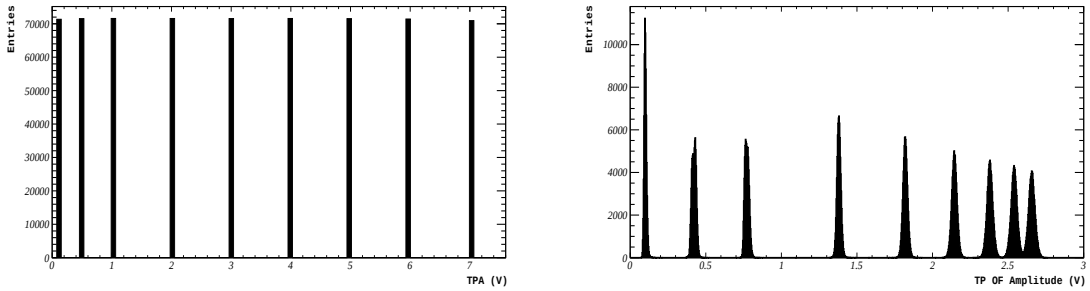

(a) Spectrum of voltages injected by the heater.

(b) Spectrum of voltages reconstructed by an OF created for test pulses.

Figure 5.18: Comparison between injected and reconstructed voltages of test pulses.

Furthermore, the reconstructed amplitudes are subject to the energy resolution of the detector and therefore show a smearing around their mean value. Another effect that causes a smearing of reconstructed amplitudes is the time dependence of the detector response. The stability cut removes time periods in which the detectors moved too far from their operating points. Still, as explained in 5.2.1.3, drifts of the operating point over time (within 3σ of the control pulse heights) can occur. This leads to a drift in the reconstructed amplitudes of all pulses. The time dependent variation of the reconstructed test pulse amplitudes within the background dataset can be seen in fig. 5.19. This behaviour is monitored with the **Test Pulse Response (TPR)**, which is created via Gaussian kernel smoothing of each separate amplitude. The kernel size for the smoothing is variable, a typical choice is 0.5 h. An example for the TPR of a single file is shown in fig 5.20.

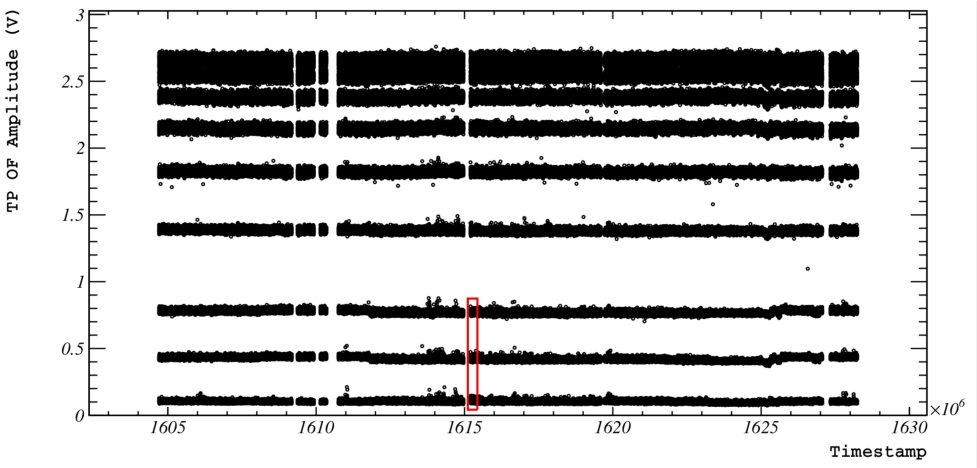

Figure 5.19: Reconstructed test pulse amplitudes over time (in seconds). The red box includes the lowest three test pulses of a single file. A close-up of this area can be seen in 5.20.

Under the assumption that the reconstruction of amplitudes have the same time

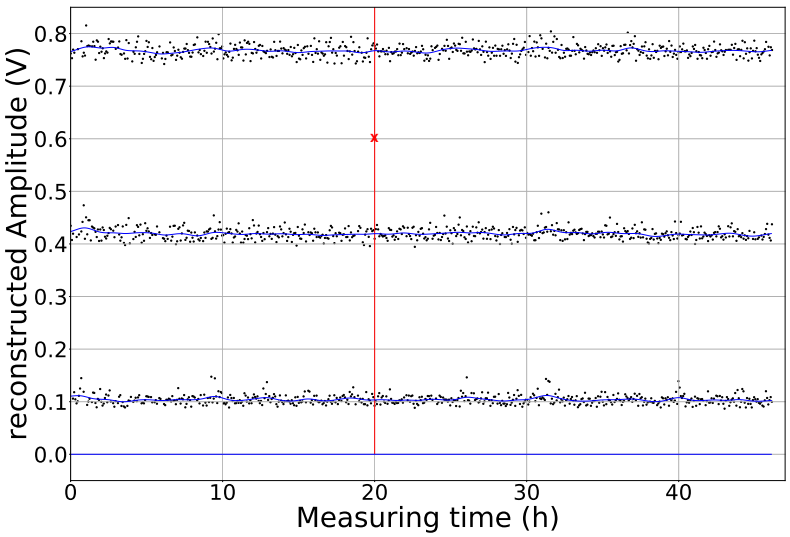

Figure 5.20: The reconstructed amplitudes of the lowest three test pulses over the measuring time of a single file (black). The blue lines show the **test pulse response (TPR)**, which is created via Gaussian smoothing of each separate amplitude. At the 20 h mark is an example of a particle event with a reconstructed amplitude of 0.6 V.

dependence for test pulses and particle pulses, the TPR can be used to correct the drift of the amplitudes of particle events over time. This is done via an **amplitude transfer function**, which is created in several steps, explained in the following example. In fig. 5.20 an example of a particle event, reconstructed at an amplitude of 0.6 V, is given. The TPR is evaluated at the exact timestamp of the particle event, depicted by the red line in fig. 5.20. An amplitude transfer function is then created by using a cubic spline interpolation between the crossing points of the red line and the TPR (blue lines). An example of this is shown in fig. 5.21. The amplitude transfer function basically maps the reconstructed amplitudes of the test pulses to their corresponding TPAs (injected voltage). Accordingly, the reconstructed amplitude of a particle event can be mapped onto a so-called **Test Pulse Equivalent (TPE)** amplitude, describing the equivalent amplitude that would have to be injected via the heater to create a pulse of the reconstructed amplitude at this particular timestamp. In other words: Pulses of a given constant energy can have a time dependent change in their reconstructed amplitude. The conversion from reconstructed voltages to a TPE amplitude corrects this time dependend behaviour.

Energy calibration: This correction for the time dependent detector response is done for every particle event. Afterwards, the spectrum of TPE amplitudes can be calibrated using a radioactive source of known energy. The constant conversion factor translating the corrected amplitudes in units of injected voltage to units of energy is called **Convert**

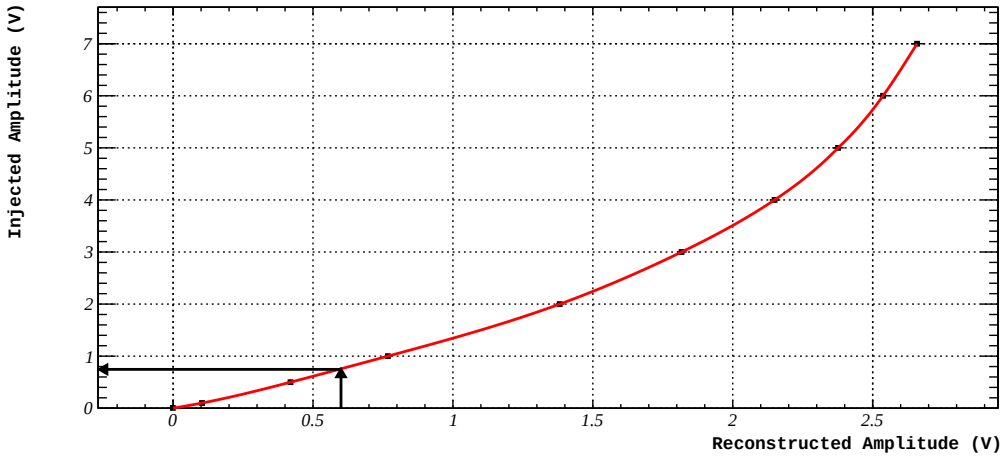

Figure 5.21: Amplitude transfer function at the timestamp corresponding to the 20 h mark in fig. 5.20. The reconstructed amplitude of the particle event of 0.6 V is mapped onto the corresponding TPE amplitude.

Pulse height to Energy (CPE) factor. For the energy calibration of the data presented in this thesis, an ^{55}Fe source is used, which decays via an electron capture to its daughter nucleus ^{55}Mn. The vacancy in the K shell of ^{55}Mn, left by the captured electron, is then filled by an electron from a higher shell. The K_α and K_β lines of the daughter nucleus ^{55}Mn are at 5.89 keV and 6.49 keV, respectively [101]. The spectrum of the reconstructed amplitudes of the ^{55}Fe events as well as the spectrum of the amplitudes after the correction for the time dependence can be seen in fig. 5.22. The corrected spectrum of TPE amplitudes is used for the energy calibration. In the detector used for this example plot, the CPE factor extracted from the fit of the iron lines is 2.78 keV/V. The pulses induced by the ^{55}Fe events are already approaching the upper edge of the transition curve of the TES and consequently suffer from some slight deviations from the nominal pulse shape from the linear regime. This affects the amplitude reconstruction of these pulses with the OF, which in turn leads to the data being not perfectly described by a model of two Gaussian distributions, as can be seen in 5.22b. Assuming that the test pulses with amplitudes close to the ^{55}Fe lines are affected in the same way, the mapping of amplitudes is still valid and can be used for the calibration. Looking at the transfer function in fig. 5.21, it can be seen that at the amplitudes at which the calibration lines are reconstructed (around 1.44 V and 1.54 V), the conversion between reconstructed and injected voltage is just at the transition between a linear and non linear behaviour. Therefore the calibration can still be considered valid.

In fig. 5.23, the spectrum used for calibration and a spectrum after all selection criteria have been applied can be seen. The energy calibration is done before a conservative linearity cut is perfomed, since it removes the iron lines from the spectrum.

In general, the light detector of a module is not calibrated with direct hits of the ^{55}Fe

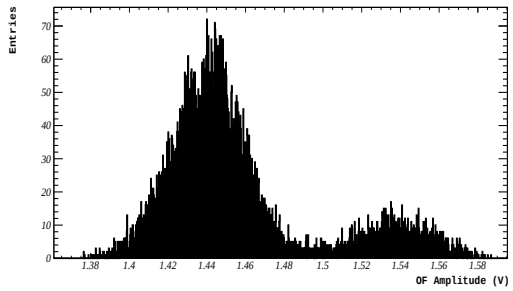

(a) Spectrum of reconstructed amplitudes of particle events from the ^{55}Fe source.

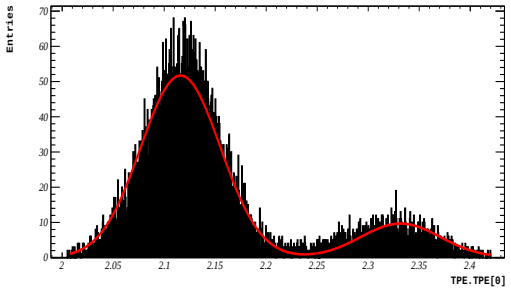

(b) Spectrum of TPE amplitudes of the ^{55}Fe events with a fit describing the K_α and K_β lines of the decay.

Figure 5.22: Reconstructed and corrected amplitudes of particle events from an ^{55}Fe source. The K_α and K_β lines at 5.89 keV and 6.49 keV are used for the energy calibration of the TPE spectrum. The resulting CPE factor of this calibration is 2.78 keV/V. The slightly poor description of the data with two Gaussian distributions is due to the pulses of these events being in the transition between the linear and the saturated regime of the TES.

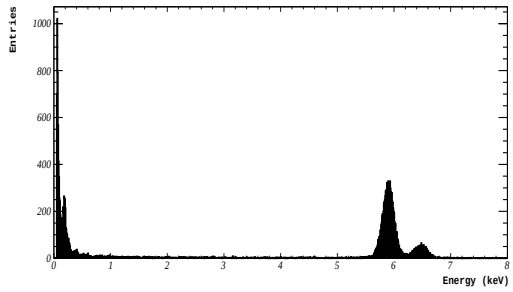

(a) Calibrated energy spectrum before the conservative linearity cut.

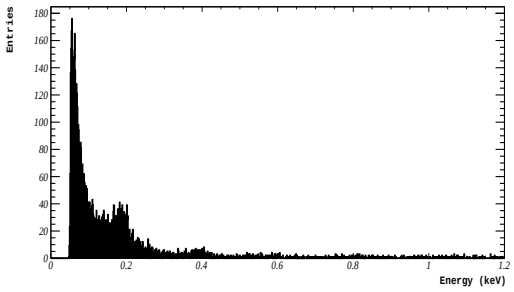

(b) Calibrated energy spectrum after all cuts.

Figure 5.23: Calibrated energy spectrum. a) Full spectrum, including the ^{55}Fe lines. b) Calibrated spectrum after all data selection criteria have been applied.

source, but using the scintillation light emitted by ^{55}Fe events in the main absorber (phonon detector). For that reason, the light detector is calibrated in terms of electron equivalent energy units (keVee). The energy spectrum of the light detector is used for the creation of the light yield plot as explained in the next section. The amount of energy that is measured as scintillation light is typically only of $\mathcal{O}(1\%)$ of the deposited energy in the main absorber.

5.2.3.2 Neutron calibration

The main purpose of the neutron calibration is the estimation of the quenching factors of the nuclear recoil bands (see 4.2.4). The light yield (LY) is defined as the ratio of the energy deposited in the light channel in units of keVee, divided by the total amount of

deposited energy in the phonon channel. By this definition, the events of the gamma source used for the energy calibration in the section above have a light yield value of 1. The incoming particles of the gamma source, as well as most radioactive backgrounds, interact with the electrons in the main absorber, leading to a higher output of scintillation light compared to nuclear recoils (quenching). CRESST is looking for interactions between dark matter particles and nuclei, which makes it important to calibrate the quenching factors of the detectors. Neutrons scatter on the nuclei in the main absorber and are therefore suitable to calibrate the light output of nuclear scatterings. For this purpose an AmBe source is used in CRESST.

The data of a $CaWO_4$ detector is used[4] to illustrate the neutron calibration. $CaWO_4$ is used in CRESST because of its good scintillating properties, allowing for a discrimination of background events and potential dark matter events down to relatively low energies.

Figure 5.24 shows the data taken during a neutron calibration (taken from [63]). An analytical description of the recoil bands can be found in [102] and [97]. The current implementation in the CRESST analysis tools is described in [103]. The data obtained during the neutron calibration populate the nuclear recoil bands with a high number of events. This makes it possible to fit the analytical model of the bands to the data. The fixed bands can then either be used to define a region of interest (ROI) for accepting events of the background dataset, or the parameters of this fit can be used in a likelihood framework; both will be described in 5.3.

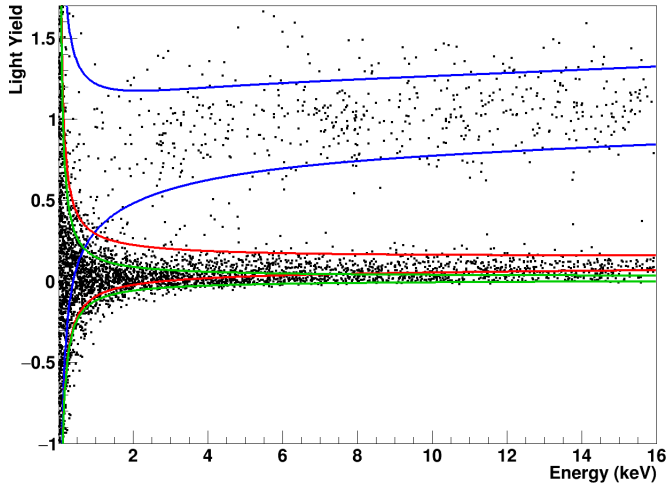

Figure 5.24: Neutron calibration data and band fits for a $CaWO_4$ detector. The 90% boundaries for the e^-/γ band are depicted in blue, the nuclear recoils off oxygen (tungsten) is depicted in red (green). Picture taken from [63].

[4]The main absorbers of the modules analyzed in the scope of this thesis, whose results will be shown in chapter 7 and which were used for the illustration of all analysis steps so far, are made of sapphire. This material is a very weak scintillator and the light output during the data taking was too low to perform a proper calibration. The overlap in light yield bands of e^- recoils and nuclear recoils is too large to make them distinguishable, so the step described in this section was omitted for these detectors.

5.2.4 Efficiency

The estimation of the probability of particle events to end up in the final spectrum is the last step of the low level analysis. In order to calculate dark matter exclusion limits or extract dark matter signal parameters, the effect of the experimental response has to be taken into account correctly. After doing so, the expected spectrum (see sec. 3.1.5) and the experimentally measured spectrum, like the one shown in fig. 5.23b, can be compared to each other. The experimental response describes the influence of the trigger threshold and the selection criteria on the spectrum. Since these are individual for each detector, it is also necessary to incorporate this correction in a comparison of the spectra of different detectors with each other.

Basic approach: On a technical level, the survival probability of the particle events can be obtained by performing a simulation. This is done by superimposing artificial events onto the continuous stream of data. These are uniformly distributed over the analyzed energy range and randomly distributed in time. The simulated data are then processed by the same analysis chain as the real data. Since the amplitudes and timestamps of the simulated events are known, the surviving fraction of events after triggering and after applying the selection criteria can be extracted as a function of their energy. This energy dependent surviving fraction of events can then be used as an estimator for the survivial probability of real particle events.

Creation of events: The artificial events are created by superimposing a scaled pulse template onto a random position in the data stream. The same pulse template that was used for creating the OF should also be used for the simulation. An example for this is shown in fig. 5.25, in which the pulse template is scaled to an amplitude of 0.25 V before being superimposed to an EBL.

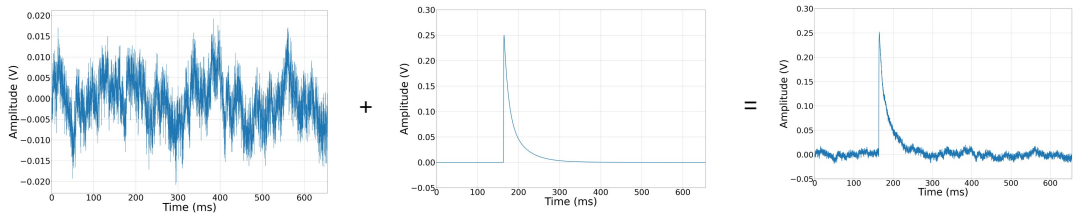

Figure 5.25: A random part of the stream (mostly EBLs) is superimposed with a scaled template pulse (in this case the amplitude of the simulated pulse is 0.25 V) to create a simulated event.

Due to the randomly distributed positions of the simulated pulses, not all of them are superimposed to a clean EBL like in this example. Some of them are superimposed on a real particle or a heater event, creating pile-up. Others are superimposed on parts of

the stream that suffer from electronic or mechanical disturbances, or in unstable time periods. With this approach all kind of artifacts are artificially created in a proportion that is representative of the real data.

Correlated simulation: For a module with several channels, typically a correlated simulation needs to be performed. The shift between pulses of the same event in different channels has been determined by running the OF over triggered pulses as explained in 5.2.1.4. This information can be used in the correlated simulation. If a pulse with energy E_S is simulated at a particular timestamp T_S in the phonon channel, a pulse with a quenched energy $Q \cdot E_S$ (corresponding to the light output of a nuclear recoil) will be superimposed on the light channel with a shift in time $T_S + t_{shift}$, corresponding to the shift in samples determined by filtering the real events. Moreover, the timestamps can be randomly drawn from an interval with a width that describes the spread of samples around the mean t_{shift} of the shift between channels.

Energy range and conversion to simulated amplitudes: Obviously, the simulation is limited to energies within the linear regime of TES. Above this energy, real pulses have a different pulse shape than the superimposed pulses. Since the selection criteria contain a linearity cut, this is not a problem.

The choice of the energy range that should be simulated is done in units of the **true energy** of incoming particles, from here also called **simulated energy**. The simulation of a single event then follows several steps, which are the exact reverse order in which the energy of a real reconstructed event is determined: The energy of the event is randomly drawn from a uniform distribution between zero and the upper boundary of the energy range. Afterwards the timestamp is randomly selected from the entire length of the dataset. At this point of the simulation, the information of the TPR created beforehand is needed. The simulated energy is divided by the CPE factor to create a **simulated TPE** amplitude. This value is then mapped to a **simulated amplitude** via the inverse of an amplitude transfer function, which is obtained by evaluating the TPR at the timestamp of the simulated event, as explained above. The value of the simulated amplitude is now used to scale the template pulse before actually superimposing it to the data. If the OF is applied to the simulated event, the reconstructed amplitude should be equal to the simulated amplitude within statistical fluctuations. Furthermore, if this reconstructed amplitude is converted into units of energy via the calibration process described above, the resulting value should be equal to the simulated energy within the resolution of the detector.

Choice on the number of events: The total number of simulated events should be large enough to have a sufficiently high number of events at every energy in the simulated range to reduce the influence of statistical fluctuations. On the other hand, if the number

of simulated events gets too large, they spoil the simulation by piling up on each other. If a higher number of simulated events in a certain energy region are needed, a separate simulation can be performed to avoid pile-up. A typical choice for the generation of simulated events is a frequency of 0.2 Hz.[5]

Estimation of trigger and cut survival probabilities: The simulated dataset is then processed following the same steps as described above for the real dataset, starting with the raw data processing. Before the data selection criteria are applied, a set of reference events is defined. The surviving fraction of events is calculated with respect to this reference dataset. This set excludes all pile-up of simulated events with each other, since in these cases it is not possible to extract an unambiguous energy dependent survival probability (both events generally have different energies). All other pile-up of simulated events with real particle events or with heater pulses remain in the reference dataset. All events that did not trigger during the raw data processing are still included in the dataset, but marked as *not triggered*. This is obviously necessary to calculate the trigger efficiency. Moreover, in the real data, during the event building every event is checked for coincidences with heater pulses. If there is a heater pulse timestamp anywhere within the record window around the triggered sample, the pulse always gets tagged as a heater event. This means in the real data there can be heater pulses that have a pile-up with a particle pulse, but never vice versa. This needs to be considered when calculating the trigger efficiency. This is done by checking every event in the reference dataset for both attributes:
1) The event has been triggered, and
2) The event is not coincident with a heater pulse.
Only then is the simulated event tagged as a *triggered* particle event. The list of triggered events is then subjected to all other selection criteria. The energy dependent survival probability of events after triggering and after the selection criteria have been applied can be seen in fig. 5.26.

The trigger efficiency as a function of energy can be analytically expressed as a convolution of a step function (constant value of the trigger threshold in units of voltage) with a Gaussian distribution describing the energy resolution of the detector, resulting in the following equation:

$$f(E) = \frac{1 - p_1}{2} \cdot \left(1 + erf\left(\frac{E - E_{thr}}{\sqrt{2}\sigma_{thr}}\right)\right) + p_2 \tag{5.8}$$

The parameters of this function are the trigger threshold in units of energy, E_{thr}, the energy resolution at the threshold, σ_{thr}, the constant fraction of sub-threshold pulses that survives the trigger due to pile-up, p_2 and the deviation from a 100% trigger efficiency,

[5] As an example, with a total measuring time of 3773 h, this leads to a total number of a little more than 2.7 million simulated events. With a linear regime from 0 to 1.2 keV, this results in an average of about 2264 simulated events per eV, which is an adequate number.

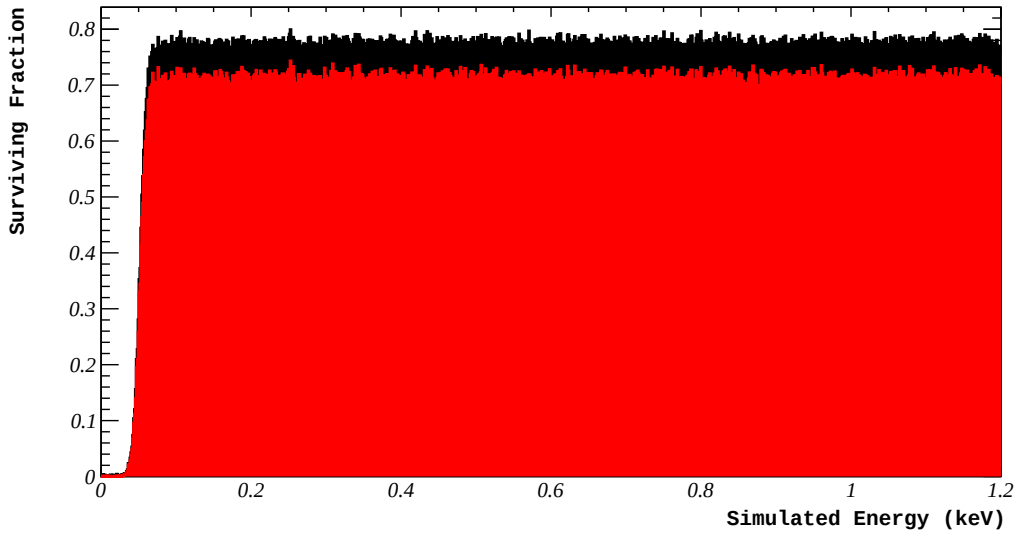

Figure 5.26: Energy dependent surviving fraction of simulated events after triggering (black) and after the selection criteria (red).

p_1. The latter is caused by the dead time of the trigger, mostly due to heater pulses. A fit of this function to the trigger efficiency is shown in fig. 5.27, the fit parameters are listed in the first column of tab. 5.1.

Table 5.1: Parameters of the trigger efficiency fit with and without including a cut removing inaccurately reconstructed events (Risetime (RS) cut), see fig. 5.29.

Parameters	Fit values	Fit values after RS cut
E_{thr} (eV)	52.2	52.3
σ_{thr} (eV)	7.4	7.5
p_1 (%)	23.10	22.65
p_2 (%)	0.2072	0.0023

Corrections: As described above, the reconstructed amplitude of simulated pulses should be equal to the simulated amplitude at which the pulse was superimposed, at least within the resolution of the filter. In some rare cases it can happen that a simulated event with a small energy is superimposed on a larger real particle event. If the difference in amplitudes between simulated and real event is large enough, the presence of the small pulse is not identified and the event is not removed by the selection criteria in the same way as other pile-up events get removed. In principle this also happens in the real data. The problem that these events cause for the simulation arises in their reconstructed energy. The small pulse will be considered as triggered, even if its simulated amplitude is way below the threshold, distorting the fit by artificially rising the flat pedestal described

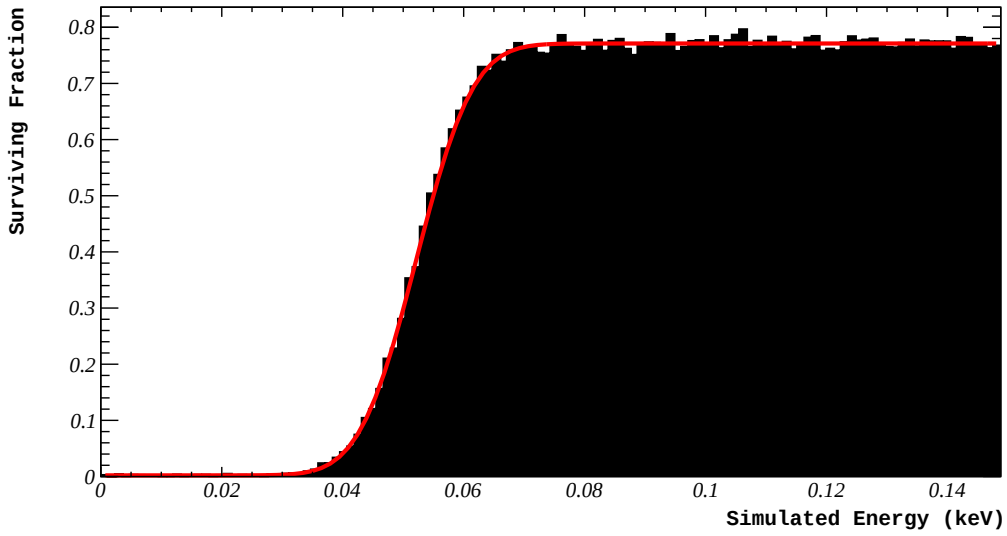

Figure 5.27: Fit of the trigger efficiency (eq. 5.8) to the surviving fraction of pulses after triggering.

by parameter p_2 in eq. 5.8. To mitigate this effect, an additional cut can be performed when creating the list of triggered events. This cut is based on the difference between the known timestamp of a simulated event and the actual timestamp at which the event was triggered. If the timestamps differ by more than two times the risetime (RS) of a pulse, it can be assumed that the pulse that fired the trigger was not the simulated event and is therefore removed. This affects only a very small number of events, as illustrated in fig. 5.28.

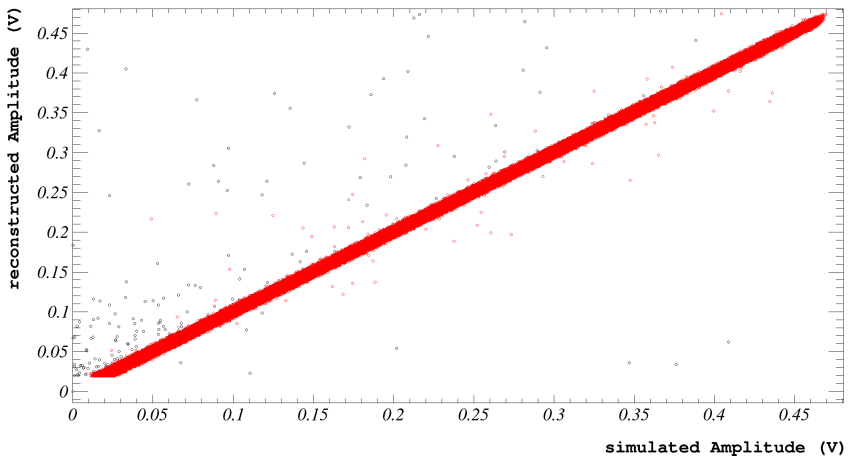

Figure 5.28: The reconstructed amplitudes of simulated events plotted against their simulated amplitude follows the identity function. The width of the band reflects the filter resolution. The events in black are wrongly reconstructed due to a coincidence with a real particle event. They are removed by a cut on the trigger timestamp.

The effect of removing these outliers is mostly important for a small number of events below the threshold. The difference this creates for the fit of the trigger efficiency is shown in fig. 5.29. The results of the fit are included in tab. 5.1.

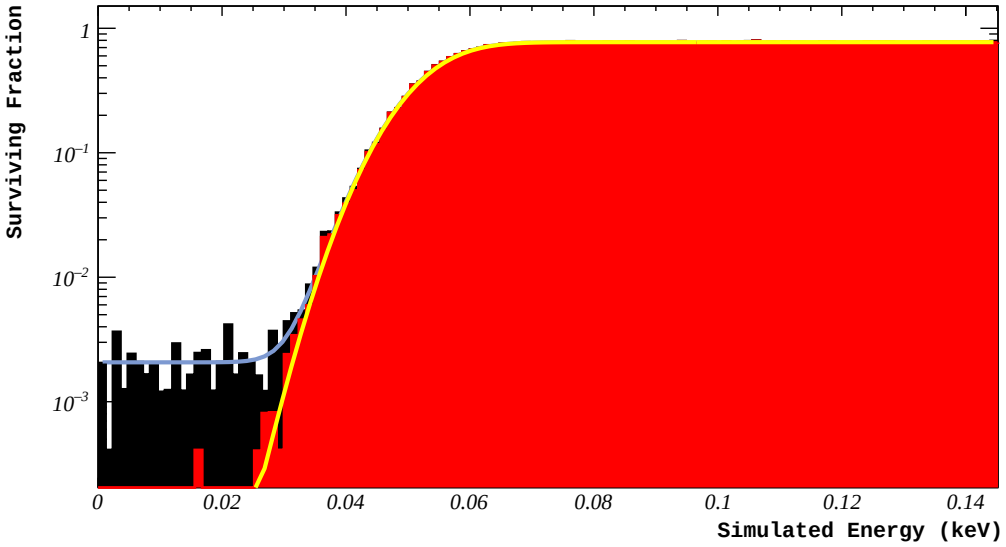

Figure 5.29: Fit of the trigger efficiency (blue) to the fraction of triggered events (black) and a fit of the trigger efficiency (yellow) to the fraction of triggered events after removing wrongly reconstructed events (red). This cut mostly affects the fraction of sub-threshold events surviving the trigger and has only minor influence on the other parameters of the trigger efficiency fit.

A comparison of the surviving fraction of events after all selection criteria with and without the removal of the wrongly reconstructed events is shown in fig. 5.30.

The effect of this cut is even smaller for the total surviving fraction of events after both triggering and the selection criteria. Since it mostly affects events below the threshold, which are not considered for the calculation of exclusion limits or for a dark matter signal claim it has only a minor impact on the results of a dark matter analysis.

A remark on how the survival probability is applied:

The estimation of the survival probability is necessary to compare the energy spectra of different detectors with each other. The most accurate method to correct the measured spectra with their respective survival probabilities would be a deconvolution of the spectrum with an analytical description of the final survival probability. Since there is no generally valid analytical description of the final survival probability (in contrast to the trigger efficiency, which is described by eq. 5.8), this is not possible. Instead, each bin of the energy spectrum is divided by the value of the corresponding bin of the histogram of the surviving fraction of events after all cuts.

For the calculation of exclusion limits or the extraction of dark matter signal parameters the correction is instead applied to the expected theoretical differential energy

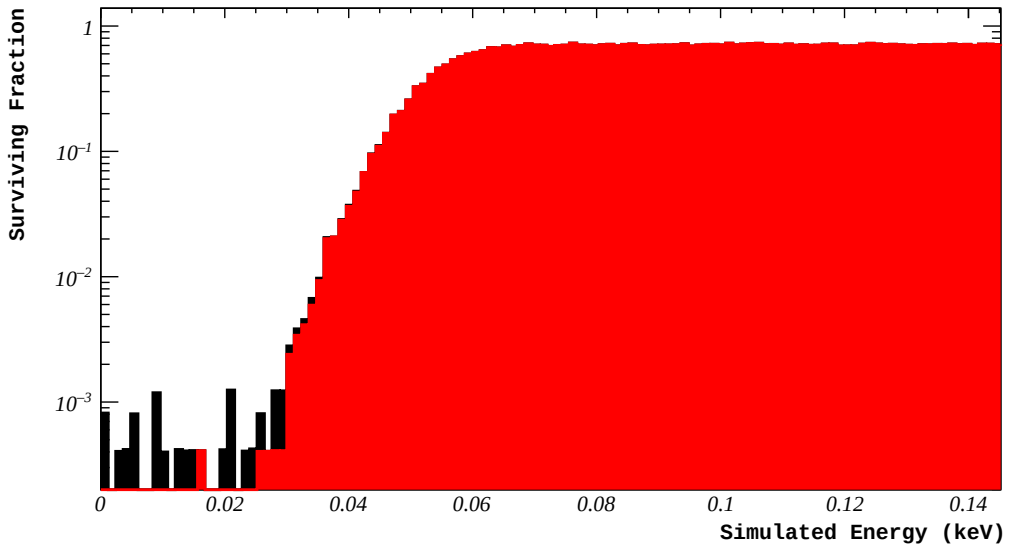

Figure 5.30: The fraction of events surviving all selection criteria (black) and the surviving fraction of events after removing the wrongly reconstructed events (red). The effect of this cut is mostly negligible.

spectrum. The most accurate way of doing this would be to perform a separate simulation for each dark matter mass individually and use the surviving spectrum of events as the experimental expectation. A faster alternative is to simulate a single box spectrum, as it was described in this section, which is then scaled according to each dark matter mass by weighting it with the corresponding dark matter spectrum. For the calculation of competitive exclusion limits or a dark matter signal claim, the more resource intensive method of performing individual simulations for each dark matter mass should be considered, but in most cases the method of re-weighting a simulated box spectrum is sufficient and more sustainable.

A technical remark:
The simulated events are not actually physically added to the real data. The CDAQ data of a normal measuring campaign in CRESST takes several $\mathcal{O}$(10 TB) of disk space. Instead of creating a copy of the CDAQ data containing the simulated events, all relevant parameters of the simulation are saved in a single file, including the timestamps and the simulated energies and simulated amplitudes. These are then superimposed on the CDAQ data on-the-spot only during the processing of the data. This is an efficient way that allows for the creation of several independent simulations without the need for an enormous amount of disk space.

5.3 High level analysis

With the final energy spectra and the survival probabilities it is possible to search for potential dark matter signals in the data. In the case of no statistically significant signal present in the data, an exclusion limit on the cross section is calculated for the range of dark matter masses the experiment is sensitive to (see sec. 5.3.1). In the case of the presence of a signal, a positive analysis can be performed to extract the parameters of interest and check the statistical significance of the signal (see sec. 5.3.2) by fitting the expected dark matter spectrum to the data. The free parameters of interest in this case are the dark matter mass and the interaction cross section of dark matter with ordinary matter.

5.3.1 Limit Calculation

For the limit calculation there are two different statistical approaches that are commonly used: The Yellin method and the Likelihood method. Both methods will be explained in the following sections, along with their advantages and disadvantages.

The range of dark matter masses in which the exclusion limit should be calculated has to be predefined in both cases. The lower boundary of this range is given by the detector threshold. The endpoint of the dark matter recoil spectrum is decreasing as a function of the dark matter mass (see sec. 3.1.5). Consequently, the expected number of events above the fixed energy threshold of a dataset decreases by reducing the dark matter mass. Eventually, at a certain mass M_{min} the expectation goes to zero, setting a natural limit to the mass range the experiment is sensitive to. The upper boundary is mainly set by the maximum of the energy that can be reconstructed. In section 3.1.5 it can be seen that for a given energy range the total number of events has a turning point at a certain mass after which it decreases with an increasing dark matter mass. This is due to the fixed value of the dark matter density in our galaxy. By increasing the dark matter mass, the number of particles in a defined volume has to decrease to keep the dark matter density at the correct value. As a consequence also the number of interactions has to decrease. Therefore, the expectated number of events in the energy interval given by the final energy spectrum (created in the low level analysis) drops for increasing dark matter masses, reducing the sensitivity to these masses. Since the CRESST-III detectors are optimized for a low mass range, the exclusion limits are not competitive with other experiments at high masses and are therefore typically stopped at $\mathcal{O}$(1 GeV - 100 GeV). The limits calculated in the scope of this thesis are calculated for masses up to 10 GeV.

In all methods explained in the following, the upper limit on the cross section has to be calculated separately for each mass in the given range of masses defined before. The mass range is therefore divided into sufficiently small steps. The limit is then drawn as an interpolation between the defined mass points.

5.3.1.1 Yellin method

This method is based on the work of S. Yellin [104], in which he describes a way to calculate upper limits in the presence of unknown backgrounds. This already points out the big advantage of this method: There is no need for an understanding of the background. Instead, all events are treated as a potential signal event, which in general leads to more conservative limits than likelihood methods. At the same time this is also a disadvantage of this method. In case there is partial or full knowlegde about the background, it can not be included in the calculation. The Yellin method is also constrained to the calculation of limits and no positive analysis can be performed in this framework.

Region of interest (ROI): Since most detectors have the possibility to discriminate e^-/γ events from nuclear recoils, based on the light yield explained in 5.2.3.2, the definition of a ROI can be used to exclude events from the e^-/γ bands from the yellin limit calculation beforehand. To reduce the overlap of the bands at low energies, usually parts of the nuclear recoil bands are cut as well. Of course this needs to be taken into account in the calculation of the expected energy spectra. As an example for a $CaWO_4$ detector, the ROI is chosen from the mean of the oxygen band down to the 99.5% lower boundary of the tungsten band [63]. This can be seen in fig. 5.31.

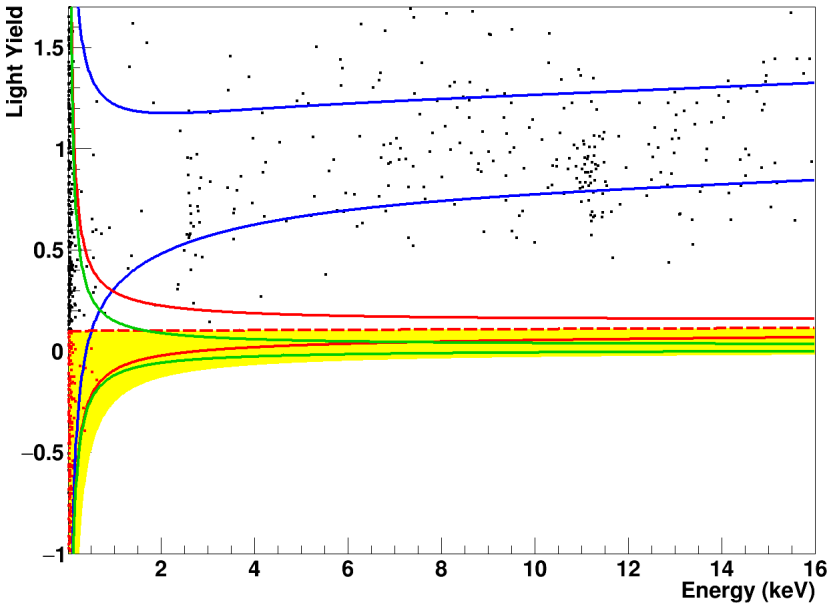

Figure 5.31: Example for the region of interest of a $CaWO_4$ detector. Only the events below the mean of the oxygen band (red dashed line) and the 99.5% lower boundary of the tungsten band are accepted (yellow region). Picture taken from [63].

The Yellin maximum gap method: The basic idea is to find the biggest gap x_{max} in the data. A gap x_i is herewith defined as the integral of the expected energy spectrum (for a given dark matter mass) in the energy range between two consecutive events at energies E_i and E_{i+1}:

$$x_i(\sigma_{DM}, m_{DM}) \equiv \int_{E_i}^{E_{i+1}} \frac{dR(\sigma_{DM}, m_{DM}, E)}{dE} dE \tag{5.9}$$

With the fixed dark matter mass m_{DM} and the interaction cross section σ_{DM}. An illustration of this is given in fig. 5.32.

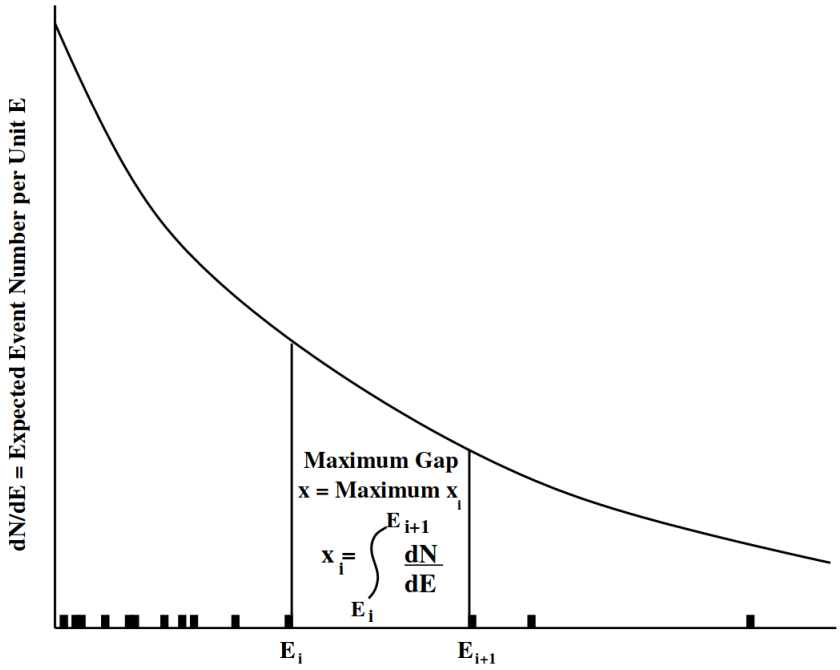

Figure 5.32: Illustraton of the Yellin maximum gap method. A gap is the integral of the expected spectrum inbetween to consecutive events. Plot taken from [104].

The value of x_i thus describes the discrepancy between the expected number of events in the energy range $[E_i, E_{i+1}]$ and zero observed events. Once the maximum gap $x_{max,obs}$ is found, a limit on the cross section can be calculated. For a given mass, the cross section σ_{DM} in eq. 5.9 can be pulled out of the recoil rate $\frac{dR}{dE}$ and the integral as a linear scaling factor. It is shown in [104], that the probability of observing an $x_{max} < x_{max,obs}$ for a given $\sigma_{DM,C.L.}$ can be calculated fully analytically. This probability defines the confidence level at which the cross section should be excluded. A typical choice is to set the confidence level to 90%. This means that, assuming dark matter exists with the given mass m_{DM} and cross section $\sigma_{DM,C.L.} = \sigma_{DM,90\%}$, identical experiments would find a value smaller than $x_{max,obs}$ in 90% of the cases. Consequently, the interaction cross section $\sigma_{DM,90\%}$ sets the upper limit for the given dark matter mass m_{DM}.

The Yellin optimum interval method: For the actual limit calculation, an extention of the maximum gap method is often used. While the maximum gap method looks for energy intervals with zero events, the optimum interval method looks for energy intervals including exactly n events. The number of events in the interval can be any number between zero (maximum gap) and the total number of observed events N. Then, following the same idea as before, it is possible to calculate the cross section at which the discrepancy between the observed number of events n and the expected number of events can be excluded with a certain confidence level.

The optimum interval method includes a numerical evaluation to obtain the number for n that leads to the strongest exclusion limit at the desired confidence level[6]. The optimal number n can generally be different for different confidence levels. After the desired confidence level (typically 90%) has been chosen, the numerical algorithm finds the best choice of n, which leads to the strongest upper limit and calculates the cross section $\sigma_{DM,90\%}$ based on this choice of n.

5.3.1.2 Likelihood method

An alternative way for the determination of exclusion limits is the use of a maximum likelihood fit. The choice of a ROI is not required in a likelihood framework, since all backgrounds are described by a parametrized model. The possibility to inlcude the knowledge about the background usually leads to more stringent limits, which in general is the preferable option. The main difficulty in applying a likelihood method is that a valid model of the background needs to exist, which is not always the case. If such a model exists and is described by the parameters $\mathbf{\Theta}_b$, then the events of the measured energy spectrum of a detector should follow a probability density function (pdf), ρ, that can be described as the sum of the dark matter signal, ρ_{DM}, and the background contribution, ρ_b:

$$\rho(E, LY|m_{DM}, \sigma_{DM}, \mathbf{\Theta}_b) = \rho_{DM}(E, LY|m_{DM}, \sigma_{DM}) + \rho_b(E, LY|\mathbf{\Theta}_b) \tag{5.10}$$

This function depends on the dark matter parameters (mass m_{DM} and cross section σ_{DM}), the energy E, and the light yield LY and the background parameters $\mathbf{\Theta}_b$. Since the limit calculation is performed stepwise for each mass of the predefined mass range, the dark matter mass parameter m_{DM} can be dropped in the following. This two dimensional pdf is used when both channels (phonon and light) are available. In the cases in which no information of a light channel is available the same concept applies, just without the LY parameter. For simplicity the light yield will be left out in this

[6] As an example: Assume 10 events with an equal distance of 10 eV to each other in an energy range from 50 eV to 150 eV. Given a particular model describing an expected distribution of events, the exclusion limit calculated from an interval containing 0 events (maximum gap, $n = 0$) might be weaker than an exclusion limit calculated from a comparison of the total number of expected events in this energy range with the observed number of events (optimum interval with $n = 10$).

section. A detailed description of the two dimensional pdf and its implementation can be found in [97].

The likelihood function $\mathcal{L}(\sigma_{DM}, \mathbf{\Theta}_b)$ is now defined as the probability of observing the measured distribution of events in energy E (and LY in the 2D case), given a certain set of parameters σ_{DM},$\mathbf{\Theta}_b$. Maximizing this likelihood therefore provides the set of parameters that most likely leads to the observed energy spectrum.

In both cases, the positive analysis (discovery case) and the negative analysis (limit calculation), the first step is to determine the set of parameters describing the data the best, denoted $\hat{\sigma}_{DM}$ and $\hat{\mathbf{\Theta}}_b$.

A technical note: Instead of maximizing the likelihood function $\mathcal{L}(\sigma_{DM}, \mathbf{\Theta}_b)$, it is common practice to minimize the negative logarithm of the likelihood $-ln(\mathcal{L}(\sigma_{DM}, \mathbf{\Theta}_b)) \equiv nLL(\sigma_{DM}, \mathbf{\Theta}_b)$. The main reason for using the logarithm is to turn the product of small numbers that appears within the likelihood function into a sum and thereby avoiding numerical precision problems. The maximization is then turned into a minimization simply because of the broad availability of minimization algorithms.

To calculate exclusion limits, a so-called likelihood ratio test is carried out:

$$\lambda(\sigma_{DM}) = \frac{\mathcal{L}(\sigma_{DM} = \text{fixed}, \hat{\hat{\mathbf{\Theta}}}_b)}{\mathcal{L}(\hat{\sigma}_{DM}, \hat{\mathbf{\Theta}}_b)} \tag{5.11}$$

The denominator here is the aforementioned result of the best fit of the maximum likelihood with $\hat{\sigma}_{DM}$ and $\hat{\mathbf{\Theta}}_b$ being the best estimators for the free parameters. This is put in relation with the conditional maximum likelihood, in which only the background parameters, also called nuisance parameters, are left free (denoted as $\hat{\hat{\Theta}}_b$) and the dark matter cross section has a fixed value ($\sigma_{DM} = \text{fixed}$). All combinations of parameters always lead to a likelihood value smaller than (or equal to) the maximum likelihood of the best fit, so the likelihood ratio is always $0 \leq \lambda(\sigma_{DM}) \leq 1$. This value can be translated into a statistical significance via a test statistic $q_{\sigma_{DM}}$:

$$q_{\sigma_{DM}} = \begin{cases} -2 \cdot \ln(\lambda(\sigma_{DM})) & , \hat{\sigma}_{DM} > \sigma_{DM,fixed} \\ 0 & , \hat{\sigma}_{DM} < \sigma_{DM,fixed} \end{cases} \tag{5.12}$$

The value of $q_{\sigma_{DM}}$ is quantifying the agreement of the model of the best fit (with $\hat{\sigma}_{DM}$) and the model with $\sigma_{DM} = fixed$. The probability of receiving a $q_{\sigma_{DM}}$ equal or larger than the observed one $q_{\sigma_{DM},obs}$, under the assumption that $\sigma_{DM} = fixed$ is the true value,

is given by the p-value, which is defined as the integral over the probability distribution function of $q_{\sigma_{DM}}$ ($f(q_{\sigma_{DM}} \mid \sigma_{DM})$):

$$p_{\sigma_{DM}} = \int_{q_{\sigma_{DM},obs}}^{\infty} f(q_{\sigma_{DM}} \mid \sigma_{DM}) dq_{\sigma_{DM}} \tag{5.13}$$

The smaller the value for $p_{\sigma_{DM}}$, the less likely the true model is described by $\sigma_{DM} = fixed$. The statistical significance Z in units of standard deviations of a Gaussian distributed variable can be written in dependence of the p-value, using the probit function:

$$Z = \Phi^{-1}(1 - p_{\sigma_{DM}}) = \sqrt{2}\, erf^{-1}(1 - 2p_{\sigma_{DM}}) \tag{5.14}$$

A higher Z in this context means an increased statistical significance of the best fit result for $\hat{\sigma}_{DM}$ in comparison to the fixed value. Wilk's theorem [105] postulates that $f(q_{\sigma_{DM}} \mid \sigma_{DM})$ follows a half χ^2-distribution. Using this theorem, it is shown in [106] that the statistical significance Z can simply be written as (see also app. A.5):

$$Z = \sqrt{q_{\sigma_{DM}}} \tag{5.15}$$

With eq. 5.14 the significance Z can be calculated for the desired confidence level. Typically 90% is used, corresponding to a p-value of $p_{\sigma_{DM}} = 0.1 (= 1 - 0.9)$. To find the fixed cross section $\sigma_{DM,90\%}$ that is excluded with the significance $Z_{90\%}$, the following relation needs to be fulfilled (using eq. 5.11 and 5.12 in 5.15):

$$Z_{90\%} = \sqrt{-2 \cdot \ln\left(\frac{\mathcal{L}(\sigma_{DM,90\%}, \hat{\hat{\boldsymbol{\Theta}}}_b)}{\mathcal{L}(\hat{\sigma}_{DM}, \hat{\boldsymbol{\Theta}}_b)}\right)} \tag{5.16}$$

Once $Z_{90\%}$ and the maximum likelihood of the best fit $\mathcal{L}(\hat{\sigma}_{DM}, \hat{\boldsymbol{\Theta}}_b)$ are determined, this effectively turns into a root search. Written in terms of the negative logarithmic likelihood:

$$nLL(\hat{\sigma}_{DM}, \hat{\boldsymbol{\Theta}}_b) - \frac{Z_{90\%}^2}{2} = nLL(\sigma_{DM,90\%}, \hat{\hat{\boldsymbol{\Theta}}}_b) \tag{5.17}$$

The left side is now a known constant number. The $\sigma_{DM,90\%}$ that fulfills this equation sets the upper exclusion limit on the interaction cross section for a single dark matter mass. This has to be repeated for all masses in the predefined mass ranged.

5.3.2 Positive analysis

If the data seem to contain a dark matter signal, there are two important questions to be answered:

1) What are the dark matter parameters that describe the data at hand the best?

2) How statistically significant is this result compared to the null hypothesis (no dark matter signal present in the data)?

Both of these questions can not be answered with the Yellin method. Therefore a positive analysis can only be done in a likelihood framework.

The approach is the same as in 5.3.1.2, apart from one difference: In the limit case the numerator of the likelihood ratio test is given by the likelihood value of a fit with a fixed non-zero cross section. The objective is to find the fixed cross section that excludes the cross section obtained from the best fit with a pre-chosen statistical significance. In the positive analysis, the numerator in the likelihood test is instead given by the null hypothesis, in which the fixed cross section is set to zero. Thus, the result of the best fit is compared to a model containing no dark matter signal, but only background. The objective is to calculate the statistical significance of the best fit compared to the null hypothesis. Equations 5.11, 5.12 and 5.15 are changed accordingly to:

$$\lambda(0) = \frac{\mathcal{L}(\sigma_{DM} = 0, \hat{\hat{\boldsymbol{\Theta}}}_b)}{\mathcal{L}(\hat{\sigma}_{DM}, \hat{\boldsymbol{\Theta}}_b)} \tag{5.18}$$

$$q_0 = \begin{cases} -2 \cdot \ln(\lambda(0)) & , \hat{\sigma}_{DM} > 0 \\ 0 & , \hat{\sigma}_{DM} < 0 \end{cases} \tag{5.19}$$

$$Z = \sqrt{q_0} \tag{5.20}$$

This way, the statistical significance Z of the signal can be extracted. In particle physics, a significance of $Z \geq 3$ is called **evidence**. For a **discovery** claim, a significance of $Z \geq 5$ is required.

Chapter 6

Observations of the Low Energy Excess

The content of this chapter was published as a collaborative effort in the proceedings of the 14th International Workshop on the Identification of Dark Matter 2022 (IDM2022) (see [107]), of which I was one of the corresponding authors. My original contribution to this work is the idea to study and compare the time dependencies of the low energy excess rate with each other and with detectors of the previous measurements. I had a major contribution to the developement of the analysis tools used to create the results shown in this chapter.

The module design of the CRESST-III phase, described in 4.2, allowed to reach unprecedented low energy thresholds of less than 100 eV. During the first data taking campaign of CRESST-III an excess of events was observed that exceeded the expected flat background, first described in [63] and shown in fig. 6.1.

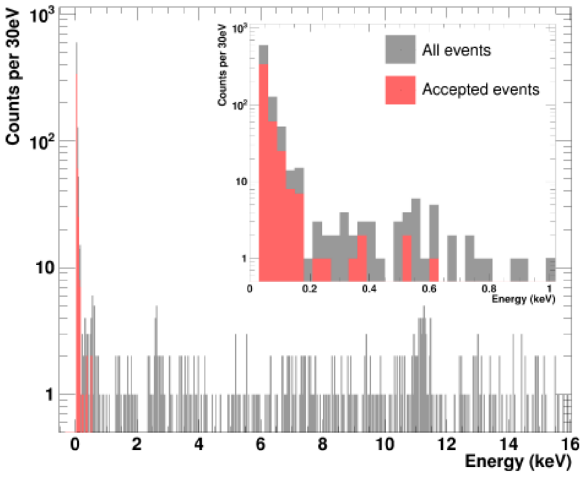

Figure 6.1: First observation of the low energy excess in CRESST in the first measurement campaign of CRESST-III. Picture taken from [63].

Similar excesses were observed in all detector modules in the same measurement, as well as the subsequent measurement campaign. Moreover, many other low-threshold experiments observed steep rises of the event rate at energies below 1 keV as well. These include experiments making use of phonon signal collection (EDELWEISS [78, 61], NUCLEUS [108, 109], SuperCDMS-HVeV [110, 62], SuperCDMS-CPD [111]) or charge

readout with CCD-sensors (DAMIC [74], SENSEI [66]). An extensive summary can be found in the report of the first EXCESS Workshop [112]. The presence of this Low Energy Excess (LEE) is the main limitation for further improvements of the dark matter sensitivity at low masses. It is therefore of great importance to identify the origin of these events and minimize their presence. For this reason, CRESST applied a number of modifications to the detector modules, each of which was implemented to test a specific hypothesis about the possible origin of the LEE events, described in 6.1. The observations acquired with these modified modules are presented in 6.2, including a comparison of the energy spectra of several modules. Furthermore the time dependence of the LEE rate is compared between different modules. The conclusions that can be drawn from these obervations are given in 6.3.

This chapter is summarizing the status of the LEE investigations in CRESST as presented in [107], including data from November 2020 until July 2022. The focus lies on the comparison of different detector modules. A more in-depth analysis of the LEE in one of the detectors will be covered in 7.5.2, additionally including data taken after July 2022.

6.1 Modifications of modules

There are various hypotheses on possible sources of the excess events. Many of them could be tested by applying specific changes to the standard module design of the CRESST-III detectors. To test dependencies relating to the target material, several different crystals materials were used. In addition to $CaWO_4$, also Al_2O_3 (Sapphire), $LiAlO_2$ and Si were used for the bulk detectors (main absorbers). The light detectors consisted mostly of Silicon on Sapphire (SOS) or pure Si. To study effects coming from the holding structure of the detectors, some of the $CaWO_4$ sticks were replaced by Cu sticks. Moreover, in some modules the sticks were completely removed and replaced by bronze clamps to examine effects coming from the point-like connection of the sticks in comparsion to the broader contact area of the clamps. The scintillating foil inside the Cu housing was removed in some detectors in order to study if events originating in the foil, which are not seen by the light detector, could be present. In addition to exchanging the scintillating holding sticks and removing the foil, one fully non-scintillating module was constructed by using Si for both, the bulk and the light detector. Since silicon is a non-scintillating material, the light detector in this module was obviously not operated to detect scintillation light of events in the main absorber, but to check for coincident events between the two detectors. After the appearance of the LEE in the first measurement campaign, a low-activity ^{55}Fe was integrated directly into the detector modules. This allowed for a fast and accurate calibration at low energies. The drawback of placing a radioactive source in the detector modules is an elevated background level, which was an acceptable compromise since the main focus of these measurements was to investigate the origin of the LEE rather than obtaining competitive dark matter limits.

An overview of all modules that are compared in this chapter is shown in tab 6.1 [107]. Some example pictures of the modified modules are shown in fig. 6.2.

Table 6.1: Overview of the modified modules that are compared in this chapter. Table taken from [107].

Module	Material	Holding	Foil	Mass (g)	Threshold (eV)
Si2	Si	Cu	No	0.35	10
Sapp1	Al_2O_3	Cu	No	16	157
Sapp2	Al_2O_3	Cu	No	16	52
Li1	$LiAlO_2$	Cu	Yes	11	84
TUM93A	$CaWO_4$	2 Cu + 1 $CaWO_4$	Yes	24	54
Comm2	$CaWO_4$	Bronze Clamps	No	24	29

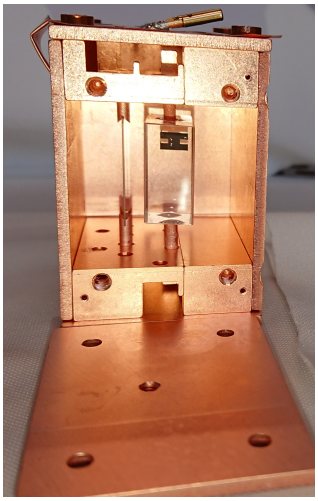

(a) Sapphire crystal with Cu sticks.

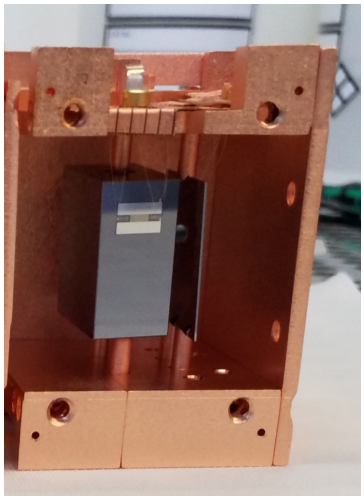

(b) Fully non-scintillating Si module with Cu sticks.

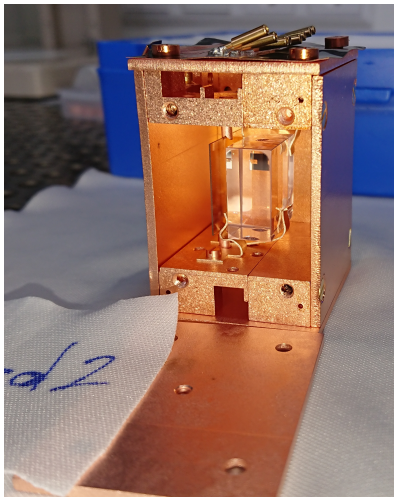

(c) $CaWO_4$ crystal with bronze clamps.

Figure 6.2: Some examples of the modified modules in which the scintillating foil was removed.

6.2 Observations

As described in 5.1.1, a typical CRESST data taking run contains different datasets, most importantly the gamma calibration, the background dataset and the neutron calibration. In the case of the run presented in this chapter, there are additional background-like datasets to test certain effects on the LEE rate.

The following sections follow a naming convention defined by the days after the first cool down of the cryostat:

- **BCK:** dataset between gamma and neutron calibration (day 90 - 380)
- **PostCal:** dataset after the neutron calibration (day 410 - 430)
- **AWU:** dataset after a warm up of the cryostat to 60 K (day 495 - 670)

6.2.1 Energy Spectra

Two of the detectors had a change in their operating point after the first weeks of the measurement. Therefore, for the comparison of the measured energy spectra, a subset of the BCK dataset of 105.4 days is used. The resulting energy spectra can be seen in fig. 6.3.

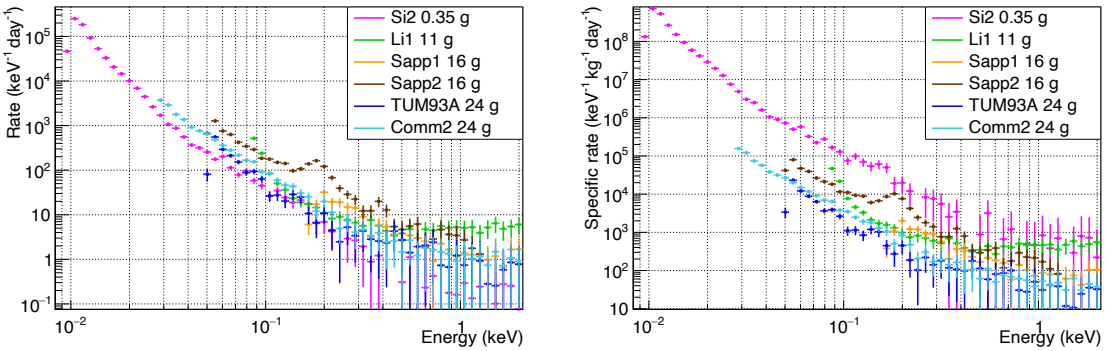

(a) Rate scaled by measuring time.

(b) Rate scaled by measuring time and detector mass.

Figure 6.3: Comparison of the energy spectra of the detector modules listed in tab. 6.1. All spectra are corrected with their corresponding survival probabilities (see 5.2.4). Figure taken from [107].

Independently of the crystal materials or the holding structures, the LEE is present in all detectors. On top of that, the sapphire detector *Sapp2* shows a bump-like feature at about 180 - 190 eV, which will be discussed in more detail in 7.5.3. Comparing the spectra in a common energy range of 60 to 120 eV (avoiding the bump in *Sapp2*), the rate differs by up to one order of magnitude between the detectors. The difference goes up to two orders of magnitude, when the spectra are scaled with the detector mass, suggesting that the rate does not scale with the mass of the detectors. The *Si2* detector has the highest specific rate (scaled by measuring time and mass), even though it has by far the lowest mass.

Based on these observations, a common single particle origin like dark matter or external radiation is disfavoured.

6.2.2 Pulse shapes

Previous works on the data analysis of the first CRESST-III run could not find any significant deviation of the pulse shape of the LEE events to the pulse shape of particle interactions in the detectors ([113], [114]). Additionally, the definition of the trigger threshold (see 5.1.4) does not allow for high numbers of noise triggers. Nevertheless, to exclude noise triggers or electronic artifacts as an origin of the excess events, pulse templates of the LEE events of the detectors shown in this chapter were created and compared to the analysis templates containing the expected pulse shapes from particle interactions. The creation of the analysis pulse templates was already explained in 5.1.3. Similarly, the LEE templates are created by averaging pulses of the energy range starting from the threshold up to two times the energy resolution of the detector above the threshold. For the comparison, only the averaged LEE templates are used instead of additionally performing a fit of the analytical pulse model, as it is done for the analysis templates. Figure 6.4 shows the comparison of the averaged LEE templates of all detectors with the analysis template for regular particle interactions.

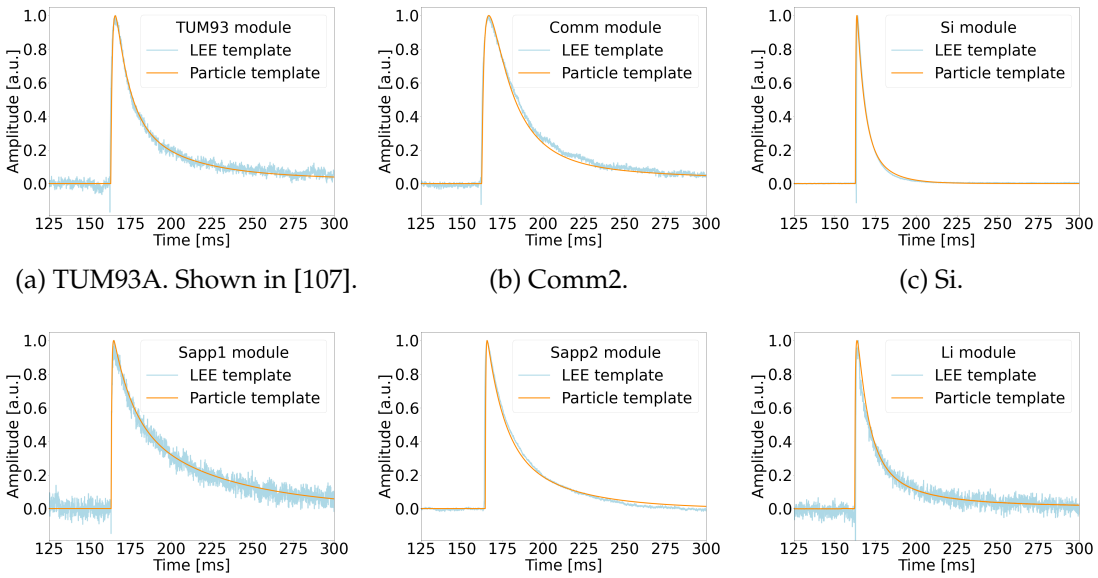

(a) TUM93A. Shown in [107]. (b) Comm2. (c) Si.

(d) Sapp1. (e) Sapp2. (f) Li1.

Figure 6.4: Comparison of averaged LEE pulses with analysis pulse shape templates for particle interactions, showing that the excess consists of valid pulses in all detectors.

The comparison shows that the averaged pulses of the low energy events in all detectors follow the same shape of particle events. This implies that the majority of these pulses can not be electronic artifacts or noise triggers.

6.2.3 Time dependence

Already during the first two measurement campaigns of CRESST-III, a time dependent decrease of the rate of the low energy excess could be observed (see fig. 6.5).

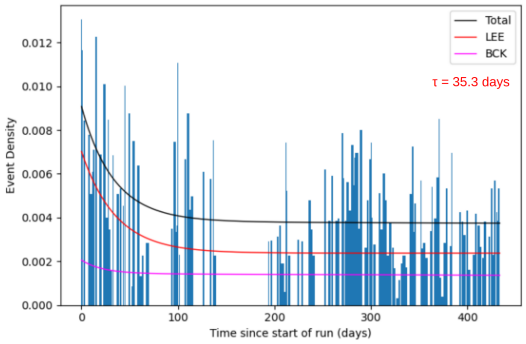

(a) $CaWO_4$ detector from first CRESST-III run.

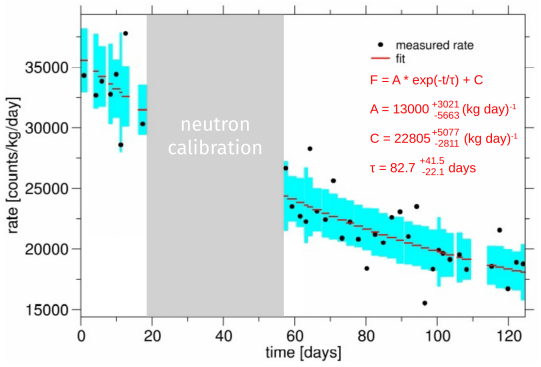

(b) Sapphire detector from second CRESST-III run.

Figure 6.5: A decaying rate over time of the LEE could be observed already during the first two measurement campaigns of CRESST-III. Plots as presented in [115].

For the current run, a more systematic study of this effect was performed. A decreasing rate of the LEE over time could be observed again in all detectors. For the comparison of several detectors a common energy range of 60 to 120 eV is chosen. This choice of the lower boundary was imposed by the detector with the highest threshold, the upper boundary was chosen in order to exclude the bump in the *Sapp2* module. Due to their higher thresholds, the detectors *Sapp1* and *Li1* are therefore not included in this comparison. The data are binned in time intervals of one week, corresponding to a measuring time of about 150 h. Each data point shows the number of measured events in the defined energy range, corrected by the measuring time and the detector dependent signal survival probability.

The decrease of the rate can be described with an exponential decay and a flat component $R(t) = A \cdot exp(-\frac{t}{\tau}) + C$, which is used as a fit function to extract the decay times of the individual detectors. The data points and the fit functions are shown in fig. 6.6a, the resulting decay times τ of each of the detectors can be seen in 6.6b. The decay times agree with each other within their uncertainties (standard error) and result in a mean decay time of τ_{BCK} = (149 $\pm$ 40) days.

Figure 6.5b already indicates that the decay of the LEE rate seems not to be influenced by the neutron calibration that was performed during the data taking of the second CRESST-III run. To confirm this observation, the PostCal dataset was taken after the neutron calibration of the current run, which is shown in fig. 6.7. No visible influence on the rate could be observed in any of the detectors.

The EDELWEISS collaboration reported an observation of an increase in the rate of heat-only events above 5 keV after an increase of the cryostat temperature during the

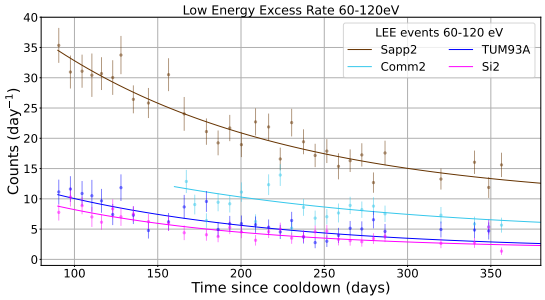

(a) Exponential decay of the LEE rate over time.

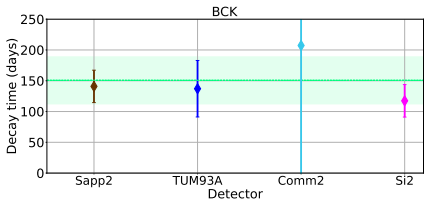

(b) Resulting decay times in the different detectors.

Figure 6.6: Decreasing rate over time in the BCK dataset and the corresponding decay times with a mean of (149 ± 40) days [107].

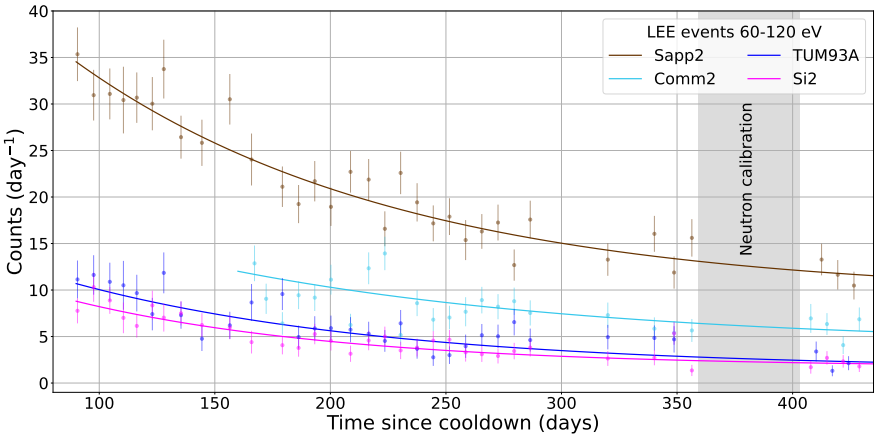

Figure 6.7: The neutron calibration has no visible influence on the rate in all detectors [107].

measurement [116]. Despite the different energy range of this observation, CRESST started to perform a systematic study of this effect. In a first test, the cryostat was warmed up to a temperature of 60 K. After being cooled down back to operation temperature, the data taking was resumed. A strong rise in the event rate of the LEE could be observed in all detectors, which again could be described by an exponential decay over time and a constant flat component. Two additional warm up tests to lower temperatures of 600 mK and 200 mK had no influence on the rate. This choice of temperatures was based on the transition temperatures of different materials connected to the detector and sensors. The AWU data and fit function can be seen in fig. 6.8a and the resulting decay times in fig. 6.8b.

The decay times of the rate in different detectors do not fully agree with each other within their uncertainies, but follow the common trend of decaying much faster compared to the BCK dataset, with a mean decay time of τ_{AWU} = (18 ± 7) days. An increased rate after a consecutive warm up and cool down of the cryostat is a strong argument

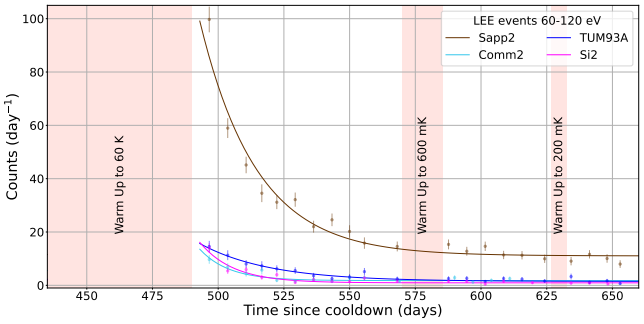

(a) Exponential decay of the LEE rate over time.

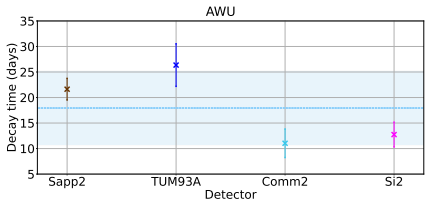

(b) Resulting decay times in the different detectors.

Figure 6.8: Decreasing rate over time in the AWU dataset and the corresponding decay times with a mean of (18 ± 7) days [107].

against a radioactive origin of the low energy events in general (external and intrinsic radioactivity). In addition to that, dark matter interactions can also be excluded by the same argument.

Additional warm up tests to different temperatures were conducted after July 2022. The results of these tests is not included in this chapter, but will be discussed in 7.5.2, focusing on the excess in a single detector.

6.3 Conclusions on the LEE

To summarize the observations presented in this chapter:

- The LEE is present in all detectors and none of the detector modifications has a significant impact on its presence.
- The rate does not scale with the mass of the detector.
- The pulse shape of events contained in the excess is the same as for particle events.
- An exponential decay of the rate over time can be observed in all detectors.
- The rate is significantly increased after warming the cryostat up to 60 K, which is decaying much faster than before the warm up.
- Warm up tests to 600 mK and 200 mK did not have a visible effect on the rate.

Based on these observations, some hypotheses on major contributions to the LEE can be excluded: dark matter interactions and external radioactivity is disfavoured by the varying absolute rate in different detectors and due to the increase of the rate after a warm up of the cryostat. The warm up effect additionally excludes intrinsic radioactivity. The averaged pulse shapes of the LEE events rule out noise triggers or electronic artifacts

as a main component. Scintillation light can be excluded as a source, since the excess is also present in the fully non-scintillating modules.

There is still a variety of possible options that are under further investigation. Some crystal intrinsic effects related to the material can not be excluded. Sensor related effects, such as stress created by the TES film deposition are another possibility. Despite the LEE being present independently of the holding structure, holding induced stress could still account for the excess, which is supported by recent observations by the SPICE/HeRALD Collaboration, in which the excess rate was increased by artificially increasing the holding related stress on the detectors [117].

The current R & D in CRESST is focused on preparing detector modules for the next measurement campaign that can adress these specific open possibilities.

The following chapter will include more details about the time dependence of the LEE rate and time dependent changes in the energy spectrum describing the excess in the *Sapp2* module specifically, including also the effects of warm up tests to 3.5 K and 30 K.

Chapter 7

Sapphire analysis

Sapphire (α-Al_2O_3) is used as a target material in CRESST already since the first phase of the experiment [118]. The choice for this material is based on the good cryogenic and phonon transport properties. On top of that, the presence of nuclear spin 5/2 in ^{27}Al nuclei allows for a spin-dependent dark matter interaction search [119].

CRESST already achieved very low background levels in the first phase. In order to further reduce the backgrounds, there was the need to be able to discriminate between nuclear and electron recoils. This could be done by simultaneously measuring the scintillation light of interactions in the crystal. Therefore in the second stage CRESST-II, the detector material was replaced by $CaWO_4$ [120] due to its good scintillation properties[1]. From a variety of different scintillating crystals, $CaWO_4$ showed a high light yield at low temperatures and no observable reduction of the light yield for events near the crystal surface [121]. Another reason for this choice for the target material was that the A^2 dependency of the cross section (see sec. 3.1.2) could be exploited by using a heavy element like tungsten, making $CaWO_4$ an excellent material for CRESST-II.

At very low recoil energies, which can be probed in the third stage CRESST-III, the discrimination power between electron and nuclear recoils starts to break down. Furthermore, when looking for light dark matter masses, target nuclei with smaller masses are favourable due to the kinematics of the scattering. Therefore, the use of sapphire crystals becomes an interesting alternative to $CaWO_4$ again. On top of that, after the LEE was observed during the first CRESST-III measurements in detector modules with sufficiently low thresholds (all $CaWO_4$ crystals), sapphire and several other materials were chosen to test for any material dependencies of the LEE.

The second CRESST-III run included two 15.9 g sapphire modules in a Cu housing, covered with scintillating foil and held by $CaWO_4$ sticks. For the third run, whose analysis is presented in this work, the same two sapphire modules were measured again, but the foil was removed and the $CaWO_4$ sticks were replaced with Cu sticks to create a fully non-scintillating housing.

This chapter will present the results of the analysis of the sapphire modules of the third CRESST-III run, in the following called *Sapp1* and *Sapp2*. The first section (sec. 7.1)

[1] Al_2O_3 also has scintillating properties, although much weaker than $CaWO_4$.

will show some particularities of the noise distribution of the sapphire modules and discuss the influence it has on the calculation of the trigger threshold. This is followed by a short section containing all relevant numbers and plots concerning the analysis of the sapphire modules (sec. 7.2). The next section (sec. 7.3) will present the results of the neutron calibration. Since pure sapphire crystals are only very weakly scintillating, the electron and nuclear recoil bands are not well distinguishable. Nonetheless the neutron calibration contains interesting results regarding a possible new method of energy calibration. The energy calibration of the light detector of *Sapp2* for an individual dark matter analysis is presented in sec. 7.4. Afterwards, sec. 7.5 discusses the calibrated energy spectra, starting with a comparison of the spectra between different runs. After this, the focus lies on the *Sapp2* module, which has the better performance. The spectrum of this module shows a peak at an energy of about 190 eV. Possible origins of this peak are discussed in 7.5.3. Finally, a detailed study of the LEE in this module is presented in 7.5.2. The last section of this chapter will show the results of a dark matter analysis (sec. 7.6).

7.1 Noise distribution

As explained in detail in sec. 5.1.4, the calculation of the trigger threshold is based on the choice of an accepted number of noise triggers. The number of noise triggers as a function of the threshold can be described analytically following the general eq. 5.4. Assuming that the samples of filtered noise traces follow a Gaussian distribution, this can be written as eq. 5.6, which is typically used for calculating the threshold. A clear deviation from a purely Gaussian distribution is apparent from the distribution of samples of filtered EBLs in the two channels (phonon and light) of both modules (*Sapp1* (fig. 7.1) and *Sapp2* (fig. 7.2)).

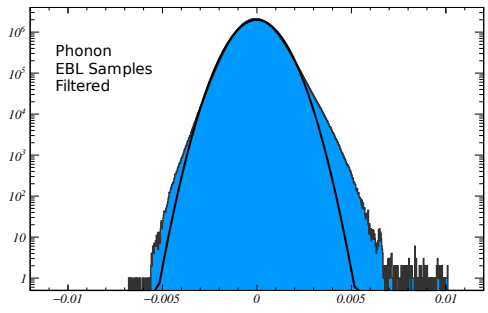

(a) Phonon channel of *Sapp1* with a Gaussian fit.

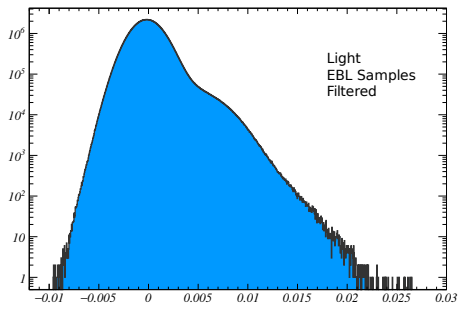

(b) Light channel of *Sapp1*.

Figure 7.1: The distribution of samples of filtered noise shows deviations from a Gaussian distribution in both channels of the *Sapp1* module.

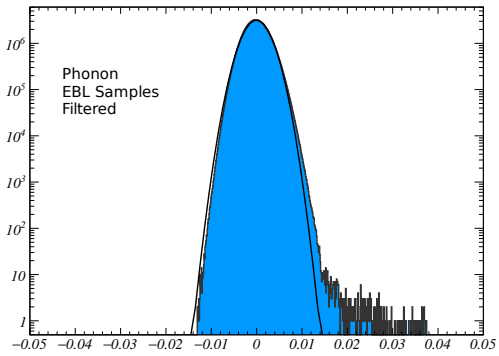

(a) Phonon channel of *Sapp2* with a Gaussian fit.

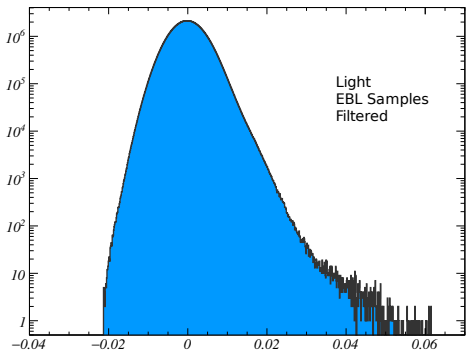

(b) Light channel of *Sapp2*.

Figure 7.2: The distribution of samples of filtered noise shows deviations from a Gaussian distribution in both channels of the *Sapp2* module. The deviation is much less pronounced compared to the *Sapp1* module.

This deviation from Gaussianity poses a problem for the standard way of calculating the trigger threshold. The first point to adress is the question whether this deviation is caused by pulses that survived the cleaning process of the EBLs or if this is caused by actual noise samples. This has an influence on how to treat this effect.

Hypothesis 1: There are very small pulses hidden in the noise that cannot be removed from the list of EBLs by cleaning the data. In this case the noise can still be considered to follow a Gaussian distribution $P(x)$ (as in sec. 5.5). Additionally a pollution distribution $F(x)$ is introduced. Assuming now that in a single filtered EBL $d-n$ samples follow $P(x)$ and n samples follow $F(x)$, the orignal equation for $P_d(x_{max})$ (eq. 5.4) has to be modified accordingly:

$$\begin{aligned} P_d(x_{max}) = &\frac{(d-n)!}{1!(d-n-1)!} \cdot P(x_{max}) \cdot \left(\int_{-\infty}^{x_{max}} F(x)dx \right)^{n} \cdot \left(\int_{-\infty}^{x_{max}} P(x)dx \right)^{d-n-1} \\ &+ \frac{n!}{1!(n-1)!} \cdot F(x_{max}) \cdot \left(\int_{-\infty}^{x_{max}} F(x)dx \right)^{n-1} \cdot \left(\int_{-\infty}^{x_{max}} P(x)dx \right)^{d-n} \end{aligned} \tag{7.1}$$

Hypothesis 2: There are different sources of noise, following different distributions. In this case the equation for the distribution of the noise can be modified: $P(x) = G(x) + F(x)$ (two sources). It is again assumed that at least one of them follows a Gaussian distribution ($G(x)$) and one of them is considered to be a pollution distribution

($F(x)$). If this is inserted into eq. 5.4, the distribution of maxima of the filtered EBLs can be written as:

$$P_d(x_{max}) = \frac{d!}{1!(d-1)!} \cdot (G(x_{max}) + F(x_{max})) \cdot \left(\int_{-\infty}^{x_{max}} (G(x) + F(x))dx \right)^{d-1} \tag{7.2}$$

In the first case, there is a clear separation of the contributions the different distributions have on the distribution of the maxima, $P_d(x_{max})$. Therefore the threshold can be chosen individually following either of these contributions. This is important for modules that turn out to actually contain small pulses in the noise. In these modules the choice of the threshold is based only on the contribution coming from the Gaussian noise $P(x)$, as will be shown later for the light channel of the *Sapp2* module.

In the second case, the separation is only possible on the level of the distribution of filtered noise samples. After applying eq. 7.2 the contribution of different sources of noise can not be distinguished anymore and the calculation of the threshold is based on the combination of these contributions. Taking a closer look at the EBLs of the phonon channels in the sapphire modules, no hints on the presence of small pulses can be found. Instead, the EBLs of *Sapp1* contain a big amount of spikes, as shown in fig. 7.3 as an example, while the EBLs of *Sapp2* generally show some unsteady behaviour. An example of this can be seen in fig. 7.4.

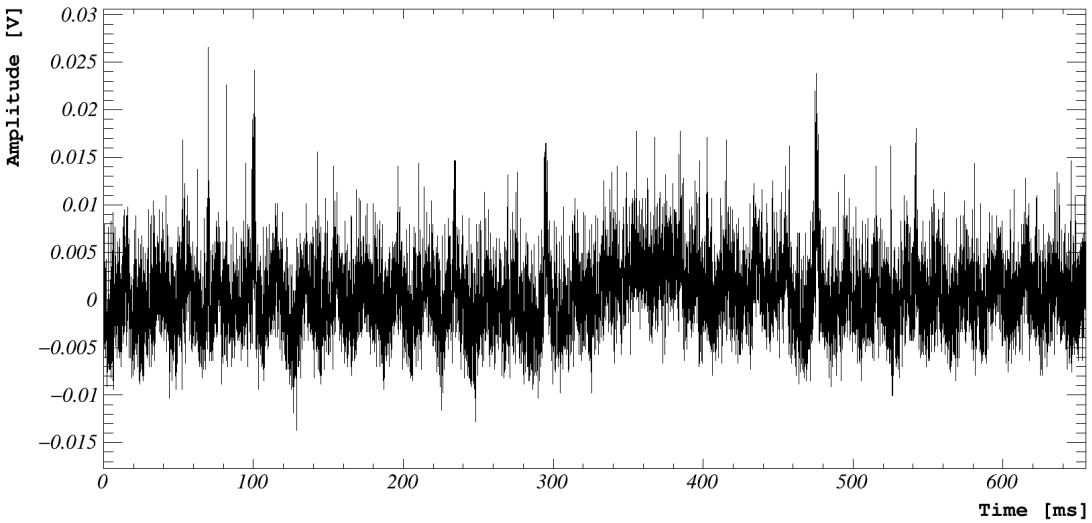

Figure 7.3: Sharp upward spikes are present in the noise of the *Sapp1* phonon channel.

At the time of this study, only a limited subset of the trainig set was available (figures 7.1 and 7.2). Repeating the same steps with the exposure of the full training set reveals that only a small fraction of EBLs caused deviations from the Gaussian behaviour in the phonon channel of *Sapp2*. Therefore the standard way of calculating the threshold could

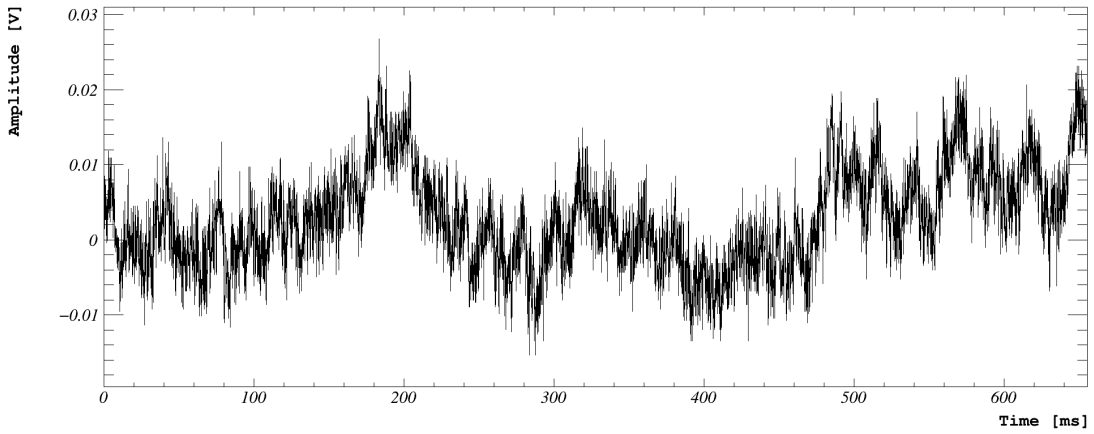

Figure 7.4: The noise in the *Sapp2* phonon channel shows a fluctuating and generally unsteady behaviour.

be used. The outcome can be seen in the figures used in section 5.1.4, which are showing the data of the *Sapp2* module.

For the *Sapp1* module, since the deviations from a Gaussian distribution seem to be caused by the spikes shown in 7.3 rather than from small pulses, the model $P(x)$ in eq. 7.2 is used to calculate the threshold. Therefore the spikes are considered as part of the noise, and thus are included in the noise trigger rate considered for the definition of the threshold.

A combination of two Gaussian distributions is chosen as a function describing the distribution of filtered noise samples. The first Gaussian distribution should be centered around zero with a standard deviation σ_1, describing the "standard" noise. The first distribution is not perfectly centered around zero, but has a slight negative shift. This is likely caused by spikes being present in the pretrigger range influencing the linear fit that is used to correct the offset of pulses (baseline offset). Therefore the mean of the first Gaussian distribution is left as a free parameter, μ_1. The second Gaussian distribution is centered around a positive mean, μ_2, describing the upward spikes with standard deviation σ_2 and an amplitude described as a fraction of the first Gaussian distribution, f:

$$P(x) = \frac{1}{\sqrt{2\pi}\sigma_1} \cdot e^{-\left(\frac{x-\mu_1}{\sqrt{2}\sigma_1}\right)^2} + \frac{f}{\sqrt{2\pi}\sigma_2} \cdot e^{-\left(\frac{x-\mu_2}{\sqrt{2}\sigma_2}\right)^2} \tag{7.3}$$

As can be seen in fig. 7.5, this function describes the distribution of the samples reasonably well.

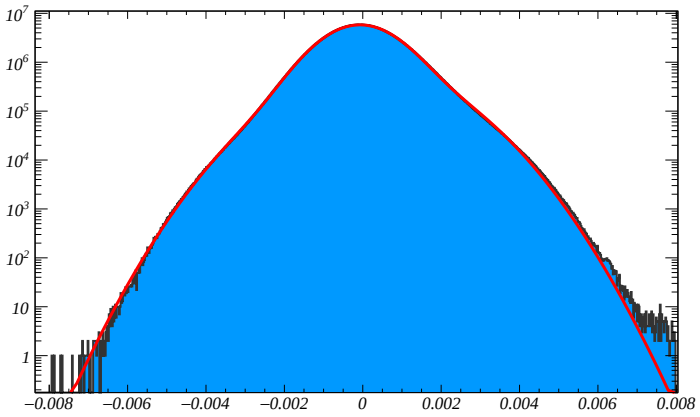

Figure 7.5: The distribution of filtered noise samples in the phonon channel of *Sapp1* can be described with two overlapping Gaussian distributions.

Inserting this into eq. 7.2 leads to:

$$P_d(x_{max}) = \frac{d \cdot A^d}{\sqrt{2\pi}} \cdot \left(\frac{1}{\sigma_1} \cdot e^{-\left(\frac{x_{max}-\mu_1}{\sqrt{2}\sigma_1}\right)^2} + \frac{f}{\sigma_2} \cdot e^{-\left(\frac{x_{max}-\mu_2}{\sqrt{2}\sigma_2}\right)^2} \right) \cdot \left(\frac{1+f}{2} + \frac{erf\left(\frac{x_{max}-\mu_1}{\sqrt{2}\sigma_1}\right)}{2} + f \cdot \frac{erf\left(\frac{x_{max}-\mu_2}{\sqrt{2}\sigma_2}\right)}{2} \right)^{d-1} \tag{7.4}$$

Figure 7.6 shows the distribution of maxima of a large set of filtered EBLs of the phonon channel of the *Sapp1* module. The distribution is fit with both analytical functions, the standard one based on a simple Gaussian noise (see eq. 5.6) and the modified function based on the noise sample distribution following a combination of two Gaussian distributions (eq. 7.4).

The fits perform comparably well. A threshold calculation is done based on both of them and compared in the following. For this, the integral over each of the distributions is calculated and scaled with the exposure corresponding to the number of EBLs used for the creation of the histograms shown in fig. 7.6, as shown in eq. 5.7. For this integral, the amplitude distribution of eq. 7.4 is corrected for the center of the first Gaussian distribution being slightly off zero (correction for μ_1). The resulting curves describing the noise trigger rate as a function of the threshold and the thresholds for one noise trigger per one kg day can be seen in fig. 7.7.

In the case of this dataset, taking the deviation of the noise sample distribution from standard assumptions into account only has a minor effect on the threshold. The increase from 9.56 mV to 9.61 mV is less than 0.6%. In terms of energy this translates to a change from 186.7 eV to 187.6 eV, which is a negligible difference. There is a difference

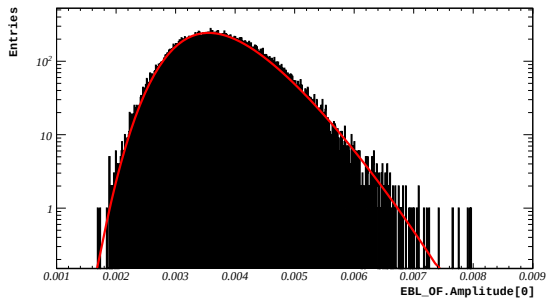

(a) Standard analytical distribution of the noise samples following a simple Gaussian distribution (eq. 5.6).

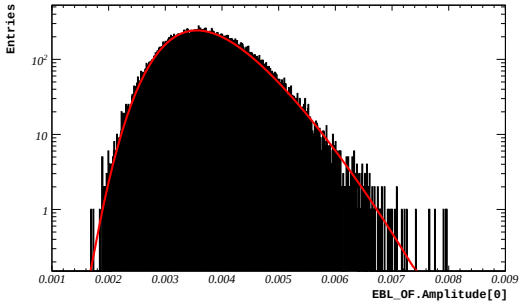

(b) Analytical description of the noise following a combination of two Gaussian distributions (eq. 7.4).

Figure 7.6: Maxima distribution of filtered EBLs of the *Sapp1* module with different analytical fits performing equally well.

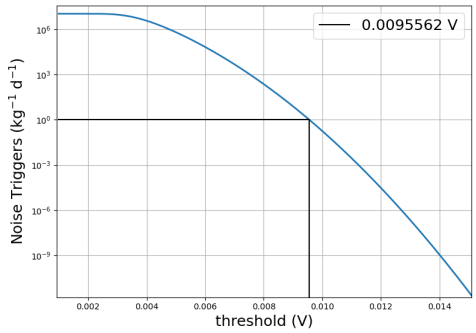

(a) Threshold calculation based on the standard method, assuming a Gaussian distribution of filtered noise samples.

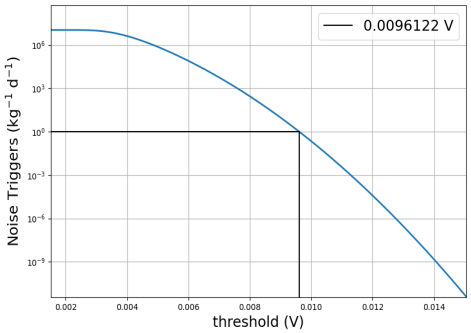

(b) Threshold calculation taking deviations from a single Gaussian distribution of the filtered noise samples into account.

Figure 7.7: Threshold calculation for *Sapp1* based on a) the standard noise distribution (single Gaussian distribution) and b) a modified noise distribution (two Gaussian distributions). The threshold based on the modified noise distribution is less than 0.6% higher than the threshold based on the standard method.

between this value and the one shown in chapter 6 and in [107], in which 157 eV is used as a threshold. The lower number is based on an older analysis, which has since then been re-evaluated and cross checked, which led to the higher value that is used in this chapter.

Sapp2 light detector: An independent full dark matter analysis is also done for the light channel of *Sapp2*. For this reason also the distribution of samples of filtered EBLs of this detector (fig. 7.2b) is investigated in detail. In this case the right tail of the sample

distribution clearly shows an exponential behaviour. Therefore the pollution distribution is described as:

$$F(x) = A \cdot e^{-\frac{x}{\lambda}} \tag{7.5}$$

with $x \in [0, \infty)$. Inspecting the EBLs describing this exponential tail, a lot of very small pulses can be seen in the noise. An example of an EBL containing small pulses is shown in fig. 7.8.

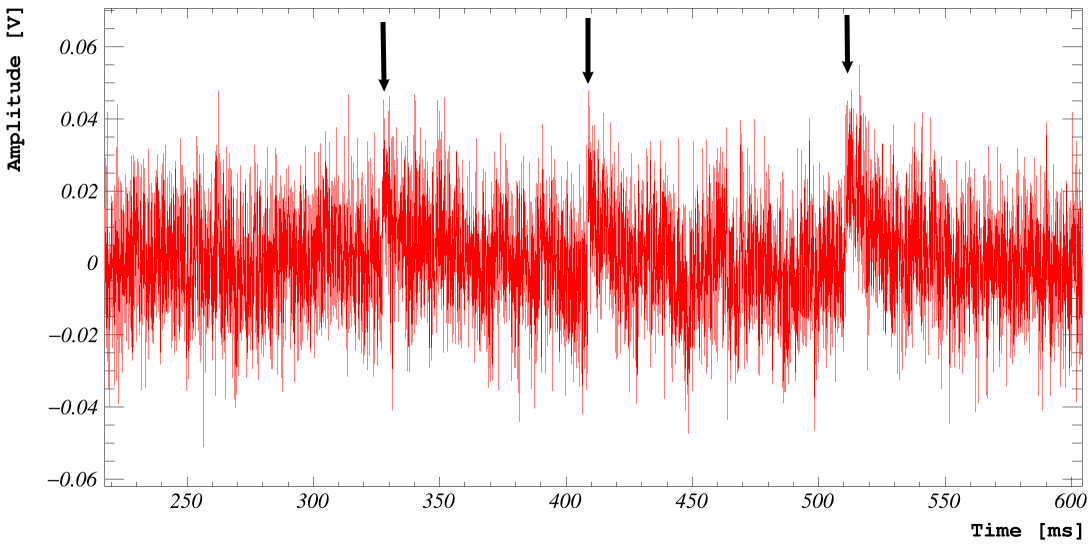

Figure 7.8: The noise in the *Sapp2* light detector contains a high number of very small pulses. This example contains three pulses, as indicated by the arrows.

These events could not be removed by cuts on the data. Therefore, the threshold is calculated based on eq. 7.1, which can be used to disentangle the contribution of the Gaussian noise $P(x)$ to the distribution of amplitudes of the filtered EBLs from the exponential pollution $F(x)$. Substituting eq. 7.5 into eq. 7.1 leads to the following expression:

$$\begin{aligned} P_d(x_{max}) = {} & \frac{(d-n)}{\sqrt{2\pi}\sigma} \cdot e^{-\left(\frac{x_{max}}{\sqrt{2}\sigma}\right)^2} \cdot \left(\frac{1}{2} + \frac{erf\left(\frac{x_{max}}{\sqrt{2}\sigma}\right)}{2}\right)^{d-n-1} \cdot \left(A\lambda \cdot \left(1 - e^{-\frac{x_{max}}{\lambda}}\right)\right)^n \\ & + nA \cdot e^{-\frac{x_{max}}{\lambda}} \cdot \left(\frac{1}{2} + \frac{erf\left(\frac{x_{max}}{\sqrt{2}\sigma}\right)}{2}\right)^{d-n} \cdot \left(A\lambda \cdot \left(1 - e^{-\frac{x_{max}}{\lambda}}\right)\right)^{n-1} \end{aligned} \tag{7.6}$$

Figure 7.9 shows the distribution of maxima of the filtered EBLs. This distribution can not be fitted under the standard assumption used in eq. 5.6. Instead, a fit with eq. 7.6 describes the data rather well.

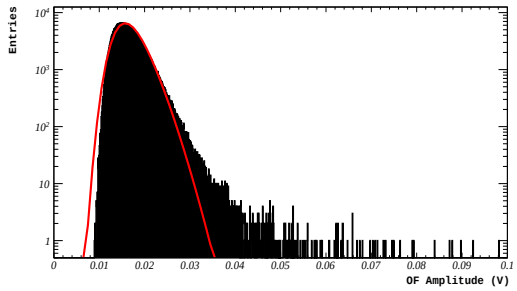

(a) A fit with the standard analytical distribution based on the noise samples following a simple Gaussian distribution (eq. 5.6).

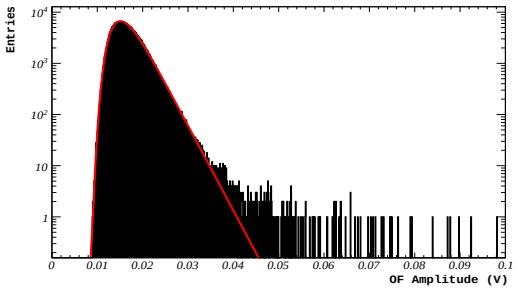

(b) Analytical description based on the noise following a Gaussian distribution including an exponential component as pollution distribution (eq. 7.6).

Figure 7.9: Distribution of maxima of filtered EBLs of the *Sapp2* light channel with different analytical fits. a) The fit under standard assumptions performs poorly. b) Including an exponential pollution term significantly improves the fit.

The first term of eq. 7.6 describes the case in which the maximum of the filtered EBL belongs to the Gaussian noise and therefore represents the actual distribution of noise amplitudes from which the noise trigger rate can be calculated, while the second term describes the case in which the maximum of a filtered EBL belongs to the exponential pollution distribution and is therefore caused by a small pulse. The contribution of the Gaussian noise to the fit shown in fig. 7.9b can be seen in fig. 7.10a. The noise trigger rate as a function of the trigger threshold is shown in fig. 7.10b. If the threshold is determined for one noise trigger per one kg day of data, based on the fit containing both, the Gaussian noise and the exponential pollution, a value of 66.12 mV is found. Considering that the exponential pollution is formed by small pulses, the actual noise trigger rate needs to be determined considering only the contribution of the Gaussian noise to the fit. By doing this, a much lower threshold of only 27.50 mV is found. In terms of energy this corresponds to a threshold as low as 6.2 eV.

7.2 Analysis details

The standard analysis of *Sapp2* is already shown in great detail in chapter 5. The analysis of the *Sapp1* module follows the same steps. This section gives a short overview over the analysis steps of *Sapp1* and compares them to *Sapp2*. Furthermore some plots not shown in the general analysis chapter are included in this section. The analysis of the light channel of *Sapp2* as an individual detector will be covered in a separate section.

Templates: Figure 7.11 shows all templates used in the analysis of the detectors presented in this work. A general trend that can be seen is that pulses in the phonon (PH) channel are slower than pulses in the light (L) channel. The shape of the heater pulses

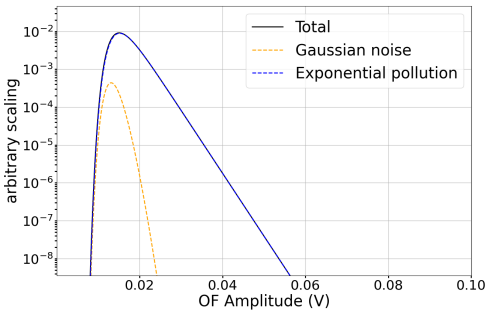

(a) Contributions of the Gaussian component in orange and the exponential pollution (small pulses) in blue to the fit of the maxima distribution of filtered EBLs in black.

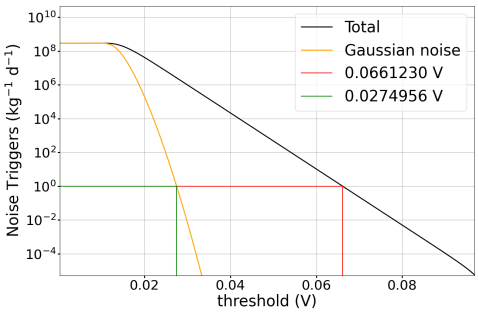

(b) Threshold determination considering the total maxima distribution in black, leading to the trigger threshold shown in red. If only triggers from the Gaussian noise are considered, the noise trigger rate follows the orange line. The trigger threshold in this case is shown in green.

Figure 7.10: The determination of the trigger threshold corresponding to one noise trigger per one kg day of data of the *Sapp2* light detector is based on the Gaussian contribution to the maxima distribution of filtered EBLs. a) The contributions of Gaussian noise and the exponential pollution to the maxima distribution fit. b) The threshold determined only from the Gaussian distribution and from the total of both contributions.

are designed to match the pulse shape of the particle events, which is needed for the analysis since the correction for the time dependence of the reconstruction of amplitudes of pulses is based on the assumption that particle and test pulses behave similarly. Indeed it can be seen that the differences in the pulse shape of particle and test pulse events are not very large for a given channel. Lastly, the templates for the light channel of *Sapp1* were not fit with the analytical model. The pulses in this channel show an extremely fast behaviour, which makes it more difficult to find good starting parameters for the fit. Since the performance of the *Sapp1* module was overall inferior to the other detectors (high threshold and resolution) it was decided to just use the averaged pulse templates.

Noise power spectra: Figure 7.12 shows the NPS for both channels of the sapphire modules. In *Sapp1*, the phonon channel shows strong fluctuations at frequencies higher than 100 Hz, which could be caused by the fast spikes. Otherwise the noise behaves quite similar in both channels. In *Sapp2*, the light channel shows a much higher level of noise than the phonon channel at higher frequencies, which is likely caused by the presence of the small pulses described in sec. 7.1.

Optimum filters: The OF for particle and test pulses for both channels of the sapphire modules are shown in fig. 7.13. In *Sapp1*, the fluctuations of the NPS of the phonon channel are also reflected in the filter kernel. The filters of the light channel of *Sapp1*

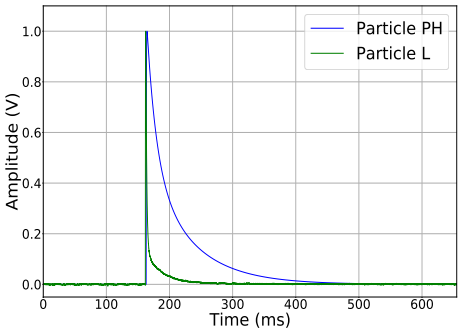

(a) *Sapp1* particle templates for both channels.

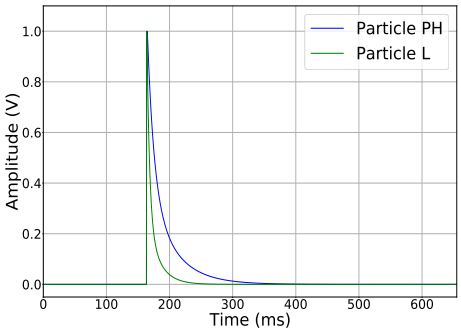

(b) *Sapp2* particle templates for both channels.

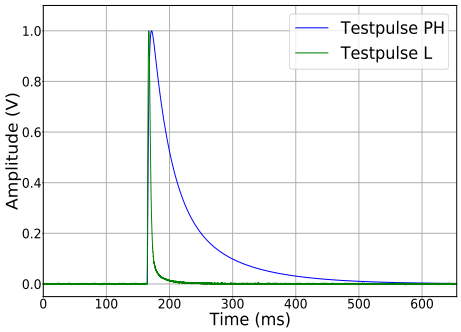

(c) *Sapp1* test pulse templates for both channels.

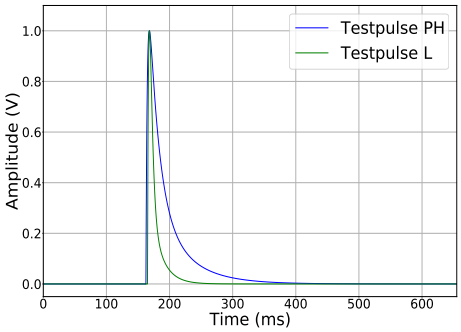

(d) *Sapp2* test pulse templates for both channels.

Figure 7.11: Particle and test pulse templates for phonon and light channels of the *Sapp1* and *Sapp2* modules.

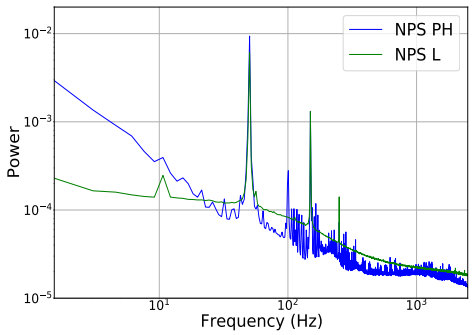

(a) *Sapp1* NPS for both channels.

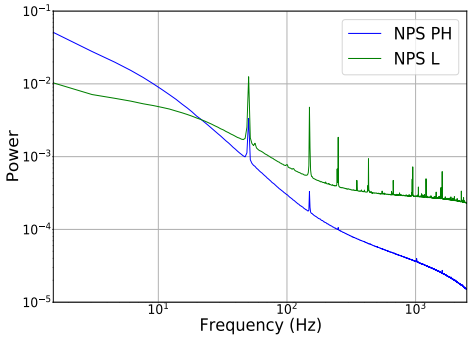

(b) *Sapp2* NPS for both channels.

Figure 7.12: Noise power spectra for both channels of the *Sapp1* and *Sapp2* modules.

have a rather flat behaviour, caused by the similarity in frequency space between the fast pulses and the noise. Effectively this means the filter is not very efficient, and the signal-to-noise ratio is only minimally improved by using the filter in this channel. Nevertheless it can be used for the amplitude reconstruction of pulses. In *Sapp2*, the

higher level of noise in the light channel leads to a stronger surpression of higher frequencies compared to the phonon channel.

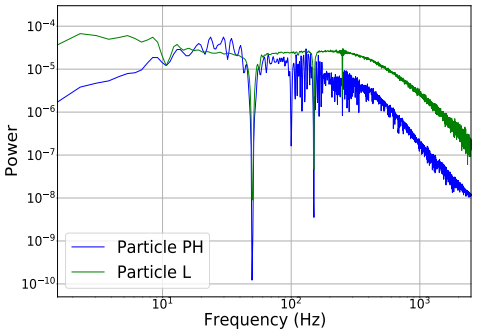

(a) *Sapp1* particle filters for both channels.

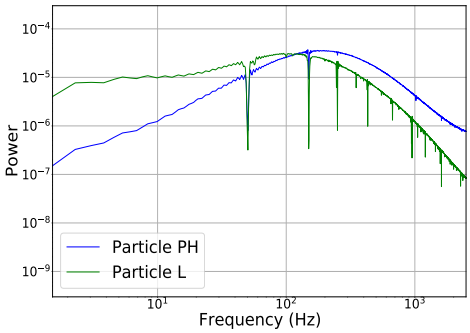

(b) *Sapp2* particle filters for both channels.

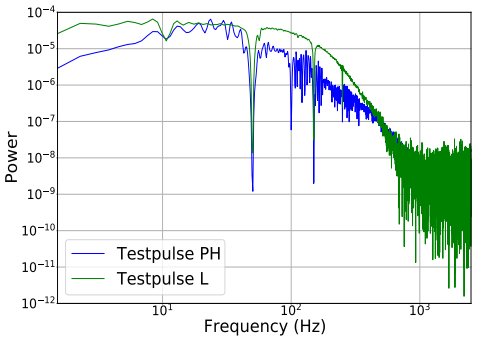

(c) *Sapp1* test pulse filters for both channels.

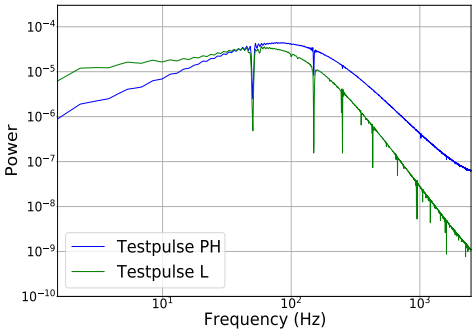

(d) *Sapp2* test pulse filters for both channels.

Figure 7.13: Particle and test pulse filters for phonon and light channels of the *Sapp1* and *Sapp2* modules.

The threshold calculation was covered in the previous section. Table 7.1 contains the resulting values for the trigger thresholds in units of reconstructed voltage and energy. Also listed are the energy resolutions at threshold and the CPE factors of both modules. The values listed for the *Sapp2* light channel (Sapp2-L) are the ones used in the analysis of this channel as an individual detector, discussed in sec. 7.4.

Table 7.1: Thresholds, energy resolutions and energy conversion factors of the relevant channels of the sapphire modules in the background (BCK) dataset.

Module	Threshold (mV)	Threshold (eV)	Resolution (eV)	CPE (keV/V_{TPE})
Sapp1	9.6	187.6	28.3	2.00
Sapp2	19.4	52.2	7.4	2.786
Sapp2-L	27.5	6.2	1.0	0.0113

The following list contains the cuts and selection criteria used in the analysis of the sapphire modules, most of which are explained in detail in 5.2.1:

- Preselection of files
- Stability cut
- Muon coincidence cut
- Baseline difference cut
- Baseline RMS cut
- Delta voltage cut
- Trigger cut
- Only in *Sapp1*: OF maximum position cut
  After leaving the maximum search of the optimum filter free, a cut on the position of the OF amplitude in the record window helps to remove some of the spike events mentioned in sec. 7.1 that survived the trigger.
- Cut on resolvable energy range:
  Before creating the TPR, a cut on the range of test pulse amplitudes that should be included is performed. This range is defined by the TPA up to which an unambigous mapping between TPA and reconstructed amplitude of test pulses is possible. The OF returns the same value for the reconstructed amplitude of test pulses above the saturation limit, rendering a mapping to specific TPA impossible. Analogous to this, the list of particle events is cut at the TPE value corresponding to that TPA. This value should be above the calibration lines, since otherwise the standard way of performing an energy calibration would not be possible.
- Linearity cut
- OF RMS cut

Analogous to what is shown for the *Sapp2* module in sec. 5.2.3, the calibration lines and the final cleaned spectrum of *Sapp1* can be seen in fig. 7.14.

The resolution in the *Sapp1* module is not good enough to resolve the two calibration lines of the ^{55}Fe source.

Finally, the curve describing the surviving fraction of events after triggering and after applying the selection criteria in *Sapp1* can be seen in fig. 7.15. The fit describes the trigger efficiency (eq. 5.8), as explained in 5.2.4. The fit values are listed in tab. 7.1.

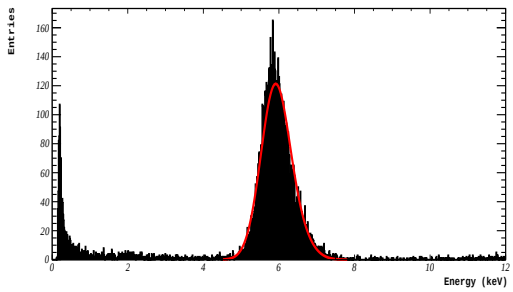

(a) Calibrated energy spectrum. The lines of the ^{55}Fe source can not be distinguished.

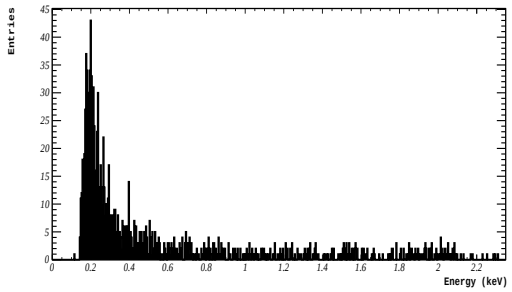

(b) Calibrated and cleaned energy spectrum.

Figure 7.14: Calibrated energy spectrum of *Sapp1*. a) Full spectrum, including the ^{55}Fe lines, which are not well resolved in this module. b) Calibrated spectrum after all data selection criteria have been applied.

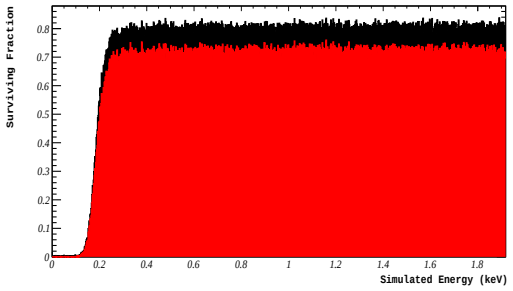

(a) Survival probability of events after triggering (black) and after applying all selection criteria (red).

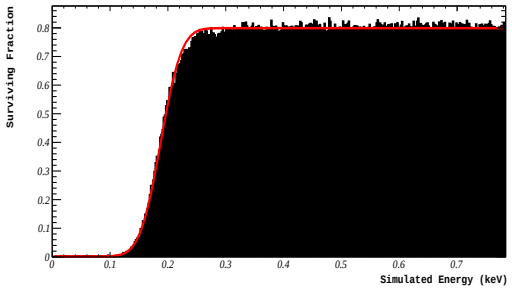

(b) Fit of the trigger survival curve.

Figure 7.15: Surviving fraction of events in *Sapp1* a) after triggering and after all selection criteria have been applied and b) a fit of the trigger efficiency to the surviving fraction of pulses after triggering.

7.3 Neutron calibration peak

Sapphire crystals are weak scintillators. This can be seen in fig. 7.16, showing the light yield plot of the bck dataset of *Sapp2*.

The light signal produced by events in the main absorber is very low and the reconstruction in the light channel of these events has a poor energy resolution. This leads to a strong smearing of the light yield of these events. The nuclear and electron recoil bands mentioned in 5.2.3.2 are strongly overlapping, making it impossible to distinguish between them. Therefore, there is no light yield information included in the dark matter analysis of the sapphire modules.

Unfortunately, there is limited useable data from the neutron calibration of the *Sapp1* module, due to strong instabilities that could not be mitigated during the data taking. Thus, the focus of this section will be only on the *Sapp2* module. Even though no useful information could be extracted by performing a band fit, the neutron calibration data

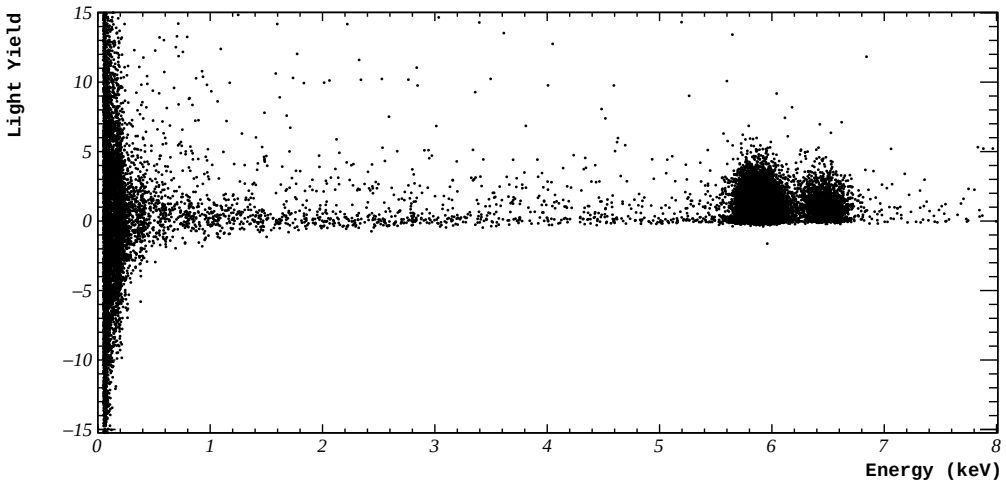

Figure 7.16: Light yield plot of the bck dataset of *Sapp2*. Interactions in the main absorber (phonon channel) of the ^{55}Fe source at around 5.9 keV and 6.5 keV produce only very little to no light signal in the light detector. In this way, the calibration of the light output in units of keVee has a very poor energy resolution. This leads to the light yield being smeared from zero up to a value of 5 and no clear centering around a light yield of 1 is identifiable, making a distinction of nuclear and electron recoils at lower energies practically impossible.

contain a very interesting feature, shown in fig. 7.17 that could potentially be used for an improved low energy calibration.

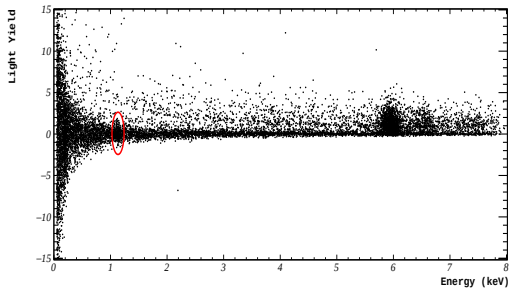

(a) Light yield plot of the neutron calibration dataset of *Sapp2*.

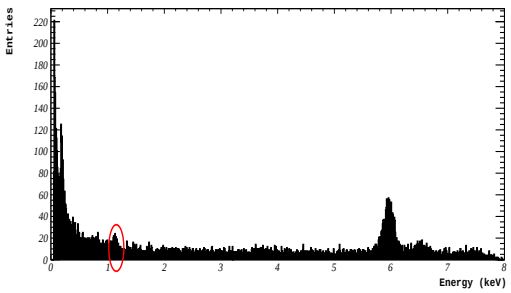

(b) Energy spectrum of the neutron calibration dataset of *Sapp2*.

Figure 7.17: Light yield plot and energy spectrum of the neutron calibration dataset of *Sapp2*. As explained above, the light output of events is too small to extract useful information from a band fit. The accumulation of events visible at around 1.1 keV might be explained by nuclear recoils resulting from a γ emission that follows the capture of a thermal neutron on ^{27}Al.

The peak at around 1.1 keV in fig. 7.17 could be explained by nuclear recoils induced by a γ emission, which follows after the capture of a thermal neutron on ^{27}Al. The CRAB Collaboration proposed to use this technique on $CaWO_4$ for an accurate calibration of nuclear recoils at the energy scale of $\mathcal{O}$(100 eV) in [122]. A more detailed description of

the process can be found in [123]. The basic principle is the capture of a thermal neutron in the nucleus, which creates a compound nucleus in an excited state. The de-excitation of this nucleus typically happens via the emission of γ-rays and conversion electrons, mostly in the form of cascades. In some cases, this de-excitation can also happen directly to the ground state by emitting only a single γ that carries the entire energy of this process. Depending on the target nucleus, these energies are usually in the order of $\mathcal{O}$(MeV). These de-exitations under emission of a single γ with energy E_γ lead to a monoenergetic peak in the nuclear recoil spectrum with a kinetic energy of $E_R = \frac{E_\gamma^2}{2 \cdot M_N c^2}$, where M_N is the mass of the compound nucleus. These energies of the recoiling nuclei E_R are typically in the order of $\mathcal{O}$(100eV).

The target nuclei need to fulfill certain criteria to make this technique useful for a low energy calibration:

- A high natural abundance of the isotope in question, Y_{ab}
- A high cross section for the capture of thermal neutrons, $\sigma_{n,\gamma}$
- A high branching ratio for single-γ transitions, I_γ^s

In [122] and [123], detector crystals containing different suitable isotopes of W and Ge are considered. Simulations on these materials show that clear peaks in the nuclear recoil spectrum should be measurable. First experimental proof on a $CaWO_4$ crystal was published by the CRAB and NUCLEUS collaborations in [124] and by the CRESST collaboration in [125]. The aluminum isotope ^{27}Al in sapphire (Al_2O_3) crystals also has appropriate properties for this technique. The key parameters are listed in tab. 7.2 below.

Table 7.2: Properties of ^{27}Al. A high natural abundance, high thermal neutron capture cross section and a high branching ratio for single-γ de-excitation make it a suitable isotope to observe the effect explained above. All numbers are taken from [126, 127, 128] except for E_R, which is calculated from the Q-value.

Isotope	Y_{ab}	$\sigma_{n,\gamma}$	I_γ^s	Q-value	E_R
^{27}Al	100%	0.23 barn	26.81%	7724 keV	1144 eV

A simplified simulation, assuming an energy dependent resolution and a 100% branching ratio for single-γ de-excitations I_γ^s, provided by the CRESST simulation group shows a clearly visible peak in a sapphire crystal, see fig. 7.18 [129]. The energy resolution at the position of the peak is 12.7 eV. The simulation was performed with the Geant4 based simulation software ImpCRESST [130]. It should be noted that the position of the neutron source in this simulation is closer to the detectors than for the real data shown in this chapter.

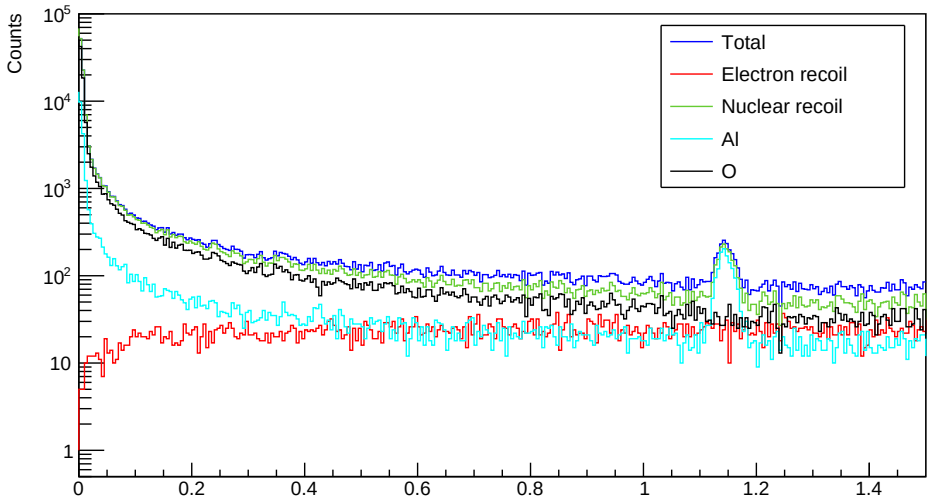

Figure 7.18: Simulated spectrum of a neutron calibration of a sapphire crystal. Simulation of $5 \cdot 10^8$ neutrons, assuming a branching ratio for single-γ de-excitations of I^s_γ= 100% and an energy resolution of 12.7 eV at the position of the peak [129].

For a more realistic simulation this peak would have to be rescaled with the true branching ratio of 26.8%. The other 73.2% of events would produce a spectrum below the peak describing the γ-cascades, which are not considered here. Moreover, the true energy resolution of the sapphire detector shows a strong dependence on the energy, as can be seen in the following. This means that the real data, in which the peak is expected to have a lower intensity and a worse resolution, are not expected to reproduce the ideal simulated spectrum shown in fig. 7.18.

The measured spectrum of the neutron calibration is scaled by the corresponding exposure and binned in 2 eV bins. Each bin is then corrected by the survival probability of events in this energy bin, determined by a simulation following the steps explained in sec. 5.2.4. The resulting histogram can be seen in fig. 7.19. To fit the spectrum a choice has to be made on the empirical fit function. For simplicity, a single function can be chosen to describe the LEE in this case. The bump of unknown origin at around 190 eV, as well as the peak at around 1.1 keV are fit with a Gaussian distribution. The full function is given by:

$$R(E) = \left(A \cdot e^{-E/\lambda} + B \cdot E^{-k} + C + \sum_{i=B,P} \frac{D_i}{\sqrt{2\pi}\sigma_i} \cdot e^{-\frac{1}{2}\left(\frac{E-\mu_i}{\sigma_i}\right)^2} \right) \cdot \Theta(E - E_{thr}) \qquad (7.7)$$

For the fits shown in this section, either the exponential or the power law term is used. The flat component of the spectrum is described by the parameter C. The two Gaussian

distributions describe the bump (B) and the peak (P). Each fit is performed once with and once without a Gaussian component describing the peak P. The improvement of adding a peak to the fit can be seen in the corresponding reduced χ^2. All fits are shown in fig. 7.19 and the resulting parameters are listed in tab. 7.3.

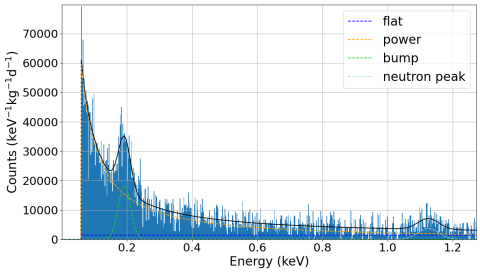

(a) Power law and two Gaussian distributions (χ^2_{red} = 1.17).

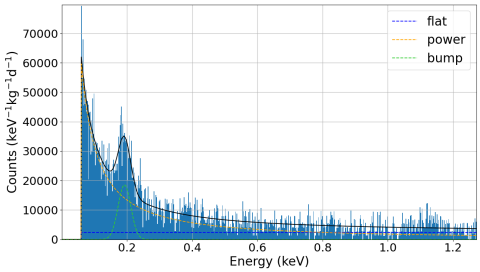

(b) Power law and one Gaussian distribution (χ^2_{red} = 1.26).

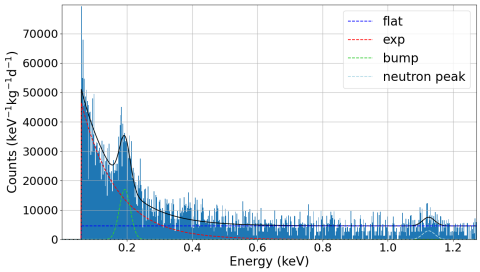

(c) Exponential and two Gaussian distributions (χ^2_{red} = 1.30).

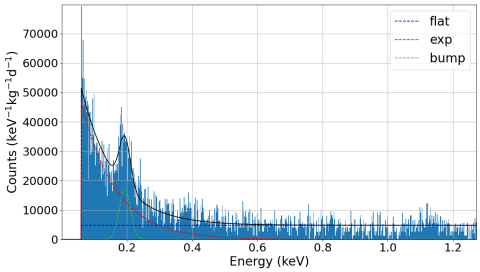

(d) Exponential and one Gaussian distribution (χ^2_{red} = 1.35).

Figure 7.19: Different fit models for the spectrum are used. All fits contain a Gaussian component to account for the unknown bump at around 190 eV and a flat component. The LEE is either fit with a power law (top) or with an exponential (bottom). An additional Gaussian distribution describing the potential neutron peak is once included in the fit model (left) and once not included in the fit model (right).

The fit generally performs better if the LEE is described by a power law. Independently of the description of the LEE, the fit improves by adding a peak describing the neutron capture induced nuclear recoils. Both fits (power law and exponential) return the same results for the position and width of the neutron peak within the uncertainties. An independent analysis was performed within the CRESST analysis group using an unbinned likelihood framework. For the likelihood analysis, the energy range was reduced to exclude part of the LEE below the peak at around 190 eV and the LEE was described by an exponential term. This analysis led to the same results for position and width of the neutron calibration peak. A likelihood ratio test resulted in a significance of 6.0 σ for this peak. This high significance justifies using this peak for calibrating the spectrum at low energies. This is the first time this effect is measured on Al_2O_3.

Table 7.3: Fit parameters of the neutron calibration spectrum. All fits contain a flat component describing the flat background and a Gaussian component to describe the peak of unknown origin ("bump", B). The LEE is described either as a power law or an exponential. In both cases the fit improves when a Gaussian distribution describing the neutron calibration peak (P) is added to the fit.

Parameter	Power law with Peak	Power law no Peak	Exponential with Peak	Exponential no Peak
A (1/(keV kg d))	-	-	80792 ± 3309	82703 ± 3522
λ (keV)	-	-	0.108 ± 0.005	0.105 ± 0.005
B ($1/(\text{keV}^{1-k}$ kg d))	2247 ± 296	1816 ± 239	-	-
k	1.17 ± 0.05	1.24 ± 0.05	-	-
C (1/(keV kg d))	1469 ± 464	2364 ± 374	4610 ± 207	4814 ± 192
D_B (1/(keV kg d))	865 ± 63	906 ± 65	727 ± 69	751 ± 71
μ_B (eV)	192 ± 1	192 ± 1	193 ± 1	193 ± 1
σ_B (eV)	18.9 ± 1.4	19.5 ± 1.4	17.0 ± 1.6	17.4 ± 1.6
D_P (1/(keV kg d))	300 ± 76	-	138 ± 58	-
μ_P (eV)	1125 ± 8	-	1125 ± 8	-
σ_P (eV)	32.4 ± 8.5	-	18.7 ± 8.6	-
χ^2_{red}	1.168	1.255	1.296	1.352

The extracted position of the peak at (1125 ± 8) eV, though close to the predicted value of 1144 eV (see tab. 7.2), does not match it within the uncertainty. This shows that the accuracy of the calibration with the ^{55}Fe lines might be slighty off at low energies in this detector. Therefore, this peak is a suitable method to fine-tune the calibration of the detector at energies around $\mathcal{O}(100$ eV).

7.4 Calibration of the Sapp2 light channel: a new method

The light channel of the *Sapp2* module can be used for an independent dark matter analysis. For this analysis, the detector needs to be calibrated to direct hits of the calibration source. Since these events lead to highly saturated pulses in this detector, the calibration requires some additional steps compared to the standard energy calibration.

Dynamic range and calibration events: The amplitudes of the test pulses cover a range from the threshold up to 0.5 V, shown in fig. 7.20a. This is still in the linear regime of the detector. The direct hits of the ^{55}Fe source are far above this value and lead to fully saturated pulses. An example of such a pulse can be seen in fig. 5.17. The amplitude of these pulses can only be reconstructed properly with a truncated template fit, as explained in sec. 5.2.2. The spectrum of reconstructed amplitudes is shown in fig. 7.20b. As can be seen, the amplitudes of the ^{55}Fe events are reconstructed at very high values

(above 20 V). As the range of test pulses ends at 0.5 V, a correction for the time dependent behaviour of the detector response cannot be performed. In this case, the calibration factor is directly applied to the reconstructed amplitudes of the template fit, omitting the step of creating the time corrected TPE amplitudes (see sec. 5.2.3). A fit of the ^{55}Fe-lines leads to a calibration factor of 0.2726 keV/V_{rec}.

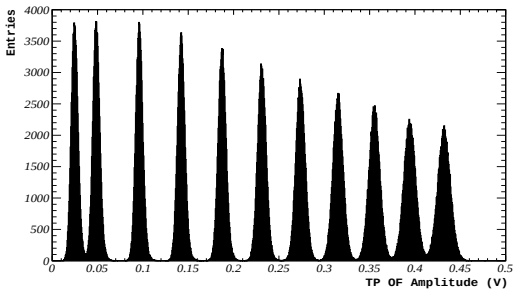

(a) The test pulses cover a range from the threshold up to about 0.5 V.

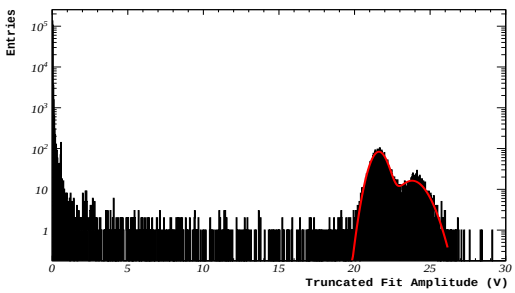

(b) Spectrum of the template fit amplitudes. The red line shows a fit of the ^{55}Fe-lines to obtain the calibration factor.

Figure 7.20: The amplitudes of the calibration events lie far above the range covered by the test pulses. This makes a correction for the time dependent behaviour of the detector response not possible at high energies.

Comparison of OF and fit amplitudes: The optimum filter has a better resolution for the determination of pulse amplitudes, which makes it the preferred method for creating the spectrum of amplitudes. A direct calibration of the OF amplitudes is not possible, due to the ^{55}Fe pulses being fully saturated. The calibration factor can only be obtained based on the spectrum of the (truncated) fit amplitudes, shown in fig. 7.20b. If the energy range of the spectrum is limited to a region in which both, the OF and the template fit give identical results for the amplitudes of pulses, the calibration factor obtained from the template fit can be applied to the OF amplitudes. In fig. 7.21 it can be seen that this is the case below reconstructed amplitudes of 0.5 V. Thus, a cut is performed, limiting the spectrum to values below a pulse amplitude of 0.5 V.

7.4.1 Vacuum ultra violet intrinsic luminescence of sapphire

A characteristic feature that can be seen in the LY plot of fig. 7.16 and in fig. 7.17a in sec. 7.3 is the inverse proportionality of positive LY values to the energy in the phonon channel (for LY > 0: LY $\propto 1/E_{phonon}$). Figure 7.22 highlights some populations of events following this behaviour.

This points towards an effect that leads to a constant energy of the light signals that are formed in the main absorber, independently of the energy deposited in the phonon channel. Figure 7.23 shows events that lead to a coincident signal in both channels,

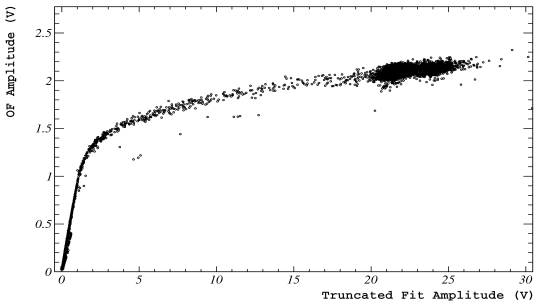

(a) OF amplitudes plottet against the template fit amplitudes in an energy range including the calibration lines.

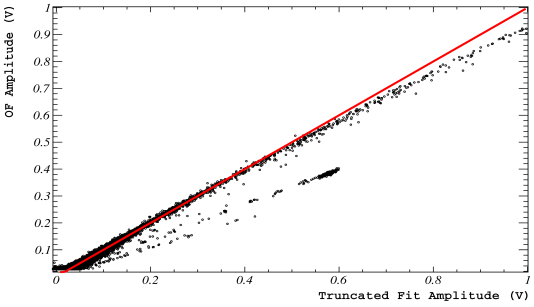

(b) Zoomed in region of the amplitude comparison. Below 0.5 V, both methods return the same amplitudes for the pulses. The events deviating from the linear behaviour (below the red line) are wrongly reconstructed due to a different pulse shape. These events are removed by the quality cuts later on.

Figure 7.21: A cut on the energy range, in which OF and fit amplitudes give identical results, makes it possible to apply the calibration factor obtained from the fit to the spectrum of the OF amplitudes, which has a better energy resolution.

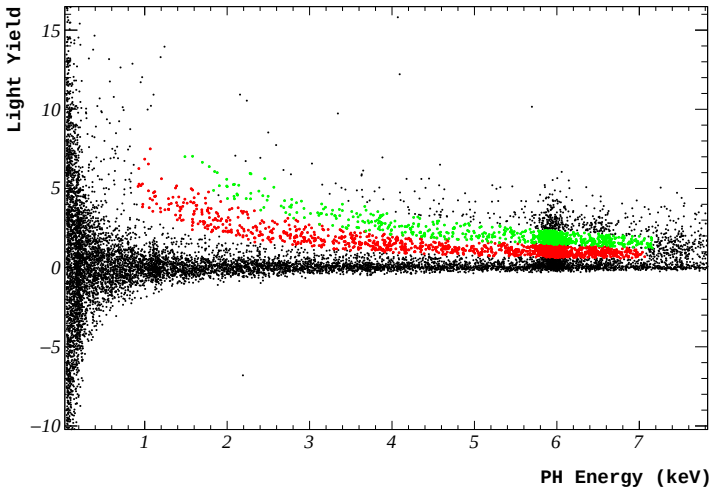

Figure 7.22: The light yield shows some populations of events (red and green) following an inverse proportionality to the energy deposited in the phonon channel.

calibrated with the absolute deposited energies in both channels (in contrast to the electron equivalent energy used for the LY). Indeed, it can be seen that events in the main aborber lead to light signals with a constant energy, as indicated by the red box in 7.23a. Most of these events are in coincidence with ^{55}Fe events in the phonon channel. A zoomed in plot of this energy region, shown in 7.23b, reveals several substructures with discrete energies in the light channel for both ^{55}Fe lines, at 5.9 keV and 6.5 keV.

Due to the excellent energy resolution that can be achieved with the OF, three distinct

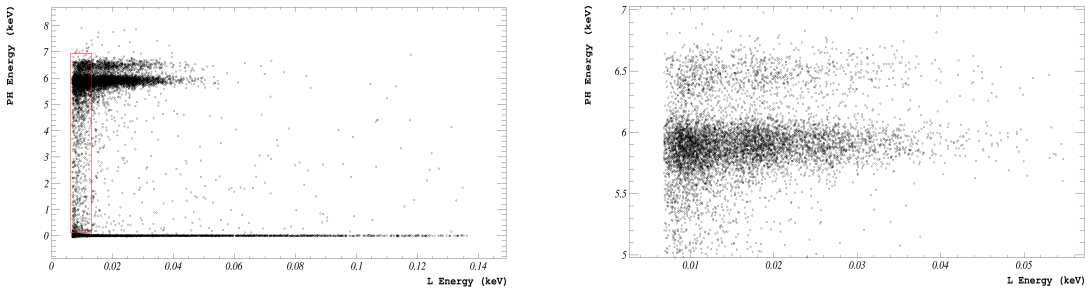

(a) At low energies, a constant amount of energy is seen in the light channel (red box), independent of the energy deposited in the phonon channel.

(b) A close-up of the ^{55}Fe events in the phonon channel reveals several substructures in the energy distribution in the light channel.

Figure 7.23: Absolute energies of events in the phonon and light channel. Since the light channel is considered as the detector of interest in this section, its energy is shown on the x-axis, while the energy in the phonon channel is shown on the y-axis.

peaks can be seen in the spectrum. Their positions can be extracted by a fit with a sum of three independent Gaussian distributions:

$$R(E) = \sum_{i=1,2,3} \frac{A_i}{\sqrt{2\pi}\sigma_i} \cdot e^{-\frac{1}{2}\left(\frac{E-\mu_i}{\sigma_i}\right)^2} \tag{7.8}$$

The fit of the spectrum is shown in fig. 7.24. Because the trigger efficiency affects the shape of the distribution at the lowest energy, the left tail is not included in the fit. The fit parameters are listed in tab. 7.4.

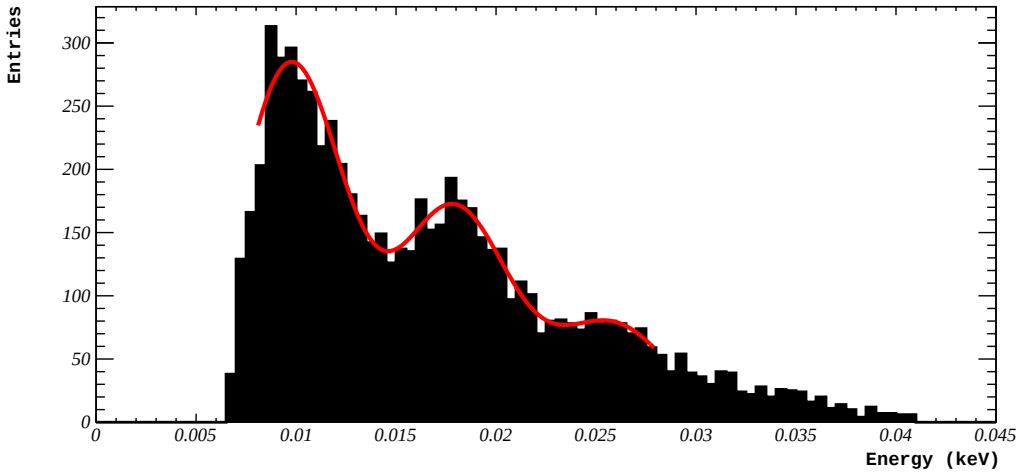

Figure 7.24: Fit of eq. 7.8 to the peaks seen in the light channel in coincidence with events of the ^{55}Fe source in the main aborber.

The absence of an energy dependent scintillation light, preventing the separation

Table 7.4: Fit parameters of eq. 7.8 from a fit to the histogram shown in fig. 7.24.

Parameter	Peak 1	Peak 2	Peak 3
Amplitude A_i (a.u.)	1.879 ± 0.184	1.161 ± 0.191	0.554 ± 0.151
Position μ_i (eV)	9.73 ± 0.15	17.86 ± 0.23	25.77 ± 0.47
Resolution σ_i (eV)	2.65 ± 0.27	2.75 ± 0.42	2.86 ± 0.75

of the nuclear recoil bands from the e^-/γ band, as explained earlier, is a sign of the high purity of the crystals at hand. There is very little to no impurity-induced extrinsic luminescence observed. On the other hand, it has been shown already in 1968 by W.A. Runciman, that an intrinsic luminescence at about 165 nm is emitted by pure sapphire crystals under irradiation with X-rays at low temperatures [131]. In this paper, the comparison among different crystals shows that a higher level of purity leads to higher intensities of this luminescence due to a strong absorption at this wavelength by impurities. This was the first example of solid state luminescence in the vacuum ultra violet (VUV)[2]. Since then, the intrinsic luminescence of pure and doped sapphire crystals has been investigated in great detail. An extensive study of different luminescence bands in sapphire in [132] interprets the origin of the 7.6 eV emission as the radiative decay of self-shrunk excitons. It is shown that the emission spectrum of a highly pure sapphire crystal is dominated by this 7.6 eV luminescence when it is excited with 6 keV electrons at 8 K. Furthermore, it is shown that this luminescence can also be effectively excited by synchrotron radiation with photon energies of 8.8 - 9.3 eV, just below the energy gap of sapphire at $E_g = 9.4$ eV [132]. Another sharp increase of the intensity is then seen at photon energies higher than 25 eV. This value describes the energy threshold necessary to create an electron-hole pair in which the energy of the electron is sufficient to form secondary excitations, known as the multiplication of electronic excitations (MEE) [132]. These results are confirmed in numerous other publications, see for example [133] and [134].

At the relatively high energies of the exciting photons of the ^{55}Fe source, it can be assumed that multiple emission photons are created by the MEE. If several of the emitted photons (each with an energy of 7.6 eV) hit the light detector with a time difference much smaller than the risetime of a pulse, their energies add up and are seen in the detector as a single event with an energy equal to a multiple of the energy of a single luminesence photon. Since the decaytime of this VUV emission is in the order of $\mathcal{O}$(ns) [132, 133, 134], while the risetime of pulses in the *Sapp2* light channel is between about 300 - 1000 µs, all luminescence photons can be considered as being simultaneously emitted. The probability of a single photon to deposit energy in the

[2]Photons with wavelengths below the ultra violet range are called vacuum ultra violet, since they are absorbed by oxygen in the air and hence need a vacuum to spread.

light detector depends on several factors, one being the absorption probability in the main crystal (phonon channel), which is small for pure crystals but might still have an effect, especially for events emitted on the opposite side of the crystal (the side not facing the light detector). Another factor is the solid angle of the light detector with respect to the position of the emission in the main crystal. The probability of measuring $n \in \{0, 1, 2, 3, 4, ...\}$ photons in the detector simultaneously is then described by a binomial distribution. The equally spaced peaks with decreasing amplitudes seen in the spectrum in fig. 7.24 are therefore interpreted as the energy depositions of single photons of 7.6 eV (first peak) and multiples of such (following peaks). The energy calibration of this detector is based on the truncated template fit of the highly saturated events of the ^{55}Fe source in the detector, so small deviations of the fit values of the position of the peaks given in tab. 7.4 are expected. Still, the distance of the peaks to each other matches the expectation. On top of that, the overall energy scale is very close to the expected values, confirming the validity of the standard calibration method.

Nevertheless, the presence of these peaks is an excellent opportunity to perform a fine-tuning of the calibration at these low energies. Moreover this energy range is covered by the test pulses, so the reconstructed amplitudes can be corrected for the time dependent response, creating the TPE amplitudes in units of "injected" voltage (V_{inj}), which are then calibrated with the peaks of the luminescence energy (see sec. 5.2.3). For the fit of the calibration lines, four Gaussian distributions with equal distances, μ, between their maxima and a constant energy resolution, σ, in this low energy regime are assumed:

$$R(E) = \sum_{i=1,2,3,4} \frac{A_i}{\sqrt{2\pi}\sigma} \cdot e^{-\frac{1}{2}\left(\frac{E-i\cdot\mu}{\sigma}\right)^2} \tag{7.9}$$

The resulting fit is shown in fig. 7.25, the fit parameters can be seen in tab. 7.5.

Table 7.5: Fit parameters of the fit of eq. 7.9 to the histogram shown in fig. 7.25.

Parameter	Fit value
Position μ (V_{inj})	0.671 ± 0.04
Resolution σ (V_{inj})	0.234 ± 0.04
Amplitude single γ A_1 (a.u.)	97.99 ± 2.19
Amplitude two γ's A_2 (a.u.)	55.02 ± 1.29
Amplitude three γ's A_3 (a.u.)	24.68 ± 0.91
Amplitude four γ's A_4 (a.u.)	6.94 ± 0.55

The CPE factor obtained from this calibration is 0.0113 keV/V_{inj}. Multiplying the peak position of the first peak with this factor gives $E_{1\gamma}$ = (7.58 $\pm$ 0.45) eV with a resolution of σ = (2.64 $\pm$ 0.45) eV.

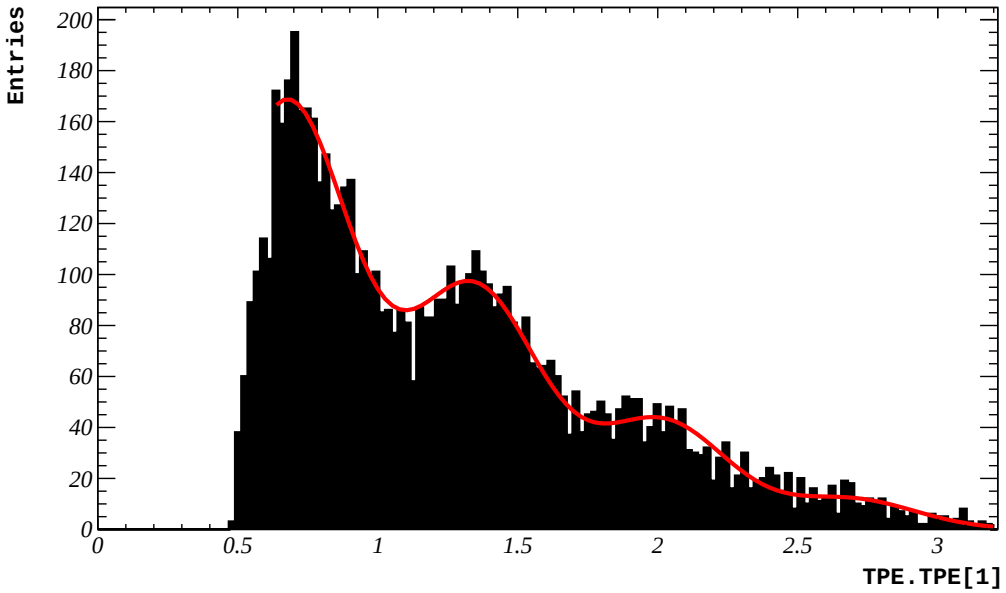

Figure 7.25: Fit of eq. 7.9 to the peaks seen in the light channel formed by the intrinsic luminescence of pure sapphire crystals in units of the time corrected TPE amplitude.

7.4.2 Final spectrum and efficiency

The same cuts are applied to clean the data as for the phonon channels of the sapphire modules (listed in sec. 7.2). Since for this analysis only the light channel was triggered, a trigger cut is not necessary. The cut on the energy range in which the OF and template fit amplitudes give identical results is analogous to the linearity cut.

Figure 7.26 shows the calibrated energy spectrum after all selection criteria have been applied.

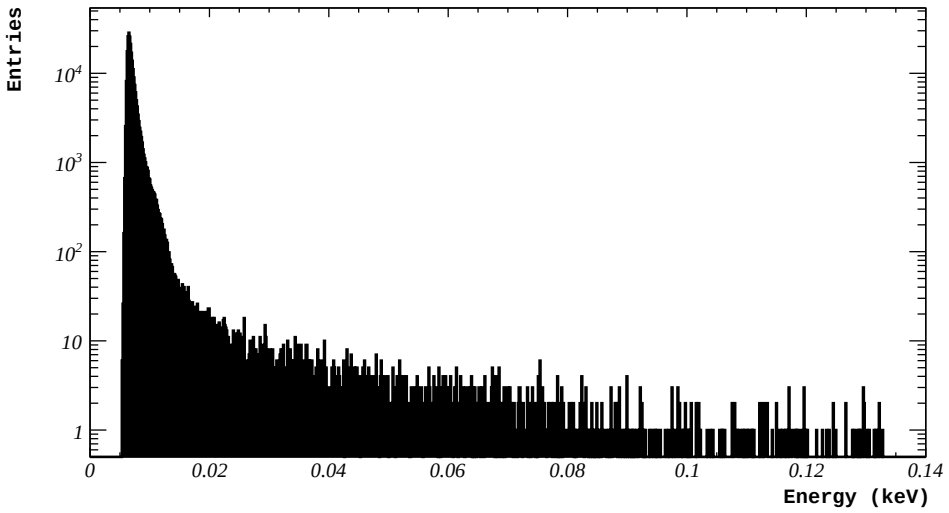

Figure 7.26: Calibrated and cleaned energy spectrum of the *Sapp2* light channel.

The survival probabilities of pulses after triggering and after applying the selection criteria can be seen in fig. 7.27. The shoulder in the efficiency curves shown in fig. 7.27a at around 0.1 keV emerges from a filter effect. The filtered output of a pulse contains small side maxima, symmetrically distributed around the pulse, as can be seen in the example of a filtered template pulse in fig. 5.3b (in sec. 5.1.3). The height of these maxima is dependent on the amplitude of the filtered pulse. The amplitude of the side maxima of control pulses corresponds to an energy of about 0.1 keV in this detector. After the filter process, particle events with energies below this value that appear close enough to a control pulse in time (before or after) can be hidden by one of these side maxima. Effectively this reduces the trigger probability for particle events with energies below 0.1 keV, leading to the shoulder in the efficiency curve. The fit in fig. 7.27b describes the trigger efficiency (eq. 5.8), as explained in sec. 5.2.4. The fit reveals a threshold of only **6.20 eV**, and a resolution at the threshold of **1.03 eV** (values also shown in tab. 7.1).

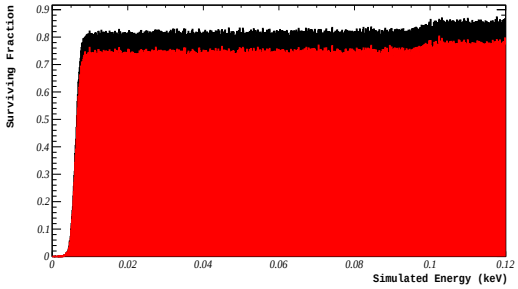

(a) Survival probability of events after triggering (black) and after applying all selection criteria (red). The shoulder at about 0.1 keV is caused by a filter effect.

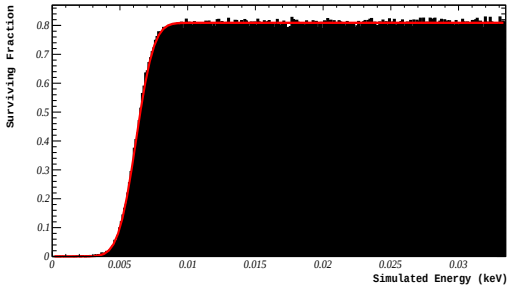

(b) Fit of the trigger survival curve.

Figure 7.27: Surviving fraction of events in the *Sapp2* light channel a) after triggering and after all selection criteria have been applied and b) a fit of the trigger efficiency to the surviving fraction of pulses after triggering.

7.5 Energy spectra

This section concentrates on the energy spectra measured in the detectors. First, the spectra of different sapphire crystals are compared with each other, as well as the spectra of the same crystals in different measurement campaigns. Afterwards, the focus moves to the energy spectrum of the *Sapp2* phonon channel. Especially the behaviour of the Low Energy Excess and the peak at about 190 eV is studied in detail.

7.5.1 Comparison of spectra

As mentioned earlier in the introduction of this chapter, the same sapphire crystals were used in two different runs in CRESST-III, in the following called Run35 and Run36. In

Run35 the crystals were kept in a Cu housing, covered in scintillating foil and held by $CaWO_4$ sticks. In Run36 the foil was removed and the holding sticks replaced with Cu sticks. The comparison of all spectra is shown in fig. 7.28. Included are the spectra of the phonon channels of the sapphire crystals in both runs and the light channel of the *Sapp2* module in the current run (Run36).

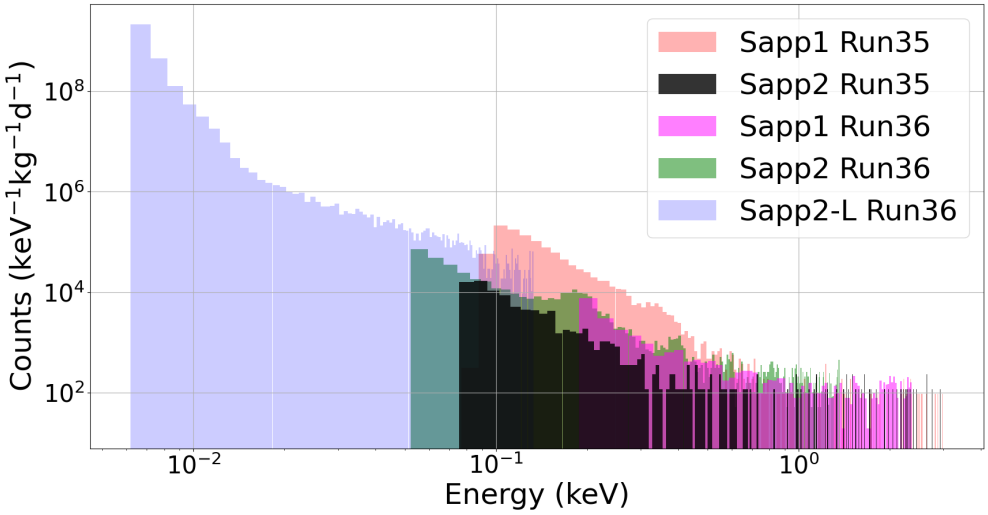

Figure 7.28: Comparison of different sapphire crystals in two different runs. *Sapp1* (red) and *Sapp2* (black) were measured with identical designs in Run35. Both modules had identical changes to their designs and were used again in Run36: *Sapp1* (magenta) and *Sapp2* (green). The light channel of *Sapp2* (blue) is analyzed as an individual detector in Run36. The binning of the histograms is chosen to match the energy resolution at threshold of each detector. All spectra are scaled by the respective measuring times and detector masses. Additionally they are corrected by their individual signal survival probabilities.

Comparison within Run35: Both modules have an identical design. A remarkable difference in the rate can be seen in Run35, in which *Sapp1* shows a much higher rate in the LEE than *Sapp2*.

Comparison within Run36: The modules have again an identical design within Run36. The phonon channels of *Sapp1* and *Sapp2* have very closely matching spectra in their common energy range (defined by the higher threshold of *Sapp1*). The shape of the *Sapp1* spectrum seems to follow very well the shape of the peak in *Sapp2* at about 190 eV. The energy spectrum of the light channel of *Sapp2* only has an overlap with the phonon channel of *Sapp2* in the range between about 52 eV to 130 eV. The light channel shows a much higher rate than the phonon channel, when they are scaled with the mass of the

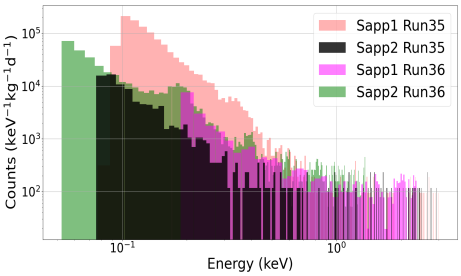

(a) Comparison of all phonon channels.

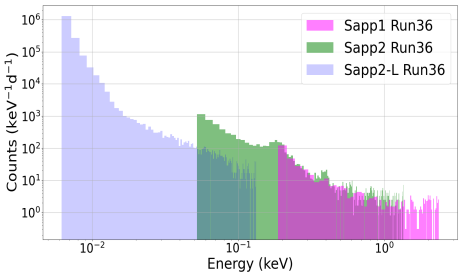

(b) Comparison of all spectra analyzed in Run36 (this work), scaled only by the measuring time.

Figure 7.29: Comparisons of the rates of a) only the phonon channels between Run35 and Run36 and b) of the rates of all sapphire detectors analyzed in Run36 scaled only by the measuring time. All spectra are corrected by their corresponding survival probabilities.

crystals and the measuring time, but a lower rate when only scaled by the measuring time, shown in fig. 7.29b.

Comparison between Run35 and Run36: The comparison of the phonon channels between the two different runs is shown in fig. 7.29a. Comparing the behaviour of a crystal in two subsequent runs, *Sapp1* has a much higher threshold in Run36. The rate in the energy range above this threshold decreased by removing the scintillating foil and $CaWO_4$ holding sticks. On the other hand, *Sapp2* has a lower threshold in Run36 and a slightly increased rate compared to Run35.

Conclusions: The removal of the scintillating foil and the change from $CaWO_4$ to Cu of the holding sticks of the crystals had completely opposite effects on the rate in the two compared crystals. Moreover, the LEE is still present in both detectors after this change. This motivates that neither the foil, nor the scintillating holding sticks can be a major source of the excess events. The spectra of the phonon channels match each other in Run36. This could potentially mean that the differences between the two crystals in Run35 were caused by the scintillating surroundings (foil and sticks).

7.5.2 LEE in sapphire

The following sections will concentrate on the spectrum of the *Sapp2* phonon channel in particular, starting with a detailed investigation of the time, temperature and energy dependencies of the LEE in Run36. The data is divided into four datasets, the first three following the same definition and naming convention as defined in sec. 6.2 (**BCK**, **PostCal**, **AWU**). The definition of the AWU dataset is extended from days 495-670 after the first cool down of the cryostat up to 686 days, including now also a warm up to a temperature of 3K. Additionally, a warm up test to 30K was performed. The dataset

following this test are called **AWU2**, including days 732-782 after the first cool down. Figure 7.30 shows the summed spectrum of all four datasets, corrected by the survival probability and scaled by detector mass and total measuring time. In addition to the peak seen at about 190 eV, a second bump at about 400 eV can be seen. Both of these features will be discussed in more detail in sec. 7.5.3.

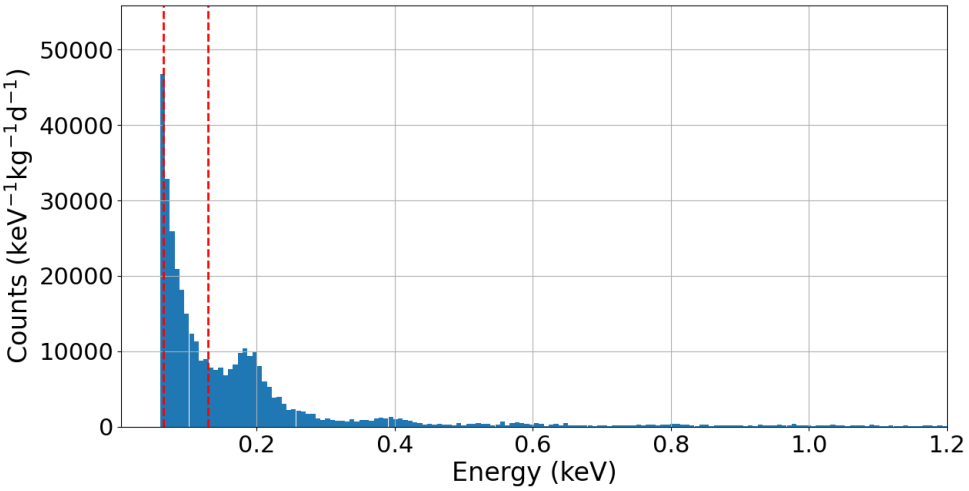

Figure 7.30: Summed spectrum of all datasets (BCK, PostCal, AWU, AWU2) with 7 eV bins, scaled by the total measuring time and detector mass and corrected by the signal survival probability. The event rate in the energy range from 65 to 130 eV, marked by the red lines, is studied in more detail in sec. 7.5.2.1.

7.5.2.1 Time dependence of the rate

The energy range considered for this analysis from 65eV to 130eV is marked by the red dashed lines in fig. 7.30. The rate of events in this range over the time of all four datasets defined above is shown in fig. 7.31.

The decay of the rate over time during the BCK, PostCal and AWU datasets was already covered in sec. 6.2.3. The additional data include a warm up of the cryostat to 3K. Like the other tests with lower temperatures before (600mK and 200mK), this warm up had no effect on the rate and is therefore included in the AWU dataset. Afterwards the cryostat was warmed up to a temperature of 30K, which led to an increase in the rate and a subsequent fast decay (AWU2), similar to the observation after the warm up to 60K. The time period covering all warm up tests is shown in fig. 7.32, where fits of the two datasets with an exponential function and a flat component $R(t) = C + A \cdot exp(-t/\tau)$ are overlayed to the data points. The extracted fit parameters are shown in tab. 7.6.

The decay time of the rate during the AWU dataset of about 18 days is compatible with the mean decay time that was found in sec. 6.2.3. After the 30K warm up the increased rate decays even faster, with a decay time of only 7 days. Considering only

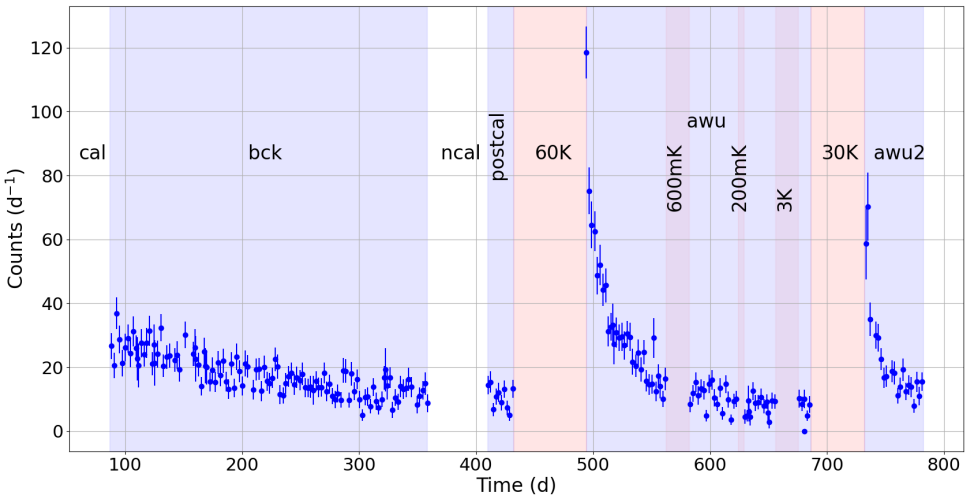

Figure 7.31: Rate of events between 65eV and 130eV over time since the first cool down of the cryostat (day 0). Each datapoint shows the number of events in a single file ($\sim$ 50h), corrected by the signal survival probability and measuring time. The datasets BCK, PostCal, AWU and AWU2 are marked in blue, the periods of warm up tests are marked in red and labeled with the corresponding temperatures the cryostat was warmed up to. The data of the gamma and neutron calibration datasets (CAL and NCAL) are not included.

Table 7.6: Fit parameters of the fits of the decaying rates during the AWU and AWU2 datasets shown in fig. 7.32.

Parameter	AWU	AWU2
Constant C (d^{-1})	10.00 ± 0.90	13.57 ± 1.72
Amplitude A (d^{-1})	94.36 ± 4.75	55.05 ± 4.72
Decay time τ (d)	18.22 ± 1.38	7.01 ± 1.38

the warm up test to 60K and 30K, the amplitudes of the increased rate seem to scale with the temperature of the warm up. No effect can be seen after the warm up tests to temperatures below 3K. This could have different interpretations:

- The effect only appears above a threshold temperature that lies somewhere between 3K and 30K
- The scaling of the increased rate with the temperature of the warm up is not linear
- The rate could be scaling with the amount of time spend above a certain threshold temperature during the warming up and subsequent cooling down of the cryostat rather than the maximum temperature the cryostat reached during the process
- The observed scaling shown above might be coincidental

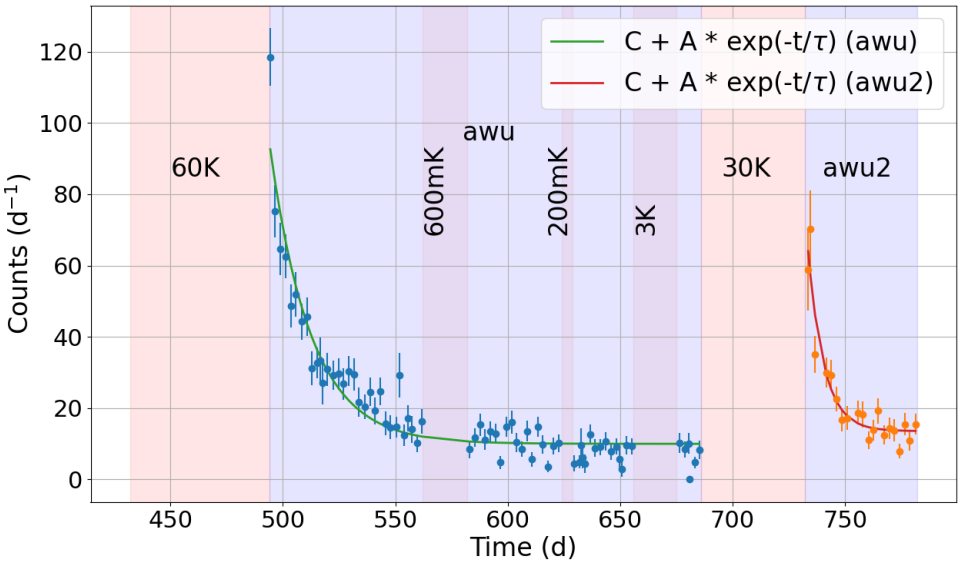

Figure 7.32: Rate of events between 65eV and 130eV over time for all warm up tests. Each datapoint shows the number of events in a single file ($\sim$ 50h), corrected by the signal survival probability and measuring time. Only the data of AWU (blue) and AWU2 (orange) are included. A fit of an exponential function and a flat component are shown for the AWU data (green) and AWU2 data (red) separately. The fit parameters are summarized in tab. 7.6.

To get a more clear picture, more tests are being performed. To disentangle the hypotheses listed above two kinds of tests are needed: 1) Warm up tests to different temperatures and 2) Warm up tests to the same temperature but with different time periods of keeping the cryostat warm.

The flat component in both fits is comparable. Furthermore it matches the level of the rate during the PostCal dataset. This raises the question if the LEE could consist of different components. One long living component, describing the slow decay of the rate over the course of the BCK and PostCal datasets and a second component with a much faster decay time, sitting on top of the slow component, which becomes visible after warming up the cryostat. It is possible that a fast decay of the LEE rate also happened at the very beginning of the run, directly after the first cool down of the cryostat. Since this phase corresponds to the commissioning of detectors, this information is not available.

To investigate the hypothesis of the excess being composed of one long living component and two short living components after the warm up tests, the data shown in fig. 7.31 are fit with a combination of three exponentials, one covering the entire length of

the datasets, while the other two have an onset, t_1 and t_2, directly after the warm up tests to 60K and 30K respectively:

$$A(t) = C + A_0 \cdot e^{\frac{-t}{\tau_0}} + A_1 \cdot e^{\frac{-(t-t_1)}{\tau_1}} \cdot \Theta(t-t_1) + A_2 \cdot e^{\frac{-(t-t_2)}{\tau_2}} \cdot \Theta(t-t_2) \tag{7.10}$$

This fit is performed with and without a flat component, C. The resulting fits are shown in fig. 7.33, the extracted fit parameters are summarized in tab. 7.7.

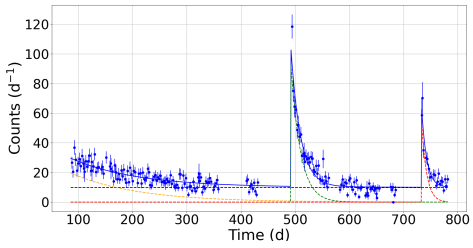

(a) Fit including a flat component (χ^2_{red}=1.65).

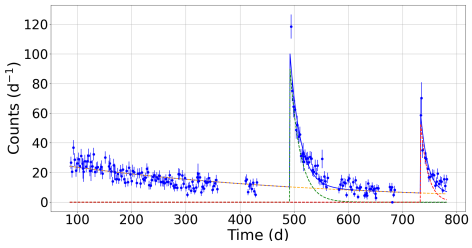

(b) Fit without a flat component (χ^2_{red}= 2.00).

Figure 7.33: Fit of the decaying rate of the LEE with eq. 7.10 in a) with a flat component, C, and b) without a flat component. The fit parameters can be seen in tab. 7.7.

Table 7.7: Fit parameters from the fit of eq. 7.10 to the decaying rate during all datasets, shown in fig. 7.33.

Parameter	with flat component	without flat component
Amplitude A_0 (d^{-1})	39.73 ± 5.64	29.08 ± 1.41
Decay time τ_0 (d)	122.6 ± 18.2	473.1 ± 41.4
A_1 (d^{-1})	94.45 ± 3.83	92.03 ± 3.99
τ_1 (d)	17.79 ± 1.02	19.12 ± 1.18
A_2 (d^{-1})	55.51 ± 3.75	54.78 ± 3.61
τ_2 (d)	9.31 ± 1.15	13.52 ± 1.51
Constant C (d^{-1})	9.95 ± 0.72	-
χ^2_{red}	1.654	2.001

Including a flat component has a marginal influence on the parameters of the amplitudes of the two exponentials describing the increased rate in the AWU and AWU2 datasets. The amplitudes are compatible with the fit results of the individual fits shown above in tab. 7.6. The decaytime of the rate during the AWU dataset matches the one of the individual fit within the uncertainties, while the decaytime during the AWU2 dataset is slightly increased. The fit finds an even slower decaytime if no flat component is included, but both decaytimes are in the same order of magnitude as the individual fit result in tab. 7.6. The slow component, which is fit over the duration of all datasets, is strongly influenced by the inclusion of a flat component in the fit. While the amplitude of

the exponential is comparable in both fits, the decaytime varies from 123 days (including a flat component) to 473 days (without the flat component). Overall, the fit performs better including the flat component, leading to a lower χ^2_{red}.

7.5.2.2 Time dependence of the spectral shape

To disentangle the influence of different components of the LEE, the shape of the spectrum is described by a parametric model. The best performance is achieved with the following parameterization:

$$R(E) = \left(C + A \cdot e^{-E/\lambda} + B \cdot E^{-k} + \sum_{i=1,2} \frac{D_i}{\sqrt{2\pi}\sigma_i} \cdot e^{-\frac{1}{2}\left(\frac{E-\mu_i}{\sigma_i}\right)^2} \right) \cdot \Theta(E - E_{thr}) \qquad (7.11)$$

The two Gaussian functions (green) are used to describe the peaks visible at around 190eV and around 400eV. The constant (blue) represents the flat part of the spectrum, mostly visible at energies above the LEE and the peaks. The combination of an exponential (red) and a power law function (orange) is used for the parameterization of the LEE. While other combinations (single exponential, single power law, two exponentials, two power laws) have been tested, this leads to the lowest value of χ^2_{red}. For all results presented in this section, eq. 7.11 is used to describe the spectrum.

In fig. 7.34 the fit of the summed spectrum of all datasets is shown, the fit results are listed in tab. 7.8.

Table 7.8: Fit parameters from the fit of eq. 7.11 to the summed spectrum of all datasets, shown in fig. 7.34.

Parameter	Fit result
A ($\mathrm{keV^{-1}kg^{-1}d^{-1}}$)	26626 ± 2483
λ (keV)	0.091 ± 0.004
B ($\mathrm{keV^{-(1-k)}kg^{-1}d^{-1}}$)	0.398 ± 0.192
k	4.02 ± 0.16
D_1 ($\mathrm{kg^{-1}d^{-1}}$)	304.5 ± 10.7
μ_1 (eV)	187 ± 1
σ_1 (eV)	20.1 ± 0.6
D_2 ($\mathrm{kg^{-1}d^{-1}}$)	32.4 ± 7.4
μ_2 (eV)	392 ± 5
σ_2 (eV)	20.1 ± 4.9
C ($\mathrm{keV^{-1}kg^{-1}d^{-1}}$)	204 ± 24

To investigate the time dependence of the individual components, the entire length

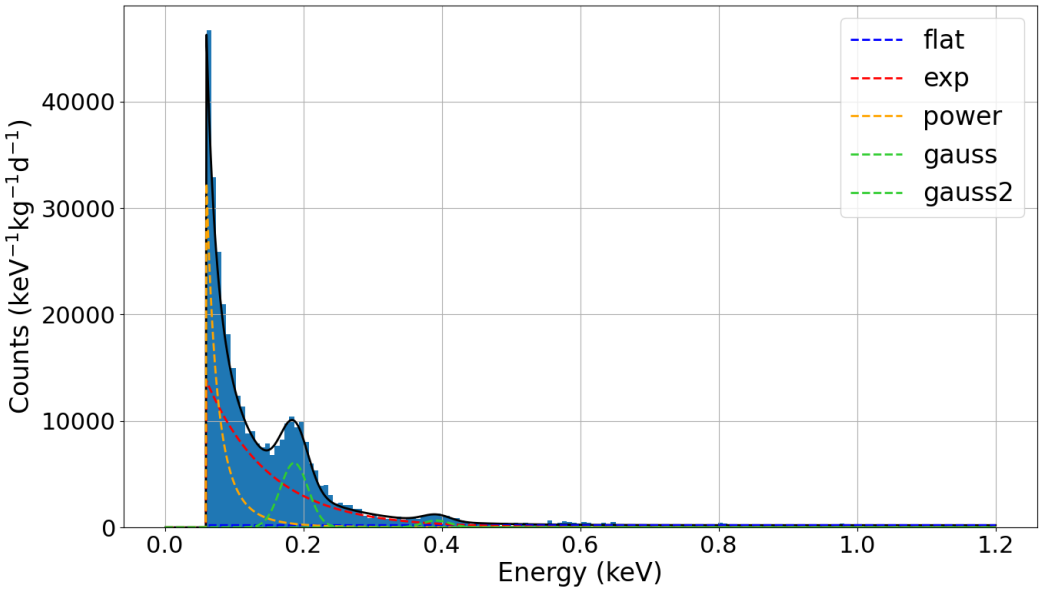

Figure 7.34: Fit of eq. 7.11 to the summed spectrum of all datasets. The fit parameters are listed in tab. 7.8.

of all datasets (BCK, PostCal, AWU and AWU2) is split into 36 roughly equally sized datasets, with each corresponding to about 2 weeks of data taking. The corresponding energy spectra are corrected by the measuring times, the detector mass and the survival probability during the respective time period. A fit of eq. 7.11 is then performed for every individual spectrum. The positions and resolutions of the two peaks, μ_1, μ_2, σ_1 and σ_2, as well as the shape parameters of the two components (exponential and power law) describing the LEE, λ and k are fixed at the fit values obtained from the summed spectrum (shown in tab. 7.8). The amplitudes (scalings) of all components, A, B, C, D_1 and D_2, are free parameters for the individual fits. The time dependent behaviour of these amplitude parameters is shown in fig. 7.35. The dashed lines and shaded areas in the plots show the fit value and uncertainty of the respective parameter extracted from the fit of the summed spectrum.

The parameter C, describing the flat component of the spectrum above the LEE does not show any time dependence, as can be seen in fig. 7.35c. The individual spectra have much less statistics than the summed spectrum, leading to the larger error bars. The time dependencies of the parameters D_1 and D_2 will be discussed in sec. 7.5.3. The behaviour of the amplitude A (fig. 7.35a) of the exponential term clearly deviates from the fit value of the summed spectrum. The amplitude of the amplitude B of the power law term is highly correlated with the shape parameter k, leading to the large uncertainties in the summed fit. In contrast to this, the individual fits of the 36 spectra, in which k is fixed,

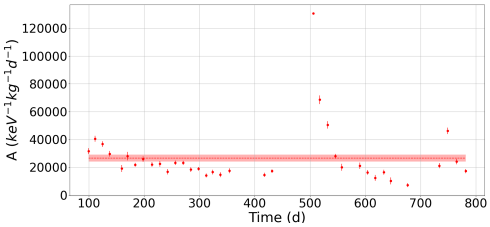

(a) Amplitude of the exponential component, A.

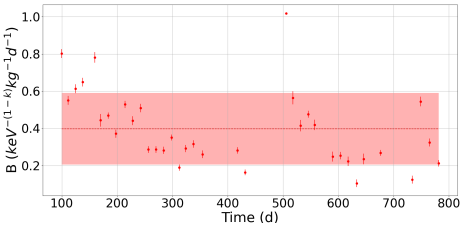

(b) Amplitude of the power law component, B.

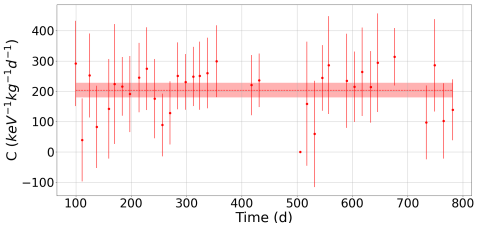

(c) Constant component, C.

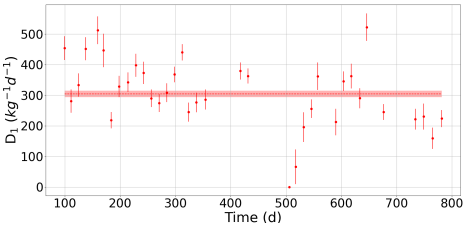

(d) Amplitude of the first Gaussian component, D_1.

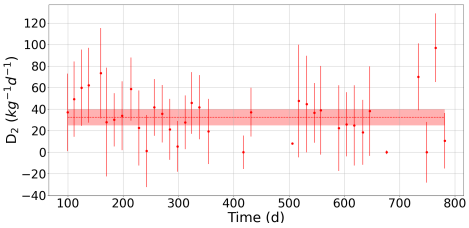

(e) Amplitude of the second Gaussian component, D_2.

Figure 7.35: Fit results of the amplitude parameters a) A, b) B, c) C, d) D_1 and e) D_2 in eq. 7.11 as a function of time. Each datapoint is extracted from a fit of a spectrum containing about 2 weeks of data. The errorbars show the uncertainties of the fit results. The dashed constant lines and red shaded areas show the fit results and uncertainties of the parameters from the fit of the sum of all spectra, shown in fig. 7.34.

lead to much smaller uncertainties on B. The behaviour of the amplitude parameter B is not incompatible with the fit value of the summed spectrum within the uncertainties. Nevertheless, a time dependent behaviour can also be recognized for this parameter (fig. 7.35b). Moreover, the time dependencies of both parameters, A and B, resembles the same behaviour as the one seen in the rate (fig. 7.31 and 7.33), which is expected for at least one of the amplitude parameters, A or B. The deviation of the amplitude of the exponential term, A, from the constant value obtained in the summed fit is much more pronounced than the one of the power law term, B. Looking at the fits of the individual spectra it can also be seen how the exponential component, which mostly describes the tail of the LEE to higher energies, is strongly influenced by the warm up tests. For a comparison, fig. 7.36 shows the spectra and fits of one of the first subsets of the BCK

dataset, where the power law component has a dominant contribution to the total rate, and one of the first subsets of the AWU dataset, in which the exponential component completely takes over.

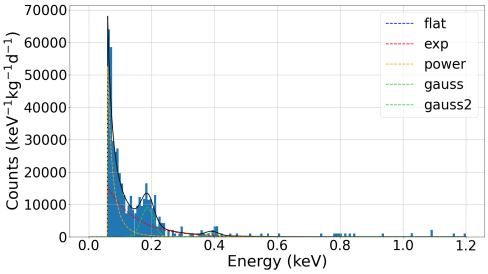

(a) Fit of a subset of the BCK dataset, in which the power law has a dominant contribution to the total rate.

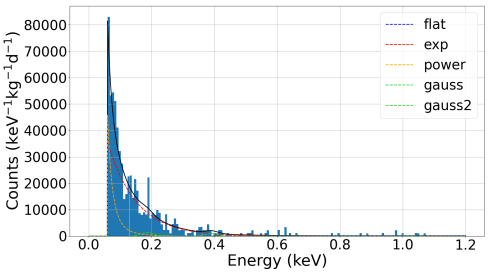

(b) Fit of a subset of data early in the AWU dataset, in which the effect of the 60 K warm up is strongly present.

Figure 7.36: Comparison of the fit of two individual spectra, a) the first one during the BCK dataset and b) the second one early in the AWU dataset.

To explore the difference between these components, the time dependence of $A(t)$ and $B(t)$ are described analytically with a combination of three exponentials and a flat component, like in eq. 7.10, with one exponential covering the entire length of the datasets with amplitude A_{bck} and decaytime τ_{bck}, while the other two have an onset, t_{awu} and t_{awu2}, at the beginning of the AWU and the AWU2 dataset, respectively with amplitudes A_{awu} and A_{awu2} and decay times τ_{awu} and τ_{awu2}. Again, the fit is performed once including a flat component, and once without it. The time dependencies of parameters $D_1(t)$ and $D_2(t)$ will be covered in the next section.

The resulting plots for $A(t)$ can be seen in fig. 7.37, the fit parameters are listed in tab. 7.9. The fit performs better, when a flat component is included in the model. For the following calculations, the fit of $A(t)$ including a constant C will be used.

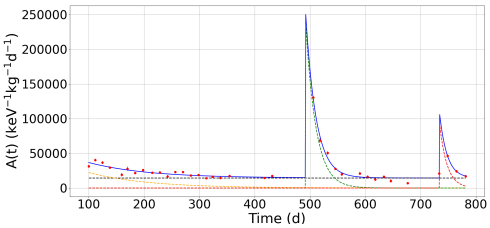

(a) Fit including a flat component (χ^2_{red}=4.41).

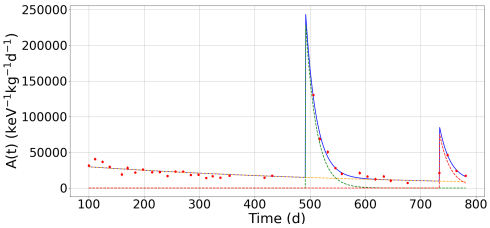

(b) Fit without a flat component (χ^2_{red}= 6.67).

Figure 7.37: Fit of the time dependent behaviour of the parameter $A(t)$ with eq. 7.10 in a) with a flat constant, C, and b) without a flat component. The fit parameters can be seen in tab. 7.9.

Table 7.9: Fit parameters from the fit of eq. 7.10 to the time dependence of the parameter $A(t)$, shown in fig. 7.37.

Parameter	with flat component	without flat component
A_{bck} ($\mathrm{keV^{-1}kg^{-1}d^{-1}}$)	56973 ± 17203	35528 ± 3252
Decay time τ_{bck} (d)	106.7 ± 28.7	566.2 ± 104.2
A_{awu} ($\mathrm{keV^{-1}kg^{-1}d^{-1}}$)	238120 ± 18142	231108 ± 20842
τ_{awu} (d)	18.75 ± 1.45	19.52 ± 1.82
A_{awu2} ($\mathrm{keV^{-1}kg^{-1}d^{-1}}$)	94408 ± 39229	76923 ± 24392
τ_{awu2} (d)	13.46 ± 4.61	19.69 ± 6.45
C ($\mathrm{keV^{-1}kg^{-1}d^{-1}}$)	14448 ± 1522	-
χ^2_{red}	4.407	6.669

The same procedure is done for the fit of the parameter $B(t)$. The amplitudes of the three exponentials describing the time dependence are named B_{bck}, B_{awu} and B_{awu2}. The fits are shown in fig. 7.38, the resulting fit parameters are listed in tab. 7.10. In this case both fits return a rather high χ^2_{red}. Still, the fit including a flat component performs slightly better and will therefore be used for further calculations.

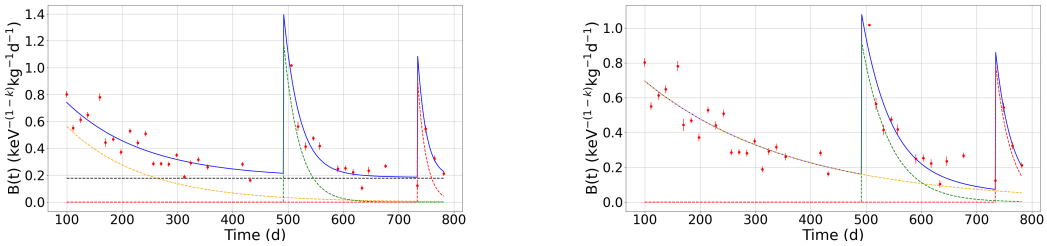

(a) Fit including a flat component (χ^2_{red}=15.61). (b) Fit without a flat component (χ^2_{red}= 17.35).

Figure 7.38: Fit of the time dependent behaviour of the parameter $B(t)$ with eq. 7.10 in a) with a flat constant, C, and b) without a flat component. The fit parameters can be seen in tab. 7.10.

At this stage, all time dependencies of the amplitude parameters are known and can be inserted into eq. 7.11:

$$R(E,t) = \left(C + A(t) \cdot e^{-E/\lambda} + B(t) \cdot E^{-k} + \sum_{i=1,2} \frac{D_i(t)}{\sqrt{2\pi}\sigma_i} \cdot e^{-\frac{1}{2}\left(\frac{E-\mu_i}{\sigma_i}\right)^2} \right) \cdot \Theta(E - E_{thr}) \tag{7.12}$$

To analytically describe the rate in a defined energy range as a function of time, the

Table 7.10: Fit parameters from the fit of eq. 7.10 to the time dependence of the parameter $B(t)$, shown in fig. 7.38.

Parameter	with flat component	without flat component
B_{bck} ($keV^{-1}kg^{-(1-k)}d^{-1}$)	1.139 ± 0.235	1.011 ± 0.118
Decay time τ_{bck} (d)	141.6 ± 35.9	267.1 ± 40.4
B_{awu} ($keV^{-1}kg^{-(1-k)}d^{-1}$)	1.190 ± 0.230	0.922 ± 0.136
τ_{awu} (d)	28.36 ± 7.08	51.53 ± 11.5
B_{awu2} ($keV^{-1}kg^{-1}d^{-1}$)	0.925 ± 0.633	0.799 ± 0.312
τ_{awu2} (d)	15.59 ± 9.90	28.20 ± 13.71
C ($keV^{-1}kg^{-1}d^{-1}$)	0.179 ± 0.044	-
χ^2_{red}	15.606	17.346

equation above has to be integrated over that energy range. So the time dependent rate between 65eV and 130eV, as shown in fig. 7.31, can be expressed as:

$$R(t) = \int_{65eV}^{130eV} R(E,t)dE \tag{7.13}$$

This can be compared to the observed rate and to the empirical fit of the rate as shown in fig. 7.33. The comparison of the empirical fit of the decaying rate and the analytically calculated integral above can be seen in fig. 7.39. As expected, the calculated rate $R(t)$ describes the behaviour of the measured rate quite well. The χ^2_{red} = 1.667 of $R(t)$ is also very close to the one of the empirical fit of χ^2_{red} = 1.654, confirming that the chosen parameterization leads to a good description of the data. As already mentioned before, the calculation of $R(t)$ is based on both $A(t)$ and $B(t)$ including a flat component respectively. Not including the flat component in the exponential amplitude $A(t)$ leads to a higher value of χ^2_{red} for the comparison between $R(t)$ and the data. Not including the flat component in the power law amplitude $B(t)$ actually leads to a lower value of χ^2_{red} = 1.588. Nevertheless, since the fit of $B(t)$ with eq. 7.10 performed better by including a flat component, all following plots will be based on $B(t)$ including a constant term.

Impact of single components: In the following, the influence of the different components on the LEE at different energy ranges will be investigated, as well as the impact of the warm up tests on the individual components. Figure 7.40 shows the contribution of all components to the total rate in different energy ranges. As can be seen in fig. 7.34, the power law component mostly describes the sharp rise directly in the first few eV above the threshold. It is therefore not surprising that in the energy range between 59 eV and 75 eV the power law is the dominant component of the total rate for most of the duration of all datasets. During the periods of the increased rate of the AWU and AWU2

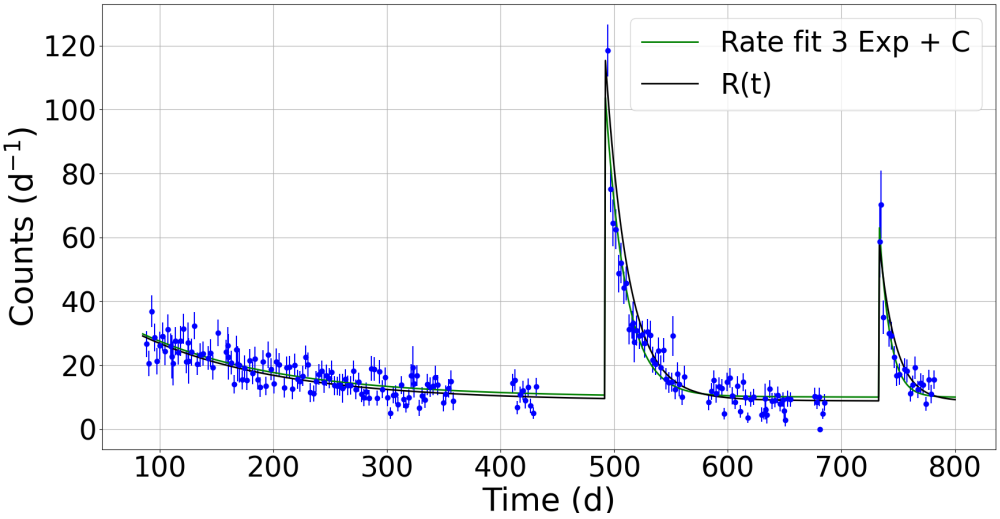

Figure 7.39: Comparison of the empirical fit of the rate with eq. 7.10 (green) and the analytically calculated integral in eq. 7.13 (black).

datasets, the exponential and power law components become comparable, showing the strong influence the warm up tests seem to have on the exponential component. This becomes also visible in the energy range between 65 eV and 130 eV. For most of the time, the contribution of both components to the rate of the LEE is comparable. Right after the warm up tests to 60 K and 30 K, the exponential component becomes completely dominant. Further away from the threshold, from 100 eV to 140 eV, the power law only contributes minimally to the total rate.

Observations and conclusions about the LEE in sapphire:

- The exponential component is strongly influenced by the warm up tests
- The impact of a warm up on the power law component is less pronounced compared to the fit value of the summed spectrum
- The power law component is very prominent at energies directly above the energy threshold
- The exponential component is more prominent further away from the threshold
- The exponential component of the energy spectrum contains a component that is not decaying over time
- It is not possible to conclude if the power law component of the energy spectrum contains a constant component over time or not

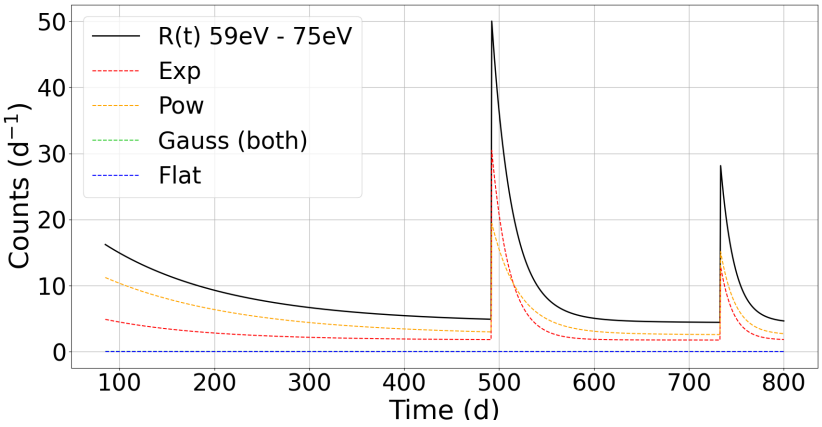

(a) Influence of components to the total rate between 59 eV and 75 eV.

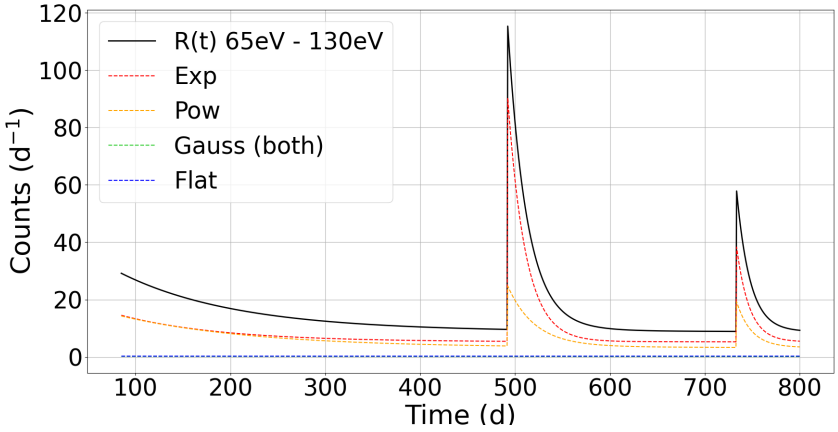

(b) Influence of components to the total rate between 65 eV and 130 eV.

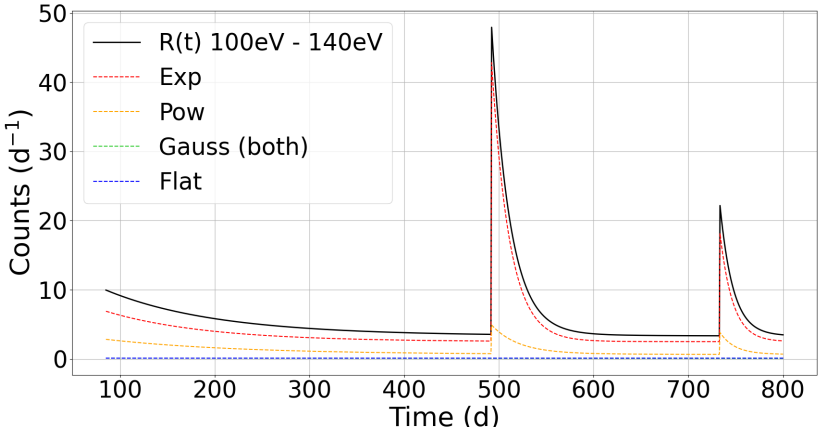

(c) Influence of components to the total rate between 100 eV and 140 eV.

Figure 7.40: Impact of single components to the total rate in different energy ranges. a) Close to the threshold (59eV - 75eV) the power law is mostly dominant, except for the time periods right after the warm up tests, b) Slighty above threshold (65eV - 130eV), the power law and exponential have mostly equal contributions, except for the time periods right after the warm up tests, in which the exponential becomes dominant, c) Further away from the threshold (100eV - 140eV), the power law component has only very little influence on the total rate.

Despite no physical explanations about the LEE origin could be found so far, its empirical description by a combination of a power law and an exponential term nicely describes the observed features. In the studies presented above, it is shown that both components react differently to the warm up tests of the cryostat and have different impacts on the total rate of the excess.

One important conclusion is that both components do not behave like a standard dark matter signal, following the same arguments as already laid out in sec. 6.3. The strongest point against a dark matter hypothesis is the increase of the rate after a warm up of the cryostat.

The exponential component, which describes mostly the region starting from a few eV above the energy threshold up to higher energies, is strongly influenced by the warm up tests to 60 K and 30 K. The fast decay times of this component during the AWU and AWU2 datasets match the decay times of the rate very well. This could hint towards a temperature induced stress on the detector, which could originate from the holding of the crystals or the sensor film on the crystal. A constant term in the description of the time dependence of this exponential component $A(t)$ in this context would suggest that the crystal is always under a minimal amount of stress leading to a constant number of events over time.

The power law component, describing mostly the high number of events in the first few eV above the energy threshold, is affected more weakly by the warm up tests and shows slower decay times in the AWU and AWU2 datasets, compared to the exponential component. The slow decay of the rate over the entire dataset, which was found with a decay time of (122.6 $\pm$ 18.2) d by a fit of the rate in an energy range from 65 eV to 130 eV (fig. 7.33, tab. 7.7), is visible in both components. In this energy range, both components contribute equally to the total rate. The fact that the exponential component reacts stronger to warm up tests of the AWU and AWU2 datasets could point towards two different sources of the LEE events.

Lastly, a fit of the time dependent behaviour of the power law amplitude $B(t)$ performs better when a constant component is included. On the other hand, a comparison of the data with an analytical integration of the parametric description of the spectrum in the energy range from 65 eV to 130 eV leads to better results if no flat component is included in $B(t)$. Hence there is no clear conclusion whether the power law component has a constant contribution to the LEE or if it decays completely. This open point can possibly be answered after more data of the currently still ongoing measurements is analyzed.

Applying the method developed in this work to other modules has the potential to clarify a common nature of the excess in the different modules.

7.5.3 Investigation of the peaks

The position of the two peaks in the spectrum are found at (187 ± 1) eV and (392 ± 5) eV by the fit of the summed spectrum with the empirical description of eq. 7.11 (fit results listed in tab. 7.8). Both peaks have the same width (σ_1 = (20.1 ± 0.6) eV, σ_2 = (20.1 ± 4.9) eV). The count rate of the peak at 187 eV is found at (304.5 ± 10.7) 1/(kg d), while the rate of the peak at 392 eV is (32.4 ± 7.4) 1/(kg d). The position of the second peak is at roughly twice the energy of the first peak, but with only about 10% of the intensity. The time dependence of the parameters D_1 and D_2 was already shown in the fig. 7.35d and 7.35e. A fit of their slow decays with an exponential function can be seen in fig. 7.41.

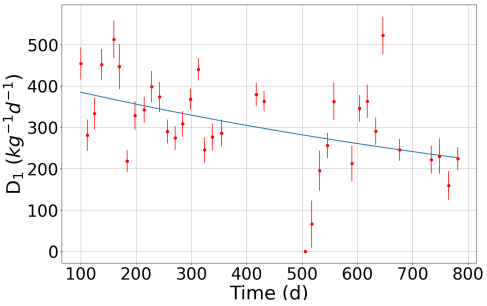

(a) The fit of the decay time of the rate within the peak at 187eV results in τ = (1285 ± 462)d.

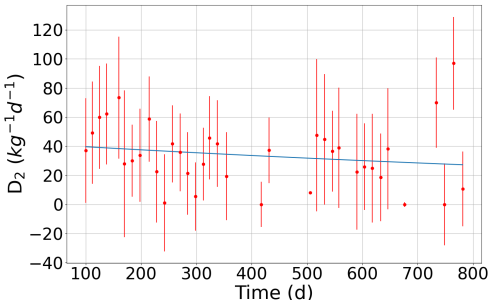

(b) The fit of the decay time of the rate within the peak at 392eV results in τ = (1819 ± 1799)d.

Figure 7.41: Fit of the decay time of the amplitude parameters describing the count rate within the peaks at a) 187 eV and b) 392 eV in the spectrum.

If the decay times of the peaks are converted into half-lifes, they result in $T_{1/2}$ = (2.439 ± 0.877) yr and $T_{1/2}$ = (3.452 ± 3.414) yr, respectively. The large uncertainty of the decay time of the peak at 392 eV is caused by the low number of counts in this peak, leading to large uncertainties of the parameter D_2. Therefore this decay time is not considered. The resulting half-live of the first peak at 187 eV appears in good agreement with the half-life of the ^{55}Fe calibration source, which has a value of $T_{1/2,Fe}$ = 2.737 yr [101]. This points towards the ^{55}Fe source as a possible origin of the events in the peaks.

Another connection to the ^{55}Fe source can be seen by looking at the coincidence of direct hits of calibration events in the light channel (i.e. events depositing ∼6 keV in the light channel), which lead to events in the phonon channel at an energy of about 200 eV. These events are removed by a cut on the OF RMS of the light channel, which can be seen in fig. 7.42. The events shown in black are removed by the cut and only the events in red survive and end up in the final spectrum. The coincidence events of direct hits in the light channel can therefore not be cause of the peaks, but since they lead to energies of roughly the right energy, this could mean that the surviving events are the result of direct hits of the ^{55}Fe source of some non-instrumented part of the detector module.

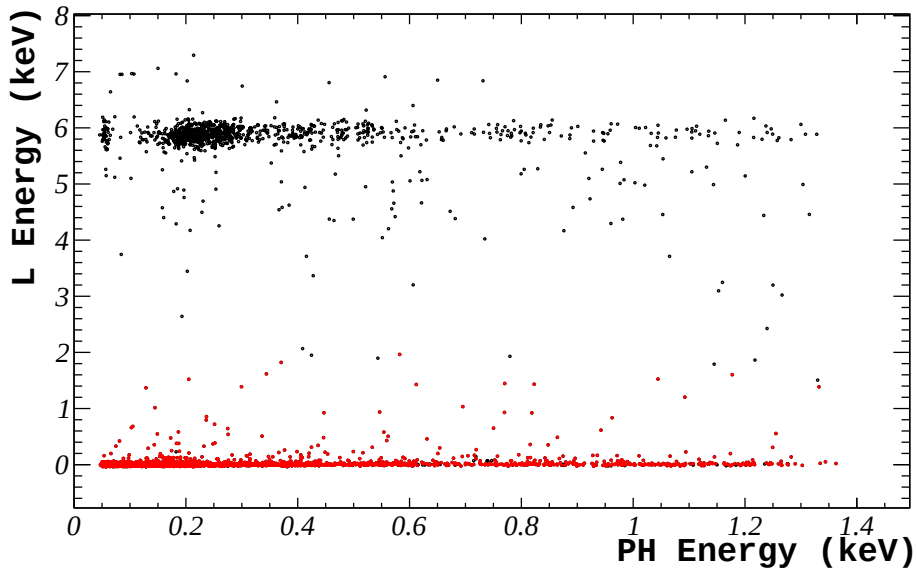

Figure 7.42: A large fraction of direct hits of the ^{55}Fe source in the light channel, shown in black, coincide with events with an energy of about 200eV in the phonon channel. After a cut on the OF RMS these events are removed and only the events shown in red survive and enter the final spectrum.

A close-up picture of the events surviving all cuts and the final spectrum can be seen in fig. 7.43. A high number of events without a coincidental signal in the light channel is left forming the peak at 187 eV and to a lesser extend the small peak at 392 eV. While the fact that a large fraction of the direct hits in the light channel lead to coincident events at roughly the right energy of the first peak in the phonon channel can be interpreted as another hint of a connection with the ^{55}Fe source, the fact that most of the events forming the peaks have no signal in coincidence in the light channel suggests that the underlying process that leads to the peak in the final spectrum is probably not happening inside the light detector, but rather somewhere in the surroundings of the detector or in the main absorber (phonon channel) itself, leaving coincident events in both detectors only in rare cases, shown in green in fig. 7.43b.

As the underlying process leading to the peaks could be in the main absorber itself, a waiting time analysis is performed, looking for any correlations between the direct hits of ^{55}Fe events in the main absorber and the events in the first peak. The time difference of each event in the peak at 187 eV to the closest preceding ^{55}Fe event is extracted and collected into a histogram, which is shown in fig. 7.44.

The histogram does not show any correlation between events from the calibration source in the main absorber and events forming the peak at 187 eV. This leads to the conclusion that the events must originate from somewhere outside of the main crystal.

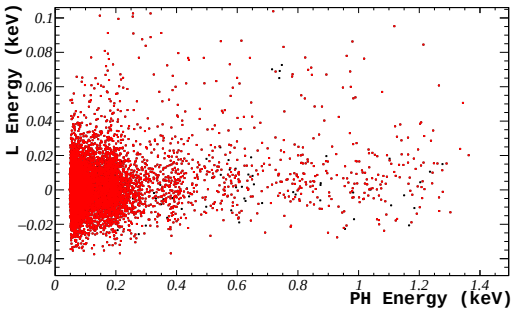

(a) Close up of the surviving events after a cut on the OF RMS. Clusters of events at the positions of the two peaks at 187eV and 392eV are clearly visible.

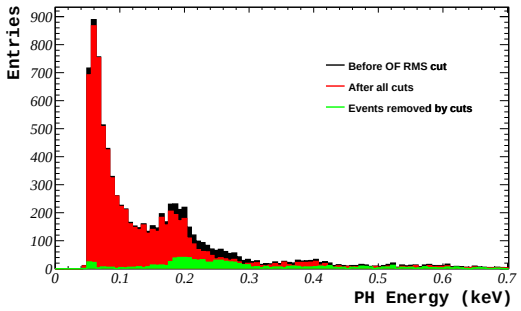

(b) Shown in red is the final spectrum after the OF RMS cut, in black the spectrum before the cut and in green the events removed by the cut.

Figure 7.43: The OF RMS cut only removes a small number of events in the energy region around 200 eV. The surviving events form the peaks in the phonon channel, with the peak at 187eV being much more pronounced. The surviving events have no coincident signal in the light channel.

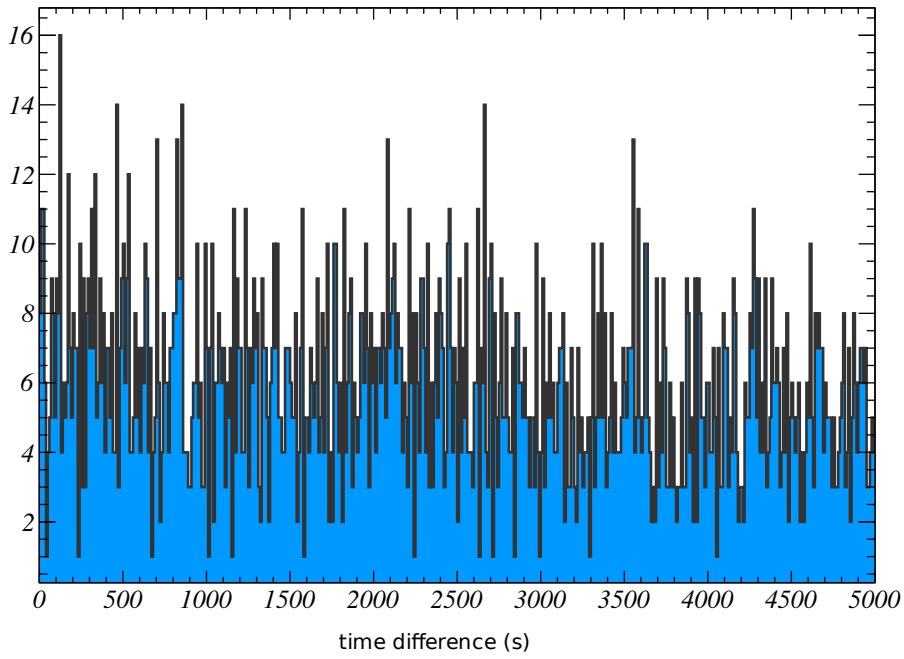

Figure 7.44: A waiting time analysis between events in the 187 eV peak and the ^{55}Fe events in the main aborber shows no correlation between these two types of events. The entries of this histogram show the time difference in seconds of a peak event to the closest preceding ^{55}Fe event.

Possible sources: The detector crystals (both main absorber and light detector) can be excluded as an origin of the events forming the peaks because, as already mentioned, only a small fraction of the events in the peak are in coincidence with a signal in the light channel. Additionally, no correlation to the calibration events in the main absorber

could be found. Other possible sources could lie in the surroundings of the detector. The housing and holding sticks both consist of pure Cu. The ^{55}Fe source is covered by a layer of glue and a thin layer of Au. The main purpose of the glue, apart from fixing the calibration source, is the reduction of Auger electrons. The Au layer is supposed to prevent possible scintillation light from the glue to reach the detector[3].

Possible processes: Three main hyptotheses have been considered as a possible origin of the peak events:

- Compton scattering of ^{55}Fe events in the detectors or in surrounding materials.
- X-rays induced by the excitation of surrounding materials with the radiation of the ^{55}Fe source.
- Scintillation light formed by ^{55}Fe irradiation of some surrounding material.

Compton scattering: The energy of a photon in a Compton scattering process is described by:

$$E_{\gamma}^{'} = \frac{E_{\gamma}}{1 + \frac{E_{\gamma}}{m_e c^2}(1 - \cos\theta)} \tag{7.14}$$

with E_{γ} being the incident energy of the photon and $E_{\gamma}^{'}$ the energy of the photon after the scattering process. The compton edge corresponds to the maximal energy a gamma particle can deposit in the detector material during a compton scattering process, corresponding to a scattering angle θ of 180°. In the case of the ^{55}Fe source, the compton edge corresponding to the 5.89 keV line would be expected at an energy of 133 eV and the compton edge corresponding to the 6.49 keV line at an energy of 161 eV. These energies both lie below the observed peaks at 187 eV and 392 eV. Simulations performed by the CRESST simulation group could also confirm that any effects due to compton scattering in the detector crystals would be expected at energies below the observed peaks.

In the case of Compton scattering outside of the detector material, the outgoing scattered gamma particle might reach the detector with a reduced energy, leading to a backscatter peak at $E_{back} = E_{\gamma,max}^{'}$, which in the case of the ^{55}Fe source would be expected at the energies 5.76 keV and 6.33 keV for the lines at 5.89 keV and 6.49 keV respectively.

Compton scattering can therefore be excluded as a possible explanation for the origin of the observed peaks.

[3]Typically, epoxy resins have scintillating properties.

X-rays: Another possibility would be the excitation of the surrounding materials by the irradiation with the ^{55}Fe source leading to the emission of X-rays. The materials most abundant in the detector modules is the Cu of the housing and the holding sticks, as well as the crystal material itself, in this case Al_2O_3. Other materials that experience a direct irradiation with the calibration source are the epoxy glue and the Au layer covering the source. All emission lines with energies higher than the maximum energy emitted by the calibration source, in this case 6.49 keV, cannot be excited and can therefore be excluded. Of all materials listed above, none has emission lines that match the energies observed in the peaks [135]. The only material that has a line matching the peak at 187 eV is B ($K\alpha_1$ line at 183.3 eV). A high enough contamination with B in the surrounding materials to explain the observed peak can be reasonably excluded. The only material matching the peak at 392 eV would be nitrogen ($K\alpha_1$ line at 392.4 eV). The epoxy glue surrounding the source indeed does contain nitrogen, but the main component of the chemical compounds in the epoxy glue is C. Assuming the X-rays emitted by nitrogen in the glue could reach the crystal, another peak with a higher intensity would be expected at 277 eV, originating from the $K\alpha_1$ line of C. Moreover, simulations performed by the CRESST simulation group could not reproduce the observed spectrum. Thus, an explanation of the peaks with X-rays seems unlikely.

Scintillation light: The scintillation of the sapphire crystals is too weak to explain the peaks at the observed energies. An open possiblity could be the emission of scintillation light from the complex chemical molecules of the epoxy glue. Gaps in the Au layer covering the glue and ^{55}Fe source would be necessary to explain scintillation light escaping the source. To verify this hypothesis, a dedicated measurement of the scintillating properties of the epoxy resin at low temperature would be required.

Conclusions: There are hints pointing to a connection of the peaks at 187 eV and 392 eV to the ^{55}Fe source. The strongest one being the matching decay time of the peaks with the half-life of the source. Moreover, some of the direct hits of ^{55}Fe events in the light channel lead to events of roughly 200 eV in the phonon channel in coincidence. The two most straight-forward explanations, Compton scattering and X-ray emission, could be excluded or seem rather unlikely. The emission of scintillation light from the epoxy glue could potentially be an explanation. This should be tested in a dedicated measurement.

7.6 Dark matter results

In the final section of this chapter the results of the dark matter analysis (high level analysis, see sec. 5.3) for the sapphire detectors analyzed in this work are presented.

Dark matter could already be excluded as a main contribution to the low energy excess. Hence, no positive analysis is performed on the data of the sapphire detectors. Instead, a standard exclusion limit on elastic spin-independent dark matter interactions is calculated with the Yellin optimum interval method (see sec. 5.3.1) with a confidence level of 90%. As explained in sec. 7.3, the light yield of sapphire crystals is too low to discriminate between the e^-/γ-band and nuclear recoil bands. Therefore, all events in the respective spectra are considered as potential signal events and are included in the calculation of the dark matter exclusion limits. The limits are calculated for the *Sapp1* and *Sapp2* phonon channels, as well as for the *Sapp2* light channel, denoted as *Sapp2-L*. The respective exposures and energy regions of interest (ROI) of the spectra used for the limit calculation are listed below in tab. 7.11. The lower boundary of the ROIs are defined by the energy threshold of the detectors, while the upper boundary is limited by the linearity of the detector. The masses of the detectors are calculated based on their dimensions and the density of sapphire.

Table 7.11: Masses and measuring times of the three sapphire spectra used for the limit calculation in this section.

Detector	Mass (g)	Measuring time (h)	Exposure (kg d)	ROI (keV)
Sapp1	15.9	3773	2.500	0.1876 - 1.9
Sapp2	15.9	5526	3.661	0.0522 - 1.2
Sapp2-L	0.6	5526	0.138	0.0062 - 0.13

The resulting dark matter exclusion limits for all detectors analyzed in this work are shown together in fig. 7.45.

Above a dark matter mass of 1 GeV/c^2, the limits calculated from the phonon channels of *Sapp1* and *Sapp2* match each other. In fig. 7.28 and 7.29 it can be seen that the spectra of these two detectors are very similar, causing the strong similarities of the exclusion limits at higher dark matter masses. At the highest masses (3 - 10 GeV/c^2), the *Sapp1* limit is slightly stronger than the one of *Sapp2*. This is partially caused by the ROI of *Sapp1* going to higher energies. Another reason are the peaks in the spectrum of *Sapp2* leading to a slightly higher count rate compared to *Sapp1*. Due to its higher energy threshold, the *Sapp1* detector looses sensitivity compared to *Sapp2* to masses below 1 GeV/c^2.

The extremely low threshold of the *Sapp2-L* detector allows to probe for dark matter masses down to 69 MeV/c^2. So far, this is the lowest mass that could ever be probed in a direct detection experiment looking for nuclear recoils. Figure 7.46 shows the *Sapp2-L* limit together with previous leading limits from CRESST measurements. In a mass

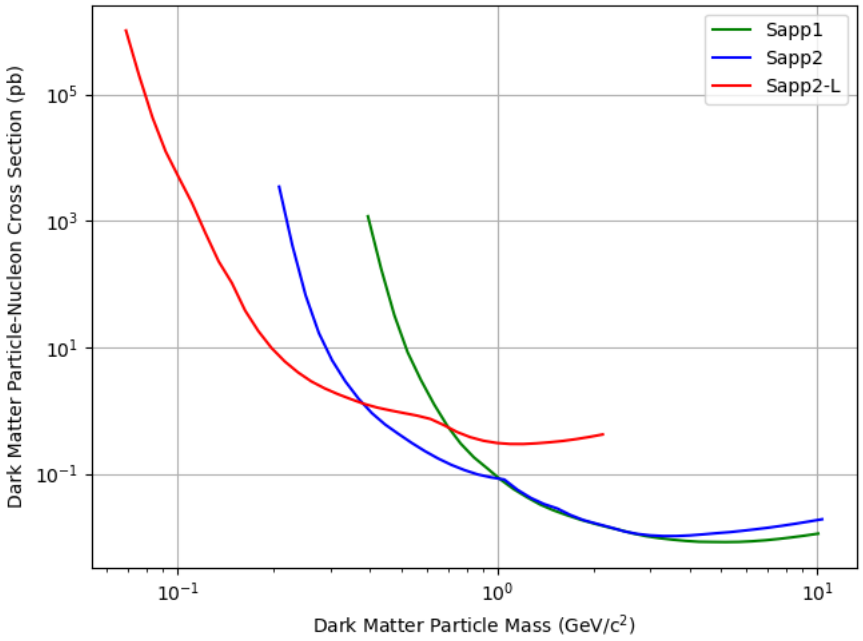

Figure 7.45: Dark matter exclusion limits on spin-independent interactions for the sapphire detectors analyzed in this work. The limits of the phonon channels of *Sapp1* and *Sapp2* are very similar above a dark matter mass of 1 GeV/c^2 due to the strong similarities of their energy spectra. The deviation of the limits below 1 GeV/c^2 stems from the much lower threshold of the *Sapp2* detector. The extremely low threshold of the *Sapp2-L* detector allows to extend the exclusion limit down to a mass of only 69 MeV/c^2.

range from 69 MeV/c^2 to 203 MeV/c^2 the *Sapp2-L* detector has leading exclusion limits on standard elastic spin-independent dark matter nucleus interactions.

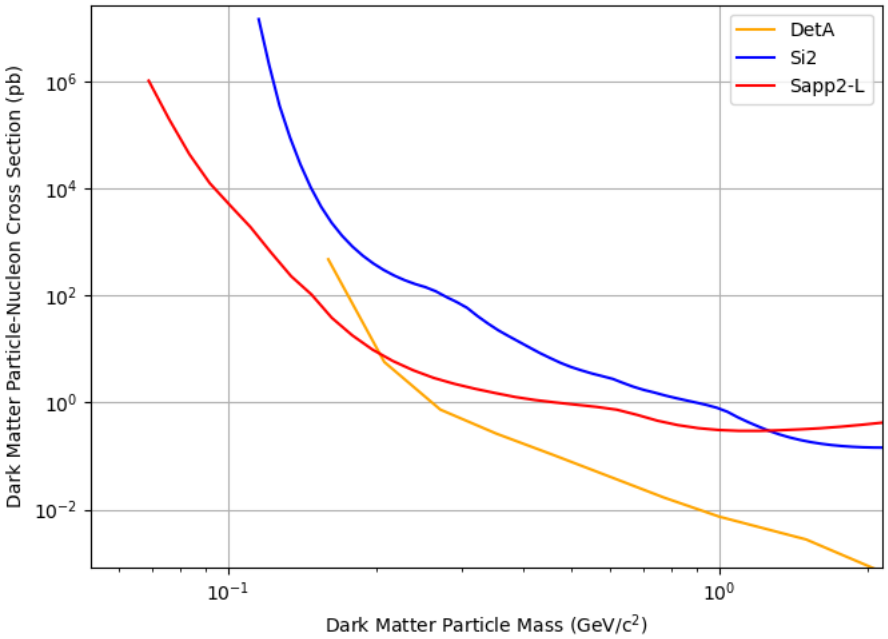

Figure 7.46: Comparison of the *Sapp2-L* exclusion limit, shown in red, with previously leading dark matter limits of CRESST. Shown in orange is the result of a $CaWO_4$ crystal [63] and in blue the limit from a Si detector [136]. The *Sapp2-L* detector gives leading exclusion limits on standard elastic spin-independent dark matter interactions in a mass range from 69 MeV/c^2 to 203 MeV/c^2.

Chapter 8

Solar neutrinos in cryogenic detectors

Direct dark matter search experiments keep improving their sensitivity into so far unexplored regions. Massive liquid scintillator and liquid noble gas experiments with huge exposures continue to drive towards smaller dark matter particle-nucleus cross sections for masses in the 10 GeV/c^2 range, while experiments like CRESST, using cryogenic solid state detectors, are setting new standards in terms of energy thresholds, opening the parameter space to sub 100 MeV/c^2 dark matter particle masses.

A common challenge for the field of direct dark matter searches in this race towards unprecedented sensitivities is the approach of the so-called neutrino floor. Coherent elastic neutrino-nucleus scattering (CEνNS) has been introduced as an irreducible background already in sec. 3.4. The relevant neutrino sources typically considered in the neutrino floor are solar neutrinos, atmospheric neutrinos and diffuse supernova neutrinos [137]. Large liquid scintillator experiments (multi-tonne liquid xenon detectors [138, 139], XENON1T experiment [52], LZ experiment [55]) are already approaching levels at which the first neutrino-nucleus interactions, mostly with the high energetic solar neutrinos (^{8}B and *hep* neutrinos, see sec. 8.1), are expected.

In the energy range considered in CRESST-III, which is optimized for low-mass dark matter searches, the neutrino flux is completely dominated by solar neutrinos. For this reason this is the only contribution to the neutrino floor that will be considered in this chapter. While the sensitivity to lower energetic neutrino interactions via CEνNS in liquid scintillator experiments is mostly limited by their energy threshold, cryogenic solid state detectors typically reach much lower thresholds. The flux of solar neutrinos increases by several orders of magnitude towards lower energies. This implies that the exposure at which the neutrino floor will become a concern is lower for experiments achieving very low energy thresholds.

A major upgrade of the CRESST-III setup to 288 read-out channels ($\mathcal{O}$(100) detector modules) with the goal of reaching tonne day exposures is already in progress. This upgrade is a big step towards testing lower scattering cross sections, and with that, also towards the neutrino floor.

Once the limitation of the LEE is overcome, an increased exposure will inevitably lead to cryogenic solid state detectors reaching the neutrino floor. Therefore, a thorough

understanding of the expected signals is necessary in order to maintain sensitivity to a potential dark matter signal even below the neutrino floor.

This chapter contains the results of simulations and sensitivity studies of a low-threshold, high-exposure cryogenic solid state detector experiment. After introducing the solar neutrino model and the associated expected signals in cryogenic solid state detectors in sec. 8.1, the chapter is divided into two main parts. In the first part, solar neutrinos are considered as a background in dark matter searches (sec. 8.2). First, the definition of the solar neutrino floor is explained. Afterwards, the sensitivity to a potential dark matter signal in the presence of a solar neutrino background is investigated. The second part focuses on solar neutrinos as the main signal of interest in the absence of any dark matter events (sec. 8.3). The possibility of measuring solar neutrinos via CEνNS and the sensitivity to the flux of different neutrino production mechanisms is explored.

8.1 Solar neutrino model

This section gives a short overview of the different neutrino production mechanisms in the Sun and introduces the solar model on which all simulations in this chapter are based.

Neutrinos are produced in the nuclear fusion processes inside the core of the Sun burning hydrogen into helium. These processes can be divided into two groups: the proton-proton chain reactions (pp-chain) and the carbon-nitrogen-oxygen cycle (CNO cycle) [140], shown in fig. 8.1 [141].

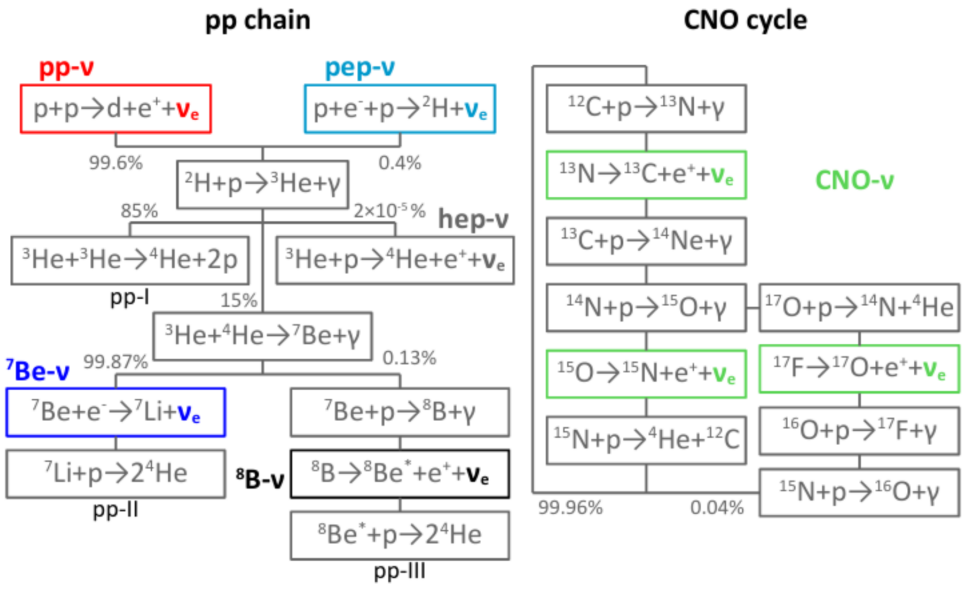

Figure 8.1: The neutrino production mechanisms in the core of the Sun, divided into the pp-chain and the CNO cycle. Figure taken from [141].

In our Sun, the pp-chain dominates over the CNO-cycle [140]. The exact flux of neutrinos produced in a specific fusion reaction depends on the choice of the solar model. For this work, all studies are based on the model BP04(Garching) [142]. The corresponding values of the neutrino flux on Earth from each individual production mechanism are listed in tab. 8.1.

Table 8.1: All neutrino production reactions and the corresponding neutrino fluxes on Earth according to the model BP04(Garching) [142]. The uncertainties represent the conservative theoretical uncertainties from all known sources [143]. In the case of asymmetric uncertainties, the higher value is chosen and used as a symmetrical uncertainty.

Solar neutrinos	Production mechanism	flux ϕ ($cm^{-2}\ s^{-1}$)	uncertainties (%)
pp	$p + p \rightarrow {}^2H + e^+ + \nu_e$	$5.94 \cdot 10^{10}$	1.0
pep	$p + e^- + p \rightarrow {}^2H + \nu_e$	$1.41 \cdot 10^8$	1.7
hep	${}^3He + p \rightarrow {}^4He + e^+ + \nu_e$	$7.88 \cdot 10^3$	15.5
${}^7Be$	${}^7Be + e^- \rightarrow {}^7Li + \nu_e$	$4.84 \cdot 10^9$	10.5
${}^8B$	${}^8B \rightarrow {}^8Be^* + e^+ + \nu_e$	$5.74 \cdot 10^6$	16.3
${}^{13}N$	${}^{13}N \rightarrow {}^{13}C + e^+ + \nu_e$	$5.70 \cdot 10^8$	31.2
${}^{15}O$	${}^{15}O \rightarrow {}^{15}N + e^+ + \nu_e$	$4.98 \cdot 10^8$	33.2
${}^{17}F$	${}^{17}F \rightarrow {}^{17}O + e^+ + \nu_e$	$5.87 \cdot 10^6$	52.2

While the flux of the neutrinos from different reactions is given by the solar model, the shape of their energy spectra just depends on the fusion reactions in which they are produced. The solar neutrino energy spectra are shown in fig. 8.2, scaled with the corresponding fluxes of tab. 8.1.

8.1.1 Expected energy spectrum

The differential CEνNS cross section, $\frac{d\sigma}{dE_R}$, was already introduced in sec. 3.4 with eq. 3.23. The expected recoil spectrum in a detector is simply given by a combination of the incoming neutrino flux, Φ_ν, and their interaction cross section with the nuclei in the detector:

$$\frac{dR}{dE_R} = \epsilon \cdot N_t \cdot \int_{E_{\nu,min}}^{\infty} dE_\nu \Phi_\nu(E_\nu) \frac{d\sigma(E_R, E_\nu)}{dE_R} \tag{8.1}$$

with N_t being the number of nuclei per kg of target mass: $N_t = \frac{N_A}{M_M}$ (N_A: Avogadro constant, M_M: molar mass) and ϵ being the exposure (detector mass $\cdot$ measuring time). The lower boundary of the integral over the neutrino energy E_ν is given by the minimal

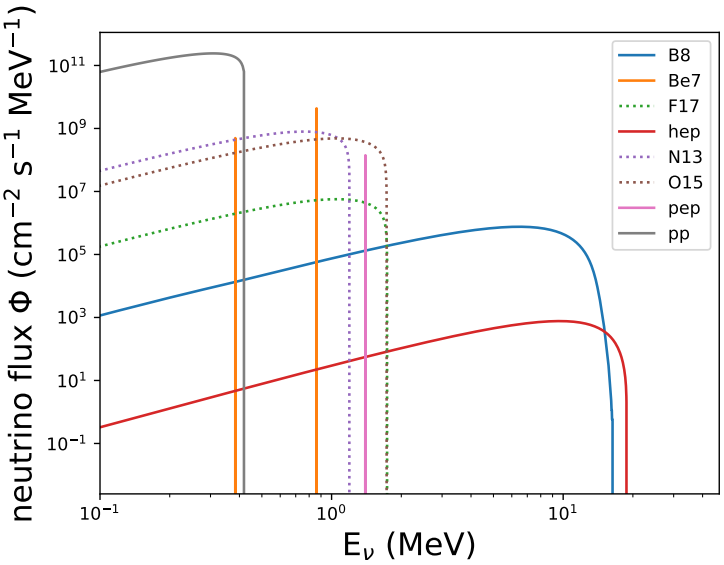

Figure 8.2: Solar neutrino energy spectra. Neutrinos produced in the fusion reactions of the pp-chain are shown with solid lines, neutrinos produced in the CNO-cycle with dashed lines.

energy a neutrino needs to lead to a recoil with energy E_R: $E_{\nu,min} = \sqrt{\frac{m_N E_R}{2}}$, with m_N being the mass of the target nucleus.

The differential recoil spectra expected in a $CaWO_4$ and a Al_2O_3 detector are shown in fig. 8.3.

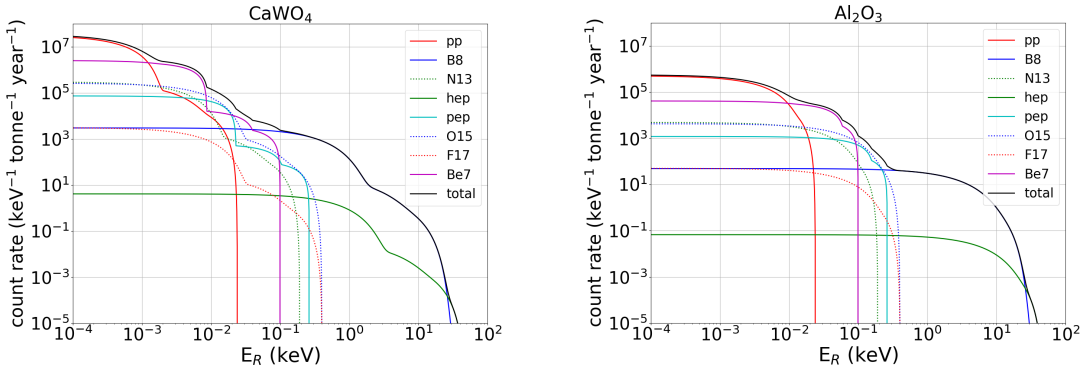

(a) Solar neutrino recoil spectrum in $CaWO_4$.

(b) Solar neutrino recoil spectrum in Al_2O_3.

Figure 8.3: Differential recoil energy spectra of solar neutrinos expected in a) a $CaWO_4$ detector and b) a Al_2O_3 detector.

The total count rate of neutrinos above an energy threshold E_{thr} is then given by an integral over the recoil spectrum:

$$\frac{dR}{dE_{thr}} = \int_{E_{thr}}^{\infty} dE_R \frac{dR}{dE_R} \tag{8.2}$$

The expected count rate of solar neutrinos as a function of the energy threshold for $CaWO_4$ and Al_2O_3 are shown in fig. 8.4.

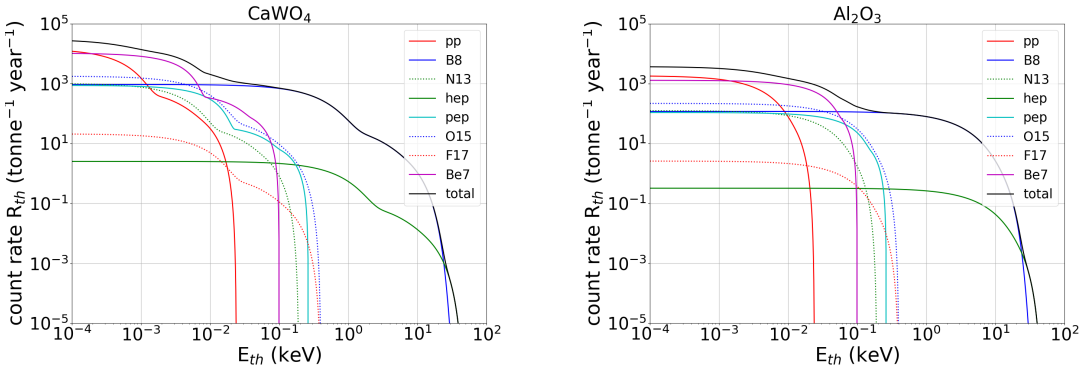

(a) Solar neutrino count rate in $CaWO_4$ as a function of the energy threshold.

(b) Solar neutrino count rate in Al_2O_3 as a function of the energy threshold.

Figure 8.4: Expected total number of solar neutrinos above the energy threshold as a function of the threshold in a) a $CaWO_4$ detector and b) a Al_2O_3 detector.

This shows the big impact the energy threshold has on the total number of expected neutrino events. Especially the *pp* and *Be7* neutrino fluxes lead to very high numbers of CEνNS interactions for energy thresholds below $\mathcal{O}$(eV).

8.2 Neutrinos as background

In this section, solar neutrinos are considered as a background in the search for a direct dark matter signal. The definition and calculation of the neutrino floor is presented in sec. 8.2.1. Subsequently, sec. 8.2.2 investigates sensitivity limits for a dark matter signal in the presence of a solar neutrino background.

8.2.1 The neutrino floor

There is no unique definition of the neutrino floor. A common choice is described in [137, 144]. For a large number of different energy thresholds, a background-free exclusion limit (defined as isovalues corresponding to zero observed WIMP events) is calculated. The exposure at which each of these exclusion lines is calculated is adjusted so that exactly one neutrino background event is expected. By defining the neutrino

floor as the minimum of these exclusion limits at each dark matter particle mass, the best possible estimate for the dark matter sensitivity for each dark matter mass in the presence of a single neutrino event can be calculated. In the following this definition is sketched out in more detail.

Step 1: For a given fixed energy threshold $E_{thr,fix}$, the expected number of neutrino events above this energy threshold can be calculated using eq. 8.2. Since this number scales linearily with the exposure, the necessary exposure, ϵ_{fix} that leads to exactly one expected neutrino event above the threshold can be easily determined.

Step 2: Given the fixed energy threshold and the exposure determined in step 1, the number of expected dark matter events for a dark matter particle with mass m_{DM} can be calculated as a function of the cross section, σ_{DM}, by integrating over the differential recoil spectrum of dark matter, $\frac{dR_{DM}(m_{DM},\sigma_{DM})}{dE_R}$ (see eq. 3.18):

$$R_{DM}(m_{DM},\sigma_{DM}) = \epsilon_{fix} \cdot \int_{E_{thr,fix}}^{\infty} dE_R \frac{dR_{DM}(m_{DM},\sigma_{DM})}{dE_R} \tag{8.3}$$

Expected number of events: The expected number of dark matter events above the threshold is distributed as a Poissonian with a mean equal to the theoretically expected number, calculated in step 2 ($\lambda = R_{DM}(m_{DM},\sigma_{DM})$):

$$P_\lambda(k) = \frac{\lambda^k}{k!} \cdot e^{-\lambda} \tag{8.4}$$

with k being the number of observed events. In the case of zero events observed, all cross sections leading to an expected number of events greater than $\lambda_{C.L.}$ can be excluded with a confidence level C.L. Accordingly, the probability to observe zero events has to be $(1 - \text{C.L.})$:

$$\begin{aligned} P_{\lambda_{C.L.}}(k=0) = e^{-\lambda_{C.L.}} &= 1 - C.L. \\ \Rightarrow \lambda_{C.L.} &= -ln(1 - C.L.) \end{aligned} \tag{8.5}$$

Fixing the required confidence level to 90% gives $\lambda_{90\%} \simeq 2.3$. This means that for zero observed events it is possible to exclude the cross section $\sigma_{90\%}$, that leads to a theoretically expected number of dark matter events larger than 2.3, at 90% C.L.

Step 3: The differential recoil rate, $\frac{dR_{DM}(m_{DM},\sigma_{DM})}{dE_R}$, and thus also the total number of dark matter events above the threshold, $R_{DM}(m_{DM},\sigma_{DM})$ scales linearily with

the cross section σ_{DM}, as can be seen in eq. 3.17. The cross section σ_{DM} that fulfills $R_{DM}(m_{DM}, \sigma_{DM}) = \lambda_{C.L.}$ (2.3 for a 90% C.L.) can now be calculated for each dark matter mass m_{DM}, defining the exclusion limit with the threshold $E_{thr,fix}$ and the exposure ϵ_{fix}. The neutrino floor is typically calculated for a dark matter mass range in which the experiment is sensitive to a dark matter signal.

Step 4: The steps above for a single fixed energy threshold $E_{thr,fix}$ have to be repeated for a range of different energy thresholds. The choice of the boundaries of this threshold range will be discussed below. This last step leads to a function $\sigma_{DM}(m_{DM}, E_{thr})$. The neutrino floor is now defined as the minimum of $\sigma_{DM}(m_{DM}, E_{thr})$ at each mass m_{DM}, giving the best achievable estimated sensitivity for each dark matter mass.

An example of the neutrino floor calculation for a $CaWO_4$ detector is shown in fig. 8.5 for a dark matter mass range from 10 MeV/c^2 to 10 GeV/c^2. Each of the single lines is corresponding to the calculations of steps 1-3 for a single energy threshold. The calculation was done for 200 different thresholds ranging from 0.1 μeV to 10 keV. The minimum of all lines at each mass, shown as a black line, represents the neutrino floor according to the definition adopted.

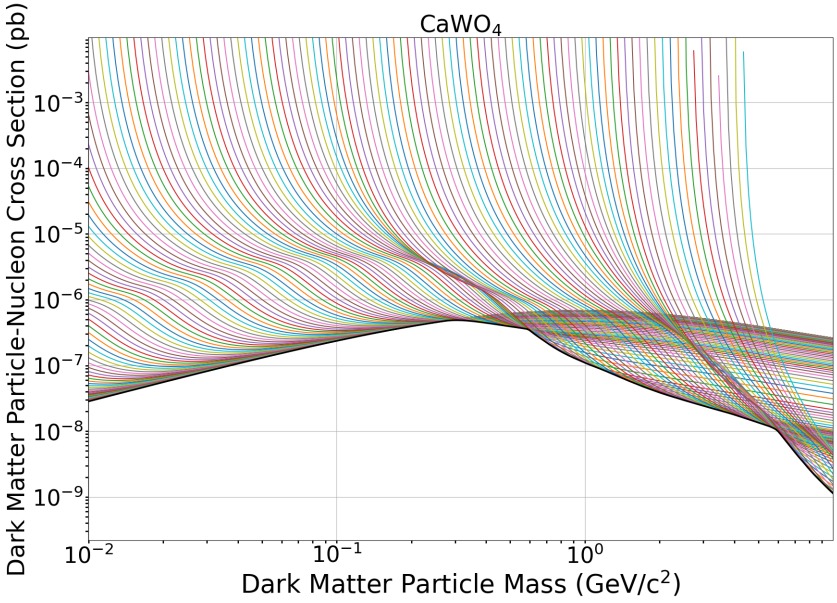

Figure 8.5: Set of background-free 90% C.L. exclusion limits for exposures corresponding to one neutrino event above the energy threshold for 200 different thresholds between 0.1 μeV and 10keV in $CaWO_4$. The black line is constructed by taking the minimum of the individual exclusion limits at each mass.

Side note: Interestingly, for lower thresholds the exclusion limits are less sensitive at higher dark matter masses, compared to the exclusion limits calculated for higher thresholds. For example, if a dark matter signal would be expected at a mass of about a few GeV/c^2 and an interaction cross section of about 10^{-7} pb, choosing a higher threshold of $\mathcal{O}$(keV) would reduce the impact of the solar neutrino floor compared to the low thresholds that can be achieved in CRESST detectors (see fig. 8.5). This is mainly caused by the sharp decrease in the count rate of solar neutrinos towards higher energies (see fig. 8.3 and 8.4). It should be noted, that this is only true if the exclusion limits are defined by the total number of expected events above the threshold, without taking the spectral information into account, as it is done in this section.

The choice for the boundaries of the range of thresholds that is used to construct the neutrino floor is dependent on boundaries of the dark matter mass range of interest. In the example calculation shown in fig. 8.5, the neutrino floor is shown in a mass range from 10 MeV/c^2 to 10 GeV/c^2. The lowest mass that could be probed in CRESST so far is 69 MeV/c^2. Therefore, in the following the lower boundary of the mass range of the neutrino floor will be set slightly below this value at 50 MeV/c^2.

The lower and upper boundaries of the range of thresholds, for which exclusion limits are calculated should be chosen such that the neutrino floor does not change anymore in the defined mass range by including lower (or higher thresholds) in the calculations. The influence of the lower boundary of the threshold range on the neutrino floor is shown in fig. 8.6a, while the influence of the upper boundary of the threshold range on the neutrino floor is shown in fig. 8.6b.

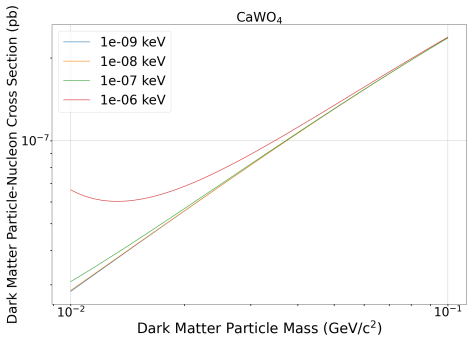

(a) Background-free exclusion limits calculated for different thresholds in a mass range of $\mathcal{O}$(50 MeV/c^2).

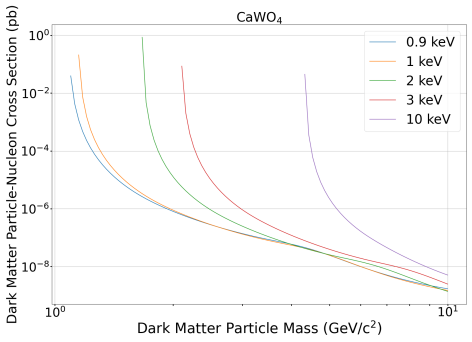

(b) Background-free exclusion limits calculated for different thresholds in a mass range of $\mathcal{O}$(1 GeV/c^2).

Figure 8.6: A close-up of the a) low-mass range and the b) high-mass range of the exclusion limits used to construct the neutrino floor. The different lines correspond to exclusion limits calculated at different energy thresholds (given in the legends).

It can be seen, that the neutrino floor for masses above 50 MeV/c^2 is not affected by including thresholds lower than 1 meV (in $CaWO_4$). On the other side, the neutrino

floor for masses below 10 GeV/c^2 is not affected by including thresholds higher than around 3 keV (in $CaWO_4$). Therefore, for the construction of the neutrino floor in a mass range from 50 MeV/c^2 to 10 GeV/c^2 in $CaWO_4$, it is sufficient to calculate exclusion limits for thresholds in a range from 1 meV to 3 keV.

The neutrino floor is not only dependent on the range of thresholds, but also on the target material. The example above was based on a $CaWO_4$ target crystal. Figure 8.7 shows the comparison of the neutrino floor in the mass range from 50 MeV/c^2 to 10 GeV/c^2 for thresholds between 1 meV and 10 keV for $CaWO_4$ and Al_2O_3.

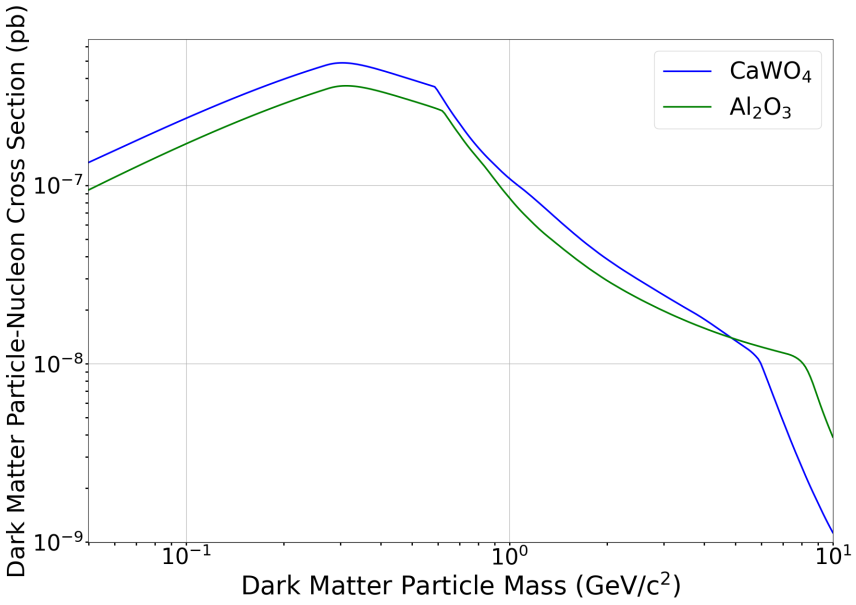

Figure 8.7: Comparison of the neutrino floor in $CaWO_4$ and Al_2O_3.

In the following, the differences between the neutrino floors in the two materials is explained. The interaction cross section of dark matter (neutrinos) scales with the A^2 (N^2) of the target material, which effectively increases the number of interactions for heavier elements. At the same time, for a fixed energy transfer the recoil energy of the target nucleus scales inversely with its mass. So while interactions with a heavier element are more frequent, they lead to lower recoil energies compared to a lighter target. As can be seen in fig. 8.8a, the count rate of solar neutrino events above the energy threshold in a Al_2O_3 detector is always lower than in a $CaWO_4$ detector for thresholds below about ∼0.86 keV and vice versa above this value. Therefore, for thresholds lower than this value, the exposure that leads to one expected neutrino event above the threshold (step 1 of the neutrino floor calculation) is higher in Al_2O_3 than in $CaWO_4$ (for the same threshold in both). For dark matter, the picture is a little more complicated. The total number of events does not only depend on the threshold, but also on the dark matter

mass. Generally, for a given fixed exposure and dark matter mass, it is possible to tune the threshold to have a larger number of events in either of the two materials. For a dark matter particle with a mass of about 5.6 GeV/c^2 the threshold at which the total count rate of events in Al_2O_3 surpasses the count rate in $CaWO_4$ is the same as for the neutrino interactions (about 0.86 keV, see fig. 8.8b).

This means, for dark matter masses below 5.6 GeV/c^2 the minimum of the background-free exclusion limits is always lower in Al_2O_3 compared to $CaWO_4$. Above this dark matter mass, the exclusion limits calculated for thresholds greater than 0.86 keV give the strongest limits (the minimal values at each mass − step 4 of the neutrino floor calculation). Therefore, the picture changes and the neutrino floor in $CaWO_4$ becomes lower than in Al_2O_3, which explains the intersection at about 5.6 GeV/c^2 in fig. 8.7.

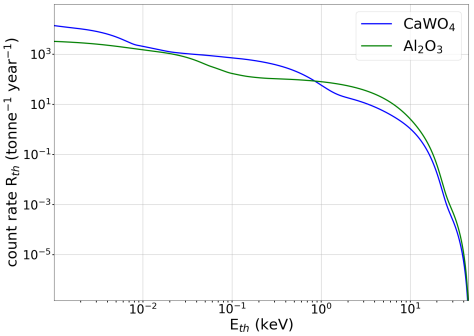

(a) Total number of expected solar neutrino events in $CaWO_4$ and in Al_2O_3 as a function of the threshold.

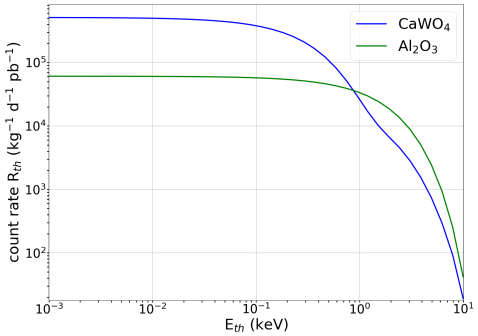

(b) Total number of expected dark matter events in $CaWO_4$ and in Al_2O_3 for a dark matter particle with a mass of 5.6 GeV/c^2 as a function of the threshold.

Figure 8.8: Total number of expected events above the energy threshold a) for solar neutrinos and b) for a dark matter particle with a mass of 5.6 GeV/c^2 in $CaWO_4$ and Al_2O_3.

8.2.2 Sensitivity to dark matter in presence of solar neutrinos

In their path to increased sensitivity, direct detection experiments will inevitably reach the neutrino floor. At this point, the sensitivity to a dark matter signal will be limited by this irreducible background. In this section, the discovery potential for a dark matter signal in the presence of the solar neutrino background in a low-threshold, high-exposure cryogenic direct detection experiment is investigated.

The definition of the neutrino floor in sec. 8.2.1 only takes the count rates of neutrinos and dark matter events above the energy threshold into account, without using any shape information of the expected recoil spectra. Due to this simplyfied definition the

neutrino floor is not really a hard limit, which is why in modern literature the term **neutrino floor** is often replaced by **neutrino fog**.

Calculations of actual sensitivity limits to a dark matter signal take the shape differences of the expected recoil spectra of neutrinos and dark matter particles into account. Typically, these limits lie below the previous definition of the neutrino floor and become stronger with increasing exposures.

The theoretical model of this background can be used in a likelihood framework. For this, the background term in the probability density function (pdf) of eq. 5.10 in sec. 5.3.1.2 is described by the solar neutrino model and the associated parameters. A detailed description of the likelihood function used for this analysis is given in the following section.

The computation of the sensitivity limits on a dark matter discovery, resulting from extensive Monte Carlo simulations, is shown in sec. 8.2.2.2.

8.2.2.1 Extended maximum likelihood

The general form of an unbinned poissonian likelihood is described by:

$$\mathcal{L} = \frac{N_e^{N_o}}{N_o!} \cdot e^{-N_e} \cdot \prod_{i=0}^{N_o} f(x_i, \overrightarrow{p}) \tag{8.6}$$

with N_e and N_o being the expected and observed number of events and $f(x_i, \overrightarrow{p})$ being the pdf of the model describing the distribution of events x_i and $\overrightarrow{p}$ being the parameter vector.

The studies performed in this chapter are assuming a detector setup with tonne-scale exposures and thus often involve very large numbers of events, causing the product over every single event in eq. 8.6 to be time consuming and computationally expensive. Therefore eq. 8.6 is modified into a binned poissonian likelihood:

$$\mathcal{L} = \frac{N_e^{N_o}}{N_o!} \cdot e^{-N_e} \cdot N_o! \prod_{i=0}^{m} \frac{f_i^{k_i}}{k_i!} \tag{8.7}$$

With m being the number of bins, k_i the observed number of events in the ith bin ($\Rightarrow \sum_i^m k_i = N_o$) and f_i being the integral of the pdf over the ith bin:

$$\begin{aligned} f_i(\overrightarrow{p}) &= \int_{x_i^{low}}^{x_i^{up}} f(x, \overrightarrow{p}) dx \\ \Rightarrow \sum_i^m f_i &= 1 \end{aligned} \tag{8.8}$$

The $N_o!$ in eq. 8.7 is cancelling out. Then, after using the relations A.31 and A.32 (see app. A.6), the likelihood can be rewritten as:

$$\mathcal{L} = \prod_{i=0}^{m} e^{-N_e f_i} \cdot \frac{(N_e f_i)^{k_i}}{k_i!} \tag{8.9}$$

For the reasons explained in sec. 5.3.1.2, the negative logarithm of the likelihood function is typically used:

$$-ln(\mathcal{L}) = \sum_{i=0}^{m} (N_e f_i - k_i \cdot ln(N_e f_i) + ln(k_i!)) \tag{8.10}$$

For a given dataset, the last term of this equation ($ln(k_i!)$) is constant and hence irrelevant for a minimization of the negative log-likelihood (nLL) and therefore will not be considered in the following.

The total number of events expected above the threshold N_e can be described by a sum of expected dark matter events $N_{e,\chi}$ and neutrino events $\sum_\nu N_{e,\nu}$ with $\nu \in \{pp, B8, N13, hep, pep, O15, F17, Be7\}$.

Accordingly, also the pdf $f(x, \overrightarrow{p})$ is a sum of the dark matter pdf $f_\chi(E_R, \sigma_\chi)$ and the eight neutrino pdf's $f_\nu(E_R, \phi_\nu)$ as a function of the recoil energy ($x \rightarrow E_R$). The parameters $\overrightarrow{p}$ of the model are the dark matter nucleon interaction cross section, σ_χ, and the flux normalizations of tab. 8.1, $\overrightarrow{\phi}$. Since in both cases the parameters are linear scaling factors in the description of the expected recoil spectra, they can be extracted from the equations:

$$\begin{aligned} \tilde{f_\chi}(E_R, \sigma_\chi) &= \epsilon \cdot \sigma_\chi \cdot \frac{dR_\chi}{dE_R}(E_R, \sigma = 1pb) \\ \tilde{f_\nu}(E_R, \phi_\nu) &= \epsilon \cdot \phi_\nu \cdot \frac{dR_\nu}{dE_R}(E_R, \phi_\nu = \phi_{\nu,M}) \end{aligned} \tag{8.11}$$

with ϵ being the exposure. The recoil spectrum of dark matter is calculated for a cross section of 1 pb, therefore the free parameter σ_χ is the interaction cross section between dark matter and a single nucleon in units of picobarn. The eight recoil spectra of the neutrinos are calculated with the flux normalizations of the theoretical model parameters, $\phi_{\nu,M}$, from tab. 8.1, making the free parameter ϕ_ν simply a scaling factor of the theoretical expectation. This is a convenient way of dealing with the large spread of the flux normalizations over several orders of magnitude. The unnormalized functions in eq. 8.11 are marked with a tilde to distinguish them from the normalized pdf.

To arrive at the final binned pdf $f_i = f_{i,\chi} + \sum_\nu f_{i,\nu}$ (for the ith bin), the functions in

eq. 8.11 need to be normalized. This is achieved by dividing the functions by the total number of expected events over the entire energy range:

$$f_i = \frac{1}{N_e} \cdot \int_{E_{R,i}^{low}}^{E_{R,i}^{up}} \tilde{f}_\chi(E_R, \sigma_\chi) + \sum_\nu \tilde{f}_\nu(E_R, \phi_\nu) dE_R \tag{8.12}$$

with:

$$N_e = \int_{E_{thr}}^{\infty} \tilde{f}_\chi(E_R, \sigma_\chi) + \sum_\nu \tilde{f}_\nu(E_R, \phi_\nu) dE_R \tag{8.13}$$

By substituting eq. 8.12 in eq. 8.10, the N_e cancel out. Therefore, the analytical description of N_e is not explicitly needed in the likelihood function.

A final modification to the nLL is the addition of so-called pull terms. This modification is often considered somewhat analogous to a "semi-bayesian" approach, since it includes prior knowledge to restrict a set of parameters in the fit. In this case, the pull terms keep the nuisance parameters $\overrightarrow{\phi}$ around their theoretical expectations within their theoretical uncertainties, σ_ν (last column in tab. 8.1). The final form of the nLL function is then:

$$-ln(\mathcal{L}) = \sum_{i=0}^{m} (N_e f_i - k_i \cdot ln(N_e f_i)) + \frac{1}{2} \sum_\nu \left(\frac{\phi_\nu - 1}{\sigma_\nu} \right)^2 \tag{8.14}$$

8.2.2.2 Computation of discovery limits

Sensitivity limits for a dark matter discovery in the presence of a solar neutrino background can be calculated for different experimental settings, defined by the:

- Target material
- Energy threshold
- Exposure

The limits calculated in this section are describing a 90% C.L. limit for a 3σ dark matter discovery. This means that a dark matter particle with mass and scattering cross section above the calculated limit would lead to a discovery with at least 3σ significance in at least 90% of the experiments with the given settings. Some important points have to be mentioned here: No other backgrounds than neutrinos and no energy resolution have been considered in the simulations presented in this section. Furthermore, an (unrealistic) energy independent efficiency of a 100% is assumed for the experiments. Hence, the limits represent a best case scenario.

Table 8.2: A 3σ discovery limit is calculated for each of these experimental settings.

Material	Threshold (eV)	Exposure (tonne · year)
$CaWO_4$	10	0.00274
$CaWO_4$	1	0.1
$CaWO_4$	1	1
$CaWO_4$	0.1	1
$CaWO_4$	1	10
Al_2O_3	1	0.1
Al_2O_3	1	1
Al_2O_3	1	10

The experimental settings for which the limits are computed are given in tab. 8.2.

The first line of tab. 8.2 corresponds to the goal of the CRESST upgrade (1 tonne day exposure with $CaWO_4$ detectors) with a threshold of 10 eV. All other experiments assume an improved energy threshold of 1 eV. For the setting with an exposure of 1 tonne year of $CaWO_4$ detectors also a limit for a threshold of only 0.1 eV is calculated to show the strong effect of a reduced threshold in the low mass regime.

Method: To quantify the statistical significance of the fit of a dark matter signal in the presence of a background (alternative hypothesis, H_1), compared to a background only hypothesis (null hypothesis, H_0), equations 5.18 and 5.19 from sec. 5.3.2 are used to create a profile likelihood ratio test statistic, q_0:

$$q_0 = \begin{cases} -2 \cdot \ln\left(\frac{\mathcal{L}(\sigma_\chi=0,\hat{\hat{\boldsymbol{\phi}}}_\nu)}{\mathcal{L}(\hat{\sigma}_\chi,\hat{\boldsymbol{\phi}}_\nu)}\right) & ,\hat{\sigma}_\chi \geq 0 \\ 0 & ,\hat{\sigma}_\chi < 0 \end{cases} \tag{8.15}$$

with $\mathcal{L}$ being the likelihood function of eq. 8.14. According to Wilk's theorem, the distribution of q_0 should follow a half χ^2 distribution with one degree of freedom under the null hypothesis ($\sigma_\chi = 0$). This has been checked and could be confirmed for all dark matter masses in the mass range investigated in this section. Figure 8.9 shows an example histogram of the observed values of q_0 from 1000 Monte Carlo simulations under H_0 (at the mass point $m_\chi = 1\ \mathrm{GeV/c^2}$ in a $CaWO_4$ detector with a threshold of 1 eV and an exposure $\epsilon = 1$ tonne year) following a half χ^2 distribution, confirming Wilk's theorem. Therefore, using eq. A.30, the statistical significance in units of sigma can be expressed as the square root of the observed test statistic ($Z = \sqrt{q_0^{obs}}$).

For a given fixed dark matter mass, the objective is to find a cross section, σ_χ, for which in at least 90% of the experiments a significance Z of 3σ or higher is found. For each experimental setting of tab. 8.2, an interval of cross sections ranging over several

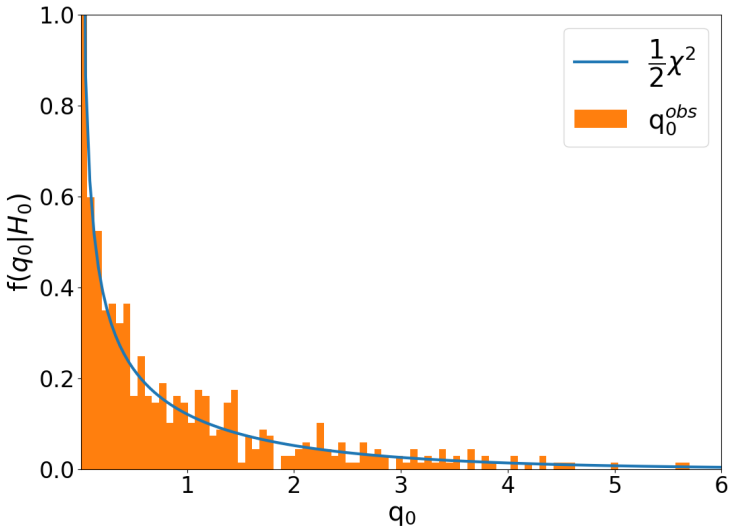

Figure 8.9: The distribution of observed q_0's for 1000 Monte Carlo datasets generated under the null hypothesis follow a half χ^2 distribution.

orders of magnitude is defined at each mass point in a given mass range[1]. For each cross section, 50 Monte Carlo datasets are generated and subsequently fit with both likelihood functions ($\mathcal{L}_{H_0}$ and $\mathcal{L}_{H_1}$), from which the observed test statistic q_0^{obs} can be computed (eq. 8.15). The fraction of $Z = \sqrt{q_0^{obs}} \geq 3$ can now be interpolated as a function of the cross sections in the defined interval. From this, using a simple root search, it is possible to determine a first approximation for the cross section σ_χ, at which about 90% of observed q_0's lead to $Z \geq 3$. Afterwards, at each mass point a finer scan of a small interval around this cross section is performed with 1000 Monte Carlo simulations for each cross section. With this approach it is possible to compute a rather precise value of the cross section σ_χ, for which $Z \geq 3$ in 90% of the experiments.

Results: The resulting dark matter discovery potentials for $CaWO_4$ detectors is shown in fig. 8.10. For each experimental setting, a dark matter particle with parameters on the corresponding curve would lead to a 3σ discovery in 90% of measurements. For the settings assumed for the planned CRESST upgrade (1 tonne day exposure, 10 eV threshold), the resulting limit (red line) is fully above the neutrino fog (gray shaded area). The limit reflects the background-free exclusion with one neutrino event above the threshold of 10 eV, as it was calculated for the construction of the neutrino fog (see sec. 8.2.1). This shows that solar neutrinos will not yet be a serious background for the CRESST upgrade. With an increased exposure and a lower threshold of 1 eV the sensitivity limits fully immerse in the neutrino fog. This shows that the neutrino floor

[1]The lower boundary of the mass range depends on the threshold. For a 1 eV threshold, 50 MeV/c^2 is chosen as the lowest mass point. All limits are calculated up to a dark matter mass of 10 GeV/c^2.

is not a hard limit and a dark matter discovery is still possible even below the classic definition of the neutrino floor (see sec. 8.2.1).

The limit for an exposure of 1 tonne year and an even lower threshold of only 0.1 eV is additionally calculated (green dotted line in fig. 8.10). For dark matter masses above about 500 MeV/c^2, this limit is identical to the one calculated for a threshold of 1 eV with the same exposure. At lower masses, the lower threshold starts to drastically increase the sensitivity towards smaller cross sections. Below a mass of about 140 MeV/c^2, the limit calculated with a threshold of 0.1 eV reaches cross sections more than one order of magnitude smaller than the limit calculated with a threshold of 1 eV. Moreover, below masses of about 200 MeV/c^2 the sensitivity limit reaches lower cross sections than the limit calculated with an exposure of 10 tonne years. This shows that, in order to **increase sensitivity to light dark matter masses in the presence of a solar neutrino background, decreasing the energy threshold is much more effective than increasing the exposure**.

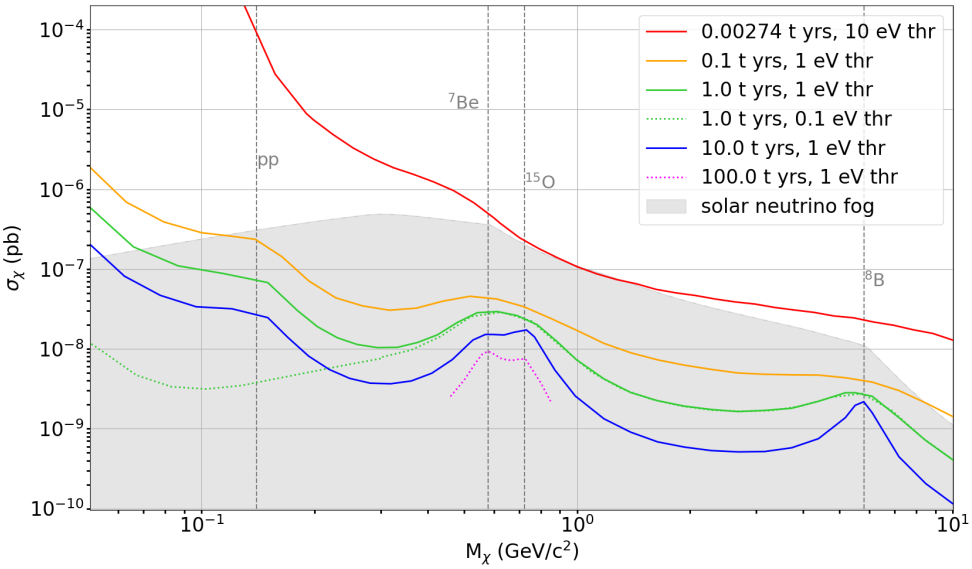

Figure 8.10: 3σ discovery potential for dark matter in different experimental settings in $CaWO_4$ detectors. The red line correponds to the targeted exposure of 1 tonne day in the CRESST upgrade with a threshold of 10 eV. The dotted green line is calculated with a threshold of 0.1 eV. All other limits are calculated with a threshold of 1 eV. The dotted magenta line is a limit calculated for a small dark matter mass range with an exposure of 100 tonne years. The vertical gray dashed lines mark the dark matter masses at which the sensitivity is limited due to the strong similarities of the expected dark matter spectrum to one of the solar neutrino components. The gray shaded area depicts the neutrino fog as calculated in sec. 8.2.1.

Generally, below the neutrino floor the sensitivity increases with the square root of the exposure ($\sim \sqrt{\epsilon}$), corresponding to a poissonian background substraction regime.

This behaviour was already observed e.g. in [145]. The dashed vertical lines in fig. 8.10 mark the dark matter masses for which the gain in sensitivity with an increased exposure deviates from this behaviour. The reason for this deviation is the strong similarity of the expected dark matter spectra with a particular component of the solar neutrino spectrum (indicated at the dashed lines). Figure 8.11 shows the dark matter spectra at these masses with interaction cross sections corresponding to the 3σ limit of an experiment with an exposure of 1 tonne year together with the respective components of the neutrino floor that cause the sensitivity at these masses to be limited. The discovery potential in $CaWO_4$ is also calculated for an exposure of 100 tonne years in a small mass range (dotted magenta line in fig. 8.10) to visualize the possibility of separating the influence of the ^{7}Be neutrinos and the ^{15}O neutrinos as a function of exposure.

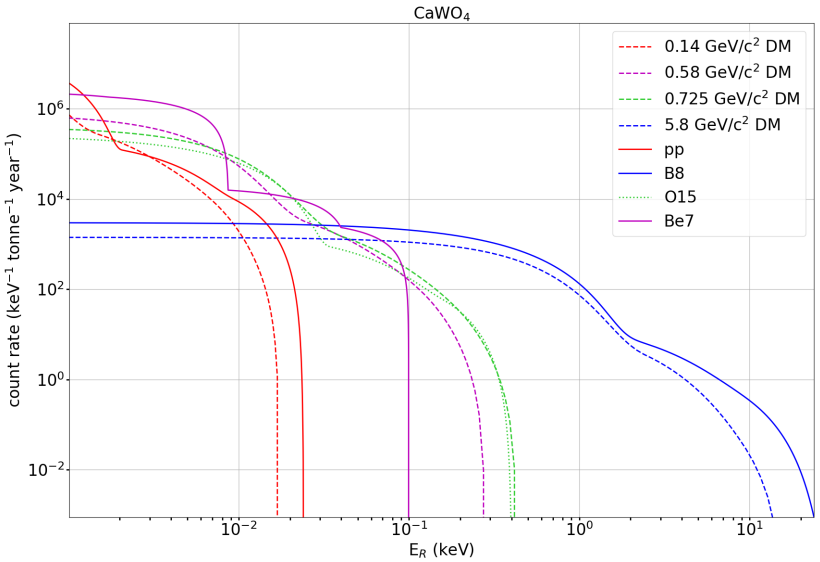

Figure 8.11: Comparison of the recoil energy spectra of selected solar neutrino fluxes with different dark matter spectra (dashed). The masses of the dark matter particles correspond to the gray dashed lines in fig. 8.10, the respective interaction cross sections are the 3σ limits for an experiment with 1 tonne year exposure and 1 eV threshold. The dark matter spectra are shown in the same color as the corresponding neutrino flux that is causing the sensitivity to a dark matter signal at this particular mass to be limited, due to the similarities in the expected shape and rate.

Similarly, also the 3σ discovery limits for Al_2O_3 detectors are shown in fig. 8.12 together with the previously calculated neutrino fog for this material. The dashed lines again represent the dark matter masses at which the sensitivity gain deviates from the $\sim \sqrt{\epsilon}$ behaviour due to the similarities of the expected dark matter spectra with specific components of the solar neutrino floor. The spectral comparison is shown in fig. 8.13.

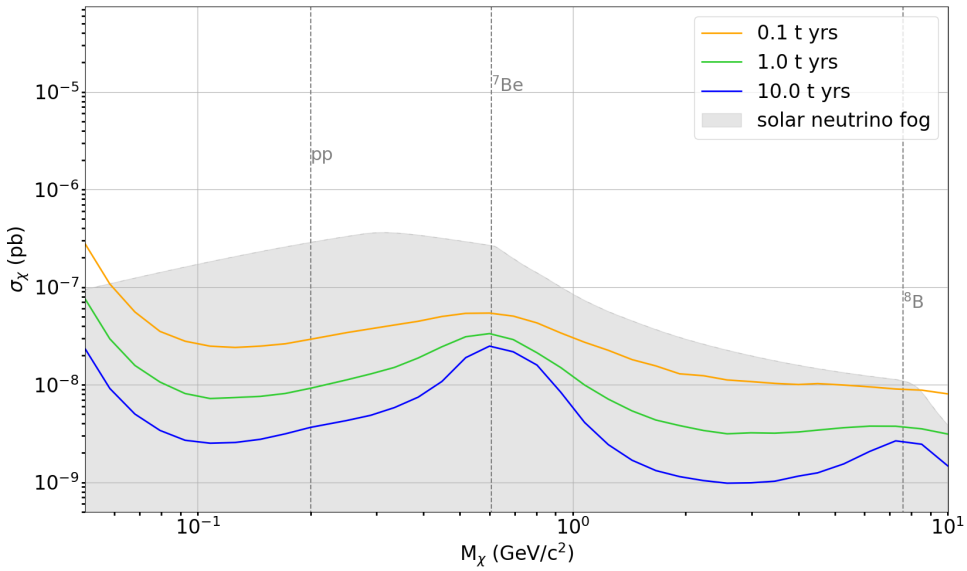

Figure 8.12: 3σ discovery limits for dark matter in different experimental settings in Al_2O_3 detectors. All limits are calculated with a threshold of 1 eV. The vertical gray dashed lines mark the dark matter masses at which the sensitivity is limited due to the strong similarities of the expected dark matter spectrum to one of the solar neutrino components. The gray shaded area depicts the neutrino fog as calculated in sec. 8.2.1.

A comparison of the discovery limits of both materials is shown in fig. 8.14. At masses below about 250 MeV/c^2, the dark matter count rate in Al_2O_3 detectors surpasses the one in $CaWO_4$ detectors, while the number of neutrino events above the 1 eV energy threshold is lower in the Al_2O_3 detectors. This leads to a much stronger dark matter discovery potential in sapphire detectors for masses below 250 MeV/c^2. Below a dark matter mass of 150 MeV/c^2 the limit of the Al_2O_3 detectors even exceed the limit of a $CaWO_4$ detector with 100 times more exposure.

In conclusion, a lighter target, such as Al_2O_3, has a highly increased sensitivity at lower dark matter masses. On the other hand, sensitivity towards dark matter particles with higher masses is enhanced with a heavier target, such as $CaWO_4$.

There are some additional methods to increase the sensitivity to dark matter signals in the presence of a solar neutrino floor that have not been mentioned in this section so far. One of them is to take into account the annual modulation of a dark matter signal [146], which can help to distinguish the expected signals of dark matter from the neutrino signals. Considering the large exposures used for the experimental settings in this section, the total number of dark matter interactions[2] would be high enough to expect an annually modulating signal. Another method involves detectors that are

[2]Considered here are dark matter particles with masses and cross sections above the experimental discovery potential.

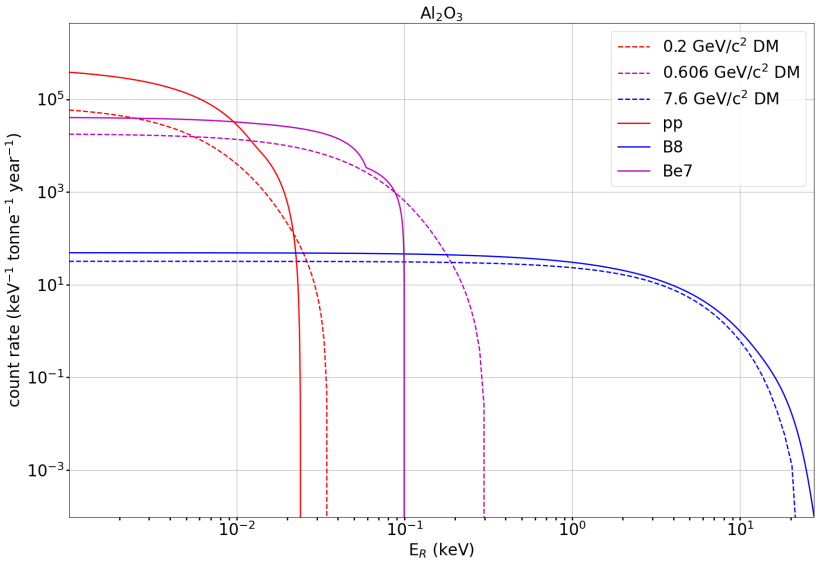

Figure 8.13: Comparison of the recoil energy spectra of selected solar neutrino fluxes with different dark matter spectra (dashed). The masses of the dark matter particles correspond to the gray dashed lines in fig. 8.12, the respective interaction cross sections are the 3σ limits for an experiment with 1 tonne year exposure and 1 eV threshold. The dark matter spectra are shown in the same color as the corresponding neutrino flux that is causing the sensitivity to a dark matter signal at this particular mass to be limited, due to the similarities in the expected shape and rate.

sensitive to the direction of incoming particles [147]. The directionality of events holds a very strong potential to distinguish solar neutrino events from dark matter events. Currently, techniques of directional detection are still in a very early R & D phase and are just mentioned here for completeness.

8.3 Neutrinos as signal

To this point, neutrinos have been considered as a background in the search for dark matter. From another perspective, reaching the neutrino floor in the low mass range also opens up the possibility to have a fully flavor independent measurement of the solar flux, with the potential of providing new strong constraints on the solar model and on neutrino physics. A precise measurement of the CNO neutrinos could shed light on the so-called "solar metallicity problem" [148] (see sec. 8.3.1).The purely neutral current (NC) measurement of solar neutrinos, so far not available at low energies, combined with the electron scatterings (NC + CC) of the low energy part of the solar neutrino spectrum, performed e.g. by Borexino [149], SNO [150] and Superkamiokande [151], would allow tests of the Mikheyev-Smirnov-Wolfenstein (MSW) effect [152] (see sec. 8.3.2). Therefore,

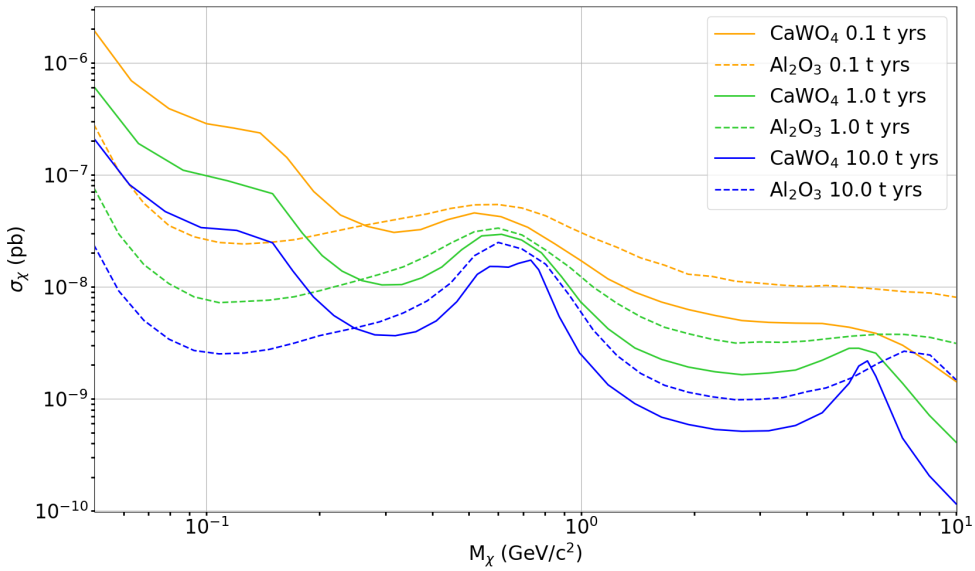

Figure 8.14: Comparison of the 3σ discovery limits for three different exposures and an energy threshold of 1 eV for $CaWO_4$ detectors (solid lines) and Al_2O_3 detectors (dashed lines). Sapphire detectors have a much higher sensitivity at dark matter masses below about 250 MeV/c^2. Below a dark matter mass of about 150 MeV/c^2, the limit of a sapphire detector with an exposure of 0.1 tonne years is comparable with the limit of a $CaWO_4$ detector with the same threshold, but two orders of magnitude higher exposure. At higher masses, $CaWO_4$ has a stronger sensitivity to a dark matter discovery.

in this section the possibility of measuring solar neutrinos via CEνNS and the sensitivity to the different neutrino fluxes is tested.

8.3.1 The solar metallicity

The theoretical predictions on the abundances of elements in the Sun depend on the solar models considered (see sec. 8.1). The fluxes of solar neutrinos hold information on the nuclear fusion processes in the Sun's core, and with that, also on the abundance of the heavy elements. A precise measurement of the different neutrino fluxes can therefore help to distinguish between a "low-metallicity" (LZ) or "high-metallicity" (HZ) scenario[3]. The flux of the CNO neutrinos is especially sensitive to the heavy-element-abundance [143, 148, 153]. At the same time, the CNO neutrinos constitute a sub-dominant component of the total solar neutrino flux (as can be seen in sec. 8.1), which makes their detection quite challenging.

Over the course of the last decades, neutrino experiments looking for neutrino-electron interactions have successfully measured neutrinos of all reactions in the pp-chain

[3] All elements heavier than H and He are considered metals in this context

(Homestake [154], SAGE [155], GALLEX [156], Superkamiokande [151], SNO [150] and Borexino [149]) with the exception of *hep* neutrinos (upper limits in [149]).

For a long time, only upper limits on the CNO neutrino flux could be estimated [149]. The first observation of neutrinos produced in the CNO cycle was published in 2020 by the Borexino collaboration [157], which was compatible with both, LZ and HZ solar models. Two years later, Borexino published an experimentally measured summed flux of the CNO neutrinos of $6.6^{+2.0}_{-0.9} \cdot 10^8$ cm^{-2} s^{-1} [153]. Their analysis finds agreement with HZ standard solar models. On the other side, small tensions are found with LZ models, altough only with a moderate statistical significance of about 2σ. An analysis of the CNO neutrino flux combined with the ^{7}Be and ^{8}B solar neutrino fluxes in [153] allows to disfavor the B16-AGSS09met (LZ solar model) with respect to the alternative model B16-GS98 (HZ solar model) at 3.1σ C.L.

Dark matter experiments reaching the neutrino floor also have the potential to contribute to the resolution of this problem by independently measuring the solar neutrino flux via CEνNS interactions. Not only do CEνNS have a much higher cross section compared to electron interactions, but they are also flavor independent and therefore reduce the systematic uncertainties introduced by neutrino flavor conversion. The key ingredients needed for such an experiment are low energy thresholds, which are already reached by experiments like CRESST, and high exposures as well as low background rates.

8.3.2 Testing the MSW effect

The MSW effect describes neutrino flavor conversions in matter of varying density [152]. Neutrinos in the Sun are produced as electron neutrinos, ν_e. The different potentials electron neutrinos and non-electron neutrinos, ν_a ($a \in \mu, \tau$), "feel" while traveling through the Sun, influences the evolution of the flavor states of the neutrinos[4]. The difference in the potentials is written as [158]:

$$V \equiv V_e - V_a = \sqrt{2} G_F n_e \tag{8.16}$$

with G_F being the Fermi coupling constant and n_e the number density of electrons.

This effect depends on the energy of the neutrino (See app. B for a brief overview on the MSW effect and its dependence on the neutrino energy). At low energies, the MSW effect is subdominant and the neutrino flavor transition is given by the vacuum oscillations. At high energies, the MSW effect has a strong influence on the expected survival probability of electron neutrinos.

Figure 8.15 shows the expected energy dependend survival probability for electron neutrinos to be measured as such ($P(\nu_e \rightarrow \nu_e)$) as a function of the neutrino energy in the Large Mixing Angle (LMA) MSW solution and the measured probabilities by the

[4]This is an additional effect on top of the standard vacuum neutrino oscillations.

Borexino collaboration for *pp*, *Be7*, *pep* and *B8* neutrinos in comparison. This shows that the LMA MSW effect provides a very good description of the measured data.

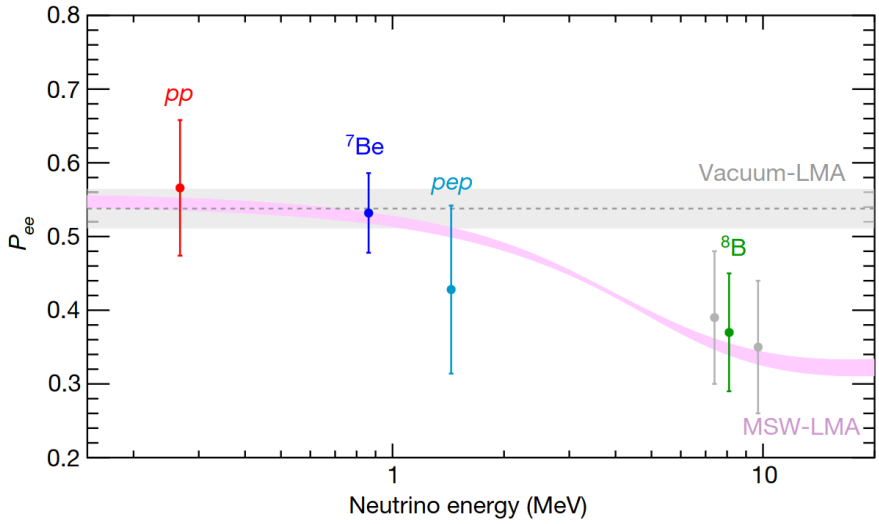

Figure 8.15: Comparison of the theoretical prediction of the LMA MSW effect and the measured values (by Borexino) of the electron neutrino survival probability as a function of energy. Figure taken from [149].

Nevertheless, the observables of the measured fluxes are highly model dependend and show large uncertainties. To determine the survival probability, the measured flux has to be compared to a model dependent expectation of the full flux given by theory. A fully flavor independent measurement of the full flux of neutrinos in combination with the results of electron scattering experiments will help to test the MSW theory with higher precision. Deviations from the MSW effect, often parametrized with the factor A_{MSW} by setting $G_F \rightarrow A_{MSW} G_F$ [159, 160], would point to physics beyond the standard model, like e.g. the existence of sterile neutrinos.

8.3.3 Likelihood framework

The simulated experiments in this section are assuming a detector setup with tonne-scale exposures. Therefore, following the reasoning of the previous section, the poissonian likelihood is used in a binned form. The final form of the nLL is the same as in eq. 8.14 with two important differences. The solar neutrino fluxes are now considered the main parameters of interest and thus neither the pdf for the generation of Monte Carlo data, nor the likelihood contain terms corresponding to a dark matter signal. Instead, a flat

background (b) with rate r_b is added to the picture. The final binned pdf $f_i = f_{i,b} + \sum_\nu f_{i,\nu}$ (for the ith bin) changes accordingly to:

$$f_i = \frac{1}{N_e} \cdot \int_{E_{R,i}^{low}}^{E_{R,i}^{up}} \tilde{f}_b(E_R, r_b) + \sum_\nu \tilde{f}_\nu(E_R, \phi_\nu) dE_R \tag{8.17}$$

with:

$$N_e = \int_{E_{thr}}^{\infty} \tilde{f}_b(E_R, r_b) + \sum_\nu \tilde{f}_\nu(E_R, \phi_\nu) dE_R \tag{8.18}$$

The terms $\tilde{f}_\nu(E_R, \phi_\nu)$ are again the same as in eq. 8.11, the background term is:

$$\tilde{f}_b(E_R, r_b) = \epsilon \cdot r_b \cdot \frac{dR_b}{dE_R}(E_R) \tag{8.19}$$

with $\frac{dR_b}{dE_R}(E_R)$ being a normalized uniform flat distribution.

Another difference to the likelihood function of the previous section are the pull-terms of the nLL (last term in eq. 8.14). In sec. 8.2, the neutrino flux parameters are considered as nuisance parameters, thus there was a pull-term for every neutrino flux parameter. Since the flux normalizations are now the main parameters of the fit, the pull-terms can be chosen to only include a subset of all neutrino fluxes, while the other flux normalization parameters are left completely free in the fit. The reason for this is explained in the following section.

8.3.4 Method and results

For the simulated experiments in this section, two different experimental settings with $CaWO_4$ detectors are used, one best case scenario (BS) and a more conservative one (CS), both are summarized in tab. 8.3. The Monte Carlo data for both settings are generated using the HZ solar model of tab. 8.1.

Table 8.3: The studies performed in this section consider two different experimental settings, both based on $CaWO_4$ as a detector material.

Setting	Threshold (eV)	Exposure (tonne · year)	Background rate (1/(keV kg d))
Best case (BS)	1	1	0.1
Conservative (CS)	1	0.1	1

In a first test, all neutrino flux parameters are left free in the fit (pull terms = 0). The fit

results of 1000 Monte Carlo datasets are shown in fig. 8.16. for the BS and fig. 8.17 for the CS.

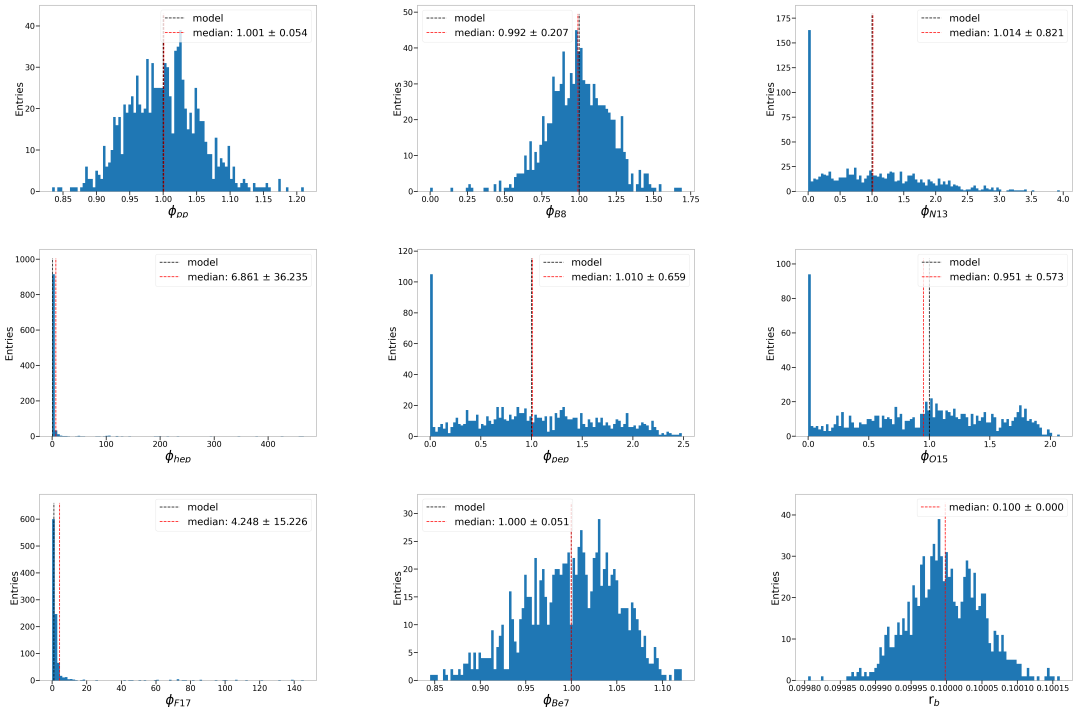

Figure 8.16: Histograms of the fit results of 1000 Monte Carlo simulations in the best case setting without pull terms in the likelihood. The only parameters that are properly reconstructed are the fluxes of *pp*, *B8* and *Be7* neutrinos and the background rate. The black dashed line depicts the model input value, the red dashed line is the median of the reconstructed values. In the legends, the corresponding mean and standard deviation of the distributions are shown.

As can be seen in both cases, the fit can reconstruct the *pp* and *Be7* neutrino fluxes, but has problems in reconstructing the sub dominant components of the neutrino spectrum. In the following two different questions shall be answered for each of the experimental settings:

1) **How well can the experiment reconstruct the fluxes of the dominant neutrino components?** For this questions, all sub dominant components (all CNO neutrinos and *hep* neutrinos) are restricted via pull terms in the likelihood function (around their model values of tab. 8.1), while all other neutrino components and the background rate are left as fully free parameters in the fit (see sec. 8.3.4.1).

2) **How sensitive is the experiment to the metallicity of the Sun?** For this question, all neutrinos of the pp-chain (which have mostly been experimentally measured rather precisely via electron scattering interactions already, with the exception of the *hep*

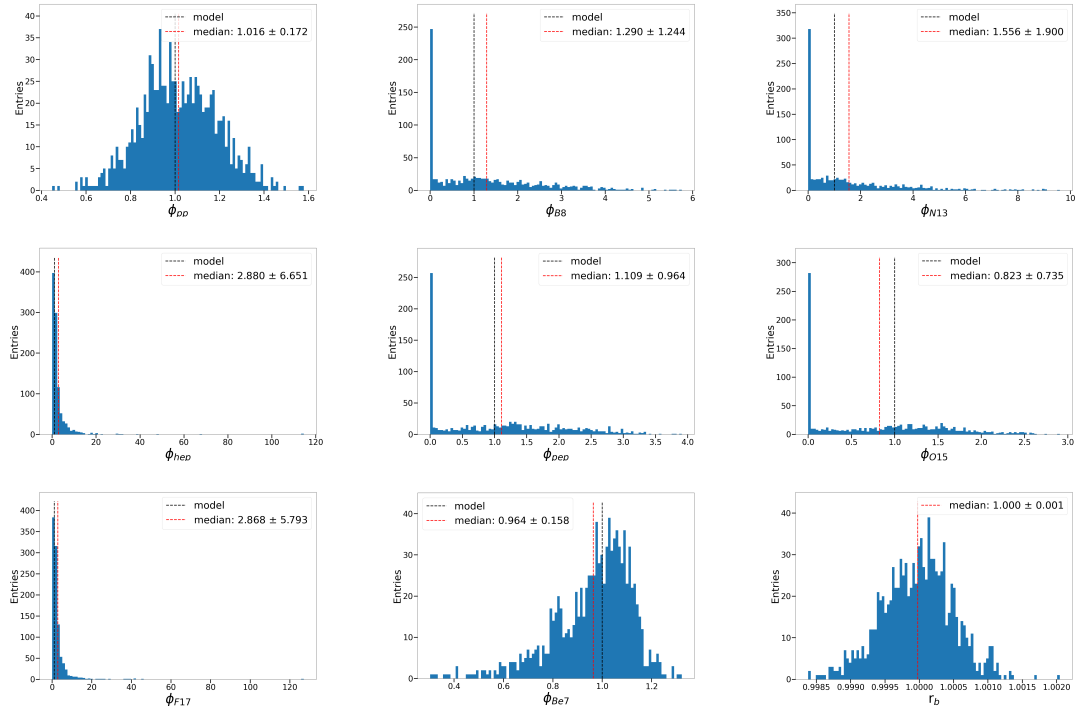

Figure 8.17: Histograms of the fit results of 1000 Monte Carlo simulations in the conservative setting without pull terms in the likelihood. The only parameters that are properly reconstructed are the fluxes of *pp* and *Be7* neutrinos and the background rate. The black dashed line depicts the model input value, the red dashed line is the median of the reconstructed values. In the legends, the corresponding mean and standard deviation of the distributions are shown.

neutrinos) are restricted via pull terms to the values of tab. 8.1, while the fluxes of neutrinos from the CNO-cycle are left as free parameters (see sec. 8.3.4.2).

8.3.4.1 Reconstruction of the dominant neutrino components

The neutrino flux parameters of *N*13, *O*15, *F*17 and *hep* neutrinos are restricted in the fit with pull terms around their model value and within their model uncertainty, assuming the HZ solar model of tab. 8.1.

An example of a fit of a randomly selected Monte Carlo dataset of each experimental setting is shown in figure 8.18. By decreasing the exposure by a factor of 10 and increasing the background rate by the same factor, the overall background level is the same in both settings. The neutrino spectrum is decreased by a factor of 10 in the CS, but the *pp* and *Be7* neutrinos still have a high enough flux, so their spectra are clearly elevated above the flat background level. This shows that even in the CS, the experiment has sensitivity to measuring the fluxes of *pp* and *Be7* neutrinos.

Figure 8.19 shows the resulting fit parameters of the neutrino fluxes and background

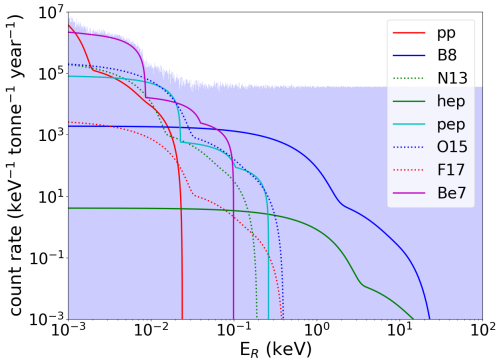

(a) Monte Carlo dataset and fit in the best case setting.

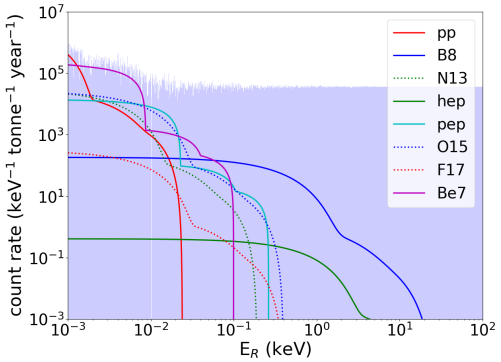

(b) Monte Carlo dataset and fit in the conservative setting.

Figure 8.18: Examples of a single Monte Carlo generated dataset in a) the best case setting and b) the conservative setting. The neutrino flux spectra are scaled with the resulting flux parameters of the fit. The reduced sensitivity in the conservative setting is mostly induced by the higher background rate.

rate for 1000 Monte Carlo simulations of the BS. The results for the CS are shown in fig. 8.20.

The correlations between the fit parameters are shown in fig. 8.21 for the BS and fig. 8.22 for the CS. The figures show the resulting fit parameters of the 1000 Monte Carlo datasets plottet against each other, including the correlation coefficient for each pair of parameters.

In the best case setting, all parameters can be reconstructed by the fit. The *pp* neutrino flux is reconstructed within a maximal deviation of only 5% in 68% of the simulated experiments (see standard deviations in legends). The reconstruction of the *Be*7 neutrino flux is even more precise, with a standard deviation of only 2%. Such high precisions on the fluxes of low energy solar neutrinos are a great opportunity. The reconstruction of fluxes is independent of the solar model or assumptions on the neutrino oscillation parameters. In combination with the measured fluxes in solar neutrino experiments sensitive to a certain neutrino flavor (electron neutrinos), this provides a possibility to test the MSW theory with high precision. The *B*8 flux is sub dominant to the flat background, which leads to a standard deviation of 19.6%. The *pep* neutrino flux shows a rather large standard deviation of 23%[5]. The flux parameter of *Be*7 is anti correlated with the ones of *pp*, *N*13 and *O*15. Below 10 eV, these four components are the dominant ones, leading to a degeneracy of the fit parameters. Other anti correlations are found between *pep* and *N*13 and the strongest one between *O*15 and *pep*, which is expected since both spectra are very similar to each other.

[5]The fit model does not take into account that the ratios of some fluxes are given by theory.

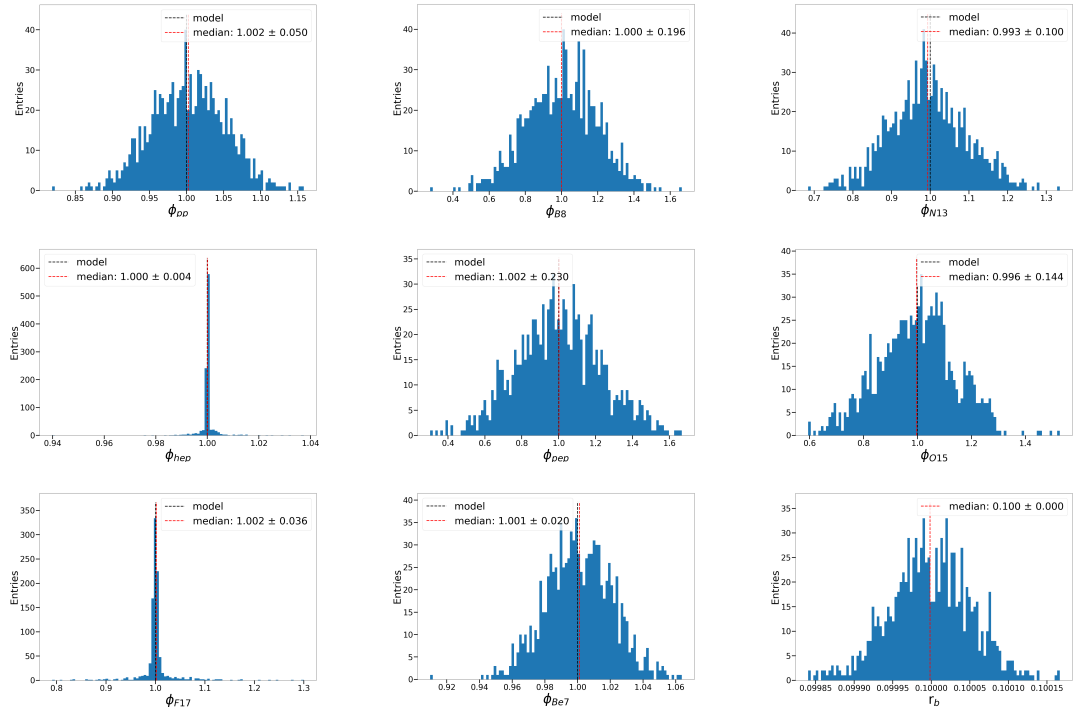

Figure 8.19: Histograms of the fit results of 1000 Monte Carlo simulations in the best case setting with pull terms in the likelihood for the CNO neutrinos and *hep* neutrinos. The black dashed line depicts the model input value, the red dashed line is the median of the reconstructed values. In the legends, the corresponding mean and standard deviation of the distributions are shown. The fit is able to reconstruct all parameters close to their model values.

In the conservative setting, all parameters are reconstructed properly by the fit with the exceptions of the *B*8 and *hep* neutrino fluxes. The *pp* neutrino flux shows a slight systematic shift of 2.9% above the model input value. This shift could be the result of a statistical fluctuation or of correlations to other parameters. The largest correlation of the *pp* flux parameter is to the one of the *Be*7 flux, which does not show a systematic shift. The standard deviations are larger compared to the BS case, due to the decreased exposure and higher background rate. The *pp* flux shows a standard deviation of about 16% and the *Be*7 flux of 6.5%. Since the *pp* and *Be*7 fluxes are the only ones high enough to dominate over the flat background, their anti correlation appears slightly stronger. At the same time, the uncertainty on both of their fluxes is increased compared to the BS, probably causing the correlations between other fluxes to be weaker in the CS. The positive correlations between *O*15 with *N*13 and *F*17 with *hep* are again visible, but weaker than in the BS. Interestingly, the strong anti correlation between the *O*15 and *pep* flux parameters disappeared completely and the correlation between the *Be*7 and *hep* flux parameters changed sign between the two settings.

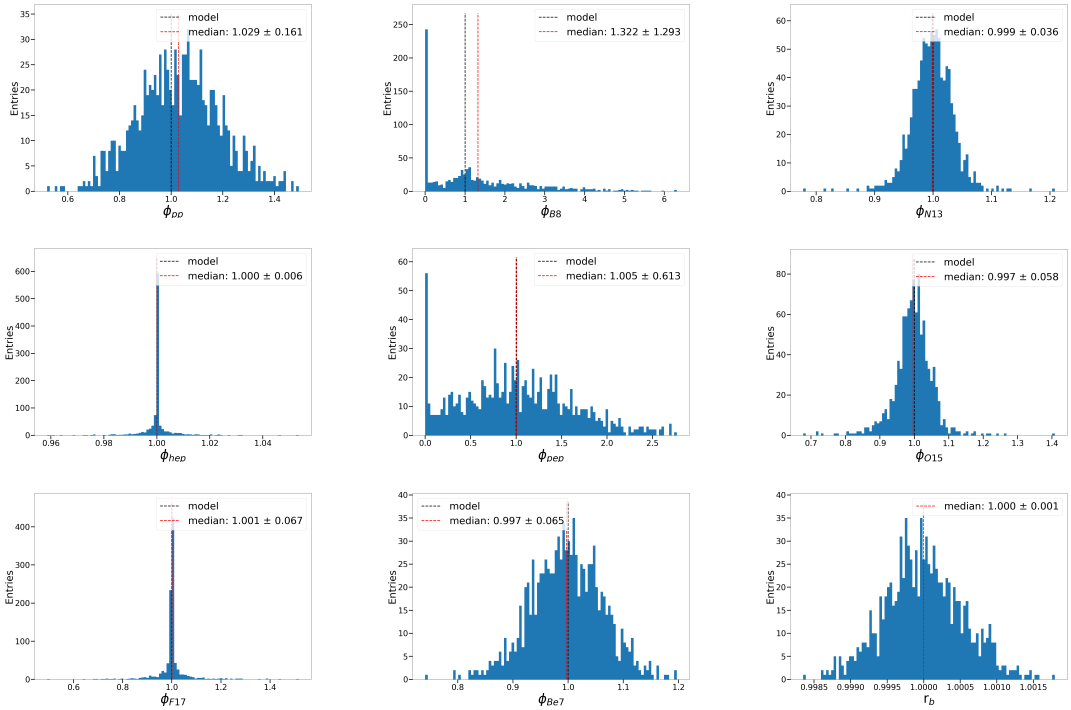

Figure 8.20: Histograms of the fit results of 1000 Monte Carlo simulations in the conservative setting with pull terms in the likelihood for the CNO neutrinos and *hep* neutrinos. The black dashed line depicts the model input value, the red dashed line is the median of the reconstructed values. In the legends, the corresponding mean and standard deviation of the distributions are shown. The fit is able to reconstruct most parameters at their model values. Both the *B*8 and the *hep* neutrino fluxes are sub dominant below the flat background or the other neutrino flux components and are not reconstructed properly in most cases.

The background rate is perfectly reconstructed by the fit in both experimental settings.

Conclusion: Given the low threshold of 1 eV, the fluxes of the *pp* and *Be7* neutrinos can be well reconstructed in both experimental settings, altough with a higher accuracy in the BS. Reconstructing the fluxes of *B*8 and *pep* neutrinos is only possible in the BS, though with rather large uncertainties of about 20% in both cases. Overall it appears that the sensitivity to the dominant neutrino fluxes is limited more by the background rate than by the exposure. To confirm this hypothesis, more experimental settings with varying exposures and background rates will be compared in a follow up of this work.

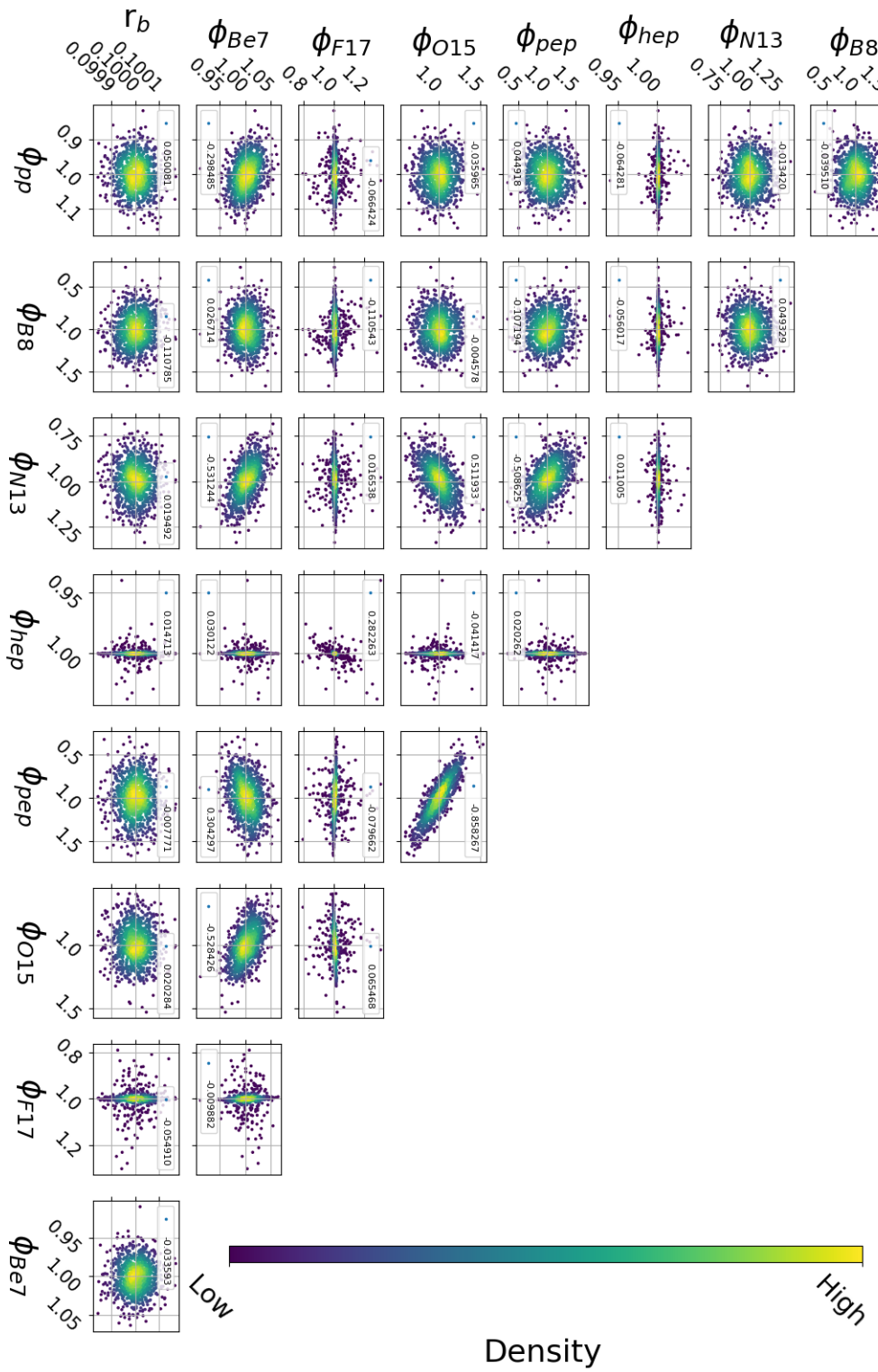

Figure 8.21: All fit parameters of 1000 Monte Carlo simulations in the best case setting plottet against each other. The CNO and *hep* neutrino fluxes are restricted with pull terms in the likelihood. The correlation coefficients for each pair of parameters is given in the legends.

Figure 8.22: All fit parameters of 1000 Monte Carlo simulations in the conservative setting plottet against each other. The CNO and *hep* neutrino fluxes are restricted with pull terms in the likelihood. The correlation coefficients for each pair of parameters is given in the legends.

8.3.4.2 Sensitivity to the solar metallicity

In this section, the flux parameters of all neutrinos of the pp-chain are restricted by pull terms in the likelihood (around their model values and within the theoretical uncertainty of tab. 8.1), while the three fluxes of the neutrinos of the CNO-cycle are left as fully free parameters.

The resulting distribution of fit parameters for the CNO neutrinos is shown in fig. 8.23 for the BS and in fig. 8.24 for the CS.

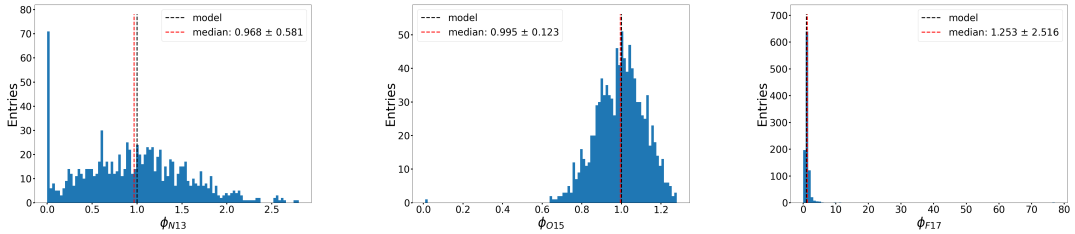

Figure 8.23: Histograms of the fit results of 1000 Monte Carlo simulations in the best case setting with pull terms in the likelihood for the flux parameters of neutrinos from the pp-chain. The black dashed line depicts the model input value, the red dashed line is the median of the reconstructed values. In the legends, the corresponding mean and standard deviation of the distributions are shown. The fits are only able to reconstruct the flux of the $O15$ neutrinos with a standard deviation of 12.3% and the $N13$ neutrinos with a very large standard deviation of 58%. The flux of the $F17$ neutrinos is far too small to be properly reconstructed.

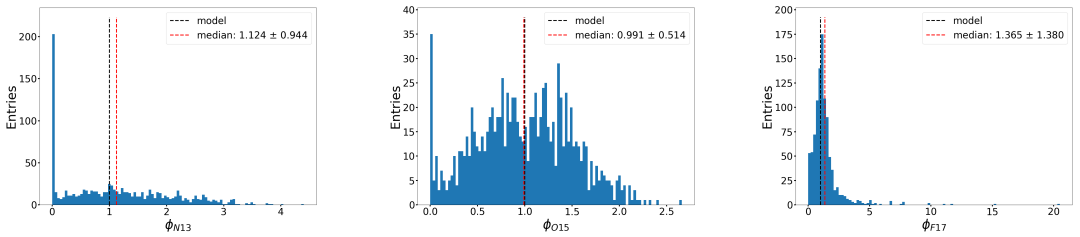

Figure 8.24: Histograms of the fit results of 1000 Monte Carlo simulations in the conservative setting with pull terms in the likelihood for the flux parameters of neutrinos from the pp-chain. The black dashed line depicts the model input value, the red dashed line is the median of the reconstructed values. In the legends, the corresponding mean and standard deviation of the distributions are shown. The fluxes of the $N13$ and $F17$ neutrinos cannot be reconstructed by the fit and the flux of the $O15$ neutrinos has a large standard deviation of 51%.

The correlations between all parameters for 1000 Monte Carlo simulations is shown in fig. 8.25 for the BS and in fig. 8.26 for the CS.

The flux of $O15$ neutrinos shows an anti correlation with the $N13$ neutrinos in both settings. In the BS, a positive correlation of the $O15$ neutrinos with $Be7$ neutrinos can be

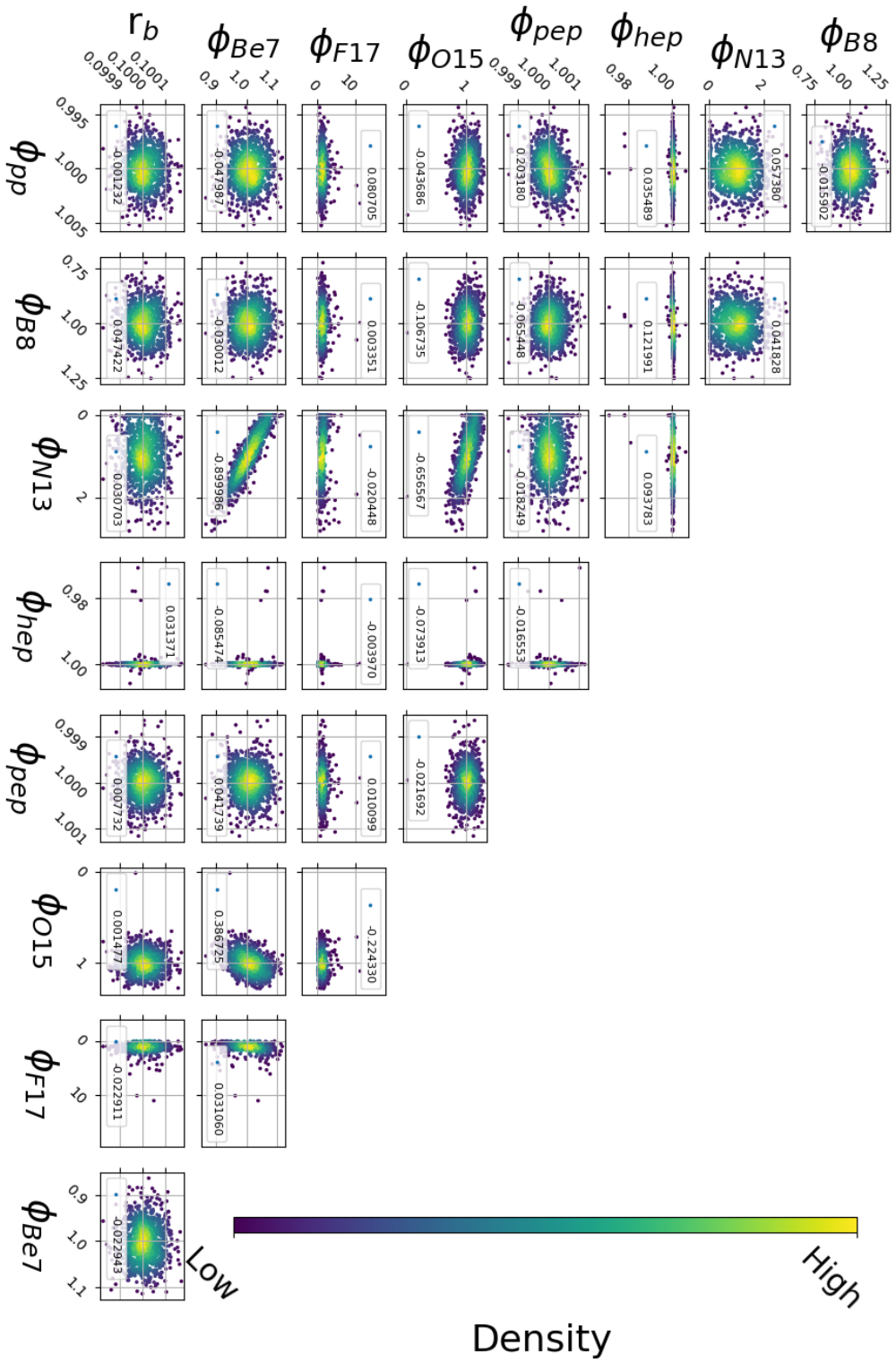

Figure 8.25: All fit parameters of 1000 Monte Carlo simulations in the best case setting plottet against each other. The pp-chain neutrino fluxes are restricted with pull terms in the likelihood. The correlation coefficients for each pair of parameters is given in the legends.

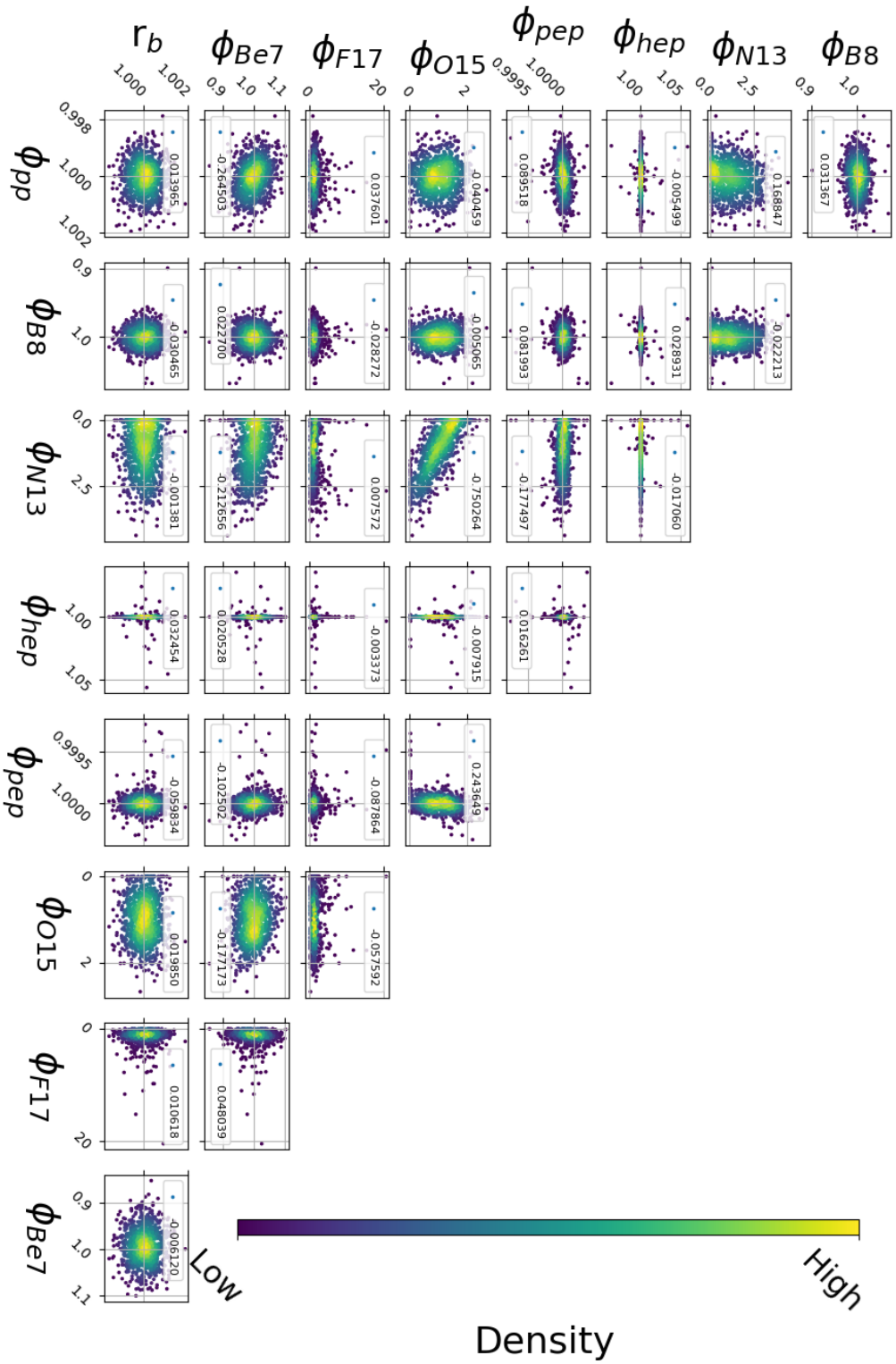

Figure 8.26: All fit parameters of 1000 Monte Carlo simulations in the conservative setting plottet against each other. The pp-chain neutrino fluxes are restricted with pull terms in the likelihood. The correlation coefficients for each pair of parameters is given in the legends.

seen, while in the CS there is a weak positive correlation with *pep* neutrinos. The $N13$ neutrino flux in turn is rather strongly anti correlated with the $Be7$ neutrinos in the BS and to a much weaker extend also in the CS. The flux of the $F17$ neutrinos show only a weak anti correlation with the $O15$ neutrinos in the BS.

Since there is essentially not much sensitivity to the individual fluxes of the CNO neutrinos, from here on the sum of the three fluxes will be combined into a single fit parameter, ϕ_{CNO}, following the approach of Borexino in [153]. The statistical significance of the fitted summed CNO neutrino flux is tested against two different hyptotheses:

- How statistically significant is the fit parameter of the CNO neutrinos compared to the null hypothesis of **no CNO neutrinos**?
- With how much confidence could an experiment reject a **LZ solar model** (null hypothesis = LZ solar model)?

The differences between the HZ model, the LZ model and the model without CNO neutrinos are rather small. The theoretical differential spectrum of the solar neutrino flux in all three cases is shown in fig. 8.27

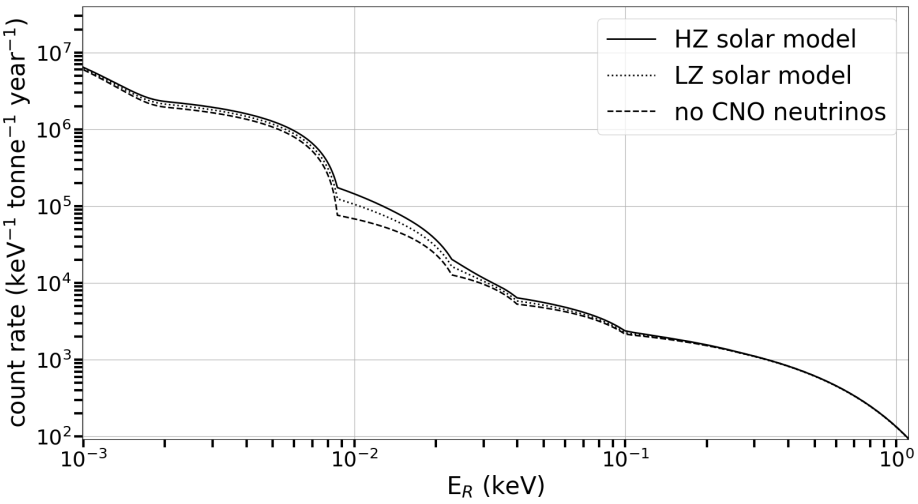

Figure 8.27: Differences in the theoretical differential spectrum of the total solar neutrino flux in the three cases of a HZ solar model, a LZ solar model and a model containing no CNO neutrinos.

The model BS05(OP) shows the largest deviations compared to helioseismological results in [142] and is therefore chosen as a LZ model in this section. Table 8.4 contains the factors for each of the flux parameters that transforms the HZ model of tab. 8.1 into the LZ model BS05(OP).

Table 8.4: Multiplying the flux parameters of the BP04(Garching) model with the factors given in this table leads to the low-metallicity BS05(OP) model.

flux ϕ_ν	pp	B8	N13	hep	pep	O15	F17	Be7
factor f_ν	1.0084	0.9913	0.5386	1.0063	1.0071	0.4679	0.9949	1.0000

As can be seen, most neutrino fluxes differ by less than 1% between the models (including the $F17$ neutrino flux), while the fluxes of $N13$ and $O15$ neutrinos are reduced by roughly a factor of two. The factor of the summed CNO flux parameter is given by (see eq. A.33 in app. A.7):

$$\phi_{CNO,LZ} = 0.5083 \cdot \phi_{CNO,HZ} \tag{8.20}$$

The fitted sum of CNO neutrinos for 2000 Monte Carlo simulations in both experimental settings is shown in fig. 8.28.

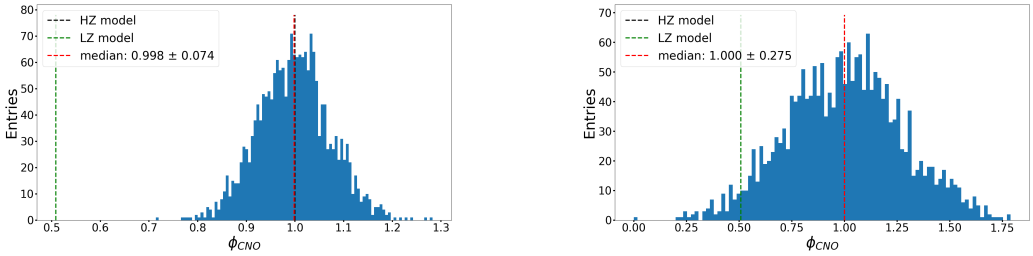

(a) Histogram of fit results for ϕ_{CNO} in the BS.

(b) Histogram of fit results for ϕ_{CNO} in the CS.

Figure 8.28: Histograms of the fit results of 2000 Monte Carlo simulations (generated with a HZ solar model) for the summed CNO flux in a) the best case and b) the conservative setting with pull terms in the likelihood for the flux parameters of neutrinos from the pp-chain. The black dashed line depicts the model input value, the red dashed line is the median of the reconstructed values. In the legends, the corresponding mean and standard deviation of the distributions are shown. Additionally, the green dashed line shows the expected value for a LZ solar model. The flux can be reconstructed by the fit in both cases, but with an increased standard deviation in the CS compared to the BS.

With a standard deviation of only 7.4%, the reconstructed CNO flux can clearly be attributed to the HZ model in the BS. The large standard deviation of 27.5% in the CS leads to some overlap of the distribution of reconstructed CNO flux parameters with the expectation for a LZ solar model.

The statistical significance of these results is quantified with two hypothesis tests. For each setting, 4000 Monte carlo simulations are performed under both null hypotheses

to create a distribution of the observed profile likelihood test statistic. For the null hypothesis of **no CNO neutrinos** the following test statistic is used:

$$q_{obs} = \begin{cases} -2 \cdot \ln\left(\frac{\mathcal{L}(\phi_{CNO}=0, \hat{\hat{\boldsymbol{\phi}}}_{pp-\nu}, \hat{\hat{r}}_b)}{\mathcal{L}(\hat{\phi}_{CNO}, \hat{\boldsymbol{\phi}}_{pp-\nu}, \hat{r}_b)}\right) & , \hat{\phi}_{CNO} > 0 \\ 0 & , \hat{\phi}_{CNO} < 0 \end{cases} \tag{8.21}$$

In the case of the null hypothesis of a **LZ solar model**, the following test statistic is used instead:

$$q_{obs} = \begin{cases} -2 \cdot \ln\left(\frac{\mathcal{L}(\phi_{CNO}=0.5083, \hat{\hat{\boldsymbol{\phi}}}_{pp-\nu}, \hat{\hat{r}}_b)}{\mathcal{L}(\hat{\phi}_{CNO}, \hat{\boldsymbol{\phi}}_{pp-\nu}, \hat{r}_b)}\right) & , \hat{\phi}_{CNO} > 0.5083 \\ 0 & , \hat{\phi}_{CNO} < 0.5083 \end{cases} \tag{8.22}$$

In both cases the description of the test statistic under the null hypothesis with a half-χ^2_1 distribution is a good, but slightly conservative approximation[6]. Therefore the statistical significance can simply be expressed by Z = $\sqrt{q_{obs}}$, using eq. A.30.

For both settings, 4000 Monte carlo datasets are generated under the HZ solar model and the corresponding observables of the test statistic of eq. 8.21 and 8.22 are calculated. The results for the CS are shown in fig. 8.29.

The mean of q_{obs} of the Monte Carlo data generated under the HZ solar model in fig. 8.29a (no CNO neutrinos) corresponds to a significance of Z = 3.26σ, with about 56.6% of all simulations leading to a Z $\geq$ 3 and 1.40% of all simulations leading to a Z $\geq$ 5. The mean of q_{obs} under the HZ solar model in fig. 8.29b (LZ solar model) corresponds to a significance of only Z = 1.74σ, with only 3.83% of the simulations leading to a Z $\geq$ 3 and 0% leading to Z $\geq$ 5. This means **under the conservative setting, there is not enough sensitivity to distinguish between a HZ and a LZ solar model**. Moreover, **the** CNO **flux can be reconstructed with a significance of at least 3σ only with a confidence level of 56.6%**.

The results for the BS are shown in fig. 8.30.

The mean of q_{obs} of the Monte Carlo data generated under the HZ solar model in fig. 8.30a (no CNO neutrinos) corresponds to a significance of Z = 14.70σ, with a 100% of all simulations leading to a Z $\geq$ 5. The mean of q_{obs} under the HZ solar model in fig. 8.30b (LZ solar model) corresponds to a significance of Z = 6.80σ, with a 100% of the simulations leading to a Z $\geq$ 3 and 95.5% leading to Z $\geq$ 5. This means **under the best case setting**, even with the conservative approximation of $f(q_{obs}|H_0) = \frac{1}{2}\chi^2_1$, **there is a 100% probability for a 5σ discovery of the summed CNO neutrino flux**. Moreover, **the LZ solar model can be excluded with a significance of 5σ at a confidence level of 95.5%**.

[6] Especially in the test statistic of eq. 8.22, the approximation with a half χ^2_1 distribution leads to conservative results.

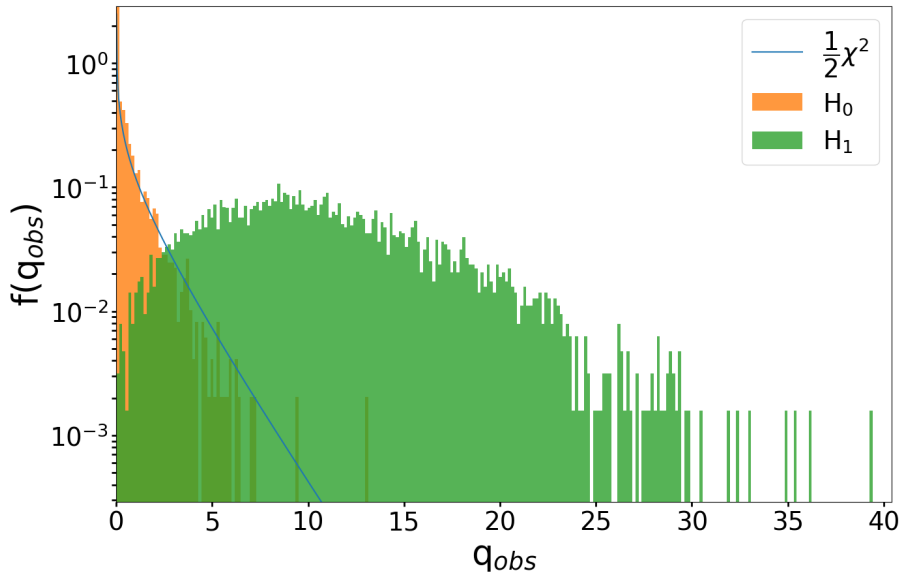

(a) Distribution of the test statistic of eq. 8.21 under H_0 'no CNO neutrinos' (orange) and H_1 (green).

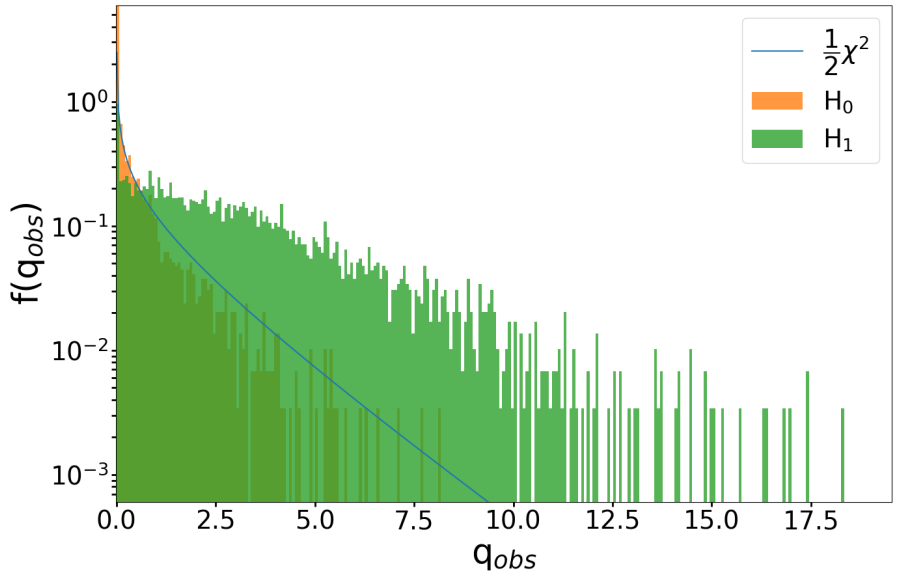

(b) Distribution of the test statistic of eq. 8.22 under H_0 'LZ solar model' (orange) and H_1 (green).

Figure 8.29: Distributions of the test statistic in the conservative setting. a) Testing the null hypothesis of 'no CNO' neutrinos, b) testing the null hypothesis of a 'LZ solar model'. In both cases, the distribution under the null hypothesis, H_0, can be approximated by a half-χ^2_1 distribution.

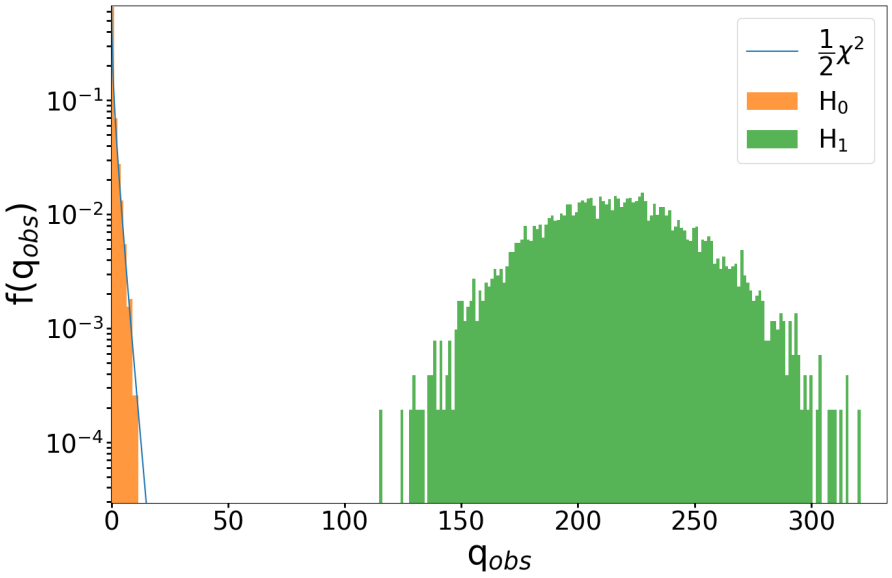

(a) Distribution of the test statistic of eq. 8.21 under H_0 'no CNO neutrinos' (orange) and H_1 (green).

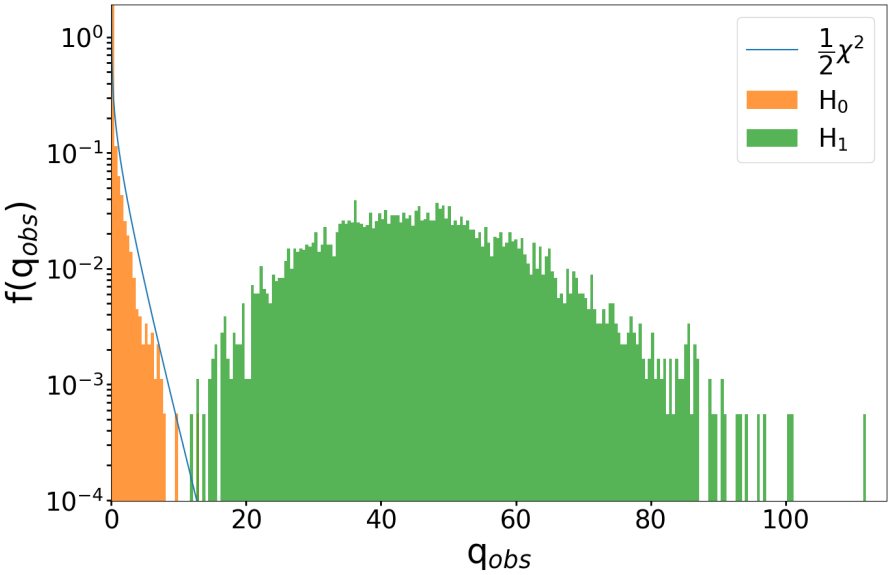

(b) Distribution of the test statistic of eq. 8.22 under H_0 'LZ solar model' (orange) and H_1 (green).

Figure 8.30: Distributions of the test statistic in the best case setting. a) Testing the null hypothesis of 'no CNO' neutrinos, b) testing the null hypothesis of a 'LZ solar model'. In both cases, the distribution under the null hypothesis, H_0, can be approximated by a half-χ^2_1 distribution.

Outlook: Only two experimental settings were investigated in this section, representing a best case scenario and a conservative one. In an upcoming work, more settings

inbetween the two tested in this work will be included. The goal is to scan through the parameters of the experimental settings in order to calculate the sensitivity as a function of the exposure, background rate and energy threshold.

Chapter 9

Conclusions and Outlook

The question about the nature of dark matter is a long-standing problem in modern physics. Since several decades a large number of experiments have been designed to solve this puzzle. One of the leading experiments in the field of dark matter direct detection is CRESST. Its aim is to measure elastic coherent scatterings of dark matter particles off nuclei occuring inside the detector. In the case of CRESST, the target are scintillating crystals of different material, equipped with a tungsten transition edge sensor and operated as cryogenic calorimeters at $\mathcal{O}$(mK) temperatures. The detector module design of the third stage, CRESST-III, allows to probe energy regions down to thresholds of only $\mathcal{O}$(10eV), making it especially sensitive to light dark matter masses in the sub-GeV regime.

At these low energies, an excess of events of unknown origin is observed, limiting the sensitivity to dark matter signals. The study of this low energy excess (LEE) is one of the major topics of this work. In chapter 6, it is discussed as several hypotheses on the origin of the LEE could be excluded based on data collected with a set of modified detector modules. The observations exclude or disfavour dark matter interactions, external and intrinsic radioactivity, noise triggers, electronic artifacts or scintillation light as a major component of the LEE. Possible origins that could not be excluded and are under further investigation are crystal intrinsic effects related to the material, sensor related effects, e.g. stress created by the TES film deposition, and holding induced stress. These observations and conclusions are published in [107]. Further detailed studies on the LEE are presented in chapter 7 as part of the analysis of two sapphire detector modules. These modules have been operated in two different data taking campaigns with changes in their module design between the measurements. The scintillating foil (covering the inside of the copper housing containing the detectors) and the scintillating holding sticks of the detectors have been removed. The comparison of the measured energy spectra leads to the conclusion that the scintillating components of the detector modules (foil and holding sticks) cannot be a major source of the excess. In particular the investigation of the time dependence of the rate, as well as the time dependence of the spectral shape of the LEE hint towards the contribution of at least two different sources making up the LEE. These components are empirically well described by a power law and an

exponential term. The time dependent behaviour of both components is not compatible with a dark matter signal, confirming the conclusions drawn in chapter 6. The strong influence a warm up of the cryostat to temperatures of 60 K and 30 K has on the rate of the LEE could hint towards a temperature induced stress on the detector, which could originate from the holding of the crystals or the sensor film on the crystal. Furthermore, the rate of the LEE is decaying over time. This decay is observed in both components of the empirical fit. Lastly, the rate of the LEE seems to converge to a stable value not further decaying. A fit of the time dependence of the two components (exponential and power law) shows that the exponential term seems to include a constant, non-decaying part. A conclusion on whether the power law component has a constant contribution to the LEE or if it decays completely cannot be drawn from the data analyzed in this work. By the time of writing this thesis, more data is already available, which could possibly answer this open point.

The analysis of one of the sapphire modules in chapter 7 resulted in several new observations, including two novel ways for an accurate low energy calibration. The phonon channel of this detector could be calibrated using a peak at 1.1 keV, appearing in the neutron calibration data. This peak is explained by nuclear recoils induced by a γ emission, which follows after the capture of a thermal neutron on ^{27}Al. While the first experimental proof of this effect was recently measured with $CaWO_4$ crystals (with a capture of thermal neutrons by W) and published by the CRAB and the NUCLEUS collaboration in [124] and by the CRESST collaboration in [125], this is the first time this effect is experimentally measured on a sapphire crystal. The light channel of the same module could be calibrated at very low energies via vacuum ultra violet intrinsic luminescence photons with an energy of 7.6 eV, emitted by the sapphire crystal of the main absorber. This is the first time single photons could be measured in a cryogenic solid state detector with a high enough resolution to clearly identify them. Due to the extremely low threshold of this module ($E_{th} = 6.2 \pm 1.0$ eV) and the accurate energy calibration at low energies a new exclusion limit on the elastic, spin-independent dark matter-nucleon scattering cross section as a function of the dark matter particle mass could be calculated, giving leading exclusion limits in a dark matter mass range from 69 MeV/c^2 to 203 MeV/c^2. Due to the high abundance of the ^{27}Al isotope (100%) with a nuclear spin of 5/2, an exclusion limit on spin-dependent dark matter interactions can also be calculated for this detector, which will be done in a future work.

Lastly, this thesis covers some future perspectives of cryogenic solid state detector experiments in chapter 8. The impact of solar neutrinos on the future of low-threshold, high-exposure dark matter direct detection experiments is investigated in the first part. Dark matter discovery potentials are computed for several experimental scenarios, including different target materials, thresholds and exposures. The calculated discov-

ery potentials reflect the best possible results under the assumption of no additional backgrounds. The results show that sensitivity to dark matter signals can be achieved even below the neutrino floor in experiments with exposures of $\mathcal{O}$(1 tonne year) and energy thresholds of $\mathcal{O}$(1 eV). The target materials tested in these sensitivity studies are $CaWO_4$ and Al_2O_3. While the discovery potentials calculated for $CaWO_4$ are stronger over a large fraction of the considered dark matter mass range ($\sim$ 250 MeV/c^2 - 10 GeV/c^2), the discovery potential calculated for the lighter material Al_2O_3 under the same experimental assumptions is much stronger in the low mass range (50 MeV/c^2 - 250 MeV/c^2).

The second part of chapter 8 considers solar neutrinos as a signal and explores the possibilities that come with a fully flavor independent measurement of the solar flux. Two experimental scenarious are tested, both assume an energy threshold of 1 eV. The first scenario considers an exposure of 1 tonne year and a background rate of 0.1 counts/(keV kg day), the second scenario considers an exposure of 0.1 tonne year and a background rate of 1 count/(keV kg day). It is shown that the dominant neutrino fluxes of *pp* neutrinos and *Be7* neutrinos can be well reconstructed in both tested experimental scenarios, although with a higher accuracy in the first setting. The precise reconstruction of the fluxes of these low energetic neutrinos in combination with the results of experiments measuring the electron scattering of such neutrinos opens up the possibility to test the MSW effect. Deviations from the expectations of the MSW effect could be a hint towards physics beyond the standard model, like e.g. the existence of sterile neutrinos. The sensitivity to the dominant neutrino fluxes seems to be limited more by the background rate than by the exposure. This hypothesis will be tested in an upcoming work. Studies on the sensitivity to the summed flux of the CNO neutrinos were additionally performed. An accurate reconstruction of this flux can help to contribute to the solution of the solar metallicity problem. Monte Carlo simulations generated considering a high metallicity solar model show that the first experimental scenario is fully sufficient to reject a low metallicity model with high probability (5σ at 95.5% C.L.). In a future work, the sensitivity to the CNO flux will be calculated as a function of the parameters defining the experimental setting, which are the exposure, the energy threshold and the background rate.

Appendix A

Auxiliary calculations

A.1 Elastic scattering in the center-of-mass frame

As can be seen in eq. 3.1, the energy transferred to the nucleus depends on the transferred momentum q, which describes the difference of the momenta of the final state (f) and initial state (i) of the nucleus:

$$|\overrightarrow{q}| = |\overrightarrow{p_{Nf}} - \overrightarrow{p_{Ni}}| = |\overrightarrow{p^0_{Nf}} - \overrightarrow{p^0_{Ni}}| \tag{A.1}$$

which is equal in the laboratory frame and the center-of-mass frame, denoted with 0. The velocity of the center-of-mass is defined as:

$$\overrightarrow{v^0} = \frac{\sum_j m_j \overrightarrow{v_j}}{\sum_j m_j} \tag{A.2}$$

The initial velocities of the dark matter particle and the nucleus in the laboratory frame are:

$$\overrightarrow{v_{\chi i}} = \begin{pmatrix} v \\ 0 \end{pmatrix} \qquad \overrightarrow{v_{Ni}} = \begin{pmatrix} 0 \\ 0 \end{pmatrix} \tag{A.3}$$

The initial velocity of the center-of-mass is therefore:

$$\overrightarrow{v^0_i} = \frac{m_\chi}{m_\chi + m_N} \overrightarrow{v_{\chi i}} \tag{A.4}$$

The initial velocities of the dark matter particle and the nucleus in the center-of-mass frame are (galilean tranformation):

$$\begin{aligned} \overrightarrow{v^0_{\chi i}} &= \overrightarrow{v_{\chi i}} - \overrightarrow{v^0_i} = \frac{m_N}{m_\chi + m_N} \overrightarrow{v_{\chi i}} \\ \overrightarrow{v^0_{Ni}} &= \overrightarrow{v_{Ni}} - \overrightarrow{v^0_i} = -\frac{m_\chi}{m_\chi + m_N} \overrightarrow{v_{\chi i}} \end{aligned} \tag{A.5}$$

from which follows:

$$\begin{aligned} \overrightarrow{p^0_{\chi i}} &= m_\chi \overrightarrow{v^0_{\chi i}} = \mu_N \overrightarrow{v_{\chi i}} \\ \overrightarrow{p^0_{Ni}} &= -\overrightarrow{p^0_{\chi i}} = -\mu_N \overrightarrow{v_{\chi i}} \end{aligned} \tag{A.6}$$

with μ_N being the reduced mass of the system of the dark matter particle and the nucleus. Furthermore, from momentum and energy conservation follows (in the center-of-mass frame):

$$\begin{aligned} |\overrightarrow{v^0_{\chi i}}| &= |\overrightarrow{v^0_{\chi f}}| \\ |\overrightarrow{v^0_{Ni}}| &= |\overrightarrow{v^0_{Nf}}| \end{aligned} \tag{A.7}$$

The momentum of the nucleus after the scattering process can now be written as:

$$\begin{aligned} \overrightarrow{p^0_{Nf}} &= |\overrightarrow{p^0_{Nf}}| \cdot \begin{pmatrix} -cos\theta \\ sin\theta \end{pmatrix} \\ &= |\overrightarrow{p^0_{Ni}}| \cdot \begin{pmatrix} -cos\theta \\ sin\theta \end{pmatrix} \\ &= \mu_N v \cdot \begin{pmatrix} -cos\theta \\ sin\theta \end{pmatrix} \end{aligned} \tag{A.8}$$

The momentum transfer in eq. A.1 can now be easily written in the center-of-mass frame as:

$$\overrightarrow{q} = \overrightarrow{p^0_{Nf}} - \overrightarrow{p^0_{Ni}} = \mu_N v \cdot \begin{pmatrix} 1 - cos\theta \\ sin\theta \end{pmatrix} \tag{A.9}$$

And therefore:

$$q^2 = 2\mu_N^2 v^2 (1 - cos\theta) \tag{A.10}$$

A.2 Differential cross section

In the center-of-mass frame, the solid angle of the scattering process only depends on $cos\theta$, so that:

$$d\Omega = 2\pi \, dcos\theta \tag{A.11}$$

The differential cross section can be divided into:

$$\frac{d\sigma}{dE_R} = \frac{d\sigma}{d\Omega} \cdot \frac{d\Omega}{dE_R} = \frac{d\sigma}{dcos\theta} \cdot \frac{dcos\theta}{dE_R} \tag{A.12}$$

Using eq. 3.1, $dcos\theta$ can be determined as:

$$dE_R = -\frac{\mu_N^2 v^2}{m_N} dcos\theta \tag{A.13}$$

An integral from zero to $E_{R,max}$ corresponds to the integral:

$$\int_1^{-1} dcos\theta = -2 \tag{A.14}$$

The differential cross section for a point-like nucleus (pl) can now be written as:

$$\frac{d\sigma}{dE_R}|_{pl} = \frac{d\sigma}{dcos\theta} \cdot \frac{m_N}{2\mu_N^2 v^2} = \sigma_0 \cdot \frac{m_N}{2\mu_N^2 v^2} \tag{A.15}$$

with the definition of the zero-momentum transfer cross section [39]:

$$\sigma_0 = \frac{d\sigma}{dcos\theta}|_{E_R=0} \tag{A.16}$$

If the scattering is approximately isotropic in the limit of the nucleus being point-like, the cross section can be parametrized as [39]:

$$\frac{d\sigma}{dE_R} = \frac{d\sigma}{dE_R}|_{pl} \cdot F^2(E_R) \tag{A.17}$$

to take the structure of the nucleus into account, which is described by the form factor $F(E_R)$ (see sec. 3.1.3).

The cross section for a single, point-like nucleon (proton, p, or neutron, n) has the form [39]:

$$\sigma_{p,n} = \frac{\mu_{p,n}^2}{\pi} f_{p,n}^2 \tag{A.18}$$

with $f_{p,n}$ being the coupling strength of dark matter to protons or neutrons respectively. Considering coherent scattering, the zero-momentum transfer cross section for a point-like nucleus can be expressed as a sum over all nucleons [39]:

$$\sigma_0 = \frac{\mu_N^2}{\pi} \cdot \big(Z f_p + (A - Z) f_n\big)^2 \tag{A.19}$$

with Z being the number of protons and $(A - Z)$ being the number of neutrons. In the isosinglet condition $f_p = f_n$ this can be written as[1]:

$$\sigma_0 = \frac{\mu_N^2}{\pi} \cdot A^2 \cdot f_n^2 \tag{A.20}$$

leading to the known A^2 dependence of the cross section. In order to have a parameter

[1] Also approximating $m_p \simeq m_n$

that is comparable between different experiments/target materials, this is usually written in terms of the material independent cross section on a single nucleon of eq. A.18:

$$\sigma_0 = \sigma_n \cdot A^2 \cdot \frac{\mu_N^2}{\mu_n^2} \tag{A.21}$$

which eventually leads to the expression given in eq. 3.7.

A.3 Integral over the velocity distribution in a non-rotating model

The analytical expression for the function $\mathcal{I}(v_{min})$ in eq. 3.17 for a non-rotating maxwellian model is given in [42] as:

$$\begin{aligned}\mathcal{I}(v_{min}) =& \frac{\mathcal{N}}{\eta}\left(\frac{3}{2\pi w^2}\right)^{1/2} \\ &\cdot \begin{cases} \chi(x_{min}-\eta, x_{min}+\eta) - 2\eta\, exp(-z^2), & x_{min} < z-\eta \\ \chi(x_{min}-\eta, z) - exp(-z^2)(z+\eta-x_{min}), & z-\eta \leq x_{min} < z+\eta \\ 0, & x_{min} \geq z+\eta \end{cases}\end{aligned} \tag{A.22}$$

with:

$$\begin{aligned}\chi(x,y) &= \frac{\sqrt{\pi}}{2}\left[erf(y) - erf(x)\right] \\ x_{min} &= \left(\frac{3 m_N E_R}{4\mu_N^2 w^2}\right)^{1/2} \\ \eta &= \sqrt{\frac{3}{2}}\frac{v_o}{w}\end{aligned} \tag{A.23}$$

and z, w, v_o and $\mathcal{N}$ having the same definition as in sec. 3.1.4.

A.4 Weak nuclear charge

The matrix element in eq. 3.20 can be written in terms of the nuclear form factors for protons, $F_p(q)$ and neutrons, $F_n(q)$ as [88]:

$$\langle g.s.|\,|\hat{\mathcal{M}}|\,|g.s.\rangle = \frac{1}{2}\left[(1-4sin^2\theta_W)Z \cdot F_p(q) - N \cdot F_n(q)\right] \tag{A.24}$$

In the approximation of equal proton and neutron form factors ($F_{p,n}(q) = F(q)$), this is often written in terms of the weak nuclear charge, defined as [88]:

$$Q_W = \left[2(g_u^L + g_u^R) + (g_d^L + g_d^R)\right] \cdot Z + \left[(g_u^L + g_u^R) + 2(g_d^L + g_d^R)\right] \cdot N \tag{A.25}$$

where g are the left- (L) and right- (R) handed couplings of u and d quarks to the Z boson. At tree level (ignoring small radiative corrections), these couplings are given by [161]:

$$\begin{aligned} g_u^L &= +\frac{1}{2} \quad -\frac{2}{3}sin^2\theta_W \\ g_d^L &= -\frac{1}{2} \quad +\frac{1}{3}sin^2\theta_W \\ g_u^R &= \quad\quad -\frac{2}{3}sin^2\theta_W \\ g_d^R &= \quad\quad +\frac{1}{3}sin^2\theta_W \end{aligned} \tag{A.26}$$

Inserting this into eq. A.25 leads to:

$$|Q_W| = \frac{1}{2}\left[(4sin^2\theta_W - 1)Z + N\right] \tag{A.27}$$

A.5 Relation of likelihood ratio test statistic and significance

In case the likelihood ratio test statistic, q, as defined in equations 5.12, 5.19, 8.15, 8.21 and 8.22, follows a half χ^2 distribution with one degree of freedom, the statistical significance, Z, of the best fit obtained with the alternative hypothesis can be simply expressed as the square root of the observed value of q: $Z = \sqrt{q_{obs}}$. This is shown in detail in the following.

Given that the distribution of q under the null hypothesis, H_0, follows a half χ^2 distribution with one degree of freedom:

$$f(q|H_0) = \frac{1}{2}\delta(0) + \frac{1}{2}\frac{1}{\sqrt{2\pi}}\frac{1}{\sqrt{q}} \cdot e^{-q/2} \tag{A.28}$$

and using the definition of the p-value in eq. 5.13, after solving the integral this results in (for $q_{obs} > 0$):

$$p = \frac{1}{2}\left(1 - erf\left(\frac{\sqrt{q_{obs}}}{\sqrt{2}}\right)\right) \tag{A.29}$$

Inserting this into eq. 5.14 for the significance results in:

$$Z = \sqrt{q_{obs}} \tag{A.30}$$

A.6 Relations for the binned poissonian extended maximum likelihood

The likelihood of eq. 8.7 can be rewritten, using the following relations:

$$N_e^{N_o} = N_e^{\sum_i^m k_i} = \prod_i^m N_e^{k_i} \tag{A.31}$$

$$e^{-N_e} = e^{-N_e \sum_i^m f_i} = \prod_i^m e^{-N_e f_i} \tag{A.32}$$

A.7 Conversion factor for the summed CNO flux

The factor in eq. 8.20, transforming the summed flux parameter of CNO neutrinos from the HZ solar model to the LZ solar model is given by:

$$\begin{aligned} \phi_{CNO,LZ} &= \frac{f_{N13} \cdot \phi_{N13,HZ} + f_{O15} \cdot \phi_{O15,HZ} + f_{F17} \cdot \phi_{F17,HZ}}{\phi_{N13,HZ} + \phi_{O15,HZ} + \phi_{F17,HZ}} \\ &= f_{CNO} \cdot \phi_{CNO,HZ} \end{aligned} \tag{A.33}$$

with:

$$\phi_{CNO,HZ} = \phi_{N13,HZ} + \phi_{O15,HZ} + \phi_{F17,HZ} \tag{A.34}$$

Appendix B

The MSW effect

In the following a very brief overview on the MSW effect is given. The difference in the potentials, experienced by electron neutrinos, ν_e, and non-electron neutrinos, ν_a, when traveling through the Sun is given in eq. 8.16. The Hamiltonian of the system changes from $H_0 \rightarrow H = H_0 + V$, with H_0 being the vacuum Hamiltonian. The eigenvalues and eigenstates of H change accordingly from $\nu_1, \nu_2 \rightarrow \nu_{1m}, \nu_{2m}$ (ν_1 and ν_2 are the neutrino mass eigenstates). In a medium of constant density, the mixing of the flavor eigenstates in matter is related to the eigenstates ν_{1m} and ν_{2m} via the mixing angle in matter, θ_m (analogous to the neutrino mixing in vacuum).

In a non-uniform medium, the density changes during the propagation of the neutrino through the medium, $n_e \rightarrow n_e(t)$. Thus, also the mixing angle in matter is changing, $\theta_m \rightarrow \theta_m(n_e(t))$, and a mixing of the eigenstates $\nu_{1m} \leftrightarrow \nu_{2m}$ can occur. If the medium fulfills the **adiabatic condition**, the change of $n_e(t)$ is slow enough, so that mixing of the eigenstates ν_{1m} and ν_{2m} can be neglected and they propagate independently (as they would do in vacuum or in a medium with a constant density). In this case, the flavor composition of the eigenstates is determined by $\theta_m(t)$ (instead of a direct dependency on $n_e(t)$). The admixture of the eigenstates is then just given by the mixing at the production point, θ_m^0.

The flavor mixing in matter ($sin^2 2\theta_m$) becomes maximal, if the **resonance condition** ($l_\nu = l_0\, cos2\theta$) is fulfilled, with l_ν being the oscillation length in vacuum and l_0 being the refraction length in matter. In terms of density and energy, E, this condition is fulfilled at the **resonance density**, n_e^R [152]:

$$n_e^R = \frac{\Delta m^2}{2E} \frac{cos2\theta}{\sqrt{2} G_F} \tag{B.1}$$

where $\Delta m^2 = m_2^2 - m_1^2$ is the quadratic difference of the mass of the eigenstates ν_1 and ν_2 and θ is the mixing angle in vacuum. There are three different scenarios that depend on the initial electron density at the production of the neutrino, n_e^0 [152]:

- The initial mixing is strongly surpressed, $n_e^0 \gg n_e^R$: In this case the flavor transition follows the density change and vacuum oscillations only have a negligible effect.

- The initial mixing is not surpressed, $n_e^0 > n_e^R$: In this regime, the adiabatic conversion interplays with the oscillations.
- No crossing of the resonance layer, $n_e^0 < n_e^R$: Matter effects only give small corrections to the vacuum oscillations.

Since $n_e^R \propto 1/E$, these three cases can also be distinguished by the neutrinos energy: A high energy corresponds to the first case, intermediate energies correspond to the second case and low energies to the third case. This dependence of the MSW effect on the neutrino energy can be seen in the red band in fig. 8.15 in sec. 8.3.2.

Bibliography

[1] J. C. Kapteyn. First Attempt at a Theory of the Arrangement and Motion of the Sidereal System. *Astrophysical Journal*, 55:302, May 1922. Provided by the SAO/NASA Astrophysics Data System. URL: https://ui.adsabs.harvard.edu/abs/1922ApJ....55..302K, doi:10.1086/142670.

[2] J. H. Jeans. The Motions of Stars in a Kapteyn-Universe. *Monthly Notices of the Royal Astronomical Society*, 82(3):122–132, 01 1922. arXiv:https://academic.oup.com/mnras/article-pdf/82/3/122/18250702/mnras82-0122.pdf, doi:10.1093/mnras/82.3.122.

[3] J. H. Oort. Observational evidence confirming Lindblad's hypothesis of a rotation of the galactic system. *Bulletin Astronomical Institute of the Netherlands*, 3:275, April 1927. URL: https://ui.adsabs.harvard.edu/abs/1927BAN.....3..275O.

[4] J. H. Oort. The force exerted by the stellar system in the direction perpendicular to the galactic plane and some related problems. *Bulletin Astronomical Institute of the Netherlands*, 6:249, August 1932. Provided by the SAO/NASA Astrophysics Data System. URL: https://ui.adsabs.harvard.edu/abs/1932BAN....6..249O.

[5] F. Zwicky. Die Rotverschiebung von extragalaktischen Nebeln. *Helvetica Physica Acta*, 6:110–127, January 1933.

[6] Vera C. Rubin and Jr. Ford, W. Kent. Rotation of the Andromeda Nebula from a Spectroscopic Survey of Emission Regions. *Astrophysical Journal*, 159:379, February 1970. Provided by the SAO/NASA Astrophysics Data System. URL: https://ui.adsabs.harvard.edu/abs/1970ApJ...159..379R, doi:10.1086/150317.

[7] V. C. Rubin, Jr. Ford, W. K., and N. Thonnard. Rotational properties of 21 SC galaxies with a large range of luminosities and radii, from NGC 4605 (R=4kpc) to UGC 2885 (R=122kpc). *Astrophysical Journal*, 238:471–487, June 1980. Provided by the SAO/NASA Astrophysics Data System. URL: https://ui.adsabs.harvard.edu/abs/1980ApJ...238..471R, doi:10.1086/158003.

[8] Planck Collaboration. Planck 2018 results - VI. Cosmological parameters. *A&A*, 641:A6, 2020. doi:10.1051/0004-6361/201833910.

[9] Edwin Hubble. A relation between distance and radial velocity among extra-galactic nebulae. *Proceedings of the National Academy of Sciences*, 15(3):168–173, 1929. URL: https://www.pnas.org/doi/abs/10.1073/pnas.15.3.168, doi:10.1073/pnas.15.3.168.

[10] Georges Lemaître. Republication of: A homogeneous universe of constant mass and increasing radius accounting for the radial velocity of extra-galactic nebulae. *General Relativity and Gravitation*, 45:1635–1646, 2013. doi:10.1007/s10714-013-1548-3.

[11] C. L. Bennett, D. Larson, J. L. Weiland, N. Jarosik, G. Hinshaw, N. Odegard, K. M. Smith, R. S. Hill, B. Gold, M. Halpern, E. Komatsu, M. R. Nolta, L. Page, D. N. Spergel, E. Wollack, J. Dunkley, A. Kogut, M. Limon, S. S. Meyer, G. S. Tucker, and E. L. Wright. Nine-year wilkinson microwave anisotropy probe (wmap) observations: Final maps and results. *The Astrophysical Journal Supplement Series*, 208(2):20, sep 2013. URL: https://dx.doi.org/10.1088/0067-0049/208/2/20, doi:10.1088/0067-0049/208/2/20.

[12] A. A. Penzias and R. W. Wilson. A Measurement of Excess Antenna Temperature at 4080 Mc/s. *Astrophysical Journal*, 142:419–421, jul 1965. Provided by the SAO/NASA Astrophysics Data System. URL: https://ui.adsabs.harvard.edu/abs/1965ApJ...142..419P, doi:10.1086/148307.

[13] R. H. Dicke, P. J. E. Peebles, P. G. Roll, and D. T. Wilkinson. Cosmic Black-Body Radiation. *Astrophysical Journal*, 142:414–419, July 1965. doi:10.1086/148306.

[14] D. J. Fixsen. The temperature of the cosmic microwave background. *The Astrophysical Journal*, 707(2):916, nov 2009. URL: https://dx.doi.org/10.1088/0004-637X/707/2/916, doi:10.1088/0004-637X/707/2/916.

[15] Planck Collaboration. Planck 2018 results - I. Overview and the cosmological legacy of Planck. *A&A*, 641:A1, 2020. doi:10.1051/0004-6361/201833880.

[16] R. K. Sachs and A. M. Wolfe. Perturbations of a Cosmological Model and Angular Variations of the Microwave Background. *Astrophysical Journal*, 147:73, January 1967. doi:10.1086/148982.

[17] Richard H. Cyburt, Brian D. Fields, Keith A. Olive, and Tsung-Han Yeh. Big bang nucleosynthesis: Present status. *Rev. Mod. Phys.*, 88:015004, Feb 2016. URL:

https://link.aps.org/doi/10.1103/RevModPhys.88.015004, doi:10.1103/RevModPhys.88.015004.

[18] Particle Data Group. Review of Particle Physics. *Progress of Theoretical and Experimental Physics*, 2022(8), 08 2022. 083C01. arXiv:https://academic.oup.com/ptep/article-pdf/2022/8/083C01/49175539/ptac097.pdf, doi:10.1093/ptep/ptac097.

[19] Douglas Clowe, Marua Brada, Anthony H. Gonzalez, Maxim Markevitch, Scott W. Randall, Christine Jones, and Dennis Zaritsky. A Direct Empirical Proof of the Existence of Dark Matter*. *The Astrophysical Journal*, 648(2):L109, aug 2006. URL: https://dx.doi.org/10.1086/508162, doi:10.1086/508162.

[20] Chandra X-ray Observatory. visited on 13.03.2023. URL: https://chandra.harvard.edu/photo/2006/1e0657/more.html.

[21] Edvige Corbelli and Paolo Salucci. The extended rotation curve and the dark matter halo of M33. *Monthly Notices of the Royal Astronomical Society*, 311(2):441–447, 01 2000. arXiv:https://academic.oup.com/mnras/article-pdf/311/2/441/2881340/311-2-441.pdf, doi:10.1046/j.1365-8711.2000.03075.x.

[22] Rotation curve of spiral galaxy Messier 33 (Triangulum).png. visited on 14.03.2023. URL: https://de.m.wikipedia.org/wiki/Datei:Rotation_curve_of_spiral_galaxy_Messier_33_%28Triangulum%29.png.

[23] Harley Katz, Federico Lelli, Stacy S. McGaugh, Arianna Di Cintio, Chris B. Brook, and James M. Schombert. Testing feedback-modified dark matter haloes with galaxy rotation curves: estimation of halo parameters and consistency with CDM scaling relations. *Monthly Notices of the Royal Astronomical Society*, 466(2):1648–1668, 12 2016. arXiv:https://academic.oup.com/mnras/article-pdf/466/2/1648/10867288/stw3101.pdf, doi:10.1093/mnras/stw3101.

[24] R. D. Peccei and Helen R. Quinn. CP Conservation in the Presence of Pseudoparticles. *Phys. Rev. Lett.*, 38:1440–1443, Jun 1977. URL: https://link.aps.org/doi/10.1103/PhysRevLett.38.1440, doi:10.1103/PhysRevLett.38.1440.

[25] C. Abel et al. Measurement of the Permanent Electric Dipole Moment of the Neutron. *Phys. Rev. Lett.*, 124:081803, Feb 2020. URL: https://link.aps.org/doi/10.1103/PhysRevLett.124.081803, doi:10.1103/PhysRevLett.124.081803.

[26] F. Wilczek. Problem of Strong P and T Invariance in the Presence of Instantons. *Phys. Rev. Lett.*, 40:279–282, Jan 1978. URL: https://link.aps.org/doi/10.1103/PhysRevLett.40.279, doi:10.1103/PhysRevLett.40.279.

[27] Steven Weinberg. A New Light Boson? *Phys. Rev. Lett.*, 40:223–226, Jan 1978. URL: https://link.aps.org/doi/10.1103/PhysRevLett.40.223, doi:10.1103/PhysRevLett.40.223.

[28] A. Ringwald. Axions and Axion-Like Particles. In *49th Rencontres de Moriond on Electroweak Interactions and Unified Theories*, pages 223–230, 2014. arXiv:1407.0546.

[29] Jihn E. Kim and Gianpaolo Carosi. Axions and the strong CP problem. *Rev. Mod. Phys.*, 82:557–601, Mar 2010. URL: https://link.aps.org/doi/10.1103/RevModPhys.82.557, doi:10.1103/RevModPhys.82.557.

[30] Joachim Kopp. Sterile neutrinos as dark matter candidates. *SciPost Phys. Lect. Notes*, page 36, 2022. URL: https://scipost.org/10.21468/SciPostPhysLectNotes.36, doi:10.21468/SciPostPhysLectNotes.36.

[31] Gerard Jungman, Marc Kamionkowski, and Kim Griest. Supersymmetric dark matter. *Physics Reports*, 267(5):195–373, 1996. URL: https://www.sciencedirect.com/science/article/pii/0370157395000585, doi:https://doi.org/10.1016/0370-1573(95)00058-5.

[32] K. Petraki and R.R. Volkas. Review of asymmetric dark matter. *International Journal of Modern Physics A*, 28:1330028, 2013. URL: https://doi.org/10.1142/S0217751X13300287.

[33] Kathryn M. Zurek. Asymmetric Dark Matter: Theories, signatures, and constraints. *Physics Reports*, 537(3):91–121, 2014. URL: https://www.sciencedirect.com/science/article/pii/S0370157313004341, doi:https://doi.org/10.1016/j.physrep.2013.12.001.

[34] Zumalacárregui, Miguel and Seljak, Uroš. Limits on Stellar-Mass Compact Objects as Dark Matter from Gravitational Lensing of Type Ia Supernovae. *Phys. Rev. Lett.*, 121:141101, Oct 2018. URL: https://link.aps.org/doi/10.1103/PhysRevLett.121.141101, doi:10.1103/PhysRevLett.121.141101.

[35] Anne M Green and Bradley J Kavanagh. Primordial black holes as a dark matter candidate. *Journal of Physics G: Nuclear and Particle Physics*, 48(4):043001, feb 2021. URL: https://dx.doi.org/10.1088/1361-6471/abc534, doi:10.1088/1361-6471/abc534.

[36] M. Milgrom. A modification of the Newtonian dynamics as a possible alternative to the hidden mass hypothesis. *The Astrophysical Journal*, 270:365–370, July 1983. doi:10.1086/161130.

[37] Antonio Boveia and Caterina Doglioni. Dark Matter Searches at Colliders. *Annual Review of Nuclear and Particle Science*, 68(1):429–459, 2018. arXiv:https://doi.org/10.1146/annurev-nucl-101917-021008, doi:10.1146/annurev-nucl-101917-021008.

[38] Jennifer M. Gaskins. A review of indirect searches for particle dark matter. *Contemporary Physics*, 57(4):496–525, 2016. arXiv:https://doi.org/10.1080/00107514.2016.1175160, doi:10.1080/00107514.2016.1175160.

[39] Eugenio Del Nobile. *The Theory of Direct Dark Matter Detection*. Springer, 2022. doi:https://doi.org/10.1007/978-3-030-95228-0.

[40] Richard H. Helm. Inelastic and Elastic Scattering of 187-Mev Electrons from Selected Even-Even Nuclei. *Phys. Rev.*, 104:1466–1475, Dec 1956. URL: https://link.aps.org/doi/10.1103/PhysRev.104.1466, doi:10.1103/PhysRev.104.1466.

[41] J.D. Lewin and P.F. Smith. Review of mathematics, numerical factors, and corrections for dark matter experiments based on elastic nuclear recoil. *Astroparticle Physics*, 6(1):87–112, 1996. URL: https://www.sciencedirect.com/science/article/pii/S0927650596000473, doi:https://doi.org/10.1016/S0927-6505(96)00047-3.

[42] F. Donato, N. Fornengo, and S. Scopel. Effects of galactic dark halo rotation on WIMP direct detection. *Astroparticle Physics*, 9(3):247–260, 1998. URL: https://www.sciencedirect.com/science/article/pii/S0927650598000255, doi:https://doi.org/10.1016/S0927-6505(98)00025-5.

[43] Martin C. Smith, Gregory R. Ruchti, Amina Helmi, Rosemary F. G. Wyse, J. P. Fulbright, K. C. Freeman, J. F. Navarro, G. M. Seabroke, M. Steinmetz, M. Williams, O. Bienaymé, J. Binney, J. Bland-Hawthorn, W. Dehnen, B. K. Gibson, G. Gilmore, E. K. Grebel, U. Munari, Q. A. Parker, R.-D. Scholz, A. Siebert, F. G. Watson, and T. Zwitter. The RAVE survey: constraining the local Galactic escape speed. *Monthly Notices of the Royal Astronomical Society*, 379(2):755–772, 07 2007. arXiv:https://academic.oup.com/mnras/article-pdf/379/2/755/3399611/mnras0379-0755.pdf, doi:10.1111/j.1365-2966.2007.11964.x.

[44] Teresa Marrodán Undagoitia and Ludwig Rauch. Dark matter direct-detection experiments. *Journal of Physics G: Nuclear and Particle Physics*, 43(1):013001, dec

2015. URL: https://dx.doi.org/10.1088/0954-3899/43/1/013001, doi:10.1088/0954-3899/43/1/013001.

[45] Mark W. Goodman and Edward Witten. Detectability of certain dark-matter candidates. *Phys. Rev. D*, 31:3059–3063, Jun 1985. URL: https://link.aps.org/doi/10.1103/PhysRevD.31.3059, doi:10.1103/PhysRevD.31.3059.

[46] R. Bernabei et al. First model independent results from DAMA/LIBRA-phase2. *Nuclear Physics and Atomic Energy*, 19(4):307–325, dec 2018. URL: https://doi.org/10.15407%2Fjnpae2018.04.307, doi:10.15407/jnpae2018.04.307.

[47] J. Amaré, S. Cebrián, D. Cintas, I. Coarasa, E. García, M. Martínez, M. A. Oliván, Y. Ortigoza, A. Ortiz de Solórzano, J. Puimedón, A. Salinas, M. L. Sarsa, and P. Villar. Annual modulation results from three-year exposure of ANAIS-112. *Phys. Rev. D*, 103:102005, May 2021. URL: https://link.aps.org/doi/10.1103/PhysRevD.103.102005, doi:10.1103/PhysRevD.103.102005.

[48] G. Adhikari et al. Three-year annual modulation search with COSINE-100. *Phys. Rev. D*, 106:052005, Sep 2022. URL: https://link.aps.org/doi/10.1103/PhysRevD.106.052005, doi:10.1103/PhysRevD.106.052005.

[49] Giulia D'Imperio, M. Antonello, E. Barberio, T. Baroncelli, Jay Benziger, Lindsey Bignell, I. Bolognino, Frank Calaprice, Simone Copello, D. DAngelo, Ioan Dafinei, G. Carlo, M. Diemoz, A. Ludovico, Alan Duffy, Francis Froborg, G.K. Giovanetti, E. Hoppe, Aldo Ianni, and M. Zurowski. The SABRE experiment for dark matter search. In *Proceedings of The 39th International Conference on High Energy Physics — PoS(ICHEP2018)*, volume 340, page 653, 08 2019. doi:10.22323/1.340.0653.

[50] M. Lai on behalf of DEAP-3600 collaboration. Recent results from DEAP-3600. *Journal of Instrumentation*, 18(02):C02046, feb 2023. URL: https://dx.doi.org/10.1088/1748-0221/18/02/C02046, doi:10.1088/1748-0221/18/02/C02046.

[51] Koichi Ichimura. Latest results from the XMASS experiment. *AIP Conference Proceedings*, 2319(1):040011, 2021. URL: https://aip.scitation.org/doi/abs/10.1063/5.0037305, arXiv:https://aip.scitation.org/doi/pdf/10.1063/5.0037305, doi:10.1063/5.0037305.

[52] E. Aprile et al. Light Dark Matter Search with Ionization Signals in XENON1T. *Phys. Rev. Lett.*, 123:251801, Dec 2019. URL: https://link.aps.org/doi/1

0.1103/PhysRevLett.123.251801, doi:10.1103/PhysRevLett.123.251801.

[53] D. S. Akerib et al. Results from a Search for Dark Matter in the Complete LUX Exposure. *Phys. Rev. Lett.*, 118:021303, Jan 2017. URL: https://link.aps.org/doi/10.1103/PhysRevLett.118.021303, doi:10.1103/PhysRevLett.118.021303.

[54] Jianglai Liu. *The first results of PandaX-4T*, pages 85–94. URL: https://www.worldscientific.com/doi/abs/10.1142/9789811269776_0005, arXiv:https://www.worldscientific.com/doi/pdf/10.1142/9789811269776_0005, doi:10.1142/9789811269776_0005.

[55] D. S. Akerib et al. Projected WIMP sensitivity of the LUX-ZEPLIN dark matter experiment. *Phys. Rev. D*, 101:052002, Mar 2020. URL: https://link.aps.org/doi/10.1103/PhysRevD.101.052002, doi:10.1103/PhysRevD.101.052002.

[56] G. Zuzel, Paolo Agnes, Ivone Albuquerque, Trenton Alexander, A. Alton, D. Asner, H. Back, B. Baldin, K. Biery, Valerio Bocci, G. Bonfini, W. Bonivento, M. Bossa, Barbara Bottino, Augusto Brigatti, J. Brodsky, F. Budano, S. Bussino, Matteo Cadeddu, and Chunfu Zhu. The DarkSide Experiment: Present Status and Future. *Journal of Physics: Conference Series*, 798, 01 2017. doi:10.1088/1742-6596/798/1/012109.

[57] Q. Arnaud et al. Spherical Proportional Counter: A review of recent developments. *Journal of Physics: Conference Series*, 1029(1):012006, may 2018. URL: https://dx.doi.org/10.1088/1742-6596/1029/1/012006, doi:10.1088/1742-6596/1029/1/012006.

[58] Q. Arnaud et al. First results from the NEWS-G direct dark matter search experiment at the LSM. *Astroparticle Physics*, 97:54–62, 2018. URL: https://www.sciencedirect.com/science/article/pii/S0927650517301871, doi:https://doi.org/10.1016/j.astropartphys.2017.10.009.

[59] Carsten Krauss. PICO-60 Results and PICO-40L Status. *Journal of Physics: Conference Series*, 1468:012043, 02 2020. doi:10.1088/1742-6596/1468/1/012043.

[60] F Aubin, M Auger, M-H Genest, G Giroux, R Gornea, R Faust, C Leroy, L Lessard, J-P Martin, T Morlat, M-C Piro, N Starinski, V Zacek, B Beltran, C B Krauss, E Behnke, I Levine, T Shepherd, P Nadeau, U Wichoski, S Pospisil, I Stekl, J Sodomka, K Clark, X Dai, A Davour, C Levy, A J Noble, and C Storey. Discrimination of nuclear recoils from alpha particles with superheated liquids. *New Journal of*

Physics, 10(10):103017, oct 2008. URL: https://dx.doi.org/10.1088/1367-2630/10/10/103017, doi:10.1088/1367-2630/10/10/103017.

[61] Q. Arnaud et al. First Germanium-Based Constraints on Sub-MeV Dark Matter with the EDELWEISS Experiment. *Phys. Rev. Lett.*, 125:141301, Oct 2020. URL: https://link.aps.org/doi/10.1103/PhysRevLett.125.141301, doi:10.1103/PhysRevLett.125.141301.

[62] D. W. Amaral et al. Constraints on low-mass, relic dark matter candidates from a surface-operated SuperCDMS single-charge sensitive detector. *Phys. Rev. D*, 102:091101, Nov 2020. URL: https://link.aps.org/doi/10.1103/PhysRevD.102.091101, doi:10.1103/PhysRevD.102.091101.

[63] A. H. Abdelhameed et al. First results from the CRESST-III low-mass dark matter program. *Phys. Rev. D*, 100:102002, Nov 2019. URL: https://link.aps.org/doi/10.1103/PhysRevD.100.102002, doi:10.1103/PhysRevD.100.102002.

[64] G. Angloher et al. COSINUS: Cryogenic Calorimeters for the Direct Dark Matter Search with NaI Crystals. *Journal of Low Temperature Physics*, 200:428–436, 2020. doi:10.1007/s10909-020-02464-9.

[65] I. Arnquist et al. The DAMIC-M Experiment: Status and First Results, 2022. arXiv:2210.12070.

[66] Liron Barak, Itay M. Bloch, Mariano Cababie, Gustavo Cancelo, Luke Chaplinsky, Fernando Chierchie, Michael Crisler, Alex Drlica-Wagner, Rouven Essig, Juan Estrada, Erez Etzion, Guillermo Fernandez Moroni, Daniel Gift, Sravan Munagavalasa, Aviv Orly, Dario Rodrigues, Aman Singal, Miguel Sofo Haro, Leandro Stefanazzi, Javier Tiffenberg, Sho Uemura, Tomer Volansky, and Tien-Tien Yu. SENSEI: Direct-Detection Results on sub-GeV Dark Matter from a New Skipper CCD. *Phys. Rev. Lett.*, 125:171802, Oct 2020. URL: https://link.aps.org/doi/10.1103/PhysRevLett.125.171802, doi:10.1103/PhysRevLett.125.171802.

[67] Julien Billard, Mark Boulay, Susana Cebrián, Laura Covi, Giuliana Fiorillo, Anne Green, Joachim Kopp, Béla Majorovits, Kimberly Palladino, Federica Petricca, Leszek Roszkowski (chair), and Marc Schumann. Direct detection of dark matter - APPEC committee report*. *Reports on Progress in Physics*, 85(5):056201, apr 2022. URL: https://dx.doi.org/10.1088/1361-6633/ac5754, doi:10.1088/1361-6633/ac5754.

[68] Z. Z. Liu et al. Constraints on Spin-Independent Nucleus Scattering with sub-GeV Weakly Interacting Massive Particle Dark Matter from the CDEX-1B Experiment

at the China Jinping Underground Laboratory. *Phys. Rev. Lett.*, 123:161301, Oct 2019. URL: https://link.aps.org/doi/10.1103/PhysRevLett.123.161301, doi:10.1103/PhysRevLett.123.161301.

[69] R. Agnese et al. Search for low-mass dark matter with CDMSlite using a profile likelihood fit. *Phys. Rev. D*, 99:062001, Mar 2019. URL: https://link.aps.org/doi/10.1103/PhysRevD.99.062001, doi:10.1103/PhysRevD.99.062001.

[70] The COSINE-100 Collaboration. An experiment to search for dark-matter interactions using sodium iodide detectors. *Nature*, 564:83–86, 2018. doi:10.1038/s41586-018-0739-1.

[71] The CRESST Collaboration. Results on MeV-scale dark matter from a gram-scale cryogenic calorimeter operated above ground. *he European Physical Journal C*, 77:637, 2017. URL: https://doi.org/10.1140/epjc/s10052-017-5223-9, doi:0.1140/epjc/s10052-017-5223-9.

[72] R. Bernabei et al. First results from DAMA/LIBRA and the combined results with DAMA/NaI. *The European Physical Journal C*, 56:333–355, 2008. doi:10.1140/epjc/s10052-008-0662-y.

[73] C. Savage, G. Gelmini, P. Gondolo, and K. Freese. Compatibility of DAMA/LIBRA dark matter detection with other searches. *Journal of Cosmology and Astroparticle Physics*, 2009(04):010, apr 2009. URL: https://dx.doi.org/10.1088/1475-7516/2009/04/010, doi:10.1088/1475-7516/2009/04/010.

[74] A. Aguilar-Arevalo, D. Amidei, D. Baxter, G. Cancelo, B. A. Cervantes Vergara, A. E. Chavarria, J. C. D'Olivo, J. Estrada, F. Favela-Perez, R. Gaïor, Y. Guardincerri, E. W. Hoppe, T. W. Hossbach, B. Kilminster, I. Lawson, S. J. Lee, A. Letessier-Selvon, A. Matalon, P. Mitra, C. T. Overman, A. Piers, P. Privitera, K. Ramanathan, J. Da Rocha, Y. Sarkis, M. Settimo, R. Smida, R. Thomas, J. Tiffenberg, M. Traina, R. Vilar, and A. L. Virto. Results on Low-Mass Weakly Interacting Massive Particles from an 11 kg d Target Exposure of DAMIC at SNOLAB. *Phys. Rev. Lett.*, 125:241803, Dec 2020. URL: https://link.aps.org/doi/10.1103/PhysRevLett.125.241803, doi:10.1103/PhysRevLett.125.241803.

[75] P. Agnes et al. DarkSide-50 532-day dark matter search with low-radioactivity argon. *Phys. Rev. D*, 98:102006, Nov 2018. URL: https://link.aps.org/doi/10.1103/PhysRevD.98.102006, doi:10.1103/PhysRevD.98.102006.

[76] P. Agnes et al. Low-Mass Dark Matter Search with the DarkSide-50 Experiment. *Phys. Rev. Lett.*, 121:081307, Aug 2018. URL: https://link.aps.org/doi

/10.1103/PhysRevLett.121.081307, doi:10.1103/PhysRevLett.121.081307.

[77] R. Ajaj et al. Search for dark matter with a 231-day exposure of liquid argon using DEAP-3600 at SNOLAB. *Phys. Rev. D*, 100:022004, Jul 2019. URL: https://link.aps.org/doi/10.1103/PhysRevD.100.022004, doi:10.1103/PhysRevD.100.022004.

[78] E. Armengaud, C. Augier, A. Benoît, A. Benoit, L. Bergé, J. Billard, A. Broniatowski, P. Camus, A. Cazes, M. Chapellier, F. Charlieux, D. Ducimetière, L. Dumoulin, K. Eitel, D. Filosofov, J. Gascon, A. Giuliani, M. Gros, M. De Jésus, Y. Jin, A. Juillard, M. Kleifges, R. Maisonobe, S. Marnieros, D. Misiak, X.-F. Navick, C. Nones, E. Olivieri, C. Oriol, P. Pari, B. Paul, D. Poda, E. Queguiner, S. Rozov, V. Sanglard, B. Siebenborn, L. Vagneron, M. Weber, E. Yakushev, A. Zolotarova, and B. J. Kavanagh. Searching for low-mass dark matter particles with a massive Ge bolometer operated above ground. *Phys. Rev. D*, 99:082003, Apr 2019. URL: https://link.aps.org/doi/10.1103/PhysRevD.99.082003, doi:10.1103/PhysRevD.99.082003.

[79] L. Hehn, E. Armengaud, and et al. Improved EDELWEISS-III sensitivity for low-mass WIMPs using a profile likelihood approach. *The European Physical Journal C*, 76:548, 2016. doi:10.1140/epjc/s10052-016-4388-y.

[80] D. S. Akerib et al. Results of a Search for Sub-GeV Dark Matter Using 2013 LUX Data. *Phys. Rev. Lett.*, 122:131301, Apr 2019. URL: https://link.aps.org/doi/10.1103/PhysRevLett.122.131301, doi:10.1103/PhysRevLett.122.131301.

[81] Xiangyi Cui et al. Dark Matter Results from 54-Ton-Day Exposure of PandaX-II Experiment. *Phys. Rev. Lett.*, 119:181302, Oct 2017. URL: https://link.aps.org/doi/10.1103/PhysRevLett.119.181302, doi:10.1103/PhysRevLett.119.181302.

[82] R. Agnese et al. Search for Low-Mass Weakly Interacting Massive Particles with SuperCDMS. *Phys. Rev. Lett.*, 112:241302, Jun 2014. URL: https://link.aps.org/doi/10.1103/PhysRevLett.112.241302, doi:10.1103/PhysRevLett.112.241302.

[83] E. Aprile et al. XENON100 dark matter results from a combination of 477 live days. *Phys. Rev. D*, 94:122001, Dec 2016. URL: https://link.aps.org/doi/10.1103/PhysRevD.94.122001, doi:10.1103/PhysRevD.94.122001.

[84] E. Aprile et al. Dark Matter Search Results from a One Ton-Year Exposure of XENON1T. *Phys. Rev. Lett.*, 121:111302, Sep 2018. URL: https://link.aps.

org/doi/10.1103/PhysRevLett.121.111302, doi:10.1103/PhysRevLett.121.111302.

[85] E. Aprile et al. Search for Light Dark Matter Interactions Enhanced by the Migdal Effect or Bremsstrahlung in XENON1T. *Phys. Rev. Lett.*, 123:241803, Dec 2019. URL: https://link.aps.org/doi/10.1103/PhysRevLett.123.241803, doi:10.1103/PhysRevLett.123.241803.

[86] E. Aprile et al. Search for Coherent Elastic Scattering of Solar ^{8}B Neutrinos in the XENON1T Dark Matter Experiment. *Phys. Rev. Lett.*, 126:091301, Mar 2021. URL: https://link.aps.org/doi/10.1103/PhysRevLett.126.091301, doi:10.1103/PhysRevLett.126.091301.

[87] Daniel Z. Freedman. Coherent effects of a weak neutral current. *Phys. Rev. D*, 9:1389–1392, Mar 1974. URL: https://link.aps.org/doi/10.1103/PhysRevD.9.1389, doi:10.1103/PhysRevD.9.1389.

[88] Dimitrios Papoulias, Theocharis Kosmas, and Yoshitaka Kuno. Recent Probes of Standard and Non-standard Neutrino Physics With Nuclei. *Frontiers in Physics*, 7:191, 11 2019. doi:10.3389/fphy.2019.00191.

[89] D. Akimov et al. Observation of coherent elastic neutrino-nucleus scattering. *Science*, 357(6356):1123–1126, 2017. URL: https://www.science.org/doi/abs/10.1126/science.aao0990, arXiv:https://www.science.org/doi/pdf/10.1126/science.aao0990, doi:10.1126/science.aao0990.

[90] R. Aaij et al. Measurement of the forward-backward asymmetry in $Z/\gamma^* \to \mu^+\mu^-$ decays and determination of the effective weak mixing angle. *Journal of High Energy Physics*, 2015:190, 2015. doi:10.1007/JHEP11(2015)190.

[91] Lars Bastian Mohrmann. *Characterizing cosmic neutrino sources – a measurement of the energy spectrum and flavor composition of the cosmic neutrino flux observed with the IceCube Neutrino Observatory*. PhD thesis, Humboldt U., Berlin, 11 2015.

[92] S. Di Lorenzo. *Multiple detector analysis in the CRESST Dark Matter experiment*. PhD thesis, Gran Sasso Science Institute, 2020.

[93] G. Bellini et al. Cosmic-muon flux and annual modulation in Borexino at 3800 m water-equivalent depth. *Journal of Cosmology and Astroparticle Physics*, 2012(05):015, may 2012. URL: https://dx.doi.org/10.1088/1475-7516/2012/05/015, doi:10.1088/1475-7516/2012/05/015.

[94] G. Angloher, M. Bauer, I. Bavykina, A. Bento, A. Brown, C. Bucci, C. Ciemniak, C. Coppi, G. Deuter, F. von Feilitzsch, D. Hauff, S. Henry, P. Huff, J. Imber, S. Ingleby, C. Isaila, J. Jochum, M. Kiefer, M. Kimmerle, H. Kraus, J.-C. Lanfranchi, R.F. Lang, B. Majorovits, M. Malek, R. McGowan, V.B. Mikhailik, E. Pantic, F. Petricca, S. Pfister, W. Potzel, F. Pröbst, W. Rau, S. Roth, K. Rottler, C. Sailer, K. Schäffner, J. Schmaler, S. Scholl, W. Seidel, L. Stodolsky, A.J.B. Tolhurst, I. Usherov, and W. Westphal. Commissioning run of the CRESST-II dark matter search. *Astroparticle Physics*, 31(4):270–276, 2009. URL: https://www.sciencedirect.com/science/article/pii/S0927650509000358, doi:https://doi.org/10.1016/j.astropartphys.2009.02.007.

[95] A. Bassignani, B.B. Bam, G. Colombo, R. Fresca Fantoni, G. Giacomelli, M. Mascoli, V. Fracchetta, L. Patrizii, and C. Sartorio. Measurements of radon concentration and gamma ray activity in Hall B of the Gran Sasso Laboratory. *Radiation Measurements*, 28(1):609–612, 1997. URL: https://www.sciencedirect.com/science/article/pii/S1350448797001510, doi:https://doi.org/10.1016/S1350-4487(97)00151-0.

[96] F. Pröbst, M. Frank, and S. et al. Cooper. Model for cryogenic particle detectors with superconducting phase transition thermometers. *Journal of Low Temperature Physics*, 100:69–104, 1995. doi:10.1007/BF00753837.

[97] Florian Reindl. *Exploring Light Dark Matter With CRESST-II Low-Threshold Detectors*. Dissertation, Technische Universität München, München, 2016.

[98] N. Ferreiro Iachellini. *Increasing the sensitivity to low mass dark matter in CRESST-III with a new DAQ and signal processing*. PhD thesis, Ludwig-Maximilians-Universität München, 2018.

[99] E. Gatti and P. F. Manfredi. Processing the signals from solid-state detectors in elementary-particle physics. *La Rivista del Nuovo Cimento (1978-1999)*, 9:1–146, 1986. doi:10.1007/BF02822156.

[100] M. Mancuso, A. Bento, N. Ferreiro Iachellini, D. Hauff, F. Petricca, F. Pröbst, J. Rothe, and R. Strauss. A method to define the energy threshold depending on noise level for rare event searches. *Nuclear Instruments and Methods in Physics Research Section A: Accelerators, Spectrometers, Detectors and Associated Equipment*, 940:492–496, 2019. URL: https://www.sciencedirect.com/science/article/pii/S0168900219308708, doi:https://doi.org/10.1016/j.nima.2019.06.030.

[101] *Update of X Ray and Gamma Ray Decay Data Standards for Detector Calibration and Other Applications*. Non-serial Publications. INTERNATIONAL ATOMIC ENERGY

AGENCY, Vienna, 2007. URL: https://www.iaea.org/publications/7551/update-of-x-ray-and-gamma-ray-decay-data-standards-for-detector-calibration-and-other-applications.

[102] Raimund Strauss et al. Energy-dependent light quenching in $CaWO_4$ crystals at mK temperatures. *The European Physical Journal C*, 74, 2014. doi:10.1140/epjc/s10052-014-2957-5.

[103] D. Schmiedmayer. Calculation of Dark-Matter Exclusion-Limits using a Maximum Likelihood Approach, 2019.

[104] S. Yellin. Finding an upper limit in the presence of an unknown background. *Phys. Rev. D*, 66:032005, Aug 2002. URL: https://link.aps.org/doi/10.1103/PhysRevD.66.032005, doi:10.1103/PhysRevD.66.032005.

[105] S. S. Wilks. The Large-Sample Distribution of the Likelihood Ratio for Testing Composite Hypotheses. *The Annals of Mathematical Statistics*, 9(1):60 – 62, 1938. doi:10.1214/aoms/1177732360.

[106] G. Cowan, K. Cranmer, E. Gross, and O. Vitells. Asymptotic formulae for likelihood-based tests of new physics. *The European Physical Journal C*, 71, 2011. URL: https://doi.org/10.1140/epjc/s10052-011-1554-0.

[107] G. Angloher et al. Latest observations on the low energy excess in CRESST-III. In *14th International Workshop on the Identification of Dark Matter 2022*, 7 2022. arXiv:2207.09375.

[108] R. Strauss, J. Rothe, G. Angloher, A. Bento, A. Gütlein, D. Hauff, H. Kluck, M. Mancuso, L. Oberauer, F. Petricca, F. Pröbst, J. Schieck, S. Schönert, W. Seidel, and L. Stodolsky. Gram-scale cryogenic calorimeters for rare-event searches. *Phys. Rev. D*, 96:022009, Jul 2017. URL: https://link.aps.org/doi/10.1103/PhysRevD.96.022009, doi:10.1103/PhysRevD.96.022009.

[109] The NUCLEUS Collaboration. NUCLEUS: Exploring Coherent Neutrino-Nucleus Scattering with Cryogenic Detectors. *Journal of Low Temperature Physics*, 199:433–440, April 2020. doi:10.1007/s10909-019-02283-7.

[110] R. Agnese et al. First Dark Matter Constraints from a SuperCDMS Single-Charge Sensitive Detector. *Phys. Rev. Lett.*, 121:051301, Aug 2018. URL: https://link.aps.org/doi/10.1103/PhysRevLett.121.051301, doi:10.1103/PhysRevLett.121.051301.

[111] I. Alkhatib et al. Light Dark Matter Search with a High-Resolution Athermal Phonon Detector Operated above Ground. *Phys. Rev. Lett.*, 127:061801, Aug 2021.

URL: https://link.aps.org/doi/10.1103/PhysRevLett.127.061801, doi:10.1103/PhysRevLett.127.061801.

[112] Prakruth Adari et al. EXCESS workshop: Descriptions of rising low-energy spectra. *SciPost Physics Proceedings*, 9, aug 2022. URL: https://doi.org/10.21468%2Fscipostphysproc.9.001, doi:10.21468/scipostphysproc.9.001.

[113] P. Bauer. *Data Analysis for the CRESST Experiment: New Methods, improved Alpha Analysis, and Results on Light Dark Matter and Backgrounds*. Dissertation, Technische Universität München, München, 2020.

[114] M. Stahlberg. *Probing Low-Mass Dark Matter with CRESST-III*. PhD thesis, Technische Universität Wien, 2020. URL: http://katalog.ub.tuwien.ac.at/AC15141142.

[115] CRESST Collaboration. Low Energy Excess in CRESST, June 2021. URL: https://indico.cern.ch/event/1013203/contributions/4364412/attachments/2264006/3843530/CRESST_EXCESS_Workshop.pdf.

[116] E. Queguiner. *Analysis of the data of the EDELWEISS-LT experiment searching for low-mass WIMP*. PhD thesis, Université de Lyon, 2018.

[117] Daniel Mckinsey. Stress Induced Background in Cryogenic Crystal Calorimeters, July 2022. URL: https://indico.cern.ch/event/1117540/contributions/4956923/attachments/2481024/4259148/EXCESS%202022%20Slides%20Romani%20Roger.pdf.

[118] M. Bühler et al. Status and low background considerations for the CRESST dark matter search. *Nucl. Instrum. Meth. A*, 370:237–240, 1996. doi:10.1016/0168-9002(95)01095-5.

[119] P. Colling, A. Nucciotti, C. Bucci, S. Cooper, P. Ferger, M. Frank, U. Nagel, F. Pröbst, and W. Seidel. Low-energy X-ray detection in cryogenic detectors with tungsten thermometers. *Nuclear Instruments and Methods in Physics Research Section A: Accelerators, Spectrometers, Detectors and Associated Equipment*, 354(2):408–416, 1995. URL: https://www.sciencedirect.com/science/article/pii/0168900294010803, doi:https://doi.org/10.1016/0168-9002(94)01080-3.

[120] Rafael F. Lang. The CRESST-II Experiment. In *43rd Rencontres de Moriond on Electroweak Interactions and Unified Theories*, pages 451–456, 5 2008. arXiv:0805.4705.

[121] P. Meunier, M. Bravin, M. Bruckmayer, S. Giordano, M. Loidl, O. Meier, F. Pröbst, W. Seidel, M. Sisti, L. Stodolsky, S. Uchaikin, and L. Zerle. Discrimination between

nuclear recoils and electron recoils by simultaneous detection of phonons and scintillation light. *Applied Physics Letters*, 75(9):1335–1337, 1999. arXiv:https://doi.org/10.1063/1.124685, doi:10.1063/1.124685.

[122] V. Wagner on behalf of the CRAB Collaboration. Accurate Calibration of Nuclear Recoils at the 100 eV Scale Using Neutron Capture. *Journal of Low Temperature Physics*, 2022. doi:10.1007/s10909-022-02816-7.

[123] L. Thulliez, D. Lhuillier, F. Cappella, N. Casali, R. Cerulli, A. Chalil, A. Chebboubi, E. Dumonteil, A. Erhart, A. Giuliani, F. Gunsing, E. Jericha, M. Kaznacheeva, A. Kinast, A. Langenkämper, T. Lasserre, A. Letourneau, O. Litaize, P. de Marcillac, S. Marnieros, T. Materna, B. Mauri, E. Mazzucato, C. Nones, T. Ortmann, L. Pattavina, D.V. Poda, R. Rogly, N. Schermer, O. Serot, G. Soum, L. Stodolsky, R. Strauss, M. Vignati, M. Vivier, V. Wagner, and A. Wex. Calibration of nuclear recoils at the 100 eV scale using neutron capture. *Journal of Instrumentation*, 16(07):P07032, jul 2021. URL: https://dx.doi.org/10.1088/1748-0221/16/07/P07032, doi:10.1088/1748-0221/16/07/P07032.

[124] CRAB Collaboration and NUCLEUS Collaboration. Observation of a nuclear recoil peak at the 100 eV scale induced by neutron capture, 2022. URL: https://arxiv.org/abs/2211.03631, doi:10.48550/ARXIV.2211.03631.

[125] CRESST Collaboration. Observation of a low energy nuclear recoil peak in the neutron calibration data of the CRESST-III Experiment, 2023. arXiv:2303.15315.

[126] R.B. Firestone, K. Abusaleem, Shamsuzzoha Basunia, Frantisek Becvar, Tamas Belgya, L.A. Bernstein, H D Choi, J.E. Escher, Christoph Genreith, A.M. Hurst, M. Krtika, Paul Renne, Zsolt Revay, A.M. Rogers, M. Rossbach, Sunniva Siem, B. Sleaford, N.C. Summers, László Szentmiklósi, and M. Wiedeking. EGAF: Measurement and Analysis of Gamma-ray Cross Sections. *Nuclear Data Sheets*, 119:79–87, 05 2014. doi:10.1016/j.nds.2014.08.024.

[127] D.A. Brown et al. ENDF/B-VIII.0: The 8th Major Release of the Nuclear Reaction Data Library with CIELO-project Cross Sections, New Standards and Thermal Scattering Data. *Nuclear Data Sheets*, 148:1–142, 2018. Special Issue on Nuclear Reaction Data. URL: https://www.sciencedirect.com/science/article/pii/S0090375218300206, doi:https://doi.org/10.1016/j.nds.2018.02.001.

[128] M. Shamsuzzoha Basunia. Nuclear Data Sheets for A = 28. *Nuclear Data Sheets*, 114(10):1189–1291, 2013. URL: https://www.sciencedirect.com/science/article/pii/S0090375213000653, doi:https://doi.org/10.1016/j.nds.2013.10.001.

[129] A. Fuss from the CRESST simulation group. Private Communication.

[130] A. H. Abdelhameed et al. Geant4-based electromagnetic background model for the CRESST dark matter experiment. *The European Physical Journal C*, 79, 2019. doi:10.1140/epjc/s10052-019-7385-0.

[131] W.A. Runciman. Sapphire luminescence under X-ray excitation. *Solid State Communications*, 6(8):537–539, 1968. URL: https://www.sciencedirect.com/science/article/pii/0038109868905061, doi:https://doi.org/10.1016/0038-1098(68)90506-1.

[132] M. Kirm, G. Zimmerer, E. Feldbach, A. Lushchik, Ch. Lushchik, and F. Savikhin. Self-trapping and multiplication of electronic excitations in Al_2O_3 and Al_2O_3 : Sc crystals. *Phys. Rev. B*, 60:502–510, Jul 1999. URL: https://link.aps.org/doi/10.1103/PhysRevB.60.502, doi:10.1103/PhysRevB.60.502.

[133] A. Lushchik, M. Kirm, Ch. Lushchik, I. Martinson, and G. Zimmerer. Luminescence of free and self-trapped excitons in wide-gap oxides. *Journal of Luminescence*, 87-89:232–234, 2000. URL: https://www.sciencedirect.com/science/article/pii/S0022231399002719, doi:https://doi.org/10.1016/S0022-2313(99)00271-9.

[134] Marco Kirm, Vachagan Harutunyan, Vladimir Makhov, and Sebastian Vielhauer. VUV luminescence of as-grown and electron irradiated corundum single crystals. In Arnold Rosental, editor, *Optical Materials and Applications*, volume 5946, page 594606. International Society for Optics and Photonics, SPIE, 2006. doi:10.1117/12.639064.

[135] A.C. Thompson. *X-ray Data Booklet*. Lawrence Berkeley National Laboratory, University of California, 2001. URL: https://books.google.de/books?id=WV05HAAACAAJ.

[136] CRESST Collaboration. Results on sub-GeV Dark Matter from a 10 eV Threshold CRESST-III Silicon Detector, 2022. URL: https://arxiv.org/abs/2212.12513, doi:10.48550/ARXIV.2212.12513.

[137] J. Billard, E. Figueroa-Feliciano, and L. Strigari. Implication of neutrino backgrounds on the reach of next generation dark matter direct detection experiments. *Phys. Rev. D*, 89:023524, Jan 2014. URL: https://link.aps.org/doi/10.1103/PhysRevD.89.023524, doi:10.1103/PhysRevD.89.023524.

[138] L. Baudis, A. Ferella, A. Kish, A. Manalaysay, T. Marrodán Undagoitia, and M. Schumann. Neutrino physics with multi-ton scale liquid xenon detectors. *Journal of Cosmology and Astroparticle Physics*, 2014(01):044, jan 2014. URL: ht

tps://dx.doi.org/10.1088/1475-7516/2014/01/044, doi:10.1088/1475-7516/2014/01/044.

[139] Marc Schumann, Laura Baudis, Lukas Bütikofer, Alexander Kish, and Marco Selvi. Dark matter sensitivity of multi-ton liquid xenon detectors. *Journal of Cosmology and Astroparticle Physics*, 2015(10):016, oct 2015. URL: https://dx.doi.org/10.1088/1475-7516/2015/10/016, doi:10.1088/1475-7516/2015/10/016.

[140] Maurizio Salaris and Santi Cassisi. *Evolution of Stars and Stellar Populations*. John Wiley & Sons, 2005. URL: https://cfas.org/data/uploads/astronomy-ebooks/evolution_of_stars_and_stellar_populations.pdf.

[141] Mariia Redchuk. Solar neutrino analysis with the Borexino detector. *Journal of Physics: Conference Series*, 1056:012050, 07 2018. doi:10.1088/1742-6596/1056/1/012050.

[142] John N. Bahcall, Aldo M. Serenelli, and Sarbani Basu. New Solar Opacities, Abundances, Helioseismology, and Neutrino Fluxes. *The Astrophysical Journal*, 621(1):L85–L88, jan 2005. URL: https://doi.org/10.1086%2F428929, doi:10.1086/428929.

[143] John N. Bahcall and Aldo M. Serenelli. How Do Uncertainties in the Surface Chemical Composition of the Sun Affect the Predicted Solar Neutrino Fluxes? *The Astrophysical Journal*, 626(1):530–542, jun 2005. URL: https://doi.org/10.1086%2F429883, doi:10.1086/429883.

[144] Achim Gütlein. *Feasibility Study for a First Observation of Coherent Neutrino Nucleus Scattering Using Low-Temperature Detectors*. Dissertation, Technische Universität München, München, 2013.

[145] F. Ruppin, J. Billard, E. Figueroa-Feliciano, and L. Strigari. Complementarity of dark matter detectors in light of the neutrino background. *Phys. Rev. D*, 90:083510, Oct 2014. URL: https://link.aps.org/doi/10.1103/PhysRevD.90.083510, doi:10.1103/PhysRevD.90.083510.

[146] Katherine Freese, Mariangela Lisanti, and Christopher Savage. Colloquium: Annual modulation of dark matter. *Rev. Mod. Phys.*, 85:1561–1581, Nov 2013. URL: https://link.aps.org/doi/10.1103/RevModPhys.85.1561, doi:10.1103/RevModPhys.85.1561.

[147] F. Mayet, A.M. Green, J.B.R. Battat, J. Billard, N. Bozorgnia, G.B. Gelmini, P. Gondolo, B.J. Kavanagh, S.K. Lee, D. Loomba, J. Monroe, B. Morgan, C.A.J. OHare,

A.H.G. Peter, N.S. Phan, and S.E. Vahsen. A review of the discovery reach of directional dark matter detection. *Physics Reports*, 627:1–49, 2016. URL: https://www.sciencedirect.com/science/article/pii/S0370157316001022, doi:https://doi.org/10.1016/j.physrep.2016.02.007.

[148] David G. Cerdeño, Jonathan H. Davis, Malcolm Fairbairn, and Aaron C. Vincent. CNO neutrino Grand Prix: the race to solve the solar metallicity problem. *Journal of Cosmology and Astroparticle Physics*, 2018(04):037, apr 2018. URL: https://dx.doi.org/10.1088/1475-7516/2018/04/037, doi:10.1088/1475-7516/2018/04/037.

[149] M. Agostini et al. Comprehensive measurement of pp-chain solar neutrinos. *Nature*, 562:505 – 510, 2018. doi:10.1038/s41586-018-0624-y.

[150] B. Aharmim et al. Combined analysis of all three phases of solar neutrino data from the Sudbury Neutrino Observatory. *Phys. Rev. C*, 88:025501, Aug 2013. URL: https://link.aps.org/doi/10.1103/PhysRevC.88.025501, doi:10.1103/PhysRevC.88.025501.

[151] K. Abe et al. Solar neutrino measurements in Super-Kamiokande-IV. *Phys. Rev. D*, 94:052010, Sep 2016. URL: https://link.aps.org/doi/10.1103/PhysRevD.94.052010, doi:10.1103/PhysRevD.94.052010.

[152] A. Yu. Smirnov. The MSW effect and Solar Neutrinos, 2003. arXiv:hep-ph/0305106.

[153] S. Appel et al. Improved Measurement of Solar Neutrinos from the Carbon-Nitrogen-Oxygen Cycle by Borexino and Its Implications for the Standard Solar Model. *Phys. Rev. Lett.*, 129:252701, Dec 2022. URL: https://link.aps.org/doi/10.1103/PhysRevLett.129.252701, doi:10.1103/PhysRevLett.129.252701.

[154] Bruce T. Cleveland, Timothy Daily, Jr. Raymond Davis, James R. Distel, Kenneth Lande, C. K. Lee, Paul S. Wildenhain, and Jack Ullman. Measurement of the Solar Electron Neutrino Flux with the Homestake Chlorine Detector. *The Astrophysical Journal*, 496(1):505, mar 1998. URL: https://dx.doi.org/10.1086/305343, doi:10.1086/305343.

[155] J. N. Abdurashitov, V. N. Gavrin, V. V. Gorbachev, P. P. Gurkina, T. V. Ibragimova, A. V. Kalikhov, N. G. Khairnasov, T. V. Knodel, I. N. Mirmov, A. A. Shikhin, E. P. Veretenkin, V. E. Yants, G. T. Zatsepin, T. J. Bowles, S. R. Elliott, W. A. Teasdale, J. S. Nico, B. T. Cleveland, and J. F. Wilkerson. Measurement of the solar neutrino capture rate with gallium metal. III. Results for the 2002–2007 data-taking period.

Phys. Rev. C, 80:015807, Jul 2009. URL: https://link.aps.org/doi/10.1103/PhysRevC.80.015807, doi:10.1103/PhysRevC.80.015807.

[156] F. Kaether, W. Hampel, G. Heusser, J. Kiko, and T. Kirsten. Reanalysis of the Gallex solar neutrino flux and source experiments. *Physics Letters B*, 685(1):47–54, 2010. URL: https://www.sciencedirect.com/science/article/pii/S0370269310000729, doi:https://doi.org/10.1016/j.physletb.2010.01.030.

[157] M. Agostini et al. Experimental evidence of neutrinos produced in the CNO fusion cycle in the Sun. *Nature*, 587:577 – 582, 2020. doi:10.1038/s41586-020-2934-0.

[158] A Yu Smirnov. The MSW Effect and Matter Effects in Neutrino Oscillations. *Physica Scripta*, 2005(T121):57, jan 2005. URL: https://dx.doi.org/10.1088/0031-8949/2005/T121/008, doi:10.1088/0031-8949/2005/T121/008.

[159] G. L. Fogli, E. Lisi, A. Palazzo, and A. M. Rotunno. Solar neutrino oscillations and indications of matter effects in the Sun. *Phys. Rev. D*, 67:073001, Apr 2003. URL: https://link.aps.org/doi/10.1103/PhysRevD.67.073001, doi:10.1103/PhysRevD.67.073001.

[160] Hisakazu Minakata and Carlos Pena-Garay. Solar Neutrino Observables Sensitive to Matter Effects, 2012. arXiv:1009.4869.

[161] M. Tanabashi et al. Review of Particle Physics. *Phys. Rev. D*, 98:030001, Aug 2018. URL: https://link.aps.org/doi/10.1103/PhysRevD.98.030001, doi:10.1103/PhysRevD.98.030001.

Acknowledgements

I would like to use these last pages to express my gratitude to all people involved in my work over the last years. After all the hard work, especially in the last months, I am immensly relieved and happy to finally having finished this thesis. On the other hand I get very nostalgic, realizing that this chapter of my life is coming to an end.

First and foremost I want to thank Federica Petricca. Not only for giving me the chance to join your group and this collaboration, but also for your continuous support and excellent supervision throughout the years. I could always rely on your valuable input for any kind of question. You also have the ability to know exactly when to give me the right amount of pushing when I need it. A huge thank you for your very fast and thorough proofreading of my thesis even over weekends and holidays. Your comments and suggestions were very appreciated and always helpful in improving the quality of this work. Your positive attitude and good sense helped to create a great working environment for me here at MPP.

Ich möchte auch Franz Pröbst dafür danken, meine Arbeit von Anfang an begleitet zu haben. Dein detailliertes Wissen über jeden Aspekt des CRESST Experiments hat mich schwer beeindruckt. Von Fragen zum experimentellen Aufbau, über die Detektoren, der Datenerfassung bishin zu den Analysemethoden, man konnte sich sicher sein dass man bei dir an der richtigen Adresse ist. Vielen Dank für deine Geduld und ausgiebigen Erklärungen. Außerdem noch vielen Dank für das gründliche Korrekturlesen meiner Arbeit.

Mein Dank geht auch an meine Doktormutter Susanne Mertens. Du hast mich dazu ermutigt nach meiner Masterarbeit weiter eine Karriere in der Wissenschaft anzustreben und mich auf eine PhD Stelle zu bewerben. Vielen Dank auch für deine immer schnelle und unkomplizierte Bereitschaft zu jeder Zeit.

I want to also thank the whole MPP group for the wonderful time I had during my time as a PhD student, of course including also the people that left the group since the time I started here, in particular the PhDs, Philipp, Johannes, Elia, Nahuel and Ahmed. Since the very beginning I felt very welcome in this open and friendly group. We had many interesting physics discussions and I enjoyed the constructive and supportive spirit here very much. Through the many activities we did together, I formed new friendships even beyond work.

I also want to thank all other groups of this collaboration. Without you this work would have been literally impossible. The data analyzed in this work would not exist

without the contribution of each and every member. Keeping the experiment running, collecting the data, providing the necessary tools to analyze the data is all possible due to the expertise of all my collaborators. Besides that it was always a pleasure to meet you all in person at the collaboration meetings. The atmosphere has always been very productive and creative with lots of interesting discussions, despite the lack of sleep that our long evenings might have caused.

In particular I would like to thank the Analysis Team of CRESST. The great discussions we had during our weekly meetings contributed a lot to the quality of my results.

The first of some special thanks goes to Nahuel Ferreiro, who invited me to visit the local labs and introduced me to the CRESST group at MPP. You have always been immensly helpful with questions related to coding in general, analysis and CAT. It was also thanks to you that I started my studies on solar neutrinos in cryogenic detectors, which developed into a major part of this thesis. In this context I want to also thank Lucia Canonica and Federica Petricca for further involving me and supporting me with this project.

Ein riesiges Dankeschön geht auch an Martin Stahlberg. Vielen Dank für deine Einführung und weitere Unterstützung in allen Fragen rund um CAT und den Analysemethoden in CRESST. Die unzähligen Stunden an skype-calls mit dir, während du mit dem Schreiben deiner eigenen Dissertation beschäftigt warst, sind nicht vergessen. Mein Verständnis der CRESST Analyse Software habe ich zu großen Teilen dir zu verdanken. Dank deiner Hilfe konnte ich auch meine Programmierkenntnisse in C++ und Root über die letzten Jahre erweitern.

Thanks also to Michele Mancuso for always patiently answering my questions and generally giving very helpful explanations. His input improved my understanding of this experiment by a lot. Thank you also for all the interesting physics discussions and of course for proofreading parts of this thesis. My thanks also go to Abhijit Garai for the proofreading of parts of my thesis, as well as always providing me with extra food during our lunch breaks, you definitely saved me a few times from starving. I am happy to have found friends in you. Also a thank you to Antonio Bento for all the interesting and funny conversations we had. Thanks also to the further proofreaders of parts of my thesis, Alexander Langenkämper and Athoy Nilima.

To Francesca Pucci, thank you for not only being a great colleague, but also a great "roommate" and a good friend. You always had an open ear and I am glad to have met you. Thank you also for the countless times I could enjoy your good cooking. Anna Bertolini, you are the best office mate I could have asked for. Working together with you on the analysis or on CAT was always a pleasure. Thank you also for proofreading parts of my thesis and for making sure I was never getting low on sugar. As fellow PhD students during most of my time here you both added very much to the great experience I had and I hope our friendship will continue also in the after-PhD-life. I must also

thank both of you for enduring my tempers and not getting completely crazy with me, especially during the last months of writing.

Also thanks to the new postdocs in our group that joined within my last year at MPP, Alexander Langenkämper and Beatrice Mauri. It was a pleasure to have you around, you also added a lot to the great time I had here. Also thanks to Felix, it was a great experience to have you as a student and I am glad you came back to fill the gap in the analysis team that I am leaving. I am sure that Anna will take good care of you.

Ich möchte auch noch Franz Pröbst, Florian Reindl und Uwe Leupold für ihre Unterstützung in der Verwaltung der CRESST Server danken. Franz und Florian, ihr habt mir zu jeder Zeit immer schnell geantwortet wenn ich Fragen hatte. Uwe, durch dich konnte ich noch viel lernen über IT Systemverwaltung. Danke auch, dass du immer schnell und unkompliziert geholfen hast, wenn ich mal nicht weiter wusste.

Vanessa, I have to thank you for so so much. In you I found much more than just a working colleague or a friend, but a partner in life. Thank you for always enduring my moods and your unconditional support. It's incredible how many late nights and weekends of work you spend on my side when you wouldn't have had to. Thank you also for the very thorough proofreading of my thesis. You had a much bigger impact on this work than you might think. Not only in helping me understand the theoretical aspects and statistical methods that I needed for some of the main results of my thesis, but also in helping me gaining more confidence in myself and my work. From you I already learned so much, in physics and way beyond physics, and I hope to keep doing so in the future.

To all the new friends I made during my PhD: Thank you for everything. The BBQ parties, Ringberg, boardgame nights, movie nights in and outside of MPP. You all had your part in making this time so special and I feel lucky having met you.

Und an meine alten Freunde, die seit jeher an meiner Seite waren und auf die ich mich immer verlassen kann: Danke, dass ich euch in meinem Leben haben darf. Ich habe gelernt, dass es nicht für jeden selbstverständlich ist, eine solche gefestigte und langjährige Freundesgruppe zu haben. Wirkliche Freunde, mit denen man nicht nur viel Spaß haben kann, sondern die auch da sind, wenn man sie braucht. Die es einem nicht übel nehmen, wenn man sich mal eine Zeit lang nicht viel meldet, sondern beim nächsten Treffen genau so sind, als hätte man sich jeden Tag gesehen. Mit denen man nicht nur Blödsinn, sondern auch über wichtiges reden kann. Ich wäre sicher nicht die Person, die ich heute bin, wenn ich euch nicht gehabt hätte.

Zu guter Letzt auch noch ein großes Danke an meine Familie, meine Eltern und Großeltern, meinen zweit-Papa und meine zweit-Oma und meine Geschwister. Wir sind zwar eine kleine Familie, aber ich weiß, dass ich immer auf euch zählen kann. Besonderer Dank geht an meine Mama, die mein Potential erkannt und immer an mich geglaubt hat, auch wenn ich es ihr nicht immer einfach gemacht habe. Ohne deine liebevolle und geduldige Unterstützung wäre ich niemals so weit gekommen.

Mein allerletzter Dank geht an Elsa, die das zwar nicht lesen kann, aber dennoch einen Platz hier verdient. Du hast mich durch so manche schwierige, aber auch durch viele gute Zeiten begleitet und ich hoffe, dass wir noch viele Jahre zusammen haben.